

COMPLETE PHOTOIONIZATION MEASUREMENTS
WITH HIGH HARMONIC SPECTROSCOPY

Dissertation

ZUR ERLANGUNG DES DOKTORGRADES
DER NATURWISSENSCHAFTEN

vorgelegt beim Fachbereich Physik
der Johann Wolfgang Goethe-Universität
in Frankfurt am Main

VON

Jan Troß

aus Lich

Frankfurt 2017
(D 30)

vom Fachbereich Physik der

Johann Wolfgang Goethe - Universität als Dissertation angenommen.

Dekan: Prof. Dr. Rene Reifarth

Gutachter: Prof. Dr. Reinhard Dörner, Dr. Carlos Trallero-Herrero

Datum der Disputation:

Contents

1	Motivation	7
2	Deutsche Zusammenfassung	9
3	Theoretical background	15
3.1	High harmonic generation	15
3.1.1	Interaction of light with matter	15
3.1.2	Factorization of High Harmonic Generation	16
3.1.3	Strong field approximation of HHG	19
3.2	Inelastic scattering and detailed balance	21
3.2.1	Principle of detailed balance	22
3.2.2	Models using the principle of detailed balance	23
3.2.3	Coherent nature of HHG	25
3.3	Molecular alignment	26
3.3.1	Classification of molecular rotors	27
3.3.2	Introduction to the rigid rotor in quantum mechanics	27
3.3.3	Particle in an external field	28
3.3.4	Asymmetric rotor	31
3.4	Fourier Optics	37
3.4.1	Transverse modes of light	37
3.4.2	Analytic Fourier Theory	40
3.4.3	Diffraction and Propagation	41
3.4.4	Beam tilt and Convergence	41
3.5	A double slit with focused light	42
3.5.1	Simple examples of shaping light by interference	42
3.5.2	Diffraction calculations	43
3.5.3	Creating two Gaussian beams without interference	49
3.5.4	Single beams for characterization of individual sources	54
4	Experimental techniques	57
4.1	Experimental setup	57
4.1.1	Spectrometer	57
4.1.2	Gas sources	59
4.2	Spatial light modulators	60
4.2.1	Spatially shaped pulses	61
4.2.2	Creation of delayed pulses via phase modulation	64
4.2.3	Chromatic dispersion	67
4.3	Youngs double slit with HHG	68
4.3.1	Resolution of a Young's double slit	71

5	Optical phase of high order harmonics	73
5.1	Experimental methods	73
5.2	A self-referencing interferometer with 12.5 as resolution	74
5.3	Phase matching scaling	77
6	Phase of the continuum electron wave packet	85
6.1	Classical action in the saddle point approximation	85
6.2	Phase of the wave packet in a single color field	87
6.2.1	Comparison to literature	95
6.3	Phase of the wave packet in a saturated medium	96
6.4	Phase of the wave packet in a two color field	99
6.4.1	Classical action in the saddle point approximation and two color field	101
6.4.2	Experimental measurements	101
6.5	Concluding remarks	104
7	High harmonics driven with elliptical fields	107
7.1	Theoretical tools for the photoionization measurements	107
7.2	The photoionization cross section of argon	109
7.3	Extension to long wavelength	112
8	The complex photoionization dipole of nitrogen	117
8.1	Fundamentals of describing the molecular frame signal	118
8.2	Measurement of the complex dipole of Nitrogen	120
9	The complex induced dipole of ethylene	129
9.1	Measurement of the absolute harmonic dipole	131
9.2	Extraction of the angle dependence out of the time-dependent observations	134
10	Conclusion and outlook	143
11	Acknowledgement	145
12	Lebenslauf	147
A	Appendix	149
A.1	Linear regression of a complex entity	149
A.2	Spot size measurements	150
A.3	Bending effects	151
A.4	SLM efficiencies	152
A.5	Rotational Constants	153

List of Figures

2.1	Eadweard Muybridge: A horse trotting 188	10
3.1	Kinetic energy of an electron in a laser field	19
3.2	High harmonic spectrum	20
3.3	Definition of the molecular and laboratory frame	28
3.4	Molecular alignment of N_2 in time	31
3.5	Energy levels of an asymmetric rotor	32
3.6	Weights of rotational states for C_2H_4 and N_2	33
3.7	Time evolution of $\langle \cos^2 \theta \rangle$ for C_2H_4	36
3.8	Time evolution of $\langle D_0^4(\theta, \chi) \rangle$ for C_2H_4	36
3.9	Time evolution of $\langle D_4^4(\theta, \chi) \rangle$ for C_2H_4	36
3.10	Hermite Gaussian modes	38
3.11	Laguerre Gaussian modes	39
3.12	Scheme for the propagation of light	41
3.13	Spatial profile in intensity and phase for a Heaviside phase profile	44
3.14	Focusing behavior of interfering light	44
3.15	Focus behavior of light without interference	45
3.16	Focusing behavior of light shaped by glass wedges	45
3.17	Spatial profile in intensity and phase for a phase profile with OAM	46
3.18	Focusing behavior of interfering Laguerre Gaussian beams	47
3.19	Spatial profile in intensity and phase for a phase profile with OAM of $l = 0, +1$	47
3.20	Focusing behavior of interfering Laguerre Gaussian beams, mimicking a single source	48
3.21	Improvements on spatial overlap through tilt	48
3.22	Focus behavior of a tilted beam	49
3.23	Spatial profile in phase and intensity for a two source focus with a Heaviside function	50
3.24	Spatial phase in the focus plane of interfering light with angular momentum	50
3.25	Spatial phase in the focus plane of interfering light with angular momentum, creating a single source	51
3.26	Shaped light in phase	52
3.27	Spatial intensity as a function of focus for a tilted two source focus	52
3.28	Spatial intensity and phase distribution of a tilted two source focus	53
3.29	Calculation for the focusing of tilted beams	54
3.30	Calculation for the focusing of tilted beams with a phase offset of π	54
3.31	Calculated focusing behavior for a single tilted beam	55
3.32	Calculated focusing behavior for a single tilted beam and a second tilted beam titled far away	55
4.1	Experimental setup	57
4.2	Image in the detector plane	58
4.3	Scheme for the manipulation of single pixels on the SLM.	60
4.4	Scheme for a tilt-manipulation on the SLM	61
4.5	Focusing behavior of tilted beams	62
4.6	Focusing behavior of intensity manipulated beams	63

4.7	Focusing behavior of interfering light	64
4.8	Experimental setup with a second color	65
4.9	Harmonic generation influenced by a weak second harmonic	66
4.10	Harmonic yield as a function of delay between red and blue	66
4.11	Chromatic dispersion through the SLM	67
4.12	Influence on CEP by the SLM	68
4.13	A Young's double slit on the XUV-detector	69
4.14	Fringe projection	69
4.15	Fourier analysis of the detector image	70
4.16	Fourier analysis for individual harmonic orders	70
5.1	Delay dependent fringe position over a delay change of 2π	75
5.2	Dependence of the delay on the phase of higher order harmonics	75
5.3	Dependence of the delay on the phase of higher order harmonics, normalized	76
5.4	Deviation from calculations	77
5.5	Dependence on the delay in a long medium	78
5.6	Dependence on the delay in a thin medium	79
5.7	Delay dependent fringe position over a delay change of 2π for various orders and targets	80
5.8	Dependence on the delay of the phase of higher order harmonics in argon, at the focus	81
5.9	Dependence on the delay of the phase of harmonics in C_2H_4 , away from the focus	81
5.10	Dependence on the delay of the phase of higher order harmonics as a function of laser focus	82
5.11	Focus dependence of the harmonic phase	83
6.1	Phase of dipole moment, due to the electron's motion	86
6.2	Excursion times of the electron as a function of harmonic order	87
6.3	Intensity dependent phase of harmonic 19	88
6.4	Intensity dependent phase with an equation out of the SFA	88
6.5	Intensity manipulation with the SLM	89
6.6	Intensity dependent harmonic spectra	90
6.7	Intensity dependent fringe position of H11 and H17	90
6.8	Intensity dependent phase for argon and krypton	91
6.9	Change in phase for krypton for all harmonic orders	92
6.10	α -coefficients for argon and krypton	92
6.11	α -coefficients for increasing laser intensities	93
6.12	α -coefficients changes as a function of intensity for select harmonics	94
6.13	α -coefficients changes as a function of intensity for all harmonics in argon	94
6.14	α -coefficients extracted from the experiment and other publications	95
6.15	Fringe position as a function of intensity of H9	97
6.16	Change in phase for all harmonic orders, driven in a saturated medium for an intensity of $3 \times 10^{14} W/cm^2$	97
6.17	Change in phase for all harmonic orders, driven in a saturated medium for an intensity of $3.8 \times 10^{14} W/cm^2$	98
6.18	Change in phase for select harmonics, driven in a saturated medium	98
6.19	α -coefficients for harmonics driven by intense laser sources	99
6.20	Experimental setup with second harmonic generation	100
6.21	Harmonic spectra driven by a two-color field	100
6.22	Spot size of the red and blue components of the shaped two-color field	101
6.23	Young's double slit for even and odd harmonics	102
6.24	Change in phase for long and short trajectory harmonics	102
6.25	Measured change in phase in a two color field	103
6.26	α -coefficients for a two color field	104
6.27	α -coefficients comparison to the single color case	104

7.1	Experimental setup for the study of ellipticity dependence	109
7.2	Ellipticity dependence of harmonics for Argon, driven by 785 nm light	110
7.3	Deviation from an exponential decay in the Cooper minimum	110
7.4	Measure of the deviation	111
7.5	The energy dependent β -parameter of Argon	111
7.6	Ellipticity dependence for different focus positions	112
7.7	Harmonic spectra in argon from 785 nm and 1500 nm lasers	112
7.8	Focus dependence in yield and ionization	113
7.9	Focus dependence in HHG from 1500 nm	114
7.10	Ellipticity dependent yield in argon	114
7.11	Normalized ellipticity dependent yield in argon	115
7.12	Yield from long wavelengths with different targets	115
8.1	Molecular orbitals nitrogen	118
8.2	Temporal evolution of expansion terms	120
8.3	Experimental setup for nitrogen measurements	120
8.4	Harmonic yield of single sources	121
8.5	Amplitude measured in the two source experiment in N_2	122
8.6	Interference pattern of H19 as a function of time	123
8.7	Phase of harmonics in N_2 extracted from the double slit	124
8.8	Delay dependent amplitudes in N_2	125
8.9	Molecular frame phase and amplitude in N_2	125
8.10	Residual harmonic 17	126
8.11	Comparison molecular frame dipole to calculated signal	127
8.12	Ionization rates from MO-ADK theory	128
8.13	Photoionization cross section to HOMO and HOMO-1	128
9.1	Sketch of C_2H_4 and its molecular orbitals	131
9.2	Experimental setup for C_2H_4 measurements	131
9.3	Delay dependent amplitudes in C_2H_4	133
9.4	Delay dependent fringe of H11 in C_2H_4	133
9.5	Delay dependent phases in C_2H_4	134
9.6	Fitted amplitude in C_2H_4	135
9.7	Fitted phases of C_2H_4	136
9.8	Residue between fit and data for $Im(S)$ of the 11th harmonic	136
9.9	Amplitude and phase of harmonic 11	137
9.10	Molecular frame phase for different extensions in the expansion	137
9.11	QRS phases for H11	138
9.12	Coherent addition in QRS, amplitude only	139
9.13	Coherent addition in QRS, phase only	140
9.14	Molecular frame signal of C_2H_4	141
A.1	Focus impurities of LG beams	150
A.2	Switch to the tilted beams and perfect focusing	151
A.3	Focus impurities of LG beams with two colors	151
A.4	Spatial phase of the fundamental in the focus as a function of ϵ	152
A.5	Ionization signal as a function of delay	152
A.6	Fringe pattern as a function of delay for harmonic 13	153

Chapter 1

Motivation

The field of attoscience [1,2] is dedicated to the study of ultrafast processes in physics and chemistry on the natural time scale of electrons. The characteristic atomic unit of time is 24.2 as, reflecting the time it takes an 1s electron of the Bohr atom to travel a distance of one Bohr radius. In order to study such processes, one has to develop technologies that are capable of sampling on an equal or shorter time scale. Historically, this field was born out of the development of modern ultrafast pulsed lasers [3,4]. These lasers originally gave birth to femtochemistry [5] and then launched the field of attoscience. The key to this development was a laser driven process called high harmonic generation (HHG) [6–8], which generates a broad spectrum of electromagnetic radiation, stretching from the VUV to the soft X-ray region between 10 eV to 3000 eV [9]. By tailoring these spectra, pulses as short as 67 as have been reported [10].

HHG is a non-linear process, depending strongly on the medium as well as the driving laser field. On a microscopic scale, the generation depends on fundamental atomic and molecular properties. On this level, HHG is often explained using the three step model [7], as detailed in the second chapter of this dissertation. Each step of the three step model affects the created electromagnetic radiation. HHG can be described as the electron probing itself and measuring its properties in situ. Using the three step model and its factorization, the steps can be studied individually and so high harmonic generation also permits a fully coherent energy-resolved measurement of single-photon ionization [11–14], as the driving laser field launches a coherent electron wave packet that emits coherent light. We get information about the electron wave packet in the continuum.

Macroscopically, high harmonic generation can be described as a coherent process, where generated photons can add up and form a bright source of XUV light. However, this is highly dependent on phase-matching between the driving laser field and the higher order fields in a gaseous medium. As the electromagnetic waves propagate through the gaseous medium and vacuum, described by Maxwell's equations, light may interfere constructively and destructively, influencing the observed high harmonic flux.

On this macroscopic level we can compare it to perturbative non linear optic, where low order harmonic generation can be described as sum frequency generation in a non-linear medium and the propagation and property of the electromagnetic radiation is described with perturbative non-linear optics and the propagation of light. It is this interplay of macroscopic phase-matching and light with matter interaction that makes HHG an interesting and challenging field of research.

It is my goal in this dissertation to study the fundamental processes of HHG and to use HHG as a spectroscopic tool of atomic and molecular targets. HHG spectroscopy has proven itself

as a coherent photoionization experiment [15–17], measuring photoionization cross sections as a function of electron energy and molecular axis angle by measuring the amplitude of high harmonic emission. In recent years, the measurement of amplitude and phase of the high harmonics has expanded this knowledge to a complete measurement of high harmonic generation and the extraction of complex-valued photoionization dipoles $d = |d|e^{i\phi}$ and the presented work in this dissertation adds valuable observations to the need of measuring amplitude and phase of HHG. On a more fundamental level, the process of HHG has similarities and drastic differences to its perturbative sibling of low order harmonic generation. I will put a new perspective on a specific aspect of high harmonic generation and also study with high precision one of the fundamentally different aspects of HHG, where the harmonic phase strongly depends on the intensity of the laser field. The dissertation is built on known techniques of non-adiabatic alignment and pulse-shaping, which will yield an angle-resolved picture of HHG from molecules and high-stability in a deployed commonpath interferometer.

Chapter 2

Deutsche Zusammenfassung

Schon im Jahr 1880 wurden Kameras genutzt, um Vorgänge aufzulösen, die für das menschliche Auge zu schnell waren. Die offene Frage in den Jahren um 1880 war, ob ein Pferd im Galopp zu einem gegebenen Zeitpunkt alle seine Hufe in der Luft hat oder ob immer ein Huf auf dem Boden ist. Eadward Muybridge veröffentlichte im Jahre 1887 seine Arbeit [18] und gab eine Antwort auf die offene Frage. Man konnte sehen, dass das Pferd im Galopp als auch im Trab zu einer bestimmten Zeit alle seine Hufe in der Luft hat. Dieses Analogon wird sehr oft in der Wissenschaft benutzt. Man benötigt eine Kamera mit einer kürzeren Auflösungszeit, um die natürliche Bewegung aufzulösen. Erste Fortschritte mit Lasern [3, 4] und Femtochemie [5] erlaubten eine Auflösungszeit von Femtosekunden. Fortschritte in Lasertechnologie ermöglichten es anschließend mit High Harmonic Generation (HHG) noch eine feinere Zeitauflösung zu erlangen [6–8]. Mit einer HHG-Quelle kann in den Attosekundenbereich vorgestoßen werden: Die natürliche Zeitskala eines Elektrons von 24.2 as wird dadurch erreichbar. Diese Zeitskala beschreibt die benötigte Zeit eines Elektrons um die Distanz eines $1s$ Bohrradius zurückzulegen. Experimentell wurden Attosekundenpulse mit einer Pulsdauer von 67 as erzeugt [10]. Die vorliegende Arbeit ist in dem Gebiet der Atomphysik angesiedelt und nutzt die Erzeugung höherer Harmonischer als Werkzeug, um Erkenntnisse in diesem Gebiet zu erlangen. In HHG werden höhere Harmonische eines zu Grunde liegenden Lasers erzeugt, wobei die Harmonischen ein Vielfaches der Photonenenergie des zu Grunde liegenden Lasers besitzen. Der Prozess kann in einem Drei-Schritte-Modell beschrieben werden [7]. Im ersten Schritt werden Elektronen von einem Atom oder Molekül freigesetzt. Die Ionisation kann durch Tunnelionisation beschrieben werden [19, 20], wenn das elektrische Feld des Lasers so stark ist, dass das Potential des bindenden Atoms verbogen wird und das Elektron durch das Potential tunneln kann. Im nächsten Schritt kann es im elektrischen Wechselfeld des Lasers kinetische Energie gewinnen. Wenn die Trajektorie des Elektrons zum Mutterion zurückführt, kann das Elektron mit dem Atom rekombinieren und die gewonnene Energie wird in der Form eines Photon ausgestrahlt. Dieser Prozess findet in einem Medium an vielen Atomen statt, wobei die erzeugten Photonen kohärent emittiert werden und eine helle Quelle von höheren Harmonischen erzeugen.

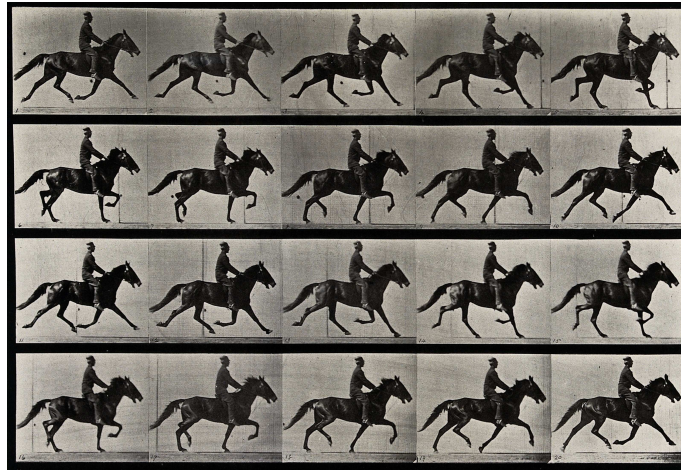


Abbildung 2.1: "Photogravure after Eadweard Muybridge, 188 ". Quelle: Wellcome Library, London

Neben dem Erzeugen von Attosekundenpulsen kann die gemessene Strahlung eines Atoms oder Moleküls Rückschlüsse über das Atom und Molekül geben und so für Spektroskopie genutzt werden, welche ein Schwerpunkt in dieser Arbeit ist.

Zu Beginn behandelt die vorliegende Arbeit eine ausführliche, theoretische Beschreibung von High Harmonic Generation in dem Drei-Schritte-Modell, mit dem HHG semiklassisch beschrieben werden kann. Dieses Modell wird dann schrittweise um genauere Kalkulationen ergänzt. Das klassische Drei-Schritte-Modell von Corkum [7] kann den experimentell beobachtbaren cutoff und das Plateau beschreiben. Das semiklassische Modell von Lewenstein [21], die Strong Field Approximation (SFA), kann eine quantitative Signalstärke der höheren Harmonischen berechnen. Zusätzlich zeigt SFA eine intensitätsabhängige Phase der höheren Harmonischen, die nicht durch perturbative nicht lineare Effekte erklärt werden kann.

In dem SFA-Modell wird der Rekombinationsschritt nur in einer Näherung betrachtet, die sowohl theoretisch [17] als auch experimentell unzufriedenstellend ist [15]. In der SFA wird das Elektron in dem Kontinuum, wenn es zu dem ursprünglichen Grundzustand übergeht, angenähert. Eine strukturlose, ebene Welle wird in den Berechnungen verwendet. Allerdings ist von Photoionisationsexperimenten und Experimenten in HHG bekannt, dass die Photoionisation und ebenso die -rekombination nicht nur von dem Ionisationspotential und der Symmetrie des Moleküls abhängen, sondern es zu Interferenzeffekten kommen kann. Diese Interferenzeffekte können durch das Prinzip des detaillierten Gleichgewichts für Photoionisation and Photorekombination berechnet werden. Dieses Prinzip ist allgegenwärtig in der Welt der Physik und postuliert, dass die Zeitumkehr eines Prozesses zum ursprünglichen Zustand zurückführe. Es ermöglicht den Vergleich von HHG-Experimenten mit Photoionisationsexperimenten.

Da HHG ein kohärenter Prozess ist, ermöglicht es die Phase der Strahlung zu messen und damit ebenso eine Phase in der Photorekombination, welche in Photoionisationsexperimenten nicht messbar ist. Durch die Benutzung von kurzen Laserpulsen in der Größenordnung von 5 bis 30 fs können ebenfalls Experimente mit schnellen Dynamiken gemessen werden. Allerdings ist HHG ein höchst verschachtelter Prozess, in dem nicht nur von einem einzelnen Atom die Strahlung gesammelt wird, sondern von Millionen Emittoren, die durch ihre Kohärenz eine Lichtquelle bilden und in optimalen Bedingungen keinen Phasenunterschied aufweisen. Sobald durch das erzeugende Medium ein Gradient in der Dichte entsteht oder das elektrische Feld ebenfalls im Fokus einen starken

Gradienten erzeugt, kann es zu einem Phasenunterschied kommen, der die Helligkeit und Phase der höheren Harmonischen beeinflusst. Durch die Verwendung eines dünnen Gasmediums und eines "weichen" Fokus können diese Effekte minimiert werden, sodass eine Lichtquelle ähnlich einer Quelle aus einem einzelnen Emitter angenommen werden kann. Mit einem "weichen" Fokus wird ein Laserfokus bezeichnet, dessen Peak-Intensität sich nicht im Medium verändert, sondern erst weit weg vom Medium abfällt. Diese Thematik des Phasenunterschied wird in Kapitel 4 und 6 im experimentellen Zusammenhang besprochen.

Nachdem Theorien von HHG vorgestellt wurden, behandelt die Arbeit Theorien über genutzte Techniken, um mehr über HHG zu erfahren. In der vorliegenden Arbeit werden in Kapitel 7 und 8 ein schwaches elektrisches Feld genutzt, um Rotationen in Molekülen anzuregen. Durch die Verwendung von Pulsen, deutlich kürzer als die Rotationsperiode der behandelten Moleküle, entsteht ein angeregtes Molekülensemble, das periodische Minima und Maxima zeigt, nachdem das elektrische Feld mit dem Molekül interagiert hat und nicht mehr präsent ist. Die Technik wird "non-adiabatic alignment" genannt [22]. Ein weiteres Kernelement dieser Arbeit ist ein "spatial light modulator". Das Gerät ermöglicht es die Phase des Lasers in der räumlichen Verteilung zu verändern und so gewünschte Fokusformen und eine Verschiebung des Pulses in der Zeit zu erzeugen. In dem theoretischen Kapitel als auch in dem dritten Kapitel werden die Grundlagen zur Manipulation und zur genauen Berechnung der genutzten Phasenmanipulation erklärt.

Kapitel 4 zeigt das erste Experiment der Dissertation. Es zeigt ein Doppelspaltexperiment, das durch zwei Laserfoki erzeugt wird (siehe Abbildung 4.5b). Der Doppelspalt ist Young's Doppelspalt ähnlich, wird aber hier nicht nur genutzt, um die Kohärenz von HHG zu beweisen [23], sondern eine relative Phase zwischen den Spalten zu messen. Dies ist Grundlage um eine komplette Messung der Strahlung durchzuführen und damit weitere Eigenschaften in HHG zu messen und zu extrahieren. Das gezeigte Experiment zeigt hervorragende Stabilität in Abbildung 5.3. Im Unterschied zu anderen Interferometern, wie einem Michelson Interferometer, kann der verwendete Aufbau als "common path interferometer" bezeichnet werden. Durch die Verwendung von zwei Pfaden oder zwei Spalten die immer denselben optischen Pfad und Elemente durchqueren, kommt es zu sehr geringem Einfluss durch Vibrationen und Luftzirkulationen, der sich in einem Fehler von weniger als 1 as realisiert. Der verwendete SLM kann dabei eine Zeitverschiebung von 2.67 fs im elektrischen Feld induzieren, in Schritten von 12.5 as. Dies wurde in Kapitel 4 und 3 genauer besprochen. Nicht nur kann die örtliche Intensitätsverteilung im Fokus in einen Doppelspalt umgewandelt werden, auch die Intensität der Spalte kann in einer asymmetrischen Weise beeinflusst werden (siehe Abbildungen 4.6c). In Kapitel 5 wird diese Manipulation genutzt, um die Phase und Intensität der Harmonischen als Funktion der Differenz in der Peak-Intensität der einzelnen Spalte zu messen. Hier zeigt sich ein weiterer fundamentaler Unterschied zur perturbativen Erzeugung von höheren Harmonischen, neben Plateau und cutoff. Im perturbativen Bild ist die Phase der Harmonischen nicht intensitätsabhängig und ihre Phase bleibt unverändert, wenn die Intensität der Fundamentalen anwächst. Hier zeigt sich in dem SFA-Modell und dem gezeigten Experiment (wie in zahlreichen anderen Experimenten) in Abbildungen 6.8a und 6.14, dass die Phase der Harmonischen sehr stark von der Intensität, aber auch von der Elektrontrajektorie abhängt (siehe Abbildung 6.24 und Abbildung 6.26). Hier erwartet man eine deutlich stärker beeinflusste Phase der Harmonischen, wenn diese mit langen Elektrontrajektorien entstanden sind, während Harmonische von kurzen Elektrontrajektorien eine deutlich schwächere Abhängigkeit zeigen. Erst, wenn Harmonische mit der maximalen kinetischen Energie erzeugt werden, kann es nur noch einen Rekombinationspfad geben und die-

se Harmonischen werden eine feste Abhängigkeit von der Peak-Intensität des Lasers aufweisen. In dem gezeigten Experiment wird diese Abhängigkeit für verschiedene Gase untersucht, aber auch für andere Größenordnungen in der Peak-Intensität. Ebenso wird auch ein zwei-Farben-Feld erzeugt, mit dem die Abhängigkeit der Phase der Harmonischen zu diesem zwei-Farben-Feld studiert wird. In dem ersten Experiment stimmen die Resultate sehr gut mit SFA-Kalkulationen überein. Die experimentelle Fehlerbalken sind sehr klein, während vergleichbare Experimente mit größeren Fehlerbalken ihre Analyse durchführen müssen. Dies zeigt ebenfalls die Stärke des gezeigten "common path interferometers".

Im Vergleich zu Kapitel 6 der Dissertation kann die komplexwertige Größe des Dipolmoments direkt gemessen werden, sofern man Phase und Amplitude der HHG Strahlung misst. Dieses Prinzip wird in Kapitel 7 und 8 genutzt, um eine detailreichere Messung in ausgerichtetem Stickstoff und Ethylen zu zeigen.

Zuerst werden allerdings Grundlagen der HHG Spektroskopie besprochen, wie die Faktorisierung des Harmonischensignals, in einem elliptizitätsabhängigen Experiment. In dem Experiment von Kapitel 6 werden diese Grundlagen genutzt: Harmonische eines 785 nm Lasers werden in Argon erzeugt. Anschließend wird die Elliptizität des Lasers geändert und dabei die Intensität der Harmonischen aufgenommen (siehe experimenteller Aufbau in Abbildung 7.1). Dieses Experiment zeigt eine Abhängigkeit der Intensität in Abbildung 7.2, die sich für jede Harmonische ändert. Besonders zeigt sich hier für Harmonische von 33. Ordnung ein deutlich langsamerer Abfall der Intensität im Vergleich zu anderen Harmonischen. Diese Messung wird dazu genutzt mit Hilfe einer Theorie von Mikhail Frolov [24] den β -Parameter in der Photoionization von Argon zu extrahieren. Der β -Parameter in Abbildung 7.5 kann hier im Falle eines p-orbitals in Argon extrahiert werden. Dieser Parameter ist eine bekannte Größe in Photoionisationsmessungen an Synchrotronanlagen. Er zeigt die Winkelabhängigkeit in Einphotonionisation und zeigt in Argon einen winkelunabhängigen Wirkungsquerschnitt für Photonenenergien um 50 eV oder in dem gezeigten Experiment für Harmonische um 33. Ordnung. Durch das Prinzip von detailliertem Gleichgewicht können Schlussfolgerungen über beide Experimente gezogen werden, welche zeigen, dass sich HHG als Photoionisationsexperiment in einem sehr einfachen und kompakten Aufbau beweisen kann. Nach dem Experiment an Argon befassen sich Kapitel 7 und 8 mit HHG von ausgerichteten Molekülen, in denen experimentell Amplitude und Phase der höheren Harmonischen gesammelt werden. Non-adiabatic alignment ermöglicht es winkelabhängige Phasen und Amplituden zu messen. Dabei wird die zeitabhängige Intensität und Phase der Harmonischen gemessen und mit der kalkulierten Molekülachsenverteilung in der Zeit eine Winkelabhängigkeit extrahiert. Dabei werden Basis-Sets verwendet, die die Symmetrie des Moleküls darstellen können. In Stickstoff wird eine starke, symmetrische Zeitabhängigkeit in Phase und Amplitude in den Abbildungen 8.7 und 8.8 beobachtet, die auf die molekulare Struktur zurückzuführen ist. Eine Shape resonance um 25 eV erzeugt eine starke Winkelabhängigkeit, die im Experiment allerdings noch ein Maximum um 90° zeigt, das nicht mit der shape resonance des HOMO zu erklären ist, siehe Abbildung 8.11c. Die Diskussion muss um HOMO-1 ergänzt werden, um damit die gemessenen Eigenschaften zu erklären. HOMO und HOMO-1 beschreiben die molekularen Orbitale, die die zwei kleinsten Ionisationspotentiale aufweisen und damit bei der Ionisation dominieren. In Ethylen folgt die Rotation des Moleküls nun nicht mehr einer einfachen Rotation um eine Achse, sondern folgt einer komplizierten Struktur mit Rotationen um einzelne Achsen und Rotationen mit Perioden aus der Summe von mehreren Trägheitsmomenten (siehe Kapitel 3.3.4). In Ethylen kann nun nicht zu einer gewissen Zeit von einem ausgerichtetem Molekül gesprochen werden,

sondern es muss das Wissen eines zeitabhängigen Verhaltens genutzt werden, um auf eine Winkelabhängigkeit zu schließen. Im Experiment werden Kalkulationen genutzt, um die Phase und die Amplitude in zwei Winkeln anzugeben. In dem gezeigten Experiment ist mit systematischen und statistischen Fehlern zu kämpfen. Nur eine Harmonische im Experiment zeigt einen akzeptablen Wert für die entsprechende Wertigkeit des Fits zu den gemessenen Werten. Alle anderen Harmonischen zeigen ein Überfitten der experimentellen Werte und die Kalkulationen haben keine eindeutige Lösung. Nichtsdestotrotz kann aus dem Ergebnis für Ethylen in [Abbildung 9.13](#) eine sehr interessante Winkelabhängigkeit für die Phase und Amplitude extrahiert werden. Genauso wie in Stickstoff sind zwei Orbitale in der Erzeugung der höheren Harmonischen involviert. Besonders in der Phase zeigt sich, dass die Resultate mit gegebenen theoretischen Kalkulationen übereinstimmen, wenn mehrere Orbitale angenommen werden.

Chapter 3

Theoretical background

3.1 High harmonic generation

With the discovery of high-order harmonic generation [25,26] and above-threshold ionization [27], new theories were required to describe these strong field processes. In high harmonic generation (HHG), studies showed a discrete spectrum, in which the lines were separated by twice the photon energy of the driving laser. These lines are the harmonics of the fundamental laser field. The spectrum generated in HHG consists of three characteristic regions: low order harmonics, a plateau and the so called cutoff. Low order harmonics can be generated perturbatively and show a high flux compared to harmonics in the plateau region, where the relative brightness of neighboring harmonics is comparable to each other and does not show a decay in brightness as the order increases. Beginning in the cutoff region, we observe a rapid fall-off of harmonic intensity with harmonic order. In 1992 and 1993, important work based on a classical model was developed and matched the characteristic plateau behavior and cutoff in above threshold ionization [28] and high harmonic generation [7, 8]. Lewenstein [21] formulated in 1994 a semi-classical theory of high harmonic generation, which describes high harmonic generation in the tunneling regime and describes the electron in the continuum as a wave function along its classical trajectory. The theory is able to give the strength of the radiation and information about its phase.

These models are based on a single active electron approximation. HHG can be qualitatively described in a three step model:

- (1) In an intense laser field, an electron can tunnel-ionize from the atom/molecule.
- (2) The freed electron gains kinetic energy in the electric field of the laser.
- (3) The electron recombines with the parent ion, emitting a single photon

The harmonic emission can then be described as the product of the three steps.

3.1.1 Interaction of light with matter

On a fundamental level, high harmonic generation can be described as the radiation emitted from a charged particle in an external, time dependent electric field. While the electron is in the external field, we can describe the electron as an electric dipole that is emitting radiation as a Hertzian dipole. This radiation can be labeled as bremsstrahlung [29, 30]. In the dipole limit, using the Larmor formula [31], the total power irradiated P can be written as

$$P = \frac{2}{3} \frac{q^2 a^2}{c^3} \quad (3.1)$$

where a is the acceleration of a charged particle with charge q and c the speed of light. The irradiated power of the dipole is proportional to the square of the acceleration. However, in Quantum mechanics, the electron is described by a wave function, $|\Psi\rangle$. We find the electron

wave function by solving the Schrödinger equation

$$i\frac{d}{dt}|\Psi\rangle = \hat{H}|\Psi\rangle, \quad (3.2)$$

where the Hamiltonian operator \hat{H} is the sum of the kinetic energy and potential energy operators $\hat{H} = \hat{T} + \hat{V}$. The Hamiltonian operator can describe an electron bound in an atomic potential $\hat{V} = V(r)$ and with the kinetic energy operator $\hat{T} = -\frac{\hat{p}^2}{2m} = -\frac{1}{2}\nabla^2$. For the given Hamiltonian operator, which has no time dependence, we find solutions of the time independent Schrödinger equation $\hat{H}|\Psi\rangle = E|\Psi\rangle$ with the energy eigenvalue $E < 0$ and find an electron wave function, $|0\rangle$, bound to the atom. When we have no atomic potential present, the Hamiltonian is written $H_0|k\rangle = \frac{k^2}{2}|k\rangle$ and we find an electron wave function $|k\rangle$, that is a solution to the Schrödinger equation with an energy eigenvalue of $E > 0$. It is the wave function of a so called continuum electron. However, an electron in the joint potential of the nucleus and an external laser field $F(t) = \epsilon \cos(\omega t)$ is expressed with a Hamiltonian

$$H(t) = -\frac{1}{2}\nabla^2 + V(r) - \epsilon \cos(\omega t) \quad (3.3)$$

in which case, the solution to the Schrödinger equation becomes more complex. The wave functions have eigenvalues in energy with $E < 0$ and $E > 0$. We can write the electron wave function as a superposition of the ground states, excited states and continuum states

$$|\Psi(t)\rangle = a(t)|0\rangle + \int d^3k b(k, t)|k\rangle + \sum c(t)|e\rangle \quad (3.4)$$

with $|e\rangle$ the wave function of an excited state and a, b, c amplitudes of the wave functions. This electron wave function has a dipole moment that can be written as

$$d(t) = e \cdot D(t) = e \langle \Psi(t) | \vec{r} | \Psi(t) \rangle \quad (3.5)$$

and radiation will be emitted. The radiation can be expressed by the acceleration of the dipole moment, where we have seen the proportionality of the irradiated power $P \propto a^2$ in the Larmor formula in Equation 3.1. We can perform a time derivative to acquire the expectation value of the acceleration $\frac{d^2}{dt^2} \langle \Psi | \vec{r} | \Psi \rangle$ or use Ehrenfest's theorem [32] to get

$$\ddot{d}(t) = \left\langle \Psi(t) \left| \frac{\delta V(r)}{\delta r} \right| \Psi(t) \right\rangle + F(t) \quad (3.6)$$

where the second term, given by the electric field $F(t)$, does not contain any light matter interaction and can be dropped. Using a Fourier transformation to change from time to frequency domain, we obtain the power spectrum

$$P(\omega) = |\ddot{d}(\omega)|^2 \quad (3.7)$$

which describes the emitted light, when the oscillating electric field is strong enough to influence the electron bound in matter.

3.1.2 Factorization of High Harmonic Generation

Classical simple man's model: Three Step Model

In this section, we introduce HHG through the semi-classical model as presented by Corkum [7]. In this model, we treat the electron's motion in the continuum fully classically. The model can explain the first experimental observations in HHG, such as the cutoff law.

Ionization As mentioned before, ionization is the first step in the process. Ionization can be described in two regimes: tunnel ionization and multiphoton ionization. Quantitatively, Keldysh [19] defined in 1964 an adiabatic parameter γ

$$\gamma = \frac{\omega_L}{\epsilon} \sqrt{2I_p} \quad (3.8)$$

with ω_L the laser frequency, ϵ the electric field strength and I_p the ionization potential of the atom/molecule. With the adiabatic parameter, we can differentiate between the multiphoton and the tunnel ionization regimes: multi photon ionization dominates over tunnel ionization when $\gamma \gg 1$, tunneling ionization dominates over multiphoton ionization when $\gamma \ll 1$. In the intermediate region with $\gamma \sim 1$, both processes can have equal probability. Qualitatively we can describe tunnel ionization with the following picture: When the laser field strength approaches the strength of the atomic potential, the potential well becomes distorted. The infinitely long barrier of the well becomes a finite barrier through which the electron can tunnel. With low-frequency lasers, where the period of the field is on the order of femtoseconds ($1 \text{ fs} = 10^{-15} \text{ s}$), the finite barrier is quasi-static compared to the time it takes for the electron to tunnel out, and this ionization process can be described with well-known theories of tunnel ionization [20, 33]. In the other limit, when the laser field strength is smaller than the strength of the atomic potential, the electron can still become free from the atomic potential. Absorbing enough photons, the electron in the ground state may be excited to a continuum state and ionized, which is described as multiphoton ionization.

In the limit $\gamma \ll 1$, the tunneling rate Γ is derived in a strong field approximation [20, 34],

$$\Gamma = \text{Exp} \left(-\frac{4}{3} I_p \tau \right) = \text{Exp} \left(-\frac{2(2I_p)^{3/2}}{3|\epsilon|} \right) \quad (3.9)$$

with a "tunneling time" of $\tau = \gamma/\omega_L$ and X an unknown factor [34]. The rate follows an exponential law, until saturation effects occur. In the multi photon regime, for $\gamma \gg 1$, the "tunneling time" changes to $\tau \approx \ln(2\gamma)/\omega_L$ [34], so that the ionization rate turns into the power law

$$\Gamma = X(2\gamma)^{-2N} \propto |\epsilon|^{2N} \quad (3.10)$$

with $N = I_p/\omega_L$ the number of photons required to reach the continuum threshold.

In the semi-classical model of HHG, the ionization is assumed to be in the tunnel-ionization regime and the electron is released into the continuum with zero energy. The only energy it gains is given by the acceleration in the electric field. The probability of ionization $P(t)$ [7] during a time interval dt is given by $P(t) = \Gamma(F(t))dt$, which describes the formation of wave packets near each crest of the laser field.

Acceleration in a classical field After the ionization, assuming a monochromatic laser field $F(t) = \epsilon \cos(\omega_L t)$ and describing the evolution of the electron in the continuum with classical mechanics, the acceleration $a(t)$ of the electron, with mass $m_e = 1$ a.u. and charge $q_e = -1$ a.u., can be written as

$$a(t) = -\epsilon \cos(\omega_L t). \quad (3.11)$$

When we integrate the acceleration in time from t_0 , the time of ionization, to t_r , the time of recombination, which defines the window of time in which the electron is in the electric field, we get the time dependent velocity $v(t_r)$

$$v(t_r) = -\frac{\epsilon}{\omega_L} [\sin(\omega_L t_r) - \sin(\omega_L t_0)] + v_0 \quad (3.12)$$

with v_0 the velocity of the electron at t_0 .

Performing the integration a second time, we get the time dependent position of the electron

$$x(t_r) = \frac{\epsilon}{\omega_L^2} [\cos(\omega_L t_r) - \cos(\omega_L t_0) + \omega_L(t_r - t_0)\sin(\omega_L t_0)] + (t_r - t_0)v_0 + x_0 \quad (3.13)$$

In order for the electron to emit a photon, we have to assume that the electron started at the origin and that it will return to its origin:

$$x(t_r) = x(t_0) = 0. \quad (3.14)$$

Given Equation 3.14, we can write the return condition for the freed electron to be

$$0 = \frac{\epsilon}{\omega_L^2} [\cos(\omega_L t_r) - \cos(\omega_L t_0) + \omega_L (t_r - t_0) \sin(\omega_L t_0)] + (t_r - t_0) v_0. \quad (3.15)$$

Under the assumption that the electron's initial velocity is zero ($v_0 = 0$), we get the electron's kinetic energy obtained in the electric field

$$E_{kin}(t_r) = 2U_p [\sin(\omega_L t_r) - \sin(\omega_L t_0)]^2 \quad (3.16)$$

with

$$U_p = \frac{\epsilon^2}{4\omega_L^2} \quad (3.17)$$

the ponderomotive energy of an electron in an oscillating electric field. A solution to Equation 3.15 can be found numerically and can be approximated with [35]

$$\frac{t_r}{T_0} = \frac{1}{4} - \frac{3}{2\pi} \sin^{-1} \left(4 \frac{t_0}{T_0} - 1 \right) \quad (3.18)$$

with T_0 the period of the laser cycle. Inserting Equation 3.18 in Equation 3.16, we get an equation that yields the kinetic energy of the electron depending on its recombination time t_r ,

$$E_{kin}(t_r) = 2U_p \left[\sin(\omega_L t_r) - \cos \left(\frac{\pi}{2} \sin \left(\frac{1}{3} \omega_L t_r \right) - \frac{\pi}{6} \right) \right]^2 \quad (3.19)$$

and an equation for its kinetic energy, depending on its ionization time t_0 ,

$$E_{kin}(t_0) = 2U_p \left[\cos \left(3 \sin^{-1} \left(\frac{2}{\pi} \omega_L t_0 - 1 \right) \right) - \sin(\omega_L t_0) \right]^2 \quad (3.20)$$

with $\omega_l = \frac{2\pi}{T_0}$. These equations show the well-known cutoff law of high harmonic generation:

$$n_{max} \hbar \omega_L = 3.17 U_p + I_p \quad (3.21)$$

where n_{max} is the highest order of harmonic emission that can be generated for a particular molecule/atom and a given laser intensity. The cutoff scales with the ponderomotive energy of the driving laser field which is proportional to $I\lambda^2$, so that a higher driving laser wavelength λ and intensity I will result in a higher harmonic cutoff.

In Figure 3.1 we plot the kinetic energy given by Equation 3.19 and Equation 3.20 as a function of time over one cycle of the fundamental laser field. In this picture, we can define three distinct types of electron trajectories, which stem from particular excursion times. Electrons emitted with the maximum kinetic energy of $3.17 U_p$ produce cutoff harmonics. For values of the energy less than the maximum, there are two additional types of trajectories. While long trajectories are ionized at the peak of the electric field at times of $t < 0.05$ and recombine at times of $t > 0.71$, short trajectories are ionized at times $t > 0.05$ and spend less time in the electric field before they recombine at times $t < 0.71$. Cutoff harmonics are generated from electrons ionized at $t \approx 0.05$ and recombining at $t \approx 0.71$, where a time of $t = 1$ corresponds to one optical cycle of length 2π . Due to the difference in excursion time in the electric field, long trajectories have a smaller rate of returning to the origin and the contribution of long trajectories to the HHG yield is smaller than the contribution from short trajectories.

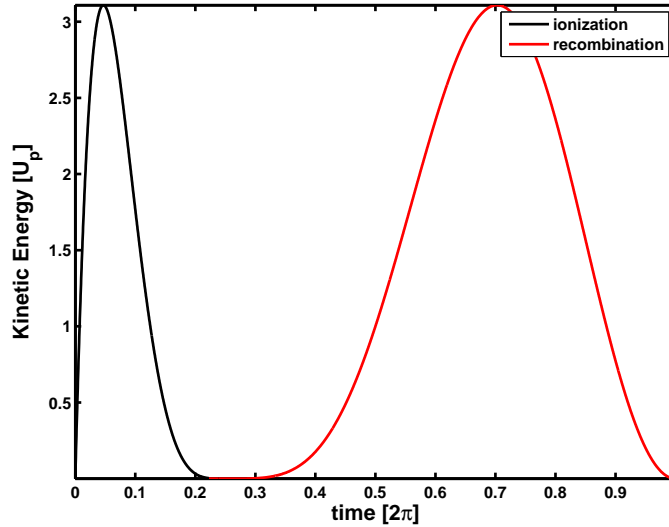


Figure 3.1: Kinetic energy of an electron gained in the electric field of a monochromatic laser for the ionization event and for the recombination event.

Recombination After the electron has been driven back to its origin, it may recombine with its parent ion. If it does, the excess energy, consisting of the kinetic energy of up to $E_{kin} = 3.17U_p$ plus the ionization potential of the ground state $|0\rangle$, is emitted in a single XUV-photon, when the electron decelerates and recombines to the ground state. Since the kinetic energy of the electron depends on the trajectory and specifically on the ionization and recombination times, the excess energy differs for each trajectory, and a single cycle laser field will produce a continuous spectrum of XUV. However, due to a long, pulsed driving laser field and the generation of harmonic emission every half cycle in time, we get a spectrum of odd harmonics spaced by $2 \cdot \hbar\omega_L$. A qualitative spectrum is given in Figure 3.2, which shows bright low order harmonics, harmonics with an equal brightness in the plateau regime and the cutoff, where the intensity decreases with harmonic order. The brightness of the plateau is given by equal amplitudes of the electron trajectories recombining and emitting photons.

3.1.3 Strong field approximation of HHG

In 1994, Lewenstein et al. [21] presented a semiclassical theory of high harmonic generation, called the strong field approximation (SFA), using the quantum nature of the electron in all steps of the three step model. As introduced in section 3.1.1, the electron is moving in a sinusoidal motion around the nucleus, driven by the external electric field. The emitted radiation is given by Equation 3.6 and the acceleration of the dipole moment. In quantum mechanics, the expectation value of the dipole moment of an atom in the time domain is given by Equation 3.5. In the SFA model, an analytical form for the dipole moment can be derived and used to calculate the emitted radiation. The assumption is made that only one ground state $|0\rangle$ is contributing and is not depleted by the electric field. In addition, we assume that the intense laser field promotes the ground state electron directly to the continuum state $|k\rangle$ and no excited states are populated. Since the electron gains roughly $3U_p$, the electron in the continuum is treated as a free particle unaffected by the parent ion's Coulomb field (just as in the previously described classical picture). The continuum state $|k\rangle$ is labeled by its kinetic momentum k . With those assumptions, the wave function can be written as

$$\langle\Psi(t)| = e^{iI_p t} \left(a(t) \langle 0| + \int d^3k b(k, t) \langle k| \right) \quad (3.22)$$

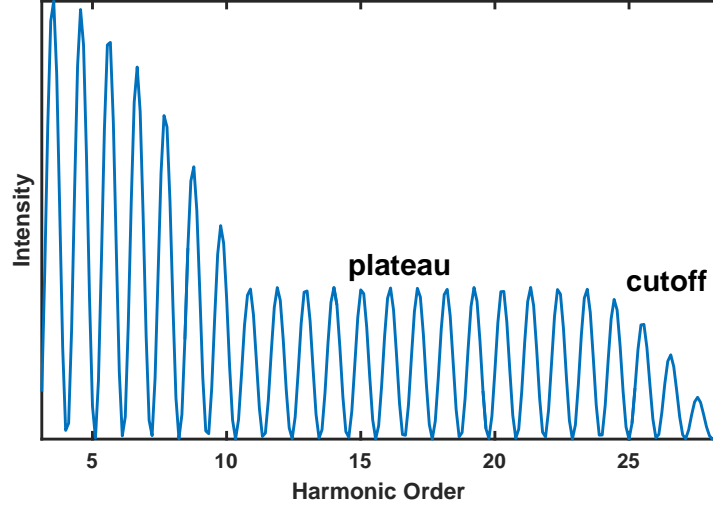


Figure 3.2: Cartoon of a high harmonic spectrum. A plateau of equal intensity harmonics is surrounded by bright low order harmonics and dim cutoff harmonics

with $b(k, t)$ the amplitude of the continuum states and $a(t)$ the amplitude of the ground state. Assuming that $|0\rangle$ is known and treating the problem only in one dimension, given by the laser polarization axis x , only a solution to the Schrödinger equation of $b(k, t)$ has to be found,

$$\dot{b}(k, t) = -i \left(\frac{k^2}{2} + I_p \right) b(k, t) - \epsilon \cos(t) b(k, t) k_x + i \epsilon \cos(t) d_x(k), \quad (3.23)$$

where $d_x(k) = \langle k | x | 0 \rangle$ is the dipole matrix element for the bound-continuum transition parallel to the laser polarization. Solving the Schrödinger equation in Equation 3.23, the solution becomes:

$$b(k, t) = i \int_0^{t_r} dt_i \epsilon \cos(t_i) d_x(k + A(t_i)) \exp \left[-i \int_{t_i}^{t_r} dt'' \left(\frac{1}{2} (vk + A(t_r) - A(t''))^2 + I_p \right) \right] \quad (3.24)$$

with $A(t) = -\epsilon \sin(t) \hat{x}$ the vector potential of the laser field. We use the solution of Equation 3.24 to form the electron wave packet from Equation 3.22. Inserting Equation 3.22 in Equation 3.5, we get

$$x(t) = a^2(t) \langle 0 | x | 0 \rangle + \int d^3 k a^*(t) b(k, t) \langle 0 | x | k \rangle + \int d^3 k a(t) b(k, t) \langle k | x | 0 \rangle + \int d^3 k b^2(k, t) \langle k' | x | k \rangle \quad (3.25)$$

with $x(t)$ the x-component of the dipole moment. The continuum-continuum transitions $\langle k' | x | k \rangle$ and the slow varying term $\langle 0 | x | 0 \rangle$ are ignored [21], forming the dipole moment

$$x(t) = \int d^3 k a^*(t) d^*(k) b(k, t) + c.c.. \quad (3.26)$$

We assume an amplitude of the ground state to be $a(t) \approx 1$ and drop the term in the following equations. Using the canonical momentum $p = k + A(t)$, we get the expression

$$x(t) = i \int_0^{t_r} dt_0 \int d^3 p \epsilon \cos(t_i) d_x(p - A(t_0)) \exp[iS(p, t_r, t_0)] d_x^*(p - A(t_r)) + c.c. \quad (3.27)$$

where the argument of the complex exponential $S(p, t_r, t_0)$ is the time integral over the classical action of the electron along the trajectory from t_0 to t_r

$$S(p, t_r, t_0) = \int_{t_0}^{t_r} dt'' \left(\frac{[p - A(t'')]^2}{2} + I_p \right). \quad (3.28)$$

Qualitatively, Equation 3.27 represents a product of probability amplitudes: the first term $\epsilon \cos(t_0) d_x(p - A(t_0))$ describes the probability amplitude for the electron to leave the atom/molecule and gain canonical momentum p . The second term describes the electron propagating along the classical trajectory in the continuum, acquiring a phase of $S(p, t_r, t_0)$. Finally the third term describes, at time t_r , the electron recombining with a probability amplitude of $d_x^*(p - A(t))$ with its parent. The HHG power spectrum is obtained by a Fourier transformation of the acceleration of the dipole moment $\ddot{x}(t)$

$$P(\omega) \propto |\ddot{x}(\omega)|^2 = \left| \int \ddot{x}(t) e^{i\omega t} dt \right|^2 \approx \omega |x(\omega)|^2 \quad (3.29)$$

We should emphasize that an approximation made in this model is given in the matrix element $d(k) = \langle 0 | x | k \rangle$ in Equation 3.23. We assume that $|k\rangle$ is a plane wave instead of the exact solution of the electron wave function. In this approximation, the dipole matrix element upon re-scattering can be written as

$$d(p) = i \left(\frac{1}{\pi\alpha} \right)^{3/4} \frac{p}{\alpha} \exp(-p^2/2\alpha) \quad (3.30)$$

Equation 3.29 with approximation 3.30 yields qualitative agreement with experiments, where the SFA theory was used to extract the Fourier transform of an atomic wave packet in the ground state [36, 37]. The SFA model can calculate the strength and the phase of the HHG radiation.

3.2 Inelastic scattering and detailed balance

As stated in the previous chapter, the continuum electron wave function is not a plane wave function with the classical action as its energy, but was approximated in such a fashion as to give an analytical form for the high harmonic yield in the SFA model. We need to introduce a better continuum wave function to describe experimental findings in HHG, where structural features were visible [15, 38, 39] that contradict the plane wave approximation. When the electron recombines with the parent ion, the process can be expressed as inelastic scattering in which the accelerated electron loses its kinetic energy, the absorbed energy is emitted by a photon (just as Bethe proved for bremsstrahlung in 1934 [40]) and the continuum wave function has to be a solution to the Schrödinger equation describing inelastic scattering. In this section we follow chapter 123 from Landau-Lifschitz [41] to formulate a relation between inelastic scattering, the photoionization and the photorecombination dipoles. For the elastic scattering case, we have to solve the Schrödinger equation

$$\nabla^2 \Psi + 2m/\hbar^2 (E - U(r)) \Psi = 0 \quad (3.31)$$

with a free electron of energy E in a spherical potential $U(r)$ given by the parent ion. If we reduced this Schrödinger equation to the case of an electron with no angular momentum $l = 0$ and in the presence of no electric field $U(r) = 0$, the solution of Equation 3.31 reduces to a plane wave and the wave function can be written as

$$\Psi \approx e^{ikz}. \quad (3.32)$$

When a radial potential is given and the electron has a well defined angular momentum, the solution to the Schrödinger equation is given by partial waves

$$\Psi = \sum_{l=0}^{\infty} A_l P_l(\cos \theta) R_{kl}(r) \quad (3.33)$$

where $P_l(\cos \theta)$ are Legendre polynomials and R_{kl} is the radial component of the wave function. Following Landau-Lifschitz [41], we get an elastic scattering wave function

$$\Psi \approx e^{ikz} + f(\theta)e^{ikr}/r \quad (3.34)$$

with the scattering amplitude $f(\theta) = \frac{1}{2ikr} \sum_{l=0}^{\infty} (2l+1)[S_l - 1]P_l(\cos \theta)$. The square of the amplitude f gives the cross section of elastic scattering, and we can define the total cross section σ

$$\sigma = 2\pi \int_0^{\pi} |f|^2 \sin \theta d\theta. \quad (3.35)$$

The cross section for elastic scattering from initial state i to the same initial state i is written as

$$d\sigma_{ii} = |f_{ii}|^2 d\Omega \quad (3.36)$$

while the inelastic scattering cross section for a different, final state $\Psi_f = f_{fi}(\theta)\sqrt{\frac{m_f}{m_i}}\frac{e^{ik_f r}}{r}$ is defined as the probability of transitioning from the initial to final state with

$$d\sigma_{fi} = |f_{fi}|^2 \frac{p_f}{p_i} d\Omega_f, \quad (3.37)$$

where the momenta of the final and initial state are $p_i = m_i v_i$ and $p_f = m_f v_f$. We write the exact scattering, recombining wave function as Ψ_k and the transition dipole, used in the strong field approximation, becomes

$$d(\vec{r}) = \langle \Psi_k | \vec{r} | 0 \rangle \quad (3.38)$$

where the dipole matrix element describes the transition from the inelastic scattering wave function to the ground state. This dipole moment is different from the dipole moment used in the SFA model, allowing one to account for structural features in the scattering process.

3.2.1 Principle of detailed balance

To calculate the exact solution of the recombination dipole in Equation 3.38, we can harness the vast body of knowledge about photoionization cross sections (PICS) [11–13]. Theories throughout the history of physics and chemistry have been formulated, using the principle of detailed balance or time-reversal: Maxwell in 1867 [42], Boltzman in 1872 [43] Onsager in 1931 [44]. At thermodynamic equilibrium, processes should be balanced by their reverse processes. We use the principle of detailed balance to connect photoionization calculations to the recombination step in HHG. The recombination process can be described as the time inverse process of photoionization. The scattering process, which we used to describe the dipole matrix element of photorecombination in the previous section, is symmetric with respect to time reversal [41], which means

$$f_{fi} = f_{i^* f^*} \quad (3.39)$$

where the states i^* and f^* differ from i, f by a change in sign of the momentum. The scattering cross sections for $i \rightarrow f$ can be expressed in relation to each other

$$d\sigma_{fi}/p_f^2 d\Omega_f = d\sigma_{if}/p_i^2 d\Omega_i, \quad (3.40)$$

which links the transition from state i to state f to the transition from f to i . This is the principle of detailed balance.

Using this principle, we can describe the dipole moment of photorecombination as the dipole moment of photoionization. With the principle of detailed balance, we achieve a quantitative comparison between theoretical HHG yields and experimental HHG yields. This has been shown theoretically by Frolov and co-workers in a first principle model [17] and used in quantitative re-scattering theory by Chii-Dong Lin and Anh-Thu Le [45].

3.2.2 Models using the principle of detailed balance

In HHG, the rate of high harmonics can be written as the parameterization [17]

$$R(E, I) \propto N(I)W(E, I)\sigma(E), \quad E = E_\Omega - I_p, \quad (3.41)$$

where $W(E, I)$ is the propagation factor and $\sigma(E)$ the photorecombination cross section $\sigma(E)$ of the electron energy E and the intensity I that can shape the harmonic spectrum depending on the atomic/molecular target, where the ionization rate $N(I)$ and the electron wave packet depend on the intensity I of the electric field. The high harmonic spectrum in Figure 3.2 was generated based on the plane wave approximation.

However, in experimental studies [15, 38, 39] it was shown that this does not hold true. Features of the photorecombination cross section are present and shape the harmonic spectrum. Theories have shown that the exact treatment of a scattering wave is able to retrieve these features [17, 45] in atomic targets and has been extended to molecular targets. Quantitative rescattering theory [45] shows very good agreement with high harmonic generation from aligned molecules, as shown in [46], where features like the shape resonance and the Cooper minimum in the photoionization cross section can be directly observed in HHG measured in the laboratory frame. These theories will be briefly explained in the next sections and we use this approach to investigate structural features encoded in the harmonic yield and phase in Chapters 8 and 9.

Quantitative rescattering theory

Quantitative rescattering theory (QRS) is based on the principle of detailed balance, where the recombination step can be more accurately described by existing models of photoionization. QRS uses a phenomenological approach to calculate the yield of high harmonics generated in molecular targets.

In a recent publication [47], Le et al. called the quantitative rescattering theory (QRS) an “extrapolation” of the factorization shown in Equation 3.27, where the treatment of the plane wave is extrapolated onto an expansion that can treat the recombination more accurately. The transition dipole is the time reverse of a one-photon process of photoionization. Computational packages [48, 49] are available and can model atomic and molecular photoionization. This approach has been used to perform studies on complex polyatomic molecules [50]. The harmonic yield is calculated using the Fourier transform of the generated harmonic dipole

$$Y(E) \propto \left| \int \ddot{D}(t)e^{i\omega t} dt \right|^2 = \omega^4 |D(\omega)|^2, \quad (3.42)$$

where we find solutions to $\ddot{D}(t)$ in the SFA and solve the integrand to find the yield. In QRS, we calculate $D(\omega)$ with calculated solutions to the transition dipole $d = \langle \Psi_k | r | \Psi_i \rangle$ from photoionization computational programs. The factorization of QRS yields a harmonic dipole,

$$|D(\omega)|e^{i\phi(\omega)} = |W(E)|e^{i\eta}|d(\omega)|e^{i\delta(\omega)}, \quad (3.43)$$

that is the product of the ionized electron wave packet in the continuum $W(E)$ with phase η and the complex-valued recombination dipole matrix element $d(\omega)$ with phase $\delta(\omega)$, where the energy of the electron is equal to $E = E_\Omega - I_p$ and E_Ω is the harmonic energy.

QRS expands the calculations to high harmonic generation from aligned molecules. We define an induced harmonic dipole $D(\omega, \theta)$ that depends on the orientation of the molecular axis, with

the angle θ defined as the angle between the molecular axis of the molecule and the polarization axis of the linearly polarized laser. Within the QRS, the induced dipole moment for an aligned molecule is written as

$$|D(\omega, \theta)|e^{i\phi(\omega, \theta)} = |W(E, \theta)|e^{i\eta}|d(\omega, \theta)|e^{i\delta(\omega, \theta)}, \quad (3.44)$$

where the square of the electron wave packet in the continuum is

$$|W(E, \theta)|^2 = N(\theta)|\tilde{W}(E, \theta)|^2 \quad (3.45)$$

with $N(\theta)$ the angle dependent ionization probability. We can use the SFA calculations to calculate the induced dipole moment $D^{SFA}(\omega, \theta)$ and use it to calculate the electron wave packet:

$$W^{SFA}(E, \theta) = \frac{D^{SFA}(\omega, \theta)}{d^{PWA}(\omega, \theta)} \quad (3.46)$$

We can calculate the electron wave packet in the continuum under the further assumption that the wave packet is independent of the target, just as it was described in the simple man's and Lewenstein models. The electron energy is solely a function of the electric field, given molecules and atoms with a similar ionization potential.

The induced dipole moment can then be written as

$$D^{QRS}(\omega, \theta) = W^{SFA}(E, \theta)d(\omega, \theta) = \frac{d(\omega, \theta)}{d^{PWA}(\omega, \theta)}D^{SFA}(\omega, \theta) \quad (3.47)$$

and the harmonic signal can be expressed as

$$Y^{QRS}(\omega, \theta) = \frac{\sigma(\omega)}{\sigma^{PWA}(\omega)}Y^{SFA}(\omega, \theta), \quad (3.48)$$

where the SFA yield calculations are ‘‘corrected’’ by the ‘‘exact’’ photorecombination cross section. The QRS allows us to calculate parts of the factorization by using atomic reference targets to expand HHG to molecular targets of the same ionization potential and can extract information about the PICS in the molecular frame.

Scattering model for harmonics driven by elliptically polarized laser fields

So far, we have shown the HHG factorization in three steps that include the ground state wave function and a complex continuum wave function, which is influenced by the atomic potential. Through the principle of detailed balance, we made use of the extensive knowledge of photoionization dipoles and improved the quantitative agreement between experiments and theory that allowed us to understand atomic and molecular structures influencing the yield of HHG. However, these models only considered linearly polarized laser fields and used the calculated dipole moments out of reference atoms to expand the calculations through QRS to molecular targets. In this section, the ground state wave function will be expanded to wave functions with angular momentum $l > 0$, and the transition dipole element from the continuum to the ground state will be calculated using the exact rescattering wave function. One of our recent publications, [51], uses the model of Frolov and coworkers [52]. In this model, we assume the electron is in a short range potential that can support two bound states of angular momentum $l = 0$ and $l = 1$, where we now have two partial wave scattering phases $\delta_l(k)$ that are nonzero. In reference [24], the electric field is expressed as

$$F(t) = \epsilon(\hat{x} \cos \omega t + \hat{y} \eta \sin \omega t) \quad (3.49)$$

where ϵ is the electric field strength and η the ellipticity of the field. The angular momentum projection m is not conserved anymore for an ellipticity $\eta \neq 0$, and field-free states $\phi_{klm}(\vec{r})$ become degenerate, resulting in $(2l+1)$ quasistationary quasienergy states with quasienergies $\epsilon_q = E_0 + \delta\epsilon_q$ (for a p state we get $q = -1, 0, 1$). The field-free states are defined by $\phi_{klm}(\vec{r})$

with $E_0 = -\hbar^2 k^2 / 2m$ and angular momentum l and its projection m . With the assumption that we are in the tunneling regime and that we can approximate the quasienergy ϵ_q with E_0 , the quasistationary quasienergy states can be written as superpositions of the degenerate bound state wave functions $\phi_{klm}(\vec{r}) = \phi_{kl0}(r)Y_{lm}(\vec{r})$ with

$$\phi_{klq}(\vec{r}) = \phi_{kl0}(r)f_{lq}(\vec{r}) \quad (3.50a)$$

$$f_{l,0} = Y_{l,0}(\vec{r}) \quad , \quad f_{l,\pm 1}(\vec{r}) = [Y_{l,1}(\vec{r}) \pm Y_{l,-1}(\vec{r})]\sqrt{2} \quad (3.50b)$$

which define states that are oriented in the three coordinate axes: $x(q = -1)$, $y(q = 1)$ and $z(q = 0)$. We insert the wave functions into the equation for the dipole moment, which is similar to the dipole moment defined in SFA, and get

$$d_{l,q}(t) = \frac{2C_{k,l}}{iT(ka)^{3/2}} \int_{T/2}^T f_{l,q}[\hat{K}_i(t)] \left(\frac{F(t_i)}{F_0} \cdot \frac{K_i(t)}{\hbar k} \right)^{-1/2} \quad (3.51)$$

$$\times \frac{\exp(-i(S(t, t_i) - Et + E_0 t_i)/\hbar)}{[v(t - t_i)]^{3/2}} \langle \phi_{klq} | r | \phi_{K(t)} \rangle dt \quad (3.52)$$

where $K(t', t, t_i)$ is the instantaneous classical momentum of an electron with a trajectory from its ionization time to its return time [24] and T the cycle length of the driving laser field. In the calculations of reference [24], the continuum electron wave function $\phi_{K(t)}(r)$ is represented in a partial wave equation, as previously shown in Section 3.2

$$\Psi_{K(t)}(r) = \sum_{l,m} \Psi_{\epsilon(t),l}(r) Y_{l,m}^*[K(t)] Y_{l,m}(r) \quad (3.53)$$

$$\phi_{\epsilon(t),l}(r) = \frac{2\pi\hbar}{aK(t)} i^l e^{i\delta_l[\epsilon(t)]} R_{K(t),l}(r) \quad (3.54)$$

We get dipole elements in r , x and y components: $\langle \phi_{k,0,0} | r | \phi_{K(t)} \rangle$, $\langle \phi_{k,1,+1} | x | \phi_{K(t)} \rangle$, $\langle \phi_{k,1,+1} | y | \phi_{K(t)} \rangle$, $\langle \phi_{k,1,-1} | x | \phi_{K(t)} \rangle$, $\langle \phi_{k,1,-1} | y | \phi_{K(t)} \rangle$. Changing the polarization from a linear driving field in the previous sections to an elliptical field, the solution to the harmonic yield contains dipole moments in multiple directions. With the proposed theory, we can understand the ellipticity-dependent yield of high harmonics. Previous papers have measured the ellipticity dependence and theories were able to explain the behavior. However, with this theory developed by Frolov and coworkers, we can extract structural information, as seen in Chapter 7.

3.2.3 Coherent nature of HHG

In this section, I will talk about coherence from a general perspective and how the coherence of the laser light is ultimately the cause of the coherence in high harmonic generation.

Waves are coherent with each other when their relative phases have a fixed relation. This principle can be expanded to describe the coherence between light and matter, when there is a well-defined phase between the electric field and the electron wave function. For the case of high harmonic generation, we can use the same argument to show the coherence of higher order harmonics, where HHG is driven by the interaction between light and matter. Light of well-defined phase launches the electron wave packet by tunnel ionization. Its phase is correlated with the phase of the laser light and forms a coherent wave packet. Each step of the three step model then imprints another well-defined phase on the electron wave function, after which the electron recombines to the ground state and emits a photon. This coherence is imprinted on the emitted high harmonic spectrum. We can find an analog between tunnel ionization and stimulated emission. Stimulated emission is the fundamental step in the coherence of a laser, while tunnel ionization is the fundamental step to start the ‘‘clock’’ in high harmonic generation.

Starting in 1998, experiments first revealed the coherent nature of HHG. Bellini [23] measured the coherence time between two harmonic sources, where the time of coherence was similar to the pulse duration of the driving laser fields. Yost [53] performed a coherence measurements of a

single-harmonic pulse for adjacent pulses of a cavity-based laser. Since the electron wave packet generates all harmonic orders in a single event, a phase relation between different harmonic orders is given as well. This has been experimentally shown with measurements based on reconstruction of attosecond beating by interference of two-photon transitions (RABBIT) [54], which proved the full coherence of HHG. Streaking experiments have further shown the realization of attosecond pulse trains [55] or isolated attosecond pulses [56].

The coherent nature of high harmonic generation can be used to perform spectroscopic studies. Ex-situ measurements [14], based on RABBIT, and in-situ interferometric studies [57] have provided valuable information on structural and dynamical features of high harmonic generation, not only in the amplitude, but also in the phase of harmonics.

Interferometric studies can be described in analogy to Young's double slit, where the two slits are illuminated by two independent harmonic sources. Due to the coherence of HHG, emission from both slits/sources can interfere destructively or constructively in the far field. Assuming the distance between the double slits to be small and the observation plane to be far away from the two slits, an equation of interference can be given by a classical Young's double slit

$$d \sin \theta \approx d\theta \quad (3.55)$$

where the minima and maxima of the interference are separated by

$$\theta_f \approx \lambda/d. \quad (3.56)$$

The position of these minima and maxima is a direct measurement of the relative phase between the two sources. If the phase of the irradiated light of one of the two sources changes, the minima and maxima will move and resolve the change in phase. In HHG, these phases hold valuable information on all steps involved in high harmonic generation.

More specifically, individual steps in HHG can be isolated from the additional steps and their influence on the phase and amplitude measured. This point is crucial to my thesis: We can isolate the third step of HHG and use HHG to study the complex-valued photoionization dipole by measuring the amplitude and phase of the harmonic sources.

Describing the photoionization dipole as $d(\omega, \theta) = |d(\omega, \theta)|e^{i\phi(\omega, \theta)}$ is in contrast to the method of describing photoionization as a perturbation. Following Dirac [58] and Fermi [59], we can describe photoionization by a perturbation. Following Fermi's golden rule, we write

$$\Gamma_{if} = \frac{2\pi}{\hbar} |\langle f | H' | i \rangle|^2 \rho \quad (3.57)$$

where Γ is the transition rate between initial state i and final state f . It is given by the magnitude of the matrix element alone. ρ describes the density of the final states. Any phase information is lost in this approach, but can be measured in a very indirect way, as long as we can express the photoionization cross section with two variables, we can extract similar knowledge out of the photoionization process. We still observe interference effects given by shape resonances or Cooper minima, which can be expressed by the double differential cross section of photoionization, known from synchrotron measurements and theory [11–13]. It is written as

$$\sigma(E, \theta) = \frac{\sigma_0(E)}{4\pi} \left[1 + \frac{\beta(E)}{2} (3 \cos^2 \theta - 1) \right] \quad (3.58)$$

which is only a real-valued function of the PICS as a function of the two variables E and θ . In HHG we have access to the real and imaginary parts of $d(\omega, \theta) = \sqrt{\sigma(\omega, \theta)}e^{i(\phi(\omega, \theta))}$.

3.3 Molecular alignment

In this section, I will introduce the concept of non-adiabatic alignment and how a rigid rotor behaves under rotational excitation. I will introduce a rotor that has different moments of inertia, which will then be used to explain a simpler rigid rotor with only one rotational axis, but will

also be used to explain an asymmetric rotor.

3.3.1 Classification of molecular rotors

Any molecule has three moments of inertia I_A, I_B, I_C about three orthogonal axes, with the center of mass as the origin. The general notion describes I_A as the smallest moment of inertia. We can put the molecules in different categories, depending on the symmetry of the molecule: linear molecules, spherical molecules, symmetric tops and asymmetric tops. Linear molecules have a typical ratio between the moments of inertia of $I_A < I_B \approx I_C$, where the moment of inertia I_A around the internuclear axis can be approximated to be zero in most cases. Examples are diatomic nitrogen or oxygen. Spherical molecules, such as sulfur hexafluoride, have the same moment of inertia in all three axes ($I_A = I_B = I_C$). Symmetric tops are similar to linear molecules, where two axes have the same moment of inertia. However, the third axis has a momentum of inertia that cannot be neglected. We can divide the symmetric tops into groups of oblate ($I_A = I_B < I_C$) and prolate symmetric tops ($I_A < I_B = I_C$). Oblate molecules are disc shaped, an example is benzene, and prolate molecules are more cigar shaped, e.g. chloromethane. In the case of asymmetric tops, we have 3 different moments of inertia ($I_A \neq I_B \neq I_C$).

3.3.2 Introduction to the rigid rotor in quantum mechanics

In the Born-Oppenheimer approximation, we can write the total wave function of our system as the product of the wave function of the nucleus and of the electrons and approximate the motion of the nucleus to be frozen compared to the fast motion of the electrons around it. The molecular wave function is described as the product [60, 61]

$$\Phi_{mol} = \Phi_{el}\Phi_{vib}\Phi_{rot}\Phi_{nu.spin} \quad (3.59)$$

where Φ_{el} is the electronic wave function, Φ_{vib} the vibrational wave function, Φ_{rot} the rotational wave function and $\Phi_{nu.spin}$ the wave function of nuclear spins. Each component can be solved by writing the individual Hamiltonian for each wave function. We assume no coupling between the vibrational and rotational Hamiltonian of the molecule. For a rigid rotor we can write the rotational Hamiltonian

$$H_{rot} = \frac{J_a^2}{2I_a} + \frac{J_b^2}{2I_b} + \frac{J_c^2}{2I_c} = AJ_a^2 + BJ_b^2 + CJ_c^2 \quad (3.60)$$

where $J_{a,b,c}$ are angular momentum operators and A, B and C are the frequencies of rotation about each axis. In the case of nitrogen, we get a one-dimensional rigid rotor, since the rotation around the b-axis and c-axis are identical and cannot be distinguished. The internal Hamiltonian for nitrogen is

$$H_{rot} = \frac{j^2 \hbar^2}{2I_B} \quad (3.61)$$

With the Schrödinger equation

$$H_{rot}\Phi = E\Phi \quad (3.62)$$

we get the energy of the rotational states

$$E_n = \frac{j(j+1)\hbar^2}{8\pi^2 I_B} \quad (3.63)$$

which can be written as $E_n = j(j+1)Bh$ with the rotational constant B . Using the energy of the rotational states, we can estimate the partition function of the rotational states:

$$\xi = \sum_{J_i} e^{-E_{J_i}/kT} \quad (3.64)$$

which describes the statistical properties of the rotational system.

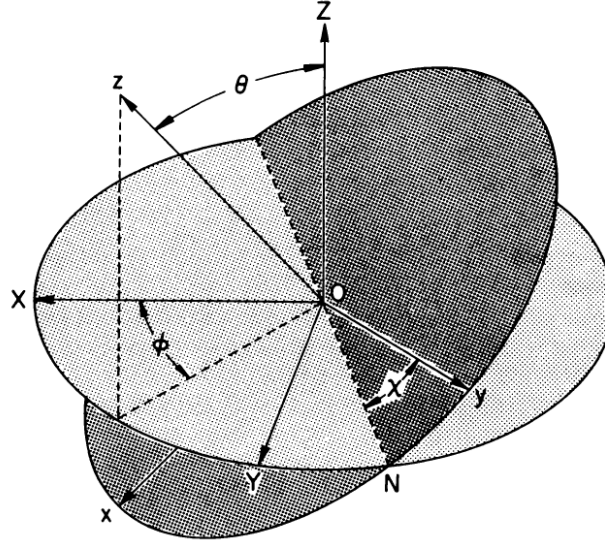


Figure 3.3: Definition of molecular frame and laboratory frame, Figure taken from [62]

3.3.3 Particle in an external field

When an atom or molecule is in an electric field of strength $\vec{\epsilon}$, the energy U of the system can be expressed in a Taylor expansion

$$U = U_0 - \mu_{perm.}\epsilon_i - \frac{1}{2}\alpha_{ij}\epsilon_i\epsilon_j - \frac{1}{6}\beta_{ijk}\epsilon_i\epsilon_j\epsilon_k - \frac{1}{24}\gamma_{ijkl}\epsilon_i\epsilon_j\epsilon_k\epsilon_l \quad (3.65)$$

where U_0 is the unperturbed energy, $\mu_{perm.}$ the permanent dipole moment, α the polarizability and β and γ the first and second hyperpolarizabilities with ijk coordinates in the cartesian coordinate system and l one of the three coordinates. In the case of the molecules and techniques treated in this thesis, the permanent dipole moment and hyperpolarizability of nitrogen and ethylene wash out over the multi-cycle laser fields, as each half cycle introduces an effect opposite to the adjacent half cycle. The energy of the system is then described as

$$U = U_0 - \frac{1}{2}\alpha_{ij}\epsilon_i\epsilon_j \quad (3.66)$$

where the energy of the system is only influenced by the interaction with the induced dipole $\mu_{ij} = \alpha_{ij}\epsilon_i$. The polarizability α is a 3x3 tensor given by

$$\alpha = \begin{bmatrix} \alpha_{XX} & \alpha_{XY} & \alpha_{XZ} \\ \alpha_{YX} & \alpha_{YY} & \alpha_{YZ} \\ \alpha_{ZX} & \alpha_{ZY} & \alpha_{ZZ} \end{bmatrix} \quad (3.67)$$

and the induced dipole moment $\mu_i = \sum \alpha_{ij}\epsilon_j$ in the lab frame is

$$\begin{bmatrix} \mu_X \\ \mu_Y \\ \mu_Z \end{bmatrix} = \begin{bmatrix} \alpha_{XX} & \alpha_{XY} & \alpha_{XZ} \\ \alpha_{YX} & \alpha_{YY} & \alpha_{YZ} \\ \alpha_{ZX} & \alpha_{ZY} & \alpha_{ZZ} \end{bmatrix} \cdot \begin{bmatrix} \epsilon_X \\ \epsilon_Y \\ \epsilon_Z \end{bmatrix} \quad (3.68)$$

where we have to perform a transformation from the molecule fixed frame to the laboratory frame, since we are only able to calculate the polarizability of the molecule in the molecule fixed frame, given by its coordinate system x, y, z . The transformation is performed using the direction

cosine matrix [62]

$$\Phi(\phi, \theta, \chi) = R_z(\chi)R_N(\theta)R_Z(\phi) \quad (3.69)$$

where ϕ is a rotation about the Z axis in the lab frame, θ a rotation about the molecular y axis and χ the rotation about the molecular z axis. Definitions for the Euler angles and rotation function can be taken from [62] and are shown in Figure 3.3. For a linear rotor with the molecular axis around the z axis and an electric field with a component in the Z-axis we get an induced dipole moment only in the Z direction:

$$\mu_Z = \mu_x \sin \theta \cos \chi + \mu_y \sin \theta \sin \chi + \mu_z \cos \theta \quad (3.70)$$

with $\mu_x = \sin \theta \cos \chi \epsilon_Z \alpha_{xx}$, which results in a laboratory induced dipole moment

$$\mu_Z = \alpha_{xx} \epsilon_Z \sin^2 \theta \cos^2 \chi + \alpha_{yy} \epsilon_Z \sin^2 \theta \sin^2 \chi + \alpha_{zz} \epsilon_Z \cos^2 \theta \quad (3.71)$$

$$= \alpha_{\perp} \epsilon_Z \sin^2 \theta + \alpha_{\parallel} \epsilon_Z \cos^2 \theta \quad (3.72)$$

which we re-write to

$$\mu_Z = \alpha_{\perp} \epsilon_Z \sin^2 \theta + \alpha_{\parallel} \epsilon_Z \cos^2 \theta \quad (3.73)$$

$$= \alpha_{\perp} \epsilon_Z \sin^2 \theta + \alpha_{\perp} \epsilon_Z \cos^2 \theta - \alpha_{\perp} \epsilon_Z \cos^2 \theta + \alpha_{\parallel} \epsilon_Z \cos^2 \theta \quad (3.74)$$

$$= \alpha_{\perp} \epsilon_Z - \alpha_{\perp} \epsilon_Z \cos^2 \theta + \alpha_{\parallel} \epsilon_Z \cos^2 \theta \quad (3.75)$$

and use the a new variable with $\Delta\alpha = \alpha_{\parallel} \epsilon_Z - \alpha_{\perp} \epsilon_Z$ to write

$$\mu_Z = \Delta\alpha \epsilon_Z \cos^2 \theta + \alpha_{\perp} \epsilon_Z \quad (3.76)$$

Following the above description and using Equation 3.66, we can write the induced Hamiltonian as

$$H_{ind}(t) = (\Delta\alpha \cos^2 \theta + \alpha_{\perp}) \cdot F^2(t) \hat{Z} \quad (3.77)$$

with $F(t) = \frac{1}{2} \epsilon(t) \cos \omega t$, where $\epsilon(t)$ describes the envelope of the electric field as a function of time, and we get

$$H_{ind}(t) = (\Delta\alpha \cos^2 \theta + \alpha_{\perp}) \cdot \frac{\epsilon^2(t)}{4} \hat{Z} \quad (3.78)$$

A linear rigid rotor in an external electric field

To describe the system under the influence of the external field, we solve the time dependent Schrödinger equation (TDSE). The Hamiltonian for the interaction between the laser pulse and the molecule is given by

$$H(t) = H_{rot} + H_{ind}(t) \quad (3.79)$$

where H_{rot} is the field free Hamiltonian described in Equation 3.60 and H_{ind} the induced Hamiltonian described in Equation 3.78. We assume that the laser pulse duration is significantly shorter than the rotational constant of the molecule, B , i.e. $\tau \ll \frac{\hbar}{B}$, with τ defined as the full width at half maximum of a Gaussian pulse, when the signal drops to $1/e$ with the envelope $\epsilon(t) = e^{-t^2/\tau^2}$. The TDSE can be written as

$$i\hbar \frac{\partial \Psi}{\partial t} = \hat{H} \Psi \quad (3.80)$$

and we can find solutions to the TDSE using the orthonormal basis set

$$|\Psi\rangle = C_M^J |JM\rangle \quad (3.81)$$

where the coefficients C_{JM} are time dependent and we can write the TDSE as

$$i\hbar \dot{C} = \sum_{J,M} C_M^J(t) (\langle JM | H_{rot} | J'M' \rangle + \langle JM | H_{ind} | J'M' \rangle) \quad (3.82)$$

where J', M' are the initial rotational states and J, M the occupied states after the interaction with the electric field. We insert the formalism for the rotational Hamiltonian and insert the exact formula of the induced Hamiltonian, so that

$$i\hbar \sum_{J,M} \dot{C} = \sum_{J,M} C_M^J(t) \left(E_{JJ'} \delta_{JJ'} - \frac{\epsilon^2(t)\Delta\alpha}{4} \langle JM | \cos^2 \theta | J'M' \rangle - \frac{\epsilon^2(t)\alpha_{\perp}}{4} \langle JM | | J'M' \rangle \right) \quad (3.83)$$

where $\delta_{J,J'}$ is a Kronecker delta and the equation turns into

$$\sum_{J,M} \dot{C}_M^J(t) = -\frac{i}{\hbar} \sum_{J,M} C_M^J(t) \left(E_{J'J} \delta_{J'J} - \frac{\epsilon^2(t)\alpha_{\perp}}{4} \delta_{J'J} - \frac{\epsilon^2(t)\Delta\alpha}{4} \langle J'M' | \cos^2 \theta | JM \rangle \right) \quad (3.84)$$

where we now have to solve the last summand out of the equation to find a solution for the coefficients $C_M^J(t)$. Solving the summand, while rewriting $\cos^2 \theta$ as a spherical harmonic, we get

$$\begin{aligned} \langle J'M' | \cos^2 \theta | JM \rangle &= \frac{1}{3} \delta_{J'J} + \frac{4}{3} \sqrt{\frac{\pi}{5}} \langle J'M' | J = 2, M = 0 | JM \rangle \\ &= \frac{1}{3} \delta_{J'J} + \frac{2}{3} \sqrt{(2J'+1)(2J+1)} \begin{pmatrix} J' & 2 & J \\ 0 & 0 & 0 \end{pmatrix} \begin{pmatrix} J' & 2 & J \\ M' & 0 & M \end{pmatrix} \end{aligned} \quad (3.85)$$

where the two brackets at the end are Wigner 3-j symbols to add the angular momentum $J = 2$ from the initial state to the final state. Inserting Equation 3.85 into Equation 3.84, we can write the solution for the time dependent coefficients as

$$\begin{aligned} \sum_{J,M} \dot{C}_M^J(t) = & - \frac{i}{\hbar} \sum_{J,M} C_M^J(t) \left(E_{J'J} \delta_{J'J} - \frac{\epsilon^2(t)\alpha_{\perp}}{4} \delta_{J'J} \right. \\ & \left. - \frac{\epsilon^2(t)\Delta\alpha}{4} \left(\frac{1}{3} \delta_{J'J} + \frac{2}{3} \sqrt{(2J+1)(2J'+1)} \begin{pmatrix} J' & 2 & J \\ 0 & 0 & 0 \end{pmatrix} \begin{pmatrix} J' & 2 & J \\ M' & 0 & M \end{pmatrix} \right) \right) \end{aligned} \quad (3.86)$$

This ordinary differential equation of the form $\dot{C} = C(t, J)$ is solved using the MATLAB ode45 function, based on the DormandPrince method, an explicit Runge-Kutta method. For each time step in the electric field, an array of coefficients is calculated and used for the next time step. The square of the coefficients is equal to the population of the corresponding J state. The coefficients in Equation 3.86 will be zero unless $\Delta J = -2, 0, 2$. Raman transitions follow these rules and we can describe the rotational excitation as a series of Raman transitions. During the pulse, these transitions happen coherently and the resulting coefficient C_M^J are real values. After the laser pulse, we calculate the time dependent behavior of the wave function by solving the time dependent Schrödinger equation for the field-free Hamiltonian. The solution is

$$|\Psi(t)\rangle = \sum_{J'} C_{J'M}(t_e) |J'M\rangle e^{-iE_{J'}(t-t_e)/\hbar} \quad (3.87)$$

with t_e the time at the end of the laser pulse and $E_{J'}$ the eigenenergies of the field-free Hamiltonian. From Equation 3.87 we can define a J-state dependent phase in the wave packet:

$$\phi_J = E_J \Delta t / \hbar = 2\pi(BJ(J+1))\Delta t \quad (3.88)$$

and look at the phase difference of neighboring J states:

$$\phi_J - \phi_{J-1} = 2\pi(2B\Delta t)J \quad (3.89)$$

where Δt is given as the time difference between the end of the pulse and the current time. If we now set the time delay Δt to be $T_{rev} = 1/(2B)$, we see that all J-states have the same phase, resulting in a full revival and all excited states align with the polarization direction of the external field. At $t = 1/4B$ the neighboring states have a phase offset of π , resulting in a half revival,

where rotational states point in opposite direction, but are indistinguishable. Fractional revivals at times $T_{rev} \cdot p/q$ with $q = 1, 2, 4$ can occur. However, calculations expect no revival at times of $t = 1/8B$, where neighboring states have a phase difference of $\pi/2$, so even J-states anti-align with the laser polarization, while odd states align with the laser polarization and are parallel to the polarization direction. Due to the spin-statistics in diatomic nitrogen, we can still observe a revival at this particular time. With a ratio of 2:1, more even states anti-align at this particular time with the laser field, resulting in a revival with a reduced degree of alignment, while then at a time of $t = 1/2B - 1/8B$, more states align with the laser and a peak in the alignment is visible. These behaviors are shown in Figure 3.4, where we plot the time dependent value of $\langle \cos^2 \theta \rangle$ as a function of time after the interaction with a laser pulse. We use the expectation of $\langle \cos^2 \theta \rangle$ as a metric to describe the degree of alignment, where $\langle \cos^2 \theta \rangle$ describes the overlap between the molecular axis and the laser polarization.

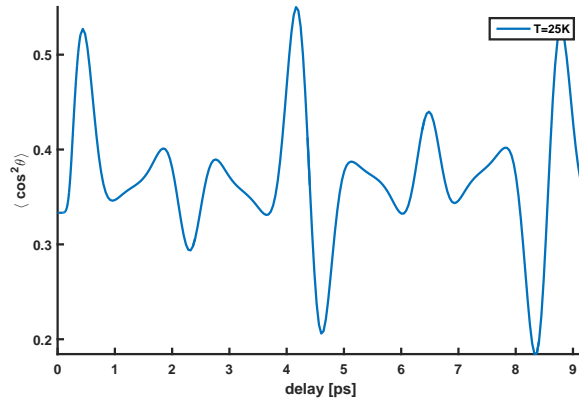


Figure 3.4: Molecular alignment of diatomic nitrogen as a function of field-free time, expressed with the expectation value $\langle \cos^2 \theta \rangle$ for a rotational temperature of $T=25$ K, rotational excited with a single pulse with a pulse duration of 80 fs and $20 \text{ TW}/\text{cm}^2$.

3.3.4 Asymmetric rotor

As described in section 3.3.1 and Equation 3.60, the Hamiltonian for a rigid asymmetric rotor has different moments of inertia in all directions. However, using Ray's parameter κ we can split the description into two limits.

$$\kappa = \frac{2B - A - C}{A - C} \quad (3.90)$$

For $\kappa > 0$, the asymmetric rotor resembles a prolate top molecule and for $\kappa < 0$, the asymmetric rotor resembles an oblate top molecule, where in the limit $A \approx B$ we have an oblate top ($\kappa = 1$) and in the limit $B \approx C$ we can describe the rotor as a prolate top molecule ($\kappa = -1$). In these extreme cases, the asymmetric rotor is reduced to a symmetric rotor again. We first show solutions to the symmetric rotor case and extrapolate this to the case of the asymmetric rotor. The field free Hamiltonians for the two cases is given by

$$H_{rot} = A\hat{J}^2 + (C - A)J_z^2 \quad (3.91)$$

for the oblate case and

$$H_{rot} = C\hat{J}^2 + (A - C)J_z^2 \quad (3.92)$$

for the prolate case, where the eigenvalues are defined as $E_{JK} = AJ(J + 1) + (C - A)K^2$ and $E_{JK} = CJ(J + 1) + (A - C)K^2$.

In the general case of an asymmetric rotor, the wave functions of the asymmetric rotor are linear

combinations of the symmetric top wave functions

$$\Psi_{JM} = \sum_K c_K |JKM\rangle. \quad (3.93)$$

where it is only a summation over K , while J, M are still good quantum numbers, when changing from a symmetric rotor to the asymmetric rotor. Following chapter 6.3 from [62], the solution to the rotational Hamiltonian can be found through a variational method, where the energies are the roots of the secular determinant

$$|H_{K'K} - E\delta_{K'K}| = 0 \quad (3.94)$$

with $H_{K'K} = \langle JK'M | H_{rot} | JK M \rangle$ and the secular determinant is of order $(2J+1)(2J+1)$. Zare follows up with a simplification of the secular determinant into four blocks through the Wang transformation [63] that uses group operations to simplify the calculations of the asymmetric rotor, since asymmetric tops belong to the point group D_2 [62]. Further to that, when again considering the limits of the oblate and prolate tops, one can define a new index for the resulting energy levels of the rotor. In the limit of prolate or oblate tops, $|K|$ reaches different values in each limit. We can define a value for $|K|$ in the oblate limit with K_1 and a value for $|K|$ for the prolate limit with K_{-1} and the resulting index for the energy levels is defined as

$$\tau = K_{-1} - K_1 \quad (3.95)$$

where K_1 is associated with a rotation around the c-axis and K_{-1} with a rotation around the a-axis. We get a set of eigenvalues in the $\langle J\tau M |$ basis set, where the energy states show energy values given in Figure 3.5.

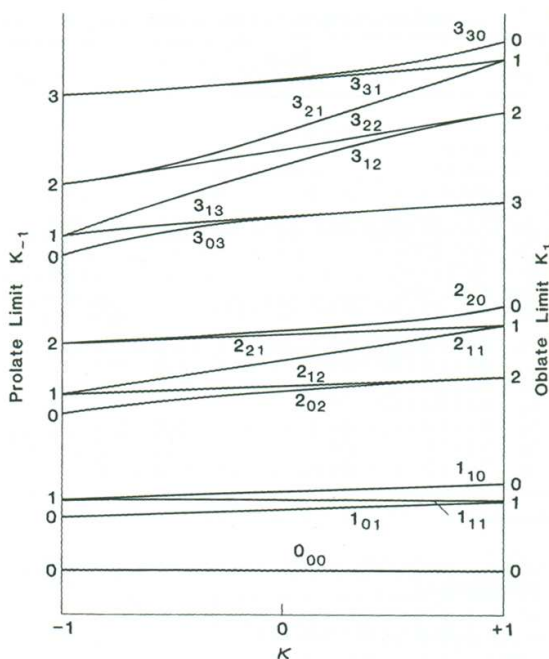


Figure 3.5: Energy levels for an asymmetric top as a function of Ray's asymmetry parameter κ , where $\kappa = 1$ corresponds to a prolate symmetric top and $\kappa = -1$ to an oblate symmetric top. Copied from [62]

Following the partition function from Equation 3.64, we get a weight associated to each rotational state as shown in Figure 3.6a. The weights were calculated by code provided by Varun Makhija [64] and also account for nuclear spin statistics. In the case of nitrogen, we get a rotational ensemble that is well described by 5 states for a rotational temperature of 5 K or 9 states for a rotational temperature of 25 K in Figure 3.6b, while for ethylene we have 35 states for a rotational temperature of 5 K and over 700 for a rotational temperature of 40 K, where the partition function was only calculated to account for 0.99 of the involved rotational states, while for nitrogen, we can set the convergence limit to 0.999.

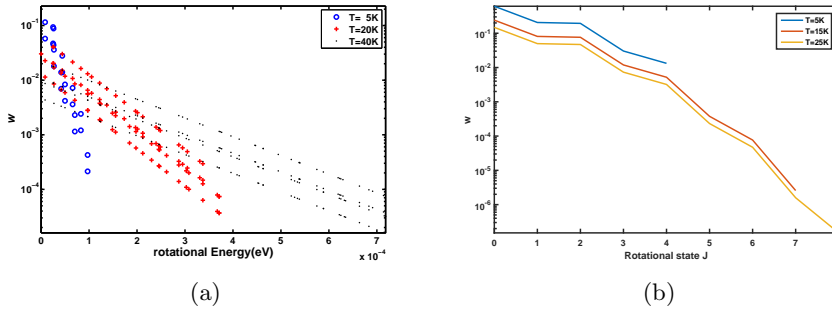


Figure 3.6: (a) Weight in the partition function of ethylene as a function of energy of occupied rotational states (b) Weight in the partition function of nitrogen as a function of rotational states for different temperatures

Induced dipole of the asymmetric rotor

As previously expressed for a linear rotor in Equations 3.68 and 3.69, the energy of the molecule is influenced by the induced dipole. The induced dipole moment is written as

$$\mu_i = -\frac{1}{2}\alpha_{ij}F_j(t) \quad (3.96)$$

where α_{ij} is the polarizability tensor in the laboratory frame with an electric field F_j with polarization components ϵ_j . The polarizability tensor can be solved by noting [65]

$$\alpha_{\rho\rho'} = \sum_{k,k'} \langle \rho|k \rangle \alpha_{kk'} \langle k'|\rho' \rangle \quad (3.97)$$

where $\langle \rho|k \rangle$ are elements of the transformation matrix between the lab frame k and the molecular frame ρ , with $k = X, Y, Z$ lab fixed cartesian coordinates. Here again, we have to perform a transformation from the molecular frame into the laboratory frame to calculate the proper potential that is introduced through the electric field on an asymmetric rotor. Instead of describing the transformation by the direction cosine transformation, given by 3.69, we use the transformation

$$\alpha_M^{[L]}(\Omega) = \sum_K D_{M,K}^{*[L]}(\Omega) \alpha_K^{[L]} \quad (3.98)$$

where $D_{M,K}^{*[L]}(\Omega)$ are Wigner-D rotation matrices connecting the molecular frame to the laboratory frame with $\Omega = \{\theta, \phi, \chi\}$ [64]. The potential becomes

$$V = -\frac{1}{2}(-1)^{L+M} \alpha_M^L U_M^L = -\frac{1}{4}(-1)^{L+M} D_{M,m'}^{*[L]}(\Omega) \alpha_{m'}^L U_M^L, \quad (3.99)$$

with U_{ij} the electric field tensor. For the case of α_{ij} being diagonal in the molecular frame, only components α_M^L with $\alpha_0^0, \alpha_0^2, \alpha_{-2}^2 = \alpha_2^2$ are non zero, which then diagonalizes the field tensor U_{ij} ,

leaving only the components U_0^0 , U_0^2 and $U_2^2 = U_{-2}^2$ and we get an expression for the potential [64]

$$V(t) = -2\pi\alpha I_0(t) \left[\frac{2-3\epsilon_x^2}{\sqrt{6}} [\alpha_0^2 D_{0,0}^2 + \alpha_2^2 (D_{0,2}^2 + D_{0,-2}^2)] + \frac{\epsilon^2}{2} [\alpha_0^2 (D_{2,0}^2 + D_{-2,0}^2) + \alpha_2^2 (D_{2,2}^2 + D_{2,-2}^2 + D_{-2,2}^2 + D_{-2,-2}^2)] \right]. \quad (3.100)$$

where the light has components in x and z . Assuming a linearly polarized pulse so that $\epsilon_x = 0$ and rewriting the Wigner function $D_{M,K}^L$ in Euler angles, we can write a simplified expression for the potential of

$$V(t) = -\frac{2\pi\alpha I_0(t)}{\sqrt{6}} \left[\alpha_0^2 \left(\frac{3}{2} \cos^2 \theta - 1 \right) + \alpha_2^2 \sqrt{\frac{3}{2}} \sin^2 \theta \cos 2\chi \right]. \quad (3.101)$$

The potential shows that with a linearly polarized electric field, we can achieve alignment in both angles θ and χ .

Interaction of light with the asymmetric rotor

We can insert the potential given in Equation 3.101 into the TDSE as previously shown in Equation 3.80 and can expand the time dependent wave function in the $|JKM\rangle$ basis with time dependent coefficients C_{JKM}

$$\Psi(t) = C_{JKM}(t) |JKM\rangle. \quad (3.102)$$

where we gain coupled differential equations for the coefficients $C_{JKM}(t)$

$$i \frac{dC_{JKM}}{dt} = C_{JK'M} H_{K,K'} + C_{J'K'M'} \langle JK M | V | J' K' M' \rangle \quad (3.103)$$

where $H_{K,K'}$ are matrix elements of the field-free Hamiltonian. Detailed description can be taken from [64], where the solution of the second term of Equation 3.103 has to be solved to find the time dependent behavior of $C_{JKM}(t)$. The second term is solved for a linearly polarized field:

$$\langle JK M | V(t) | J' K' M' \rangle = -2\pi\alpha I_0(t) \sqrt{\frac{2J+1}{2J'+1}} \left[\frac{2}{\sqrt{6}} \langle J, M; 2, 0 | J' M' \rangle [\alpha_0^2 \langle J, K; 2, 0 | J' K' \rangle + \alpha_2^2 (\langle J, K; 2, 2 | J', K' \rangle + \langle J, K; 2, -2 | J', K' \rangle)] \right]$$

The expression for the matrix elements of V provides selection rules for transitions between rotational states. The terms on the right excite coherences between states with $\Delta J = -2, 0, 2$, $\Delta M = 0$ and $\Delta K = -2, 0, 2$. The excitations occur via Raman transitions and form our rotational wave packet. The wave function evolves in time as a function of the angles θ, χ during and after the laser pulse. The above expression can then be used to numerically propagate Equation 3.103 to calculate the values of $C_{JKM}(t_e)$. The Clebsch-Gordon coefficients are calculated using known analytic expressions [62]. The solutions for Equation 3.103 is supplied by Varun Makhija [64]. And as already shown in the linear rotor case in Equation 3.87, we calculate the field free wave function after the interaction with the laser pulse at the end time t_e with

$$C_{J\tau M}(t) = C_{J\tau M}(t_e) e^{-i2\pi E_{J\tau M}(t-t_e)}, \quad (3.104)$$

The time dependent expectation value of a physical quantity can then be calculated from these coefficients.

Nuclear spins

As introduced in Section 3.3.2 in Equation 3.59, the molecular wave function is described as the product

$$\Phi_{mol} = \Phi_{el}\Phi_{vib}\Phi_{rot}\Phi_{nu.spin} \quad (3.105)$$

where Φ_{el} is the electronic wave function, Φ_{vib} the vibrational wave function, Φ_{rot} the rotational wave function and $\Phi_{nu.spin}$ the wave function of nuclear spins. The rotational eigenfunctions have to be combined with the nuclear spin eigenfunctions $\Phi^{nu.sp}$ to fulfill the symmetrization postulate. Looking into the nuclear spins of the constituents for ethylene, ^{12}C and 1H , we get zero nuclear spin for ^{12}C and nuclear spin of $1/2$ for 1H , giving rise to 16 spin states for ethylene, which have a different symmetry following the point group of ethylene in Table 3.1.

Γ^{rot}	$\Gamma^{nu.sp}$	$g_{\Gamma^{nu.sp}}$
A	A	7
B_a	B_a	3
B_b	B_b	3
B_c	B_c	3

Table 3.1: Character table for ethylene and the D_2 point group. More details in [60]

These states can be associated with the rotational wave function and show their weight in accordance with the rotational ensemble of the molecule. Each symmetry has a different weight that is additionally put into Figure 3.6a. For the case of diatomic nitrogen we have the constituents of two nitrogen atoms. ^{14}N has a nuclear spin of 1 so that the entire nuclear wave function must be symmetric with respect to the exchange of the nuclei. For $I = 1$ there are 6 symmetric and 3 antisymmetric spin states for the two nuclei, giving rise to the ratio between even and odd rotational states of 2 : 1, explaining the observation of higher order fractional revivals in nitrogen.

Calculation examples

As shown for nitrogen in Figure 3.4, we can estimate our degree of alignment by using the expectation value $\langle \cos^2 \theta \rangle$. Expanding this to other functions, we can write for any function O

$$\langle O \rangle_{J_0, \tau_0, M_0}(t) = C_{JKM}^*(t) C_{J'K'M'}(t) \langle JKM | O | J'K'M' \rangle \quad (3.106)$$

where O can be chosen arbitrarily, however the expectation value of a random function would be 0 as a function of time. We choose a basis set that will describe the rotational motion well and will have a expectation value $\neq 0$. We discuss our selection in Chapters 8 and 9. For the projection $\langle \cos^2 \theta \rangle$ we get for a given set of temperature, pulse duration and intensity a time dependent behavior shown in Figure 3.7, while we can also calculate the expectation value for other functions $O = \langle D_0^4(\theta, \chi) \rangle, \langle D_4^4(\theta, \chi) \rangle$ in Figures 3.8 and 3.9. For ethylene we have moments of inertia with $A = 145.82$ GHz, $B = 30.009$ GHz and $C = 24.823$ GHz, which results in a Ray's parameter of $\kappa = 0.91$ and makes ethylene prolate. For a prolate asymmetric rotor we can describe rotational revival structures:

Revival	position	time
A-type	$t = n/4A$	1.71 ps
C-Type	$t = n/4C$	10.07 ps
K-Type	$t = n/4A - 2B - 2C$	2.11 ps
J-Type	$t = n/2(B + C)$	9.12 ps

where the times are calculated for the case of ethylene gas. We can see features in Figure 3.7 that show oscillations of similar times, while $\langle \cos^2 \theta \rangle$ cannot represent a A-type revival with the angle χ .

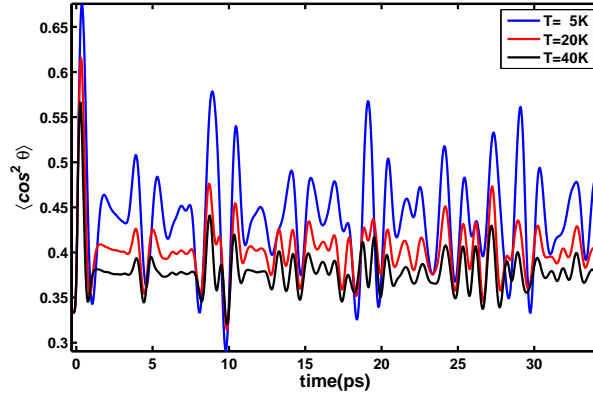


Figure 3.7: Degree of alignment, described with the expectation value of $\langle \cos^2 \theta \rangle$ as a function of time after an interaction with an intense laser field with 16 TW cm^{-2} and 150 fs.

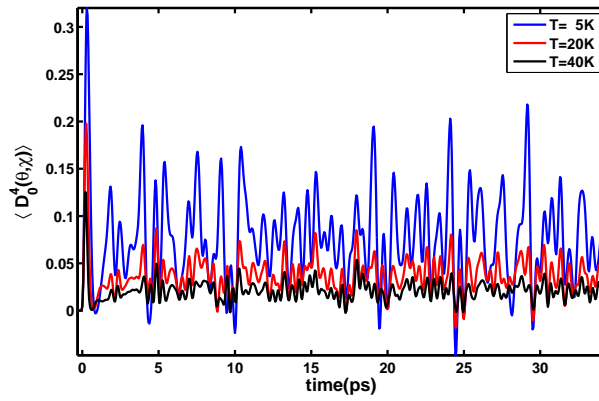


Figure 3.8: Expectation value of $\langle D_0^4(\theta, \chi) \rangle$ as a function of time after an interaction with an intense laser field with 16 TW cm^{-2} and 150 fs.

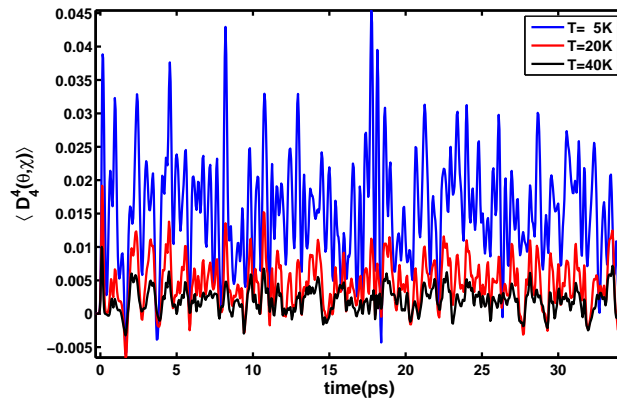


Figure 3.9: Expectation value of $\langle D_4^4(\theta, \chi) \rangle$ as a function of time after an interaction with an intense laser field with 16 TW cm^{-2} and 150 fs.

3.4 Fourier Optics

In this section, I will explain in detail the steps and theory behind generating the focus spots for the two source interferometry experiments. These two sources serve as a Young's double slit to perform interferometric studies on HHG. To create the two sources, we have to control the spatial profile $U(x, y)$ of the incoming laser light and calculate the propagation of light. To do so, I introduce the well-known concept of Fourier transformations to show calculations of the expected spot size and phase distribution of spatially shaped light. We describe the electric field for beams with different orbital angular momentum (OAM) or tilt. Explicitly, when mentioning phase masks, I am making reference to a spatial light modulator (SLM), introduced in Chapter 4, that allows us to manipulate the spatial phase of light. Most of the discussion is based on the book Computational Fourier transformation by Voelz [66].

3.4.1 Transverse modes of light

As a reminder, the typical modes of light from a laser system are described with transverse modes of light. A transverse mode of light describes the electromagnetic field in a plane perpendicular (or transverse) to the propagation direction. Unguided or unobstructed electromagnetic waves in free space can be described as a superposition of plane waves. However, when light is traveling through any sort of waveguide, where boundary conditions are applied by physical structure, the modes follow different propagation constants. In Ti:Sapphire lasers we typically describe the transverse mode of light as a Gaussian profile or as a TEM_{00} mode.

Gaussian laser mode

In Ti:Sa lasers, the modes of the laser can be described well with a Gaussian mode. We define the mode as

$$E(r, z) = E_0 \hat{x} \frac{w_0}{w(z)} \exp\left(\frac{-r^2}{w(z)^2}\right) \exp\left(-i\left(kz + k\frac{r^2}{2R(z)} - \Phi(z)\right)\right) \quad (3.107)$$

where r is the radial distance from the center of the beam axis, z the propagation distance from the beam's focus position, $k = 2\pi/\lambda$ the wave number and E_0 the electric field amplitude at t_0 . $w(z)$ describes the Gaussian beam waist, which is defined as the distance from the center of the beam, where the intensity falls below $1/e$. $R(z)$ is the radius of curvature and $\Phi(z)$ is the Gouy phase. The beam waist follows

$$w(z) = w_0 \sqrt{1 + \left(\frac{z}{z_R}\right)^2} \quad (3.108)$$

where $z_R = \frac{\pi w_0^2}{\lambda}$ is called the Rayleigh range, at which point in propagation distance the intensity of the laser is reduced by a factor of 2. The Gouy phase of the beam is described by

$$\Phi(z) = \arctan\left(\frac{z}{z_R}\right) \quad (3.109)$$

which describes a phase offset due to the deviation of the Gaussian mode from a plane wave.

Relation between the beam profile and the Gouy phase

From Feng et al. [67], we take the math to understand the Gouy phase: A monochromatic wave of frequency ω and wave number $k = \omega/c$ is propagating along the z direction. For an infinite plane wave the momentum is directed towards z and has no transverse components. A Gaussian beam will have a spread in transverse momentum and the wave number is now related to these

components by $k^2 = k_x^2 + k_y^2 + k_z^2$. We can define an effective axial propagation constant:

$$k_z = \frac{\langle k_z^2 \rangle}{k} = k - \frac{\langle k_x^2 \rangle}{k} - \frac{\langle k_y^2 \rangle}{k} \quad (3.110)$$

where k_z is associated with the overall propagation phase $\phi(z)$ on axis through $k_z = \delta\phi(z)/\delta z$. While the first term yields the phase of an infinite plane wave, the two later terms give rise to the Gouy phase shift:

$$\phi_G = -\frac{1}{k} \int \langle k_x^2 \rangle + \langle k_y^2 \rangle dz \quad (3.111)$$

If we now take a Gaussian transverse distribution

$$f(x, y) = \sqrt{\frac{2}{\pi}} \frac{1}{w(z)} e^{-\frac{x^2 + y^2}{w^2(z)}} \quad (3.112)$$

after some calculations in [67], we get:

$$\phi_G = -\frac{1}{k} \int \langle k_x^2 \rangle + \langle k_y^2 \rangle dz = -\frac{2}{k} \int \frac{1}{w^2(z)} dz \quad (3.113)$$

Carrying out the integral in Equation 3.113 we get the Gouy phase of a fundamental Gaussian beam:

$$\phi_G = -\arctan(z/z_R) \quad (3.114)$$

The Gouy phase gives rise to a phase deviation between a Gaussian beam and a plane wave. This phase deviation has to be considered, when generating HHG in the medium as a phase mismatch between laser and generated harmonics will reduce the harmonic yield.

Hermite Gaussian modes

In a more general description, the Gaussian mode is a TEM_{00} mode or a Hermite Gaussian mode of order 00. This Hermite Gaussian mode is depicted in Figure 3.10.

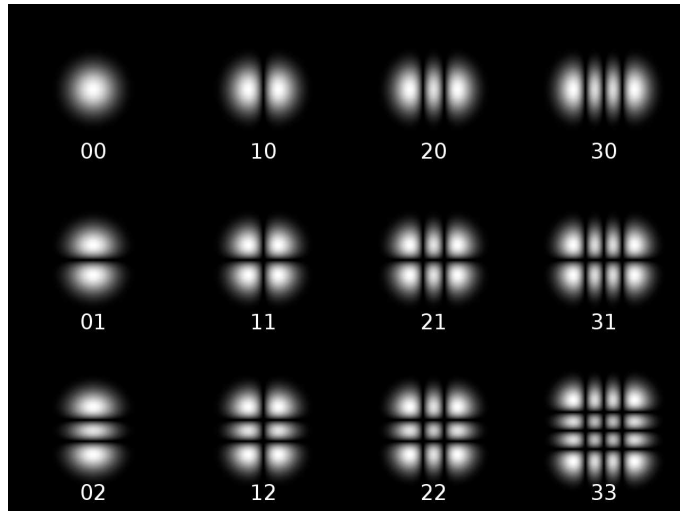


Figure 3.10: Orders of Hermite Gaussian modes, adapted from [68]

Higher order modes of Hermite Gaussians are described in categories of TEM_{lm} modes. The number of l and m can be associated with the number of nodes in the spatial profile of the mode.

The electric field of the Hermite Gaussian is defined as

$$E(r, z) = E_0 \hat{x} \frac{w_0}{w(z)} H_l \left(\frac{\sqrt{2}x}{w(z)} \right) H_m \left(\frac{\sqrt{2}y}{w(z)} \right) \exp \left(-\frac{x^2 + y^2}{w(z)^2} \right) \exp \left(-i \left(kz + k \frac{x^2 + y^2}{2R(z)} - \Phi(z) \right) \right) \quad (3.115)$$

with the same definitions as previously described for a Gaussian mode, while here the profile depends on Hermite polynomials H_l and H_m . The Gouy phase of a Hermite Gaussian beam is written as

$$\phi_G = (N + 1) \arctan(z/z_R) \quad (3.116)$$

where N is defined as $N = l + m$, due to the higher order modes.

Laguerre Gaussian modes

Laguerre Gaussian beams are an equivalent description of transverse electromagnetic modes, but in cylindrical rather than cartesian coordinates. In Figure 3.11 a Laguerre Gaussian of order $l = 0, p = 0$ has the same spatial profile as a Hermite Gaussian beam with $l = 0, m = 0$. However, higher order terms have different structures. Additionally, these modes carry orbital angular momentum. I am introducing these modes, as we, later on, use beams similar to Laguerre Gaussian modes to perform selected experiments. The use of Laguerre Gaussian modes will yield the production of a Young's double slit in the focus of a lens and the production of individual slits of this double slit.

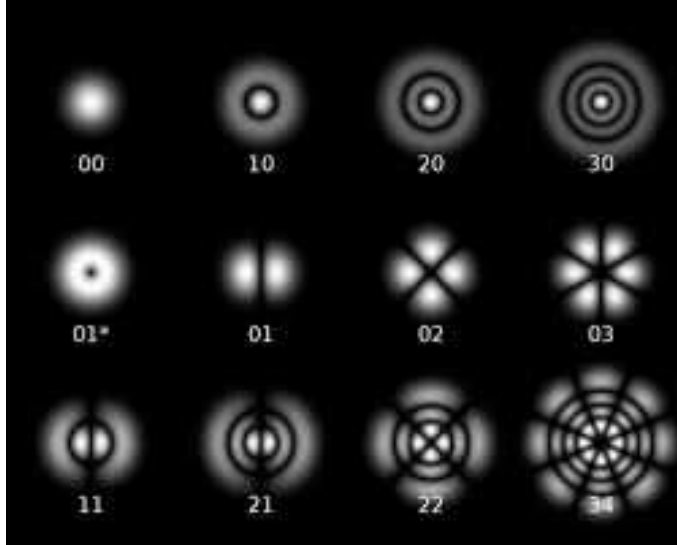


Figure 3.11: Orders of Laguerre Gaussian modes, adapted from [68]

Describing the electromagnetic wave with Laguerre Gaussian modes, we write [69]

$$E(r, \phi, z) = \frac{C_{lp}^{LG}}{w(z)} \left(\frac{r\sqrt{2}}{w(z)} \right)^{|l|} \exp \left(-\frac{r^2}{w(z)^2} \right) L_p^{|l|} \left(\frac{2r^2}{w^2(z)} \right) \exp(il\phi) \exp \left(-i \left(kz + k \frac{r^2}{2R(z)} - \Phi(z) \right) \right) \quad (3.117)$$

with $L_p^{|l|}$ Laguerre polynomials, $\Phi(z)$ the Gouy phase and C_{lp}^{LG} normalization constants. $w(z)$ and $R(z)$ are defined by the same definitions valid for TEM-modes. In this equation, we notice the term $\exp(il\phi)$ that gives rise to orbital angular momentum (OAM). In the later experiment we use beams with $l = 1$ and $p = 0$, which results in a Laguerre polynomial $L_0^1 = 1$ and the electric

field is reduced to

$$E(r, \phi, z) = C_{10}^{LG} \frac{r\sqrt{2}}{w(z)^2} \exp\left(-\frac{r^2}{w(z)^2}\right) \exp(i\phi) \exp\left(-i\left(kz + k\frac{r^2}{2R(z)} - \Phi(z)\right)\right) \quad (3.118)$$

and beams with $l = -1, p = 0$ yield an electric field

$$E(r, \phi, z) = C_{10}^{LG} \frac{r\sqrt{2}}{w(z)^2} \exp\left(-\frac{r^2}{w(z)^2}\right) \exp(-i\phi) \exp\left(-i\left(kz + k\frac{r^2}{2R(z)} - \Phi(z)\right)\right) \quad (3.119)$$

resulting in a phase difference between the two different LG modes of $\Delta\Phi = 2\phi$. The Gouy phase of a Laguerre Gaussian mode is written as

$$\phi_G = (N + 1) \arctan(z/z_R) \quad (3.120)$$

with $N = |l| + 2p$, so that beams with same $|l|$ have the same Gouy phase.

3.4.2 Analytic Fourier Theory

The electric fields in the following sections are reduced to a scaled function $U(\eta, \nu)$, where the transverse modes of light are $E(\eta, \nu) = E_0 \times U(\eta, \nu)$. All propagation calculations in the following chapter are based on fast Fourier transformations, so that this section will serve as a reminder of the concept of Fourier transformations. We define the Fourier transformation of a function U of two variables η and ν as

$$U'(f_\eta, f_\nu) = \iint U(\eta, \nu) \exp[-i2\pi(f_\eta\eta + f_\nu\nu)] d\eta d\nu, \quad (3.121)$$

where $U'(f_\eta, f_\nu)$ is the transformation result and f_η, f_ν are independent frequency variables associated with η, ν . However, in our calculations we perform transformation in space from the coordinates (η, ν) to (x, y) , where the frequency variables are substituted by $f_\eta \rightarrow \frac{x}{\lambda z}$. A laser beam with the spatial profile $U(\eta, \nu)$ propagates through an optical element with the impulse response h . The spatial profile of the laser will be different than the spatial profile before the optical element. We can calculate the laser beam after the optical element with the output function $U'(x, y)$

$$U'(x, y) = \iint U(\eta, \nu) h(x, y; \eta, \nu) d\eta d\nu. \quad (3.122)$$

This leads to the Fourier transformation of U'

$$\mathfrak{F}\{U'(f_\eta, f_\nu)\} = \mathfrak{F}\{U(\eta, \nu)\} \mathfrak{F}\{h(\eta, \nu)\} \quad (3.123)$$

where $\mathfrak{F}\{h\}$ is the Fourier transformation of the impulse response h and is known as the transfer function. The solution of the output field can then be solved by calculating the inverse Fourier transformation

$$U'(x, y) = \mathfrak{F}^{-1}\{\mathfrak{F}\{U(\eta, \nu)\} \mathfrak{F}\{h(\eta, \nu)\}\} \quad (3.124)$$

We have found a mathematical description for the output field U' after the initial electric field has interacted with an optical element and we will use this description to calculate the actual spot sizes in our experiments.

3.4.3 Diffraction and Propagation

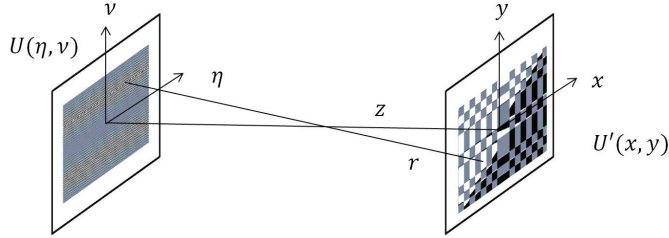


Figure 3.12: The propagation of a source field U by a distance z onto the observation plane U'

When monochromatic light with a spatial profile of $U(\eta, \nu)$ propagates from the source plane (η, ν) to the observation plane (x, y) (as shown in Figure 3.12), we can formulate the propagation with an impulse function h , where the impulse function is now a propagator $h = \frac{e^{ikr}}{r}$. The field $U'(x, y)$ in the observation plane can be predicted using the first Rayleigh-Sommerfeld diffraction solution

$$U'(x, y) = \frac{z}{i\lambda} \iint U(\eta, \nu) \frac{e^{ikr}}{r^2} d\eta d\nu \quad (3.125)$$

Here, λ is the wavelength, k the wave number and z the distance between the source and observation plane. In Equation 3.125, r is the distance between a position on the source plane and a position on the observation plane. It translates to $r = \sqrt{z^2 + (x - \eta)^2 + (y - \nu)^2}$. Approximations for the square root term [66], result in the Fresnel (and Fraunhofer) diffraction formulas, giving solutions to the diffraction through an aperture with the characteristic size a . Solutions to Equation 3.125 can be found either with the Fresnel diffraction for the near field or with the Fraunhofer diffraction in the far field. We choose between the Fraunhofer or Fresnel approximation based on the Fresnel number $N = \frac{a^2}{L\lambda}$, where L is the distance of the observation plane from the aperture. For $N \ll 1$, we use the Fresnel diffraction formula and for $N \gg 1$, we can use Fraunhofer diffraction to calculate the field in the observation plane. For the Fraunhofer diffraction we can write

$$U'(x, y) = \frac{e^{ikz}}{i\lambda z} \exp\left(i\frac{k}{2z}(x^2 + y^2)\right) \iint U(\eta, \nu) \exp\left(-i\frac{2\pi}{\lambda z}(x\nu + y\eta)\right) d\eta d\nu \quad (3.126)$$

which will give us an appropriate representation of the electric field, when propagated over a long distance L , which will be used to calculate the spatial distribution of light in the focus of a lens.

3.4.4 Beam tilt and Convergence

In this section, we show first calculations for the propagation of light. We calculate electric fields in the far field for tilted and converging beams, following Equation 3.124. These calculations will then be later used to show theoretical spot size calculations. Our manipulations in the experiment are based on a spatial light modulator that can influence the phase $\phi(\eta, \nu)$ of the light, where the electric field is written as $U(\eta, \nu) = |U(\eta, \nu)|e^{i\phi(\eta, \nu)}$. We can produce a spatial tilt α in the phase of the source plane $U(\eta, \nu)$. We define α with $\alpha = \arctan(\frac{\nu}{z})$ and write

$$\phi(\eta, \nu) = k(\eta \cos \theta + \nu \sin \theta) \tan \alpha, \quad (3.127)$$

where θ is the angle in the plane of η, ν and defined as $\theta = \arctan(\frac{\nu}{\eta})$. When the light is propagating in free space, we calculate the electric field in the observation plane by solving

Equation 3.126. We get for the observation plane a field U'

$$U'(x, y) = U(\eta, \nu) \exp(ik(\eta \cos \theta + \nu \sin \theta) \tan \alpha), \quad (3.128)$$

that describes an electric field in the far field, tilted by the angle α . When light is propagating through a lens and converging, we can express the electric field with an additional parabolic phase, where the distance $z = f$ is given by the focal length of a convex lens. The phase is written as

$$\phi(\eta, \nu) = -\frac{k}{2f}(\eta^2 + \nu^2), \quad (3.129)$$

and the resulting electric field in the observation plane is expressed by Equation 3.124 and becomes

$$U'(x, y) = \frac{\exp(ikf)}{i\lambda f} \exp\left[\frac{ik}{2f}(x^2 + y^2)\right] \int \int U(\eta, \nu) \exp\left[-i\frac{2\pi}{\lambda f}(x\eta + y\nu)\right] d\eta d\nu, \quad (3.130)$$

This is the expression for a spatial distribution of light propagating through a lens, when measured at the focal plane. We can compare this equation to the Fraunhofer diffraction in Equation 3.126, and observe identical behavior for $z = f$, where we can write the Fraunhofer diffraction equation with

$$U'(x, y) = \mathfrak{F}^{-1} \{ \mathfrak{F} \{ U(\eta, \nu) h_{FF}(f) \} \} \frac{d\eta d\nu}{\lambda f}. \quad (3.131)$$

Equation 3.131 is a scaled calculation of the Fraunhofer diffraction of the input field by a factor of $\frac{1}{\lambda f}$ with the impulse response $h_{FF}(f)$, a propagation of the input beam by the distance f . It yields the field in the observation plane, when we are in an optical geometry, where the observation plane is one focal length away from the focusing lens with a focal length of f .

3.5 A double slit with focused light

To prepare a focus in the interaction region of laser and gas, that can generate a Young's double slit of HHG light, we spatially shape the fundamental light by manipulating its phase, as we have shown in Section 3.4.4 with the example of a spatial tilt. We introduce two methods to generate a double focus: Interference in the focus or a redistribution of light in the focus. We'll start with a full description of shaping light through interference and then describe the technique of light redistribution.

3.5.1 Simple examples of shaping light by interference

For the sake of simplicity, I am reducing the initial discussion about the interference of light to two plane waves. Considering two light waves $U_1 = |U_1|_1 e^{i\phi_1}$ and $U_2 = |U_2|_2 e^{i\phi_2}$, the superposition of both will form an intensity pattern in space given by

$$I = |U_1 + U_2|^2 \quad (3.132)$$

When we apply $U = U_1 = U_2$, we get an intensity I following

$$I = 2U^2(1 + \cos \Delta\phi) \quad (3.133)$$

with $\Delta\phi = \phi_2 - \phi_1$, where constructive interference occurs at integer multiples of 2π in $\Delta\phi$. This will cause complete destructive or constructive interference of light. However, when the light beams have a vertical offset in space and are propagating parallel to the optical axis of the lens, an additional tilt is introduced, reducing the area of destructive interference to the optical axis of the lens in the far field. In references [70–73] a single Gaussian TEM₀₀ mode is manipulated by inserting a phase plate with a phase difference of π between the upper and lower halves, resulting in two beams parallel to the optical axis of the lens. With this, a quasi-Hermite Gaussian of order

TEM₀₁ can be generated. At positions, where the spatial phase of beams shows a difference of π , destructive inference occurs and the resulting spot size at the focus is similar to two foci.

Interference between a Laguerre-Gaussian and a Gaussian beam If we now look into the interference of a plane wave with $U_1 = |U|e^{i\phi_1}$ and a high-order beam with $U_2 = |U|e^{i(l\theta+\phi_2)}$, as here given with a Laguerre-Gauss mode, we now get a phase difference of

$$\Delta\phi = \phi_1 - l\theta - \phi_2 \quad (3.134)$$

where a condition for constructive interference is given at a particular value of θ , where θ describes the angle in the x, y -plane. Here we do not have complete destructive or constructive inference anymore, but can select a specific angle of interference, without applying a “trick“ as in the last paragraph.

Interference between two Laguerre-Gaussian beams When two high-order beams interfere, here given with Laguerre-Gauss modes with $U_1 = |U|e^{i(-l\theta+\phi_1)}$ and $U_2 = |U|e^{i(l\theta+\phi_2)}$, we get a phase difference of

$$\Delta\phi = \phi_1 - 2l\theta - \phi_2 \quad (3.135)$$

where over 2π in the angle θ , we can reach destructive interference $2l$ times. For $|l| = 1$, we get two destructive interferences over 2π , resulting in a two source focus.

3.5.2 Diffraction calculations

We switch now to more detailed and accurate diffraction calculations, where the spatial profiles are given by Gaussian distribution $E(\eta, \nu) = E_0 \cdot |U(\eta, \nu)|e^{i\phi}$ that are shaped by the spatial light modulator. We use the theory introduced in the previous section. In our experiments, we use a 75 cm lens and a spatial light modulator (SLM) that supports a 12 mm diameter beam. The spatial light modulator will be introduced in detail in Section 4.2 of Chapter 4. We insert the exact focal length, aperture size of SLM and Gaussian distribution into our calculations and simulate expected magnification and focus behaviors. We start with a diffraction calculation for light manipulated by a phase plate, as briefly described in the previous section and references [70–73]. The light $E(\eta, \nu)e^{i\phi}$ has a phase $\phi(\eta, \nu)$ with a Heaviside step function H between the upper and lower part of the beam

$$\phi(\eta, \nu) = H\left(\nu - \frac{\nu_{max}}{2}\right)\pi - \pi/2 \quad (3.136)$$

$$|E(\eta, \nu)| = E_0 \cdot |U(\eta, \nu)| \quad (3.137)$$

We show the spatial profile for the intensity and phase in Figure 3.13 for the electric field $E(\eta, \nu)exp(i\phi)$ and use Fraunhofer and Fresnel propagation to calculate $E'(x, y)$ for different propagation distances to generate a focus dependent projection of the beam waist in Figure 3.14. We are able to produce a focus similar to a TEM₀₁ mode, with a node in one dimension, similar to two focus spots.

Each half can be expressed by an electric field with

$$\phi(\eta, \nu) = H\left(\nu - \frac{\nu_{max}}{2}\right)\pi - \pi/2 \quad (3.138)$$

$$|E(\eta, \nu)| = H\left(\nu - \frac{\nu_{max}}{2}\right) \cdot E_0 \cdot |U(\eta, \nu)| \quad (3.139)$$

We block part of the beam, as illustrated by Equation 3.139, and calculate the focus waist as a function of focus in Figure 3.15. The focus behavior does not match the individual behavior of a single source of our two source focus. There is no more destructive interference in the center and the focus is tilted, resulting in a propagation direction with a small angle compared to the optical axis of light, which results in harmonic sources traveling away from the optical axis of our optical system.

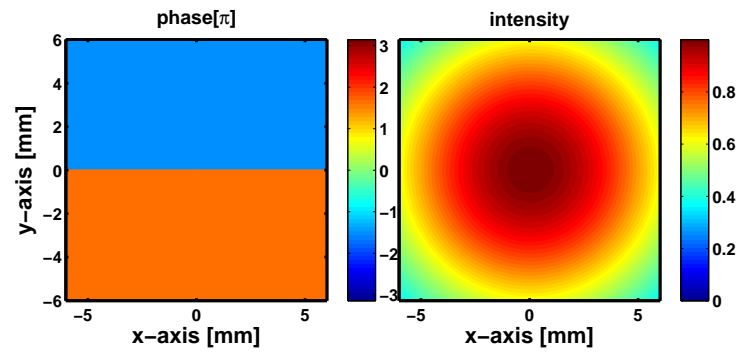


Figure 3.13: Spatial phase and intensity distribution in the source plane (on the SLM) after manipulation of the phase with a Heaviside function, applying a π phase difference.

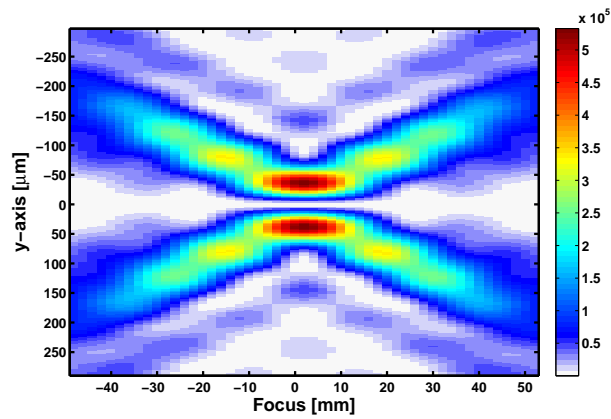


Figure 3.14: Projected focus of a laser beam, manipulated by a phase mask that introduces a phase jump between parts of the beam, as shown in Figure 3.13.

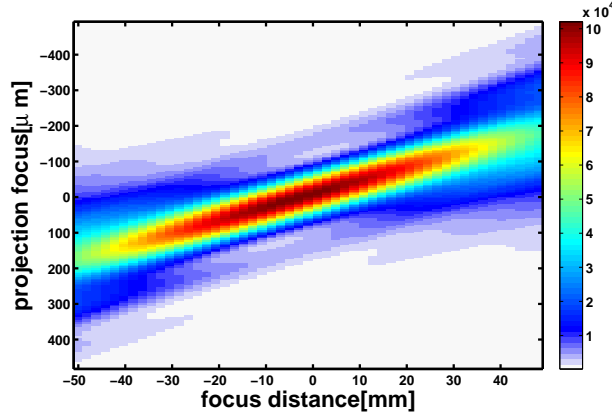


Figure 3.15: Projected focus of a laser beam, manipulated by a phase mask that blocks part of the light

Similar to the phase plate and using single beams as shown in Figure 3.15, the spatial light can be manipulated by glass wedges. In references [57, 74] a single Gaussian TEM₀₀ mode is manipulated by inserting two glass plates of opposite tilting angle into the focusing beam. By manipulating the tilt angle, the laser focus of each half has a vertical offset and two foci can be generated. The spatial phase distribution can be expressed as

$$\phi(\eta, \nu) = H\left(\nu - \frac{\nu_{max}}{2}\right) \cdot k(\eta \cos \theta + \nu \sin \theta) \tan(+\alpha) + |H\left(\nu - \frac{\nu_{max}}{2}\right) - 1| \cdot k(\eta \cos \theta + \nu \sin \theta) \tan(-\alpha) \quad (3.140)$$

that is similar to the inserted glass wedges. The spatial intensity distribution is given with a Gaussian distribution $E(\eta, \nu) = E_0|U(\eta, \nu)|$. The propagation is calculated with Equation 3.131. Experimentally, big angles and separations have to be used to keep the crossing of the beams at a position before the focus far away from the gas source. Calculations in Figure 3.16 show

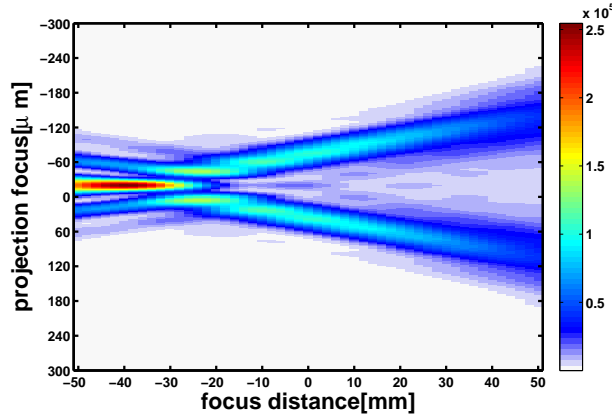


Figure 3.16: Projected focus of a laser beam, manipulated by a phase mask similar to inserting glass wedges at an angle

interference effects far away from the focus of the individual beams. At the focus of the lens, the light is separated well and two independent spots are generated that can produce high harmonics. However, both sources propagate with an angle towards the far field and are not completely parallel with each other.

The shown calculations have very stringent requirements on the pointing of the laser light through the optical elements which introduces the phase manipulation, as any imbalance between the upper and lower halves can cause an altered interference. As a first improvement to avoid pointing

issues, we introduce phase masks which separate the two electric fields into sections homogeneously distributed across the aperture/SLM. We use a spatial phase distribution with alternating “rings”, containing phase information for individual electric fields. The description of the “rings” is done in cylindrical coordinates ρ, θ, z . We use phase patterns with angular orbital momentum (OAM) and can create two sources and individual sources, based on the interference shown in Equations 3.134 and 3.135. In addition to the better pointing stability, it results in the ability to create a good representation of a single slit of the Young’s double slit. We use a phase mask $\phi(\eta, \nu)$ with a product out of a dirac comb $III_\rho = \frac{1}{\tau} \sum_0^{300/\rho-1} e^{2\pi i n \frac{1}{\rho}}$ and a boxcar function $\Pi_{a,b}(\rho) = H(\rho - a) - H(\rho - b)$ function, with $\rho = 2 * (a + b)$. ρ' is off set by $a + b$ with respect to ρ , which will result in adjacent ”rings” on the SLM to hold an applied phase value of $\pm l\theta$. A Dirac comb is a series of Dirac-delta functions separated by the distance ρ and a, b define the “width” of the rings, as the boxcar function is similar to a top-hat function. The mask reads

$$\phi(\rho, \theta) = III_\rho \cdot \Pi_{a,b}(\rho) \cdot l\theta + III_{\rho'} \cdot \Pi_{a,b}(\rho') \cdot (-l)\theta \quad (3.141)$$

and is shown in the left panel of Figure 3.17, with the intensity profile in the right panel, given by a Gaussian beam with the exact dimensions from the experiment. The source plane $E(\eta, \nu)$ contains OAM with alternating rings of OAM of $l = 1, -1$.

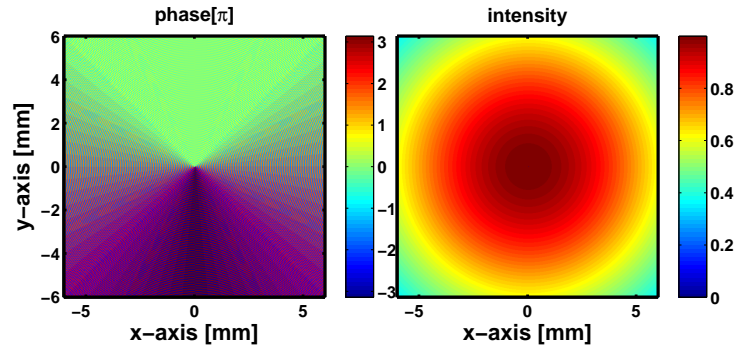


Figure 3.17: Spatial phase and intensity distribution in the source plane after manipulation of the phase with OAM $l = 1, -1$

In Figure 3.18, we show beam waist calculations of $E'(x, y)$ as a function of distance around the focus of a lens. We can observe interference of light, forming two separated foci as proposed in Equation 3.135.

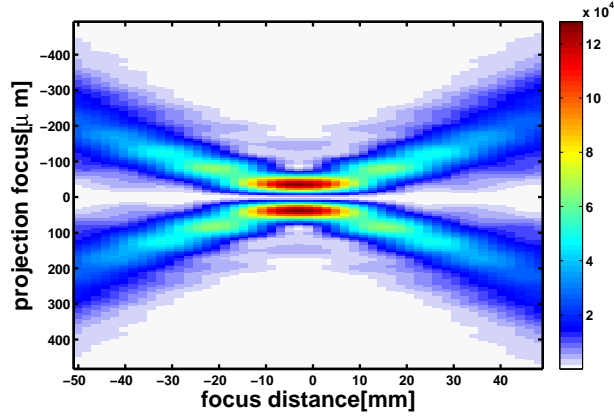


Figure 3.18: Projected focus of a laser beam, manipulated by a phase mask that introduces two beams with OAM $l = 1, -1$

When switching to a single source scheme, we write a spatial phase mask following

$$\Phi(\rho, \theta) = III_{\rho} \cdot \Pi_{a,b}(\rho) \cdot l\theta + III_{\rho'} \cdot \Pi_{a,b}(\rho') \cdot \phi_2, \quad (3.142)$$

where part of the light carries OAM and the other part carries a constant phase ϕ_2 to control the angle of interference on the observation plane and the electric field $E'(x, y)$. The spatial profile of the phase and intensity is shown in Figure 3.19. In Figure 3.20 we plot the beam waist of the light as a function of focus position for the given phase mask. The resulting focusing behavior matches the behavior of a single source of the two source focus as shown in Figure 3.18. Equation 3.142 uses a value of ϕ_2 so that a destructive interference at an angle of the second source is occurring and no light is present at the angle of the second source.

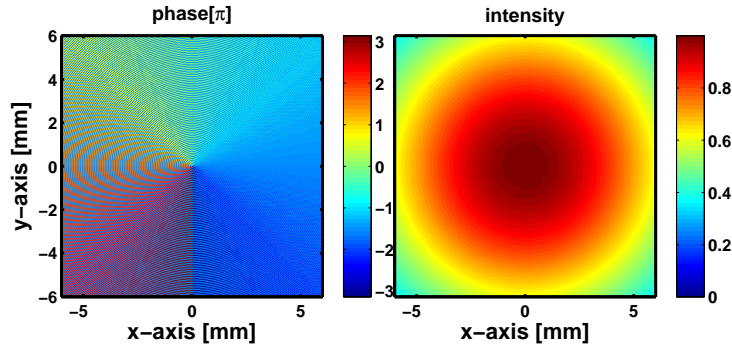


Figure 3.19: Spatial phase and intensity distribution in the source plane after manipulation of the phase with OAM $l = 1, 0$

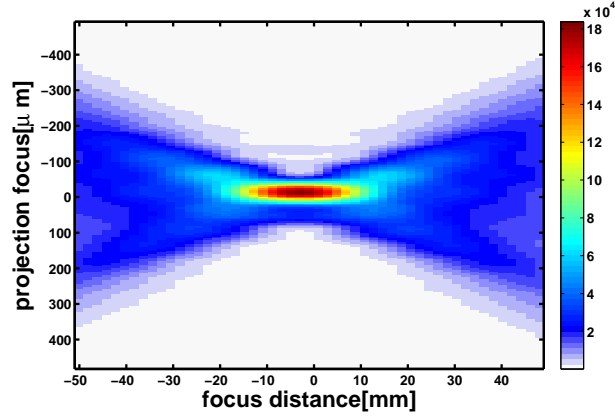


Figure 3.20: Projected focus of a laser beam, manipulated by a phase mask that introduces two beams with OAM $l = 1, 0$. We observe a single focus with a center of mass similar to the center of mass of one of two foci in Figure 3.18.

Tilt control

To improve the generation of an identical copy of the individual sources, we are faced with the issue that the superposition of beams with OAM $l = 1, 0$ does not form the same constructive interference as beams with OAM $l = 1, -1$, but forms the constructive interference closer to the optical axis. Imposing a wavefront tilt as described in Eq. 3.127 on the beam results in an optimized overlap between single and two source pattern. The tilt applied to the wavefront is on the order of 10's of μrad and shows good agreement in Figure 3.21. The focusing behavior in Figure 3.22 shows no overall change as a function of focus, except the desired offset in the ordinate of the projected beam waist.

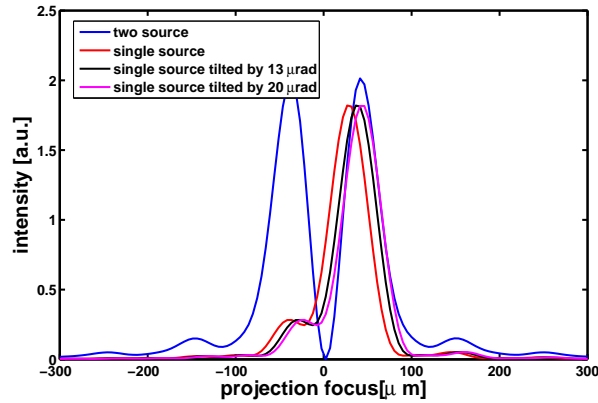


Figure 3.21: Overlap between single and two source focus as a function of tilt angle applied to the single source pattern.

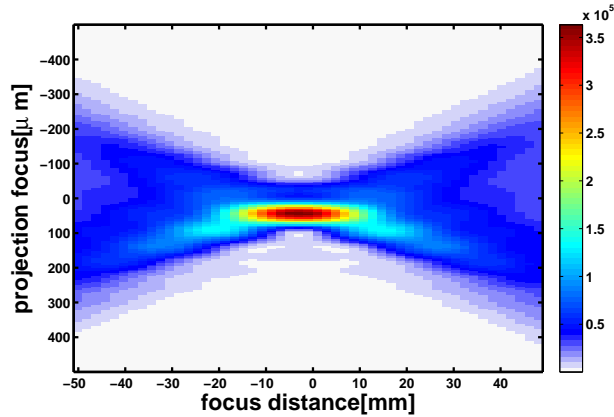


Figure 3.22: Projected focus of a laser beam, shifted by $20 \mu\text{rad}$ and shifted to overlap better with its individual in the two source focus

Spatial phase in the focus plane

An important characteristic of our laser beams is the spatial distribution of the phase. A phase mismatch between different laser foci can yield a reduced intensity of harmonic emission. If we use techniques to shape the intensity distribution in the focus of the laser, we also have to consider the phase properties to minimize effects from potential phase mismatches between sources.

When we consider a laser focus manipulated by a phase plate, as given in Equation 3.137, we can create the phase distribution and the intensity distribution in the focus of a lens in Figure 3.23a and in Figure 3.23b. A phase discontinuity of π between the two focus spots is visible in Figure 3.23a. The phase distribution of a beam generated of a phase mask that blocks half of the light, as given by Equation 3.139, in Figure 3.23c, shows a continuous change at the center of the plane. The phases do not match between panel (a) and (c) of the figure and we are not able to reproduce a single source in phase and intensity. For the approach of beams with OAM, we were able to show very similar intensity distributions between a single spot out of the interference of beams with OAM $l = 1, -1$ and the single spot created with OAM $l = 0, 1$. A limitation here again is the phase of the spatial profile. The phase profile of the two source pattern in Figure 3.24 shows a phase jump of π between the two foci, but the phase of the single source pattern in Figure 3.25 does not match. We still have a change in phase, that does not match the phase properties of a single spot in the beam with OAM $l = -1, 1$. We made improvements in the intensity distributions, but have differences in phase. Nonetheless, this still allows us to use the single focus spot as an experimental tool to validate the optical alignment in the experiment, while the yield of the high harmonics may be different than from a single source in the two focus experiment. We used this technique in Chapters 8 and 9.

3.5.3 Creating two Gaussian beams without interference

Instead of shaping the focus plane through interference of light, we can shape the spatial properties of the light to create two independent light sources, that are Gaussian beams of order TEM_{00} , rather than a mode similar to a TEM_{01} mode in Section 3.5.1 or a mode of two interfering Laguerre-Gaussians. In Section 3.5.2 we described the distribution of beams with different OAM onto alternating rings. In this chapter we will use alternating patterns in x and y, resulting in a grid. Both patterns can create two completely parallel beams in the focus. However, the ring-like structure produces fresnel-lensing that can damage optical elements in the beam path and the grid-based pattern introduces higher order diffractions that reduces the efficiency of the light "deposited" in the 0th order beam that we use to generate harmonics. Depending on the spacing used with the ring-based pattern, we can move the lensing effect across the propagation direction and depending on the line-density of the grating, we can move higher order diffractions closer to the 0th order diffraction. For the grating based pattern, experimentally, line-densities

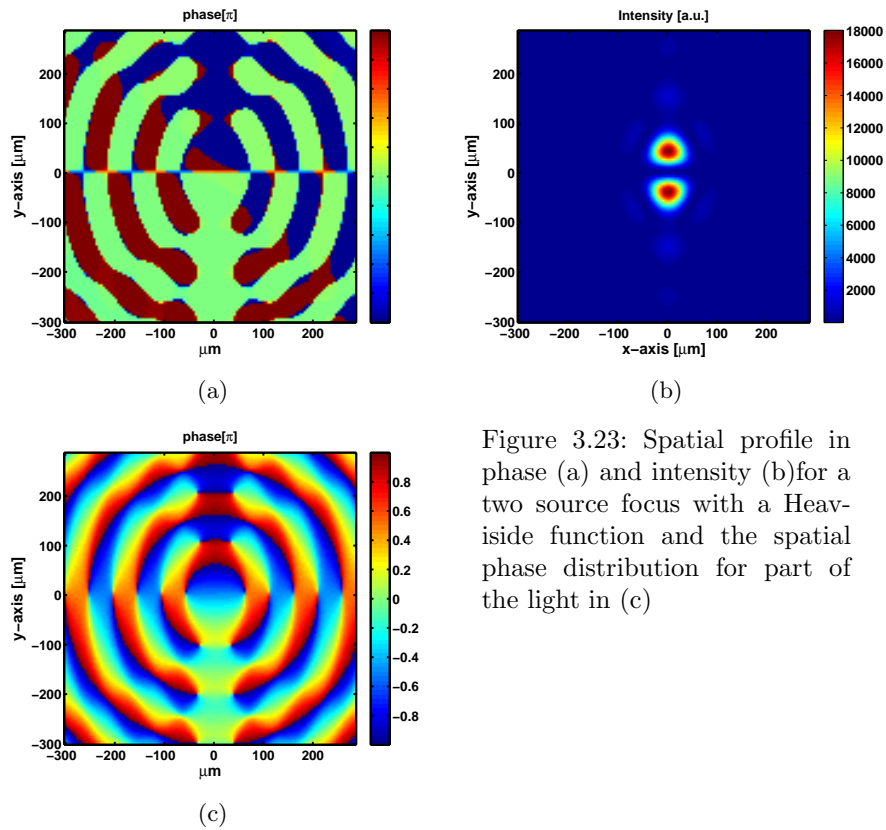


Figure 3.23: Spatial profile in phase (a) and intensity (b) for a two source focus with a Heaviside function and the spatial phase distribution for part of the light in (c)

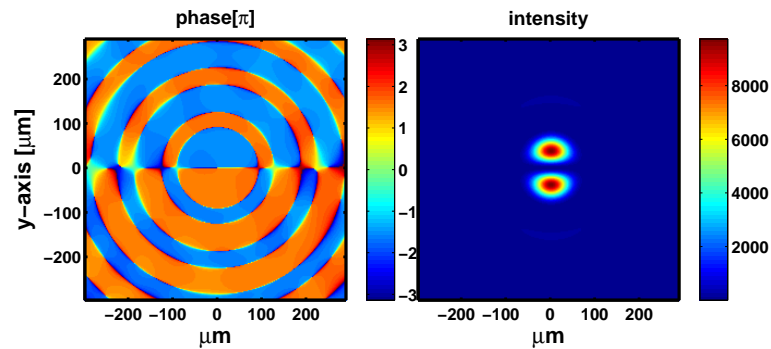


Figure 3.24: Spatial intensity distribution at the focus of a 75 cm lens of a two source focus, created by two counter rotating Laguerre-Gaussian modes

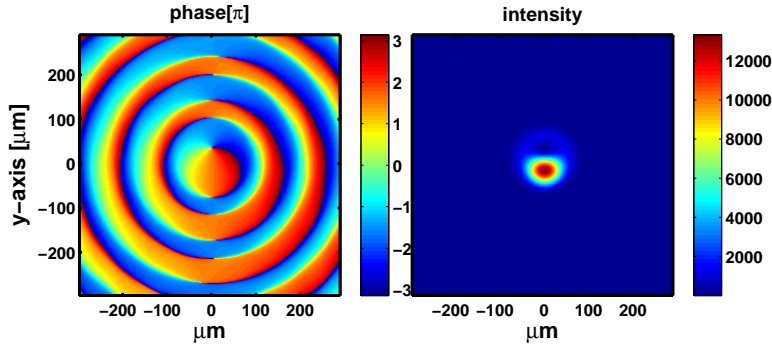


Figure 3.25: Spatial phase distribution at the focus of a 75 cm lens of a single source focus, created by two Laguerre-Gaussian modes with $l = -1, 0$. The intensity profile matches the intensity profile of a single source in Figure 3.24, but the phase profile shows bigger deviations from a flat to a tilted phase profile.

higher than 20 lines across the full SLM height result in higher order terms that are far away from the gas jet and cannot interact with the gas. The experimental data, shown in Section 4.2.1, was taken with line-densities of 80 to 300 lines across the SLM.

To create two Gaussian beams without an interference, we apply a tilt following Equation 3.127 to our incoming laser light. With the SLM we apply the phase pattern

$$\phi(x, y) = k(x \cos \theta + y \sin \theta) \tan(+\alpha) \quad \text{for "beam 1"} \quad (3.143)$$

$$\phi(x, y) = k(x \cos \theta + y \sin \theta) \tan(-\alpha) \quad \text{for "beam 2"} \quad (3.144)$$

where θ is in the plane of x, y and α the angle between y and the propagation direction z . When applying either of the spatial profiles to $U(x, y)$, we get a electric field $U'(x, y)$ in the observation plane of a lens with the scaled Fourier transformation following 3.131, while the center of the focus spot is shifted by $f \cdot \tan \alpha$ in the y -direction.

To generate two foci at the same time, we apply the spatial profiles in Equation 3.143 to half of the array in the source plane and Equation 3.144 to the other half of the array in the source plane. We show the resulting spatial distribution in Figure 3.26. The spacing between the two sources in the focus is then given by $2f \cdot \tan \alpha$.

Using a Gaussian profile, matching our experimental parameters, we calculate the focusing behavior with Fresnel diffraction in the near field of the laser focus in Figure 3.28. The observation plane $U'(x, y)$ at the focal distance f is shown in Figure 3.28 panel (a) It shows two separate foci at the focus of the laser with zero phase difference. Far away from the focus, constructive interference creates on axis bright spots that do not interact with the gas medium close to the focus. Calculating the phase and intensity profile of the beams at different positions with respect to the laser, we see similar features. In Figure 3.28 panel (c) we show the intensity and phase distribution in an observation plane 10mm after the focus. Both foci have the same intensity and phase. When we calculate the phase and intensity 6 mm before the focus in Figure 3.28 (b), we can observe the rectangular aperture given by the rectangular SLM and an identical phase for both foci.

If we introduce a bigger tilt of $\alpha = 200 \mu\text{rad}$ in the fundamental beams, instead of $\alpha = 100 \mu\text{rad}$ in Figure 3.28, we expect a focus as calculated in Figure 3.29, where the two beams are now separated by $300 \mu\text{m}$. The interference pattern far away from the focus becomes dimmer (when compared to the on axis bright spot in Figure 3.28). We can see multiple lines, where the two

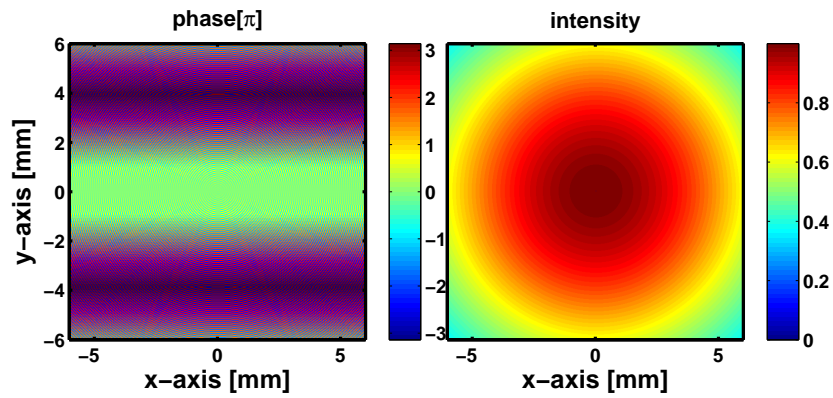


Figure 3.26: Phase and Intensity pattern reflected off the spatial light modulator for a focus of two beams separated by $150 \mu m$

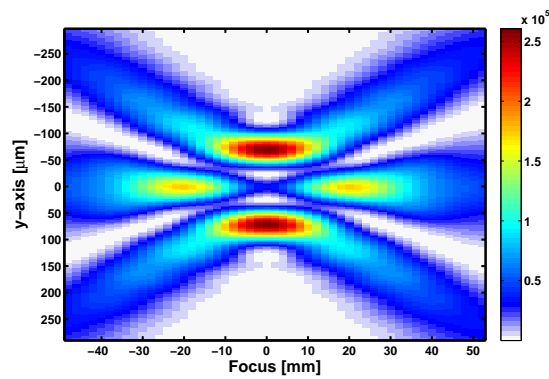


Figure 3.27: Calculated intensity as a function of focus for a 75 cm lens with a phase mask given by Equation 3.144

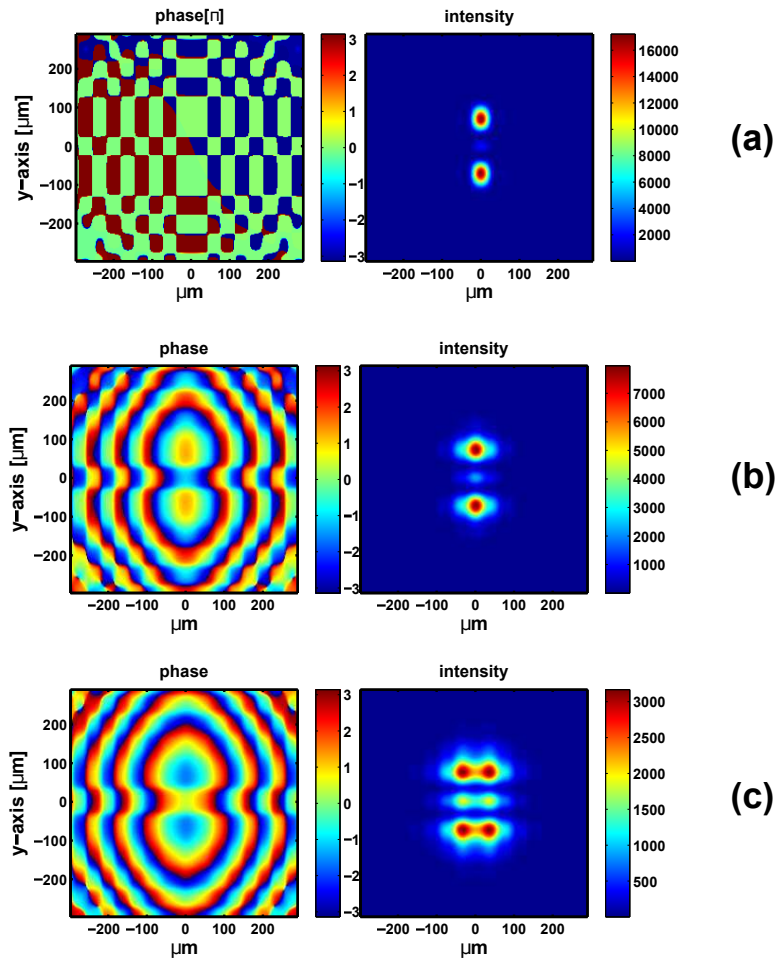


Figure 3.28: (a) Calculated spatial phase and intensity at the focus of a 75 cm lens with a phase mask given by Equation 3.144 (b) Calculated spatial phase and intensity 10 mm after the focus of a 75 cm lens (c) Calculated spatial phase and intensity 6 mm before the focus of a 75 cm lens

sources interfere.

In addition, we can also apply a constant phase offset between the two sources. We show the focus waist projection as a function of focus in Figure 3.30, with one source with an additional phase offset of π . We cannot observe a change in intensity of the individual foci, but see a change in the interference region far away from the center of the jet. The two foci do not change, since there is no spatial overlap between the two beams in the focus. These calculations will be later used for the experiments presented in Chapters 5 and 6.

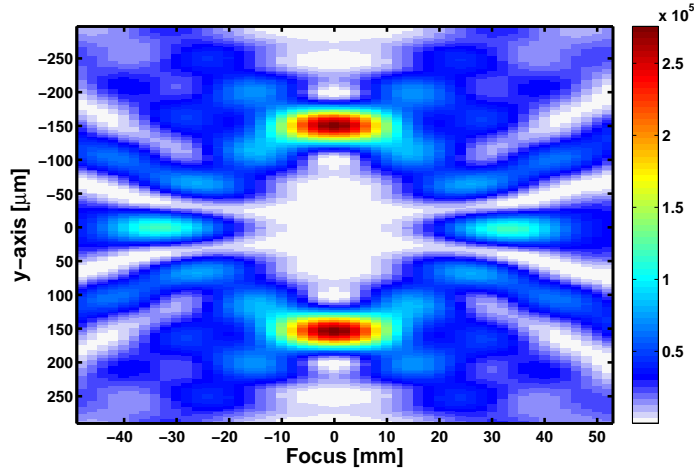


Figure 3.29: Calculated projection of the focus of two beams tilted by $\pm 200 \mu rad$, generating two bright harmonic sources parallel to the optical axis with an offset of $150 \mu m$ each.

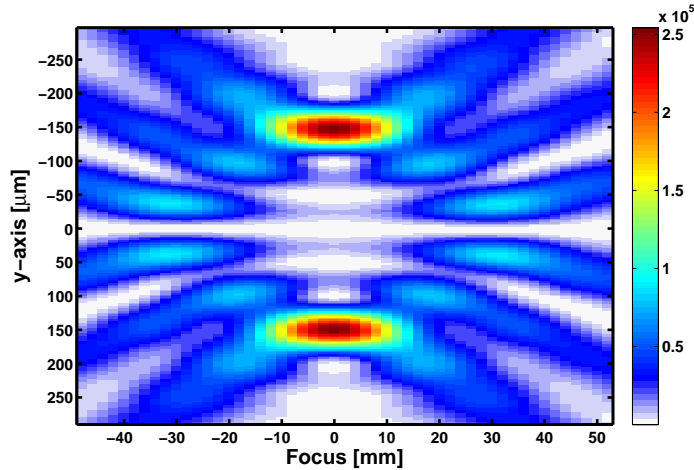


Figure 3.30: Calculated projection of the focus of two beams tilted by $\pm 200 \mu rad$, generating two bright harmonic sources parallel to the optical axis with an offset of $150 \mu m$ each. A phase offset of π is incorporated, changing the interference pattern before and after the focus, where the electric fields overlap again.

3.5.4 Single beams for characterization of individual sources

The great advantage of the tilted beams is shown in this section: We can generate a single tilted beam with the same spatial character as one of the two foci. By simply applying a single tilt

to the whole phase mask, we create a single focus matching the focus of a source in the double focus. A second method allows for greater accuracy: by tilting a beam by the previously given angle α and tilting the beam on the other half of the mask by a much bigger angle α_2 , we do not have to adjust the intensity of the laser pulse. With a single tilted beam, the intensity has to match the intensity of the previously generated spot in the two-source focus. The intensity of the shaped single beam has to be reduced by a factor of 4. The resulting focusing behavior is given in Figure 3.31

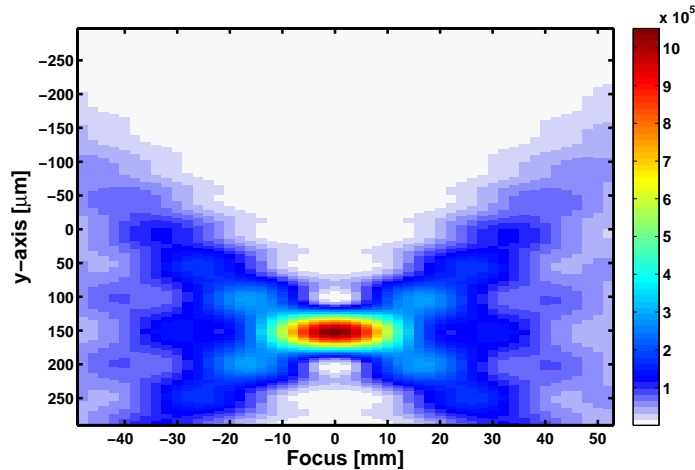


Figure 3.31: Calculated projection of a focus with a single beam tilted by $200 \mu\text{rad}$

By applying a big tilt angle α_2 to the second beam, no intensity corrections are needed. In the experiment, we apply a tilt on the order of $3000 \mu\text{rad}$, instead of $100 \mu\text{rad}$, so that the second beam is vertically displaced by 3 mm away from the gas jet and cannot generate harmonic emission. We remove a degree of freedom, since we do not have to alter the intensity of the light.. In Figure 3.32, we show the focusing behavior of such a field.

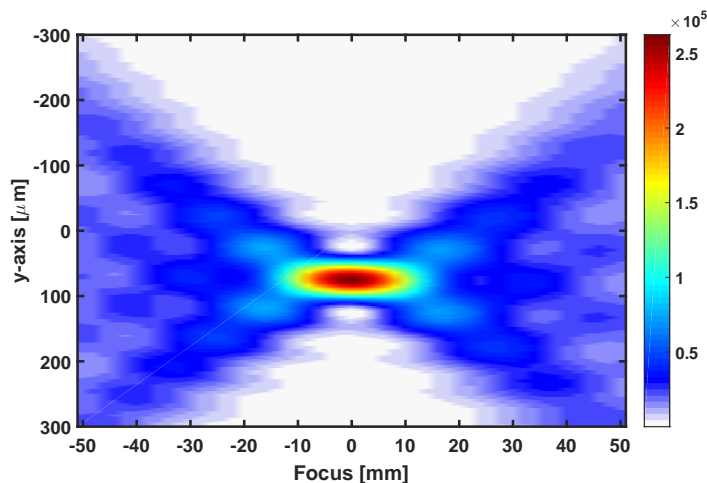


Figure 3.32: Projection of the focus waist in one dimension as a function of the laser focus. In this picture two foci are generated. One focus is tilted 3.5 mm away from the optical axis and away from the interaction region, while the second beam has the same tilt as the original two source pattern.

From shafts to LCDs

In 1909, Poynting [75] described the orbital angular momentum of light using the analogy of "the wave motion of a rotating shaft" and suggested a gedankenexperiment of circular polarized light traveling through discs that are suspended by a fiber. The circular light would wield a torque on the birefringent plate and one would be able to describe a ratio between angular and linear momentum equal to $\lambda/2\pi$. He stated: "my present experience of light forces does not give me much hope that the effect could be detected". Beth in 1936 performed an experimental study [76] with birefringent plates in vacuum, hung on a quartz fiber. By rotating a quartz wave plate and measuring the torque, he was able to confirm direction and amplitude of the torque. He measured changes in the torque on the order of 10^{-9} dyne cm, which roughly translates to $4 \cdot 10^{-14}$ Nm or 20000 atomic units. In 1992 Allen et al. [69] applied the idea of orbital angular momentum to laser beams and generated Laguerre Gaussian beams, concluding that any light beam which possesses a field gradient, will have orbital angular momentum. They are usually degenerate, being of opposite character or randomly fluctuating in time, so that the beam has zero average orbital angular momentum. Beams with orbital momentum can now be generated with computer programable devices like LCOS displays and used in this thesis to shape the laser beam spatially. In other fields of research, they are used as optical traps.

Chapter 4

Experimental techniques

4.1 Experimental setup

In Figure 4.1 a experimental setup is shown: High harmonics are generated from an intense driving laser that is transported by reflective optics to a spatial light modulator (SLM) that reflects the light into the vacuum chambers. To reach high peak intensities, we focus the light with a lens, here given with a focal length of 75 cm, into a gas jet. The light is focused from a collimated beam diameter of 12 mm to a spot size of $60 \mu\text{m}$. The peak intensity of the driving laser field reaches $10^{14} \text{W}/\text{cm}^2$ in the focus. In the experiment, we adjust the distance between focusing lens and gas source to gain an optimized harmonic yield. The harmonics propagate in the direction of the optical axis, defined by the propagation direction of the laser, and are detected in the spectrometer. The spectrometer is described in Section 4.1.1, while the gas source is described in Section 4.1.2. The laser is HITS [77], a Ti:Sa laser, with a pulse energy of up to 20 mJ, a pulse duration of 27 fs full width at half maximum (FWHM) and a repetition rate of 1 kHz. The laser is used in the experiment, described in Chapter 7, to pump an optical parametric amplifier (OPA) to give high intensity pulses at tunable wavelengths between 1100 and 2500 nm. The OPA is a HE:TOPAS from Light Conversion and the Ti:Sa laser is a two stage KMLabs Dragon that is amplifying pulses from the laser oscillator, a KMLabs Griffin.

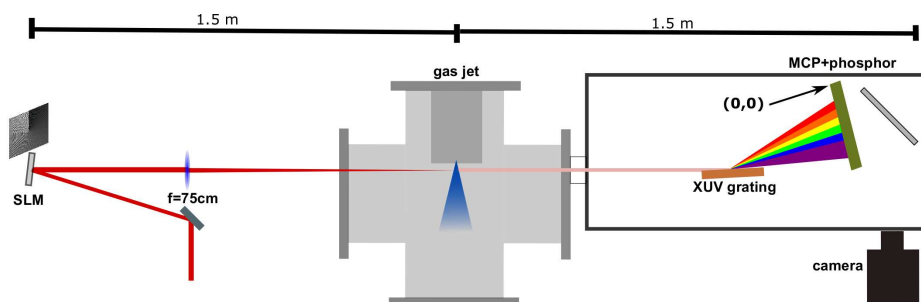


Figure 4.1: Experimental setup with a spatial light modulator and vacuum chambers

4.1.1 Spectrometer

To measure light in the ultra-violet to extreme ultra-violet, we use a flat field polychromator. The central element of the polychromator is a laminar type replica grating [78], with variably spaced grooves and an effective groove density σ of 1200 grooves/mm. It is a grating that produces a flat

detector plane for a wide wavelength range. Since HHG produces a wide spectrum of harmonic emission in a single laser shot, we would like to collect the information of all harmonic orders at the same time. A curved grating without variable groove density will produce an imaging circle called a Rowland circle, that would require a curved detector plane to detect multiple wavelengths with high fidelity at the same time. The spatial profile of each frequency component is recorded in the vertical direction and is limited by the effective aperture of slit and grating in the spectrometer. Our slit is 12.5 mm tall and adjustable in width between 0 μm and 5 mm in steps of 10 μm . The slit is typically set to 200 to 400 μm , but not shown in the experimental setup. It is placed 240 mm in front of the grating. The detector plane of the grating, specified by the manufacturer, is 5-20 nm (with measured performance up to 40 nm in [78]) over a length of 25.3 mm. However, we are using the grating to resolve harmonic emission from 100 nm to 5 nm with a detector that spans more than 25 mm in size. An MCP-based detector is used for its sensitivity in the VUV through soft X-ray region. It is placed 237 mm away from the center of the grating and the edge of the detector is placed at the right edge of the specified grating's detector plane. The angle of diffraction θ of the harmonic emission, diffracted off the grating, is given by

$$\theta = \sin^{-1}\left(\sigma n \frac{\lambda}{q} - \sin \theta_i\right), \quad (4.1)$$

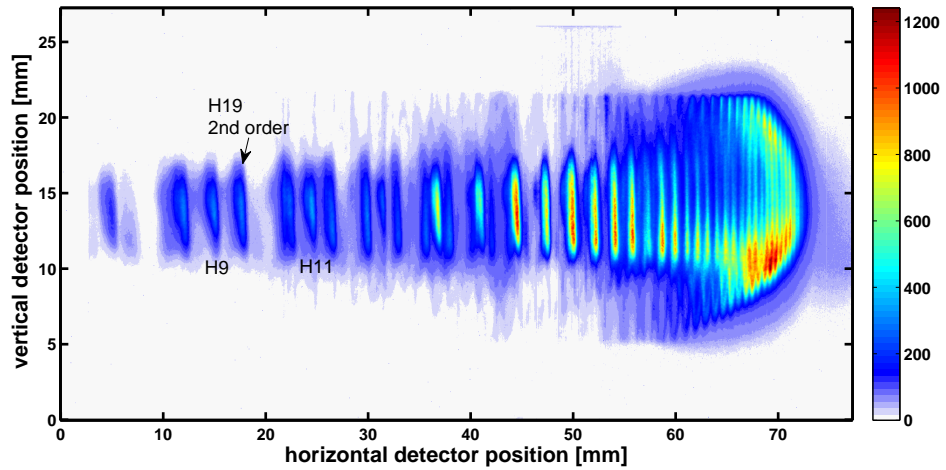


Figure 4.2: Detector image as seen from HHG in Neon gas. Driven with light at 785 nm

where $\frac{\lambda}{q}$ is the wavelength of the q -th harmonic, λ the wavelength of the fundamental laser, σ the groove density of the grating, θ_i the grazing incidence angle in respect to the incoming light and n the order of diffraction. The grating has a reduced efficiency for higher order diffractions, so that orders higher than $n = 2$ can be neglected. Figure 4.2 shows a spectrum of HHG, detected in our setup, driven with an intense 785 nm laser pulse. The spectrum stretches up to harmonic order 69 at an energy of 110 eV or a wavelength of 11.4 nm. The spacing between harmonics is given by Equation 4.1, which we can approximate with $\theta \approx \sigma\lambda/q$, to show the equivalent spacing of wavelengths by the diffraction grating. However, harmonics are equally spaced in frequency by $2h\nu$, so that higher order harmonics are more tightly spaced on the grating's detector plane, since the wavelength is the inverse of the frequency. The axes of Figure 4.2 are defined by the lower left corner of the detector with the coordinates (0,0) (see Figure 4.1 and the reference arrow on the detector) and harmonics with a bigger horizontal position have a smaller diffraction angle from the grating. In the collected spectrum in Figure 4.2 we can observe a change in divergence on the vertical axis for different harmonics: while low order harmonics have a smaller divergence, higher order harmonics positioned on the detector at 60 mm have a bigger divergence, before it gradually decreases in the cut-off of the spectrum. This is target specific and can differ for

different targets.

UV light striking the MCP detector ejects electrons from the surface. These electrons are accelerated down the channels by a high voltage applied across the plate. Collisions with the channel walls then create secondary electrons, leading to an avalanche effect. Multiple MCP plates are stacked together to produce sufficient gain so that a signal can be recorded. The used detector stacks have a typical electron gain of $1 - 3 \cdot 10^7$. A phosphor screen is placed after the stack of MCPs. The ejected electrons are accelerated towards the phosphor, due to a positive potential difference between MCP and phosphor, and generate luminescence at a center wavelength of 540 nm upon impact on the phosphor screen. The light is measured with a Hamamatsu Orca Flash 2.8, a low noise camera with a 12 bit resolution. The detector was switched between experiments. Initially, we used a Chevron stack MCP with two 75 mm circular MCP plates and a slow, high quantum efficiency P20 phosphor screen that we then replaced by a Z-stack of three MCP's with an effective area of 105x35 mm and a fast, low quantum efficiency P46 phosphor screen. The overall gain remained similar, as the additional gain from the third MCP compensated the lower efficiency of the fast phosphor. The micro channel plates and phosphor screen are supplied by Photonis.

We require low pressures in the chamber for two reasons: absorption of XUV light in atmospheric pressures and the operation of high voltage detectors in low pressure to avoid sparking inside the detector. A pressure of $1e - 7$ torr is held in the spectrometer chamber by two turbo pumps with pumping speeds of 250 l/s and 360 l/s. To align the optical axis through the spectrometer, the grating can be moved out of the optical path and we can align the laser to a set of irises placed before and after the vacuum chambers.

4.1.2 Gas sources

High harmonic generation is driven by intense lasers focused in gases. The brightness of harmonics scales with the number of emitters quadratically [79], due to the coherent addition of the electric fields of individual emitters and under the assumption of negligible phase mismatch. To increase the number of emitters, higher gas pressures are needed. We separate the production and detection into different chambers that are connected through a differential stage. In the generation chamber, gas pressures are high and we have to create a pressure differential to adjacent chambers, since they require low pressures to operate the detectors. In the source chamber we produce a dense gas target by using a capillary with a inner diameter of 200 μm that leaks gas into the chamber. Leak rates resulting in an average pressure of $5 - 10 \cdot 10^{-5}$ torr in the source chamber produce bright harmonic sources in the setup. Backing pressures of 1 atm are regulated with a leak valve (Pfeiffer EVN-116) and the leak rate is adjusted to $1 \cdot 10^{-2}$ mbar l/s.

Further to that, we can also produce a cold gas jet with a bell shaped nozzle [80]. Through the bell shaped form and a supersonic expansion, cooling in the gas is enhanced and we observe rotational temperatures of 25 to 40K in nitrogen and ethylene gas (as seen in Chapters 8 and 9). The gas jet is pulsed to reduce the gas load in the production chamber. The pulses are generated through the rapid motion of a piezoceramic which is designed as a cantilever. Switching between two sets of voltages, the ceramic can either compress a sealing o-ring or open the seal of the o-ring. By opening the seal, gas can bypass the seal and flow through the nozzle into the gas chamber. When the seal is compressed, no gas can leak into the chamber. The pulsed operation reduces gas loads in the chambers, as the interaction between light and matter is limited to the pulse duration of the laser with 30 fs at a repetition rate of 1 kHz. The temporal length of the gas pulse is 30 μs , which results in a duty cycle of 3%, compared to the 1 ms spacing of the laser pulses. The gas load is managed with a Leybold MAG drive CT2200, with a pumping speed of 1800l/s for nitrogen. A differential tubing between the production chamber and the spectrometer can hold a differential of 3 magnitudes in pressure. The laser light is sent into the chamber through fused silica windows.

4.2 Spatial light modulators

Spatial light modulators (SLM) influence the spatial profile of coherent light. In our laboratory we use a modulator of the X10468 series from Hamamatsu. It is based on liquid crystal on silicone (LCOS) technology [81] and uses the birefringent properties of liquid crystals. Birefringent materials have a polarization and propagation dependent refractive index. As an example, crystals like Calcite are uniaxial, where one direction is anisotropic, but all directions perpendicular to it behave equally. We define the axis with the anisotropic behavior as the ordinary axis and the axis perpendicular to the anisotropy and perpendicular to the light propagation as the extraordinary axis. We observe a difference in index of refraction Δn between both:

$$\Delta n = n_e - n_o \quad (4.2)$$

where n_e is the refractive index of the extraordinary axis and n_o the index of refraction for the ordinary axis. Liquid crystals are phases of matter that can behave like liquids and/or solids. For the phase-only modulation that we seek in our device, nematic phases work well. In the nematic phase, molecules tend to align in the same direction, but have no positional order. They behave more like a liquid compared to smectic phases that show a translational order, i.e. they align in planes and behave more like a solid. Additionally, the phase of the liquid crystals is a function of temperature and changes behavior under external influence (e.g. electrically controlled birefringence [82, 83]). Liquid crystals are also uniaxial like Calcite, since they inherently have a short and long axis, resulting in a different index of refraction for its ordinary and extraordinary axis. By applying a voltage, the liquid crystals can align with the ordinary or extraordinary axis parallel to the laser polarization, which will result in a phase retardation for the incident light. The maximum phase retardation that light of wavelength λ acquires, when traveling through an LCOS device of thickness d , is given by

$$\phi = 2\pi\Delta nd/\lambda \quad (4.3)$$

In the case of a reflective device, the phase retardation is increased by a factor of 2, since it travels through the liquid crystal twice. To then acquire a maximum phase retardation of 2π through the device, the thickness is fixed to $d = \lambda/2\Delta n$.

11	21	31	41
21	22	32	42
31	32	33	43
41	42	43	44
51	52	53	54

Figure 4.3: Scheme for the manipulation of single pixels on the SLM.

The device in our laboratory delivers 2π phase modulation pixel by pixel with a pitch size

of 20 μm . Every pixel has individual circuitry that can change the voltage and change the birefringence. The LCD consists of 800 by 600 pixels with a bit depth of 8 bit. In Figure 4.3, we show a simplified model of our SLM array. Each pixel indicated with XY is controlled with a different voltage and we illustrate the phase on the SLM as an opacity, where a more opaque blue will correspond to a higher phase value. By applying a 8-bit image to the SLM, we get a phase resolution of 30 mrad per voltage unit on the SLM. As described in section 3.4.3 of Chapter 3, we start with a manipulated spatial profile $U(x, y)$ and will have a propagated spatial profile $U'(x, y)$ after propagating it through a lens, using Equations 3.126 and 3.131, which is scaled by the focal length of the used lens.

4.2.1 Spatially shaped pulses

To generate a focus with a spatial offset in the focus, we apply a tilt in the direction of the designated offset. We introduced the tilt in Section 3.4.4 in Equation 3.127. On the SLM, we can display a mask that will result in a tilted phase front as illustrated in the top left of Figure 4.4, where we call this modulated light "beam 1" for this section. From bottom to top, the phase of "beam 1" increases and the beam will have a vertical offset in the focus plane. In the experiment, we use a 800x600 pixel array, instead of a 4x5 array. When we switch the direction, as shown in the top right of Figure 4.4, and increase the phase from the top to the bottom, we impose an opposite offset to the beam in the focus plane and will call this modulated light "beam 2" for this section.

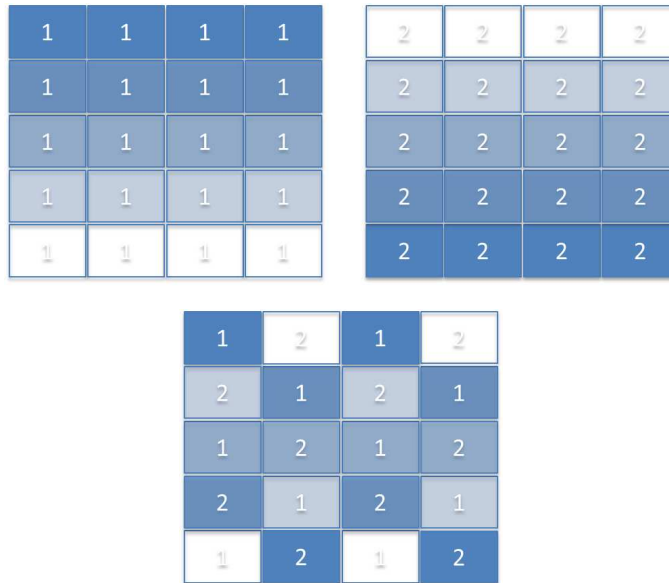


Figure 4.4: Scheme for a tilt-manipulation on the SLM

If we now want to generate two independent beams, we can associate a set of pixels to "beam 1" and the remaining pixels to "beam 2". Associating adjacent pixels in the bottom of Figure 4.4 to the first or second beam by alternating between the appropriate phase masks of "beam 1" and "beam 2", we can generate a new phase mask that will now spatially shape half of the pixels on the device to tilt the beam vertically in one direction and will spatially shape the other half of pixels on the device to tilt the beam vertically in the opposite direction. Half of the light is tilted upwards and the other half of the light is tilted downwards, forming a vertically separated double focus. These calculations were introduced in Chapter 3 in Section 3.5.3 and calculations of the focus dependence were shown in Figure 3.26 and Figure 3.28. We choose an alternating distribution function to switch between "beam 1" and "beam 2", as illustrated in the bottom of Figure 4.4. However, the SLM has 800x600 pixels and we choose a number of pixels that we

would like to associate with one of the two sources. We choose to associate a certain line width to individual beams. In the experiment in section 5.1 of Chapter 5, we use a checker board pattern to switch between "beam 1" and "beam 2". Each checker will have 10×10 pixels so that our checker board reduces to an array of 80×60 subarrays. We also can use a completely random distribution function to either of the two sources, as long as both beams have an equal amount of pixels associated with them. Given our Gaussian intensity distribution, possible intensity fluctuations or beam drifts, it is best to sample each of the two beams equally over the whole SLM and over the whole incoming beam to increase the stability of the shaping process.

Further to this, we can purposely unbalance the amount of pixels associated with one of the two beams and change the relative intensity of the two beams.

In an imaging setup, we measure the spot sizes as a function of lens position on a CMOS camera. As we move the lens in respect to the camera, the light's spot size reduces until a minimum spot size w_0 is reached, given by Gaussian optics and introduced in Section 3.4.1. After the focus the spot size will start to increase again following Equation 3.108. If we now apply a phase mask, creating two vertically offset beams, and collect a focus projection as a function of lens position, we can see each beam focus and defocus as a function of lens position, as seen in Figure 4.5b. Both beams have the same focusing behavior as the original laser beam, measured in Figure 4.5a. Far away from the focus, the two beams are overlapping spatially and can interfere. A bright spot on axis appears, e.g. at a focus position of 15 mm in Figure 4.5b. This is an artifact of the beam attenuator, that was inserted for the spot size measurements. It is cross-polarized light that is not shaped by the SLM and focuses at this focus position. Without the attenuator present, the cross-polarized light is low in intensity and does not influence the experiment. Further to that, the cross-polarized light is focused 2 cm away from the actual focus and will not interact with a gas jet placed at 0 mm. When applying an additional constant phase of π between "beam 1" and "beam 2" in Figure 4.5d, the shape of the two beams is not changed. The condition for interference in the far field is shifted by π and we get two spots of bright light before the focus at -15 mm. In the spot after the focus at +15 mm the cross polarized light washes out this feature.

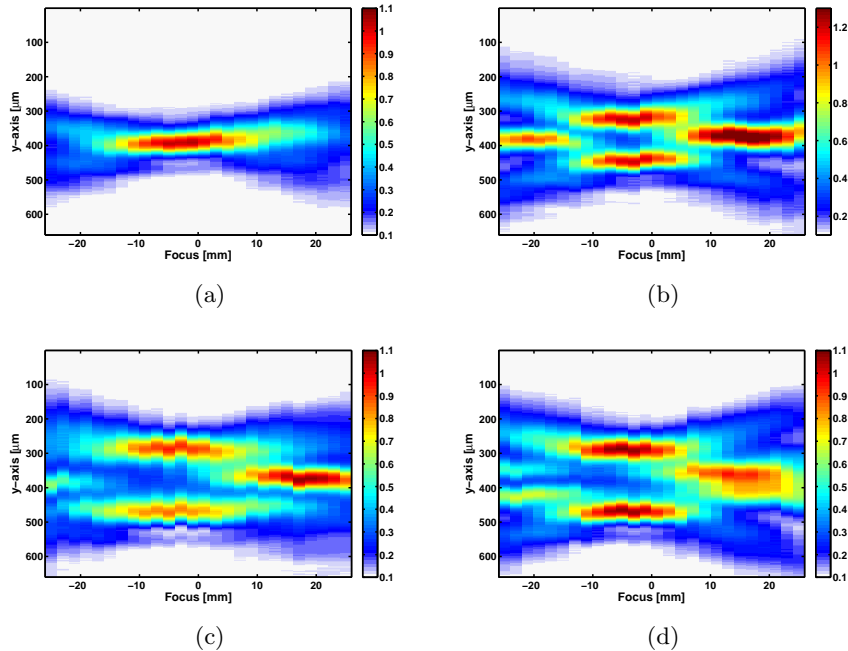


Figure 4.5: Focus projection as a function of lens position, captured by a CMOS camera for a flat phase mask (a), a phase mask producing two foci separated by $120 \mu\text{m}$ (b), by $180 \mu\text{m}$ (c) and by $180 \mu\text{m}$, when one source is delayed by 1.31 fs or 1π in respect to the other source (d).

When changing the relative distribution of light towards one of the two beams, we can influence the relative intensity of the beams. By distributing the pixels equally between the two beams, we get a balanced intensity of the two sources in Figure 4.6a, where the maximum brightness between "beam 1" and "beam 2" are equal. However by associating 60% of the pixels towards one of the two beams, we can generate unbalanced focus spots in Figure 4.6b, where the brightness of "beam 1" is higher than the brightness of "beam 2", and an unbalanced focus spot in Figure 4.6c, where the brightness of "beam 2" is brighter than the brightness of "beam 1". This technique will be used in Chapter 6.

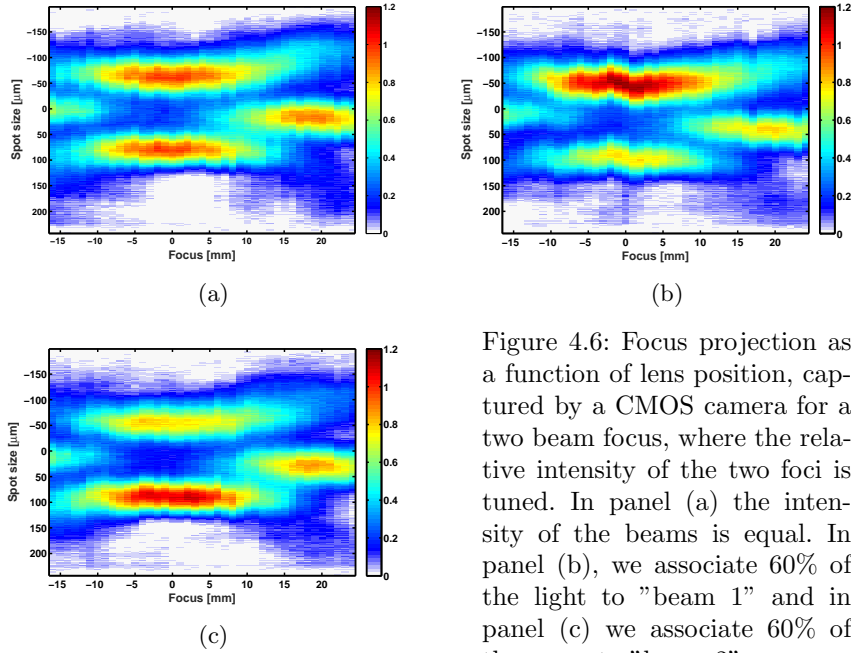


Figure 4.6: Focus projection as a function of lens position, captured by a CMOS camera for a two beam focus, where the relative intensity of the two foci is tuned. In panel (a) the intensity of the beams is equal. In panel (b), we associate 60% of the light to "beam 1" and in panel (c) we associate 60% of the array to "beam 2"

Spatial shaping through interference effects

Instead of the technique of redistributing light by applying a tilt, we can also shape the beam spatially through interference. When causing destructive interference between light in space, we can reduce the intensity to zero and, when causing constructive interference between light in space, we can increase the intensity by a factor of 4. As described in Section 3.5.1, we use two Laguerre Gaussian beams with opposite orbital angular momentum (OAM). These beams interfere destructively as a function of angle in the observation plane. With opposite OAM, the light interferes destructively twice over 360° , causing a tightly spaced double focus. In the experiment we produce a phase mask with a ring structure, where alternating rings have opposite OAM of $l = 1$ and $l = -1$. The resulting focus is shown in the middle panel of Figure 4.7, where we create a double focus through the interference of Laguerre Gaussian beams and plot the focus projection as function of lens position. By adjusting the OAM of the interfering beams, we can generate a single source in the left with OAM of $l = 1$ and $l = 0$ and the second source in the right panel with OAM of $l = 1$ and $l = 0$, while an additional phase offset of π is given to move the angle of destructive inference by π .

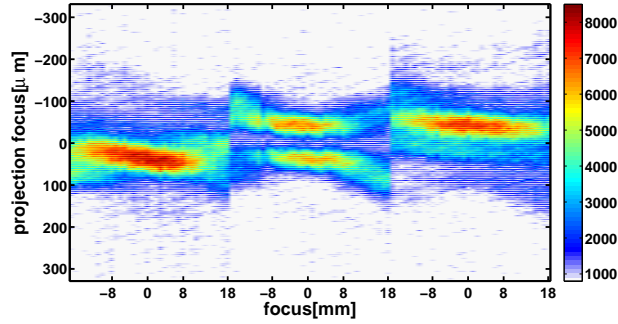


Figure 4.7: Projected focus of a laser beam as a function of lens position. The light carries OAM. On the left, through combination of $l = 0, 1$, we get the bottom source, in the middle panel through the combination of $l = 1, -1$ we get the two source focus and on the right, we produce with $l = 0, 1$ the top source

4.2.2 Creation of delayed pulses via phase modulation

Not only can we shape the light in space, but also change its temporal behavior with the SLM. The electric field has a spatial and temporal distribution, resulting in an electric field

$$E(t, \vec{r}) = A(\vec{r})\epsilon(t) \cos(\omega t - \Phi_{CE}) \quad (4.4)$$

where $A(\vec{r})$ describes the spatial intensity and phase distribution and $\epsilon(t)$ the temporal domain accordingly. Both distributions are Gaussian distributions. We introduced the spatial properties of the Gaussian laser mode in Equation 3.107 and can write the temporal property of the laser with an electric field in time with $\epsilon(t) \propto e^{-(t)^2/\sigma^2}$. When applying a constant spatial phase to the beam, we get $A'(\vec{r}) = A(\vec{r}) + e^{-i\Phi}$ and our electric field E' becomes

$$E'(t, \vec{r}) = A'(\vec{r})\epsilon(t) \cos(\omega t - \Phi_{CE}) \quad (4.5)$$

$$= A(\vec{r})e^{-i\Phi}\epsilon(t) \cos(\omega t - \Phi_{CE}) \quad (4.6)$$

which corresponds to a constant offset in time, following the shift theorem for Fourier transforms. This theorem states that delaying a signal $x(t)$ by τ multiplies its Fourier transform by $e^{-j\omega\tau}$, with $\Phi = \omega\tau$. In our case, we add the later term to our beam and delay our beam by τ and write $\epsilon'(t) = \epsilon(t - \tau)$. We can now write the electric field in time and space as

$$E'(t, \tau, \vec{r}) = \epsilon(t - \tau)\cos(\omega(t - \tau) - \Phi_{CE})A(\vec{r}) \quad (4.7)$$

where $\epsilon(t - \tau) \propto e^{-((t-\tau)^2/\sigma^2)}$ describes a Gaussian carrier envelope and Φ_{CE} the phase between the oscillations and the carrier envelope.

Delayed pulses in the experiment

As a proof of principle experiment, we measure the delay dependence on HHG, when driven by a two color laser field in argon gas. We want to prove the ability of the SLM to act as a delay stage. The experimental setup is shown in Figure 4.8, where an incoming 785 nm laser field produces a second harmonic in a beta barium borate (BBO) crystal. When combined, the beams produce a two color field. Optimizing the phase matching for second harmonic generation in the crystal, the 200 μm thick crystal has a conversion efficiency of 30-35% for second harmonic generation. In our experiment, we optimize for a transform limited pulse of the Ti:Sa laser in the interaction region, inside the vacuum chamber. At the position of the BBO, the laser will have negative chirp and the pulse duration is increased. This results in a reduced conversion efficiency on the order of 15% and a chirped 2nd harmonic pulse. After the generation, the co-propagating beams are

sent into a Michelson interferometer and split with a dichroic mirror (DC). The 785 nm beam is reflected and shaped by the spatial light modulator, while the 392 nm beam is reflected off a 0° aluminum mirror. A linear stage underneath the aluminum mirror is adjusted for a matching delay between the two beams. The beams recombine on the dichroic mirror and are focused collinearly with a $f=50$ cm lens into a gas jet. The beams are cross-polarized after the BBO and the second harmonic can act as a gate on the process of high harmonic generation [84]. Depending on the delay between 785 and 392 nm, the electron is driven perpendicular to the fundamental and can miss the parent ion at re-collision, illustrated in Figure 4.9. Harmonic generation is suppressed. At other times, more ionization and re-collisions can occur and the harmonic yield can be increased. This behavior is strongly influenced by the present electron trajectories and excursion times of different harmonics. With the SLM, the delay can only be scanned over one full oscillation of the fundamental field, yielding a range of 2.62 fs. In these 2.62 fs we can measure the delay dependence on high harmonic generation. In Figure 4.10, we collect the integrated yield of individual harmonics as a function of delay between 785 nm and 392 nm light. The individual harmonic yield is normalized to its own maximum. Both columns in Figure 4.10 are acquired at the same time. The even harmonics 12 and 16 in the right panel show a peak at a delay of 1200 as, while the harmonic yield of the 15th harmonic produced by long electron trajectories in the same panel shows a minimum at this particular delay. We can separate harmonic 15 into two different contributions: a on-axis contributions stemming from short trajectories and an off-axis distributions from long trajectories. These two contributions show opposite behavior. The short trajectory harmonic shows a value of 0.95 at 1200 as and a local minimum of 0.9. The long trajectory spends more time in the electric field and can experience a bigger spatial offset, due to the cross polarized second harmonic, resulting in a bigger contrast of 0.7 to 1, compared to the short trajectory, which spends less time in the electric field and is less influenced by the gating field.

Harmonic 9, with an energy below the ionization potential of argon, shows strong fluctuations as a function of delay, while plateau harmonics 15 and 21 show a small delay dependence. However, once we reach the cutoff with harmonic 31, the yield is again strongly influenced by the delay between 392 nm and 785 nm. As stated earlier, the SLM should allow us to control the delay of the incident light and we have shown through this experiment that the SLM gives us the ability to apply a delay, as the yield of individual harmonics is a function of the phase applied to the SLM and behaves differently for different electron trajectories and harmonic orders.

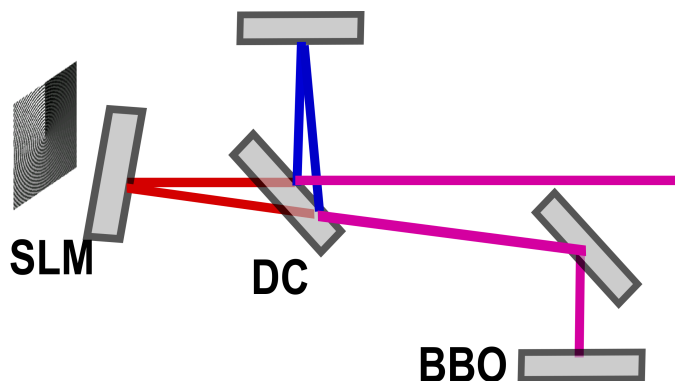


Figure 4.8: Experimental proof of principle: A 16 mm beam passes through a 15 mm BBO crystal, generating the second harmonic of the Ti:Sa laser, The fundamental and second harmonic are split and recombined on a dichroic beam separator. The arms of the interferometer are tuned so that the two pulses are temporally overlapped. By changing the voltage on the SLM, the delay can be adjusted in steps of 12.5 as.

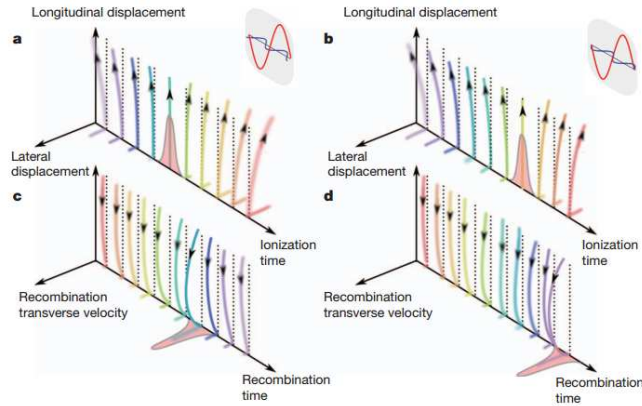


Figure 4.9: Gating process in high harmonic generation by a two color field. By delaying the 392 nm in respect to the 785 nm light, the ionization gate in (a) and (b) results in electron born at a certain time with little lateral offset. When recombining in (c) and (d), only certain trajectories in time can recombine with an optimized re-collision angle, resulting in enhanced harmonic emission. Picture taken from [85]

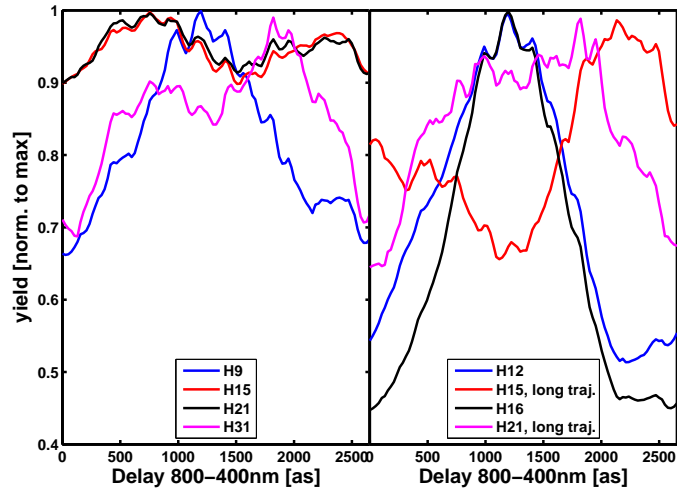


Figure 4.10: Harmonic yield of even and odd harmonics produced from short and long trajectories as a function of delay between the fundamental and second harmonic. The delay is varied in steps of 25.5 as and the yield of individual harmonics oscillates by a factor of 2 between certain delays.

4.2.3 Chromatic dispersion

As stated before, with the SLM, we align the liquid crystals so that the light is being refracted of the oriented birefringent crystal, where the slow axis can rotate between an orientation parallel or perpendicular to the light's polarization, which leads to a phase modulation for the light between 0 and 2π . However, since we use pulsed lasers with an associated bandwidth, we have to consider the influence of the SLM on all wavelengths. As we change the refractive index, we also change the dispersion for each wavelength differently. Through this, we could potentially not only change the delay of the laser pulse, but influence phase and group velocity differently, which leads to a changing CE-phase as we change the voltage on the liquid crystals. In reference [86], the CE-phase is described as the change in wedge thickness and a scaling chromatic dispersion. For each μm of fused silica, the carrier envelope phase changes. However, further to that, the delay changes in a much bigger fashion. In our setup, we change the voltage on our liquid crystal and potentially can alter the carrier envelope phase of our beams, beyond the change of delay. Following the supplied characterization by the manufacturer in the top panel of Figure 4.11, we plot the calibration value for a 2π manipulation as a function of wavelength and we can calculate the change of phase as a function of wavelength in the bottom panel of the figure. The chromatic dispersion of materials is described as $dn/d\lambda$. Through the given calibration curve, we can describe the chromatic dispersion as $d\Phi/dVd\lambda$ and then multiply the fraction by the voltage that applies a 2π phase difference to the incident beam. We calculate the derivative of

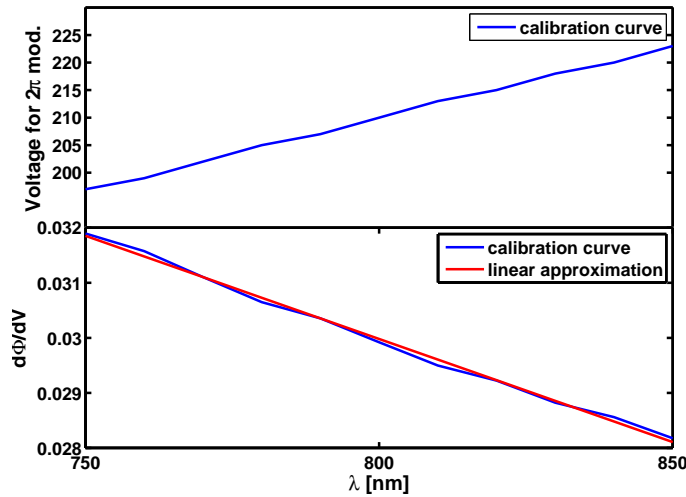


Figure 4.11: Top panel: calibration curve, supplied by Hamamatsu, describing the voltage applied to the SLM to reach 2π phase modulation to a given wavelength. Bottom panel: derivative of the change of phase per unit voltage as a function of wavelength.

the change in phase per unit voltage and do a linear approximation. We calculate the derivative to be $d\Phi/dVd\lambda$ and multiply the given number by 205, the calibration number for 780 nm, equal to a 2π manipulation. With this, we get a maximum carrier envelope phase change over the device of 0.008 rad, when comparing a liquid crystal at the minimum phase manipulation of 0 rad versus the maximum phase manipulation of 6.283 rad. In our experiment, we use complex phase masks that tilt the wavefronts, correct for the curvature of the SLM and apply an additional phase offset. After applying these phase corrections, the phase is wrapped on the device and the differences are convoluted into the wrapped phase and the CE-phase is an averaged carrier envelope phase offset that is manipulated by the whole phase mask on the SLM. We take each pixel value, convert it to the corresponding chromatic dispersion and convert it into a CE-phase offset. In Figure 4.12, we show the average CE-phase offset $\langle\Delta CE\rangle$ in mrad for additional voltage values between 0 and 255 applied to the phase mask. We can see a CEP offset of 3 to 5.5 mrad across all voltage offsets and different masks applied to the SLM. As we apply the additional

constant voltage to the masks, we change the CE-phase as a function of voltage on the order of 2 mrad. A minuscule number in the Ultrafast community. As previously described in Section 4.2.1, we apply the phase pattern for two beams on the SLM and group the phase manipulation in squares of certain line width. Independent of line width or tilt, the CE offset has a maximum value of 5.5 mrad, but reaches this value at a different voltage value. We do, however, have to discuss the general concept of phase delay versus group delay: While we tilt the phase front of a single source, we do not tilt the group front of the pulse and introduce an offset between the phase and group front that is permanent. This translates to a permanent, spatial CE offset in the focusing plane. We can define an effective CE-phase of the fundamental in the focus and treat the measurements as a relative phase measurements, as it always is.

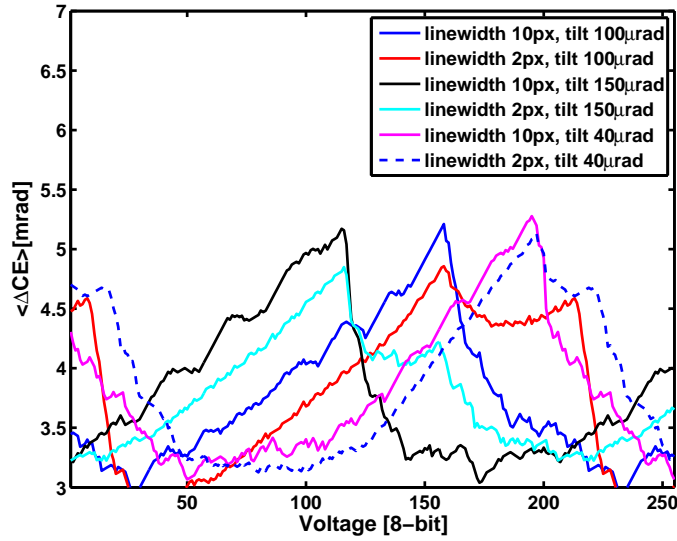


Figure 4.12: Change in the mean CEP as a function of offset applied to the SLM between one source in respect to the second source. Phase wrapping has been performed at the value for 2π of 780 nm light.

4.3 Young's double slit with HHG

To realize a Young's double slit of two identical HHG sources, we use a phase mask on the SLM that introduces an opposite beam tilt for adjacent pixels of the SLM, where the spot sizes were shown in Section 4.2.1. The theoretical calculations have been performed in Section 3.5.3. We define a signal and reference source in the experiment: The signal is defined as our observable that is influenced by an external field (e.g. a pump pulse) or by changing the source directly through a change in delay or intensity. The reference signal is left unchanged and serves as the reference to which we can define a change in phase. When high harmonics are generated from both sources and travel into the far field, we observe an interference pattern on the detector as shown in Figure 4.13, where higher order harmonics (on the right) have a smaller fringe angle than lower order harmonics (on the left), as given by Equation 3.56 in Section 3.2.3. The contrast in the fringes is given by a formula for a Young's double slit

$$I_{total} = I_1 + I_2 + 2\sqrt{I_1 I_2} \cos\left(2\pi \frac{\delta Y}{\lambda z}\right) \quad (4.8)$$

where Y is the ordinate of the fringe projection, $I_{1,2}$ the intensities of the harmonic sources, λ the wavelength of the light and z the distance to the observation plane. Integrating over the ordinate, the total signal on the detector is $I_{total} = I_1 + I_2$. Following Equation 4.8, we should see the harmonic signal drop to zero for given values of the ordinate. However, in Figure 4.13, we do not observe this behavior. As we increase the harmonic order, the contrast in the fringe is

decreasing further. This can be explained by two factors in our experiment: detector resolution and finite slit size of the Young's double slit. In the detector, single events on the MCP/phosphor detector cover an area of 4x4 pixels on the camera, which will yield a reduced resolution of a perfect fringe contrast.

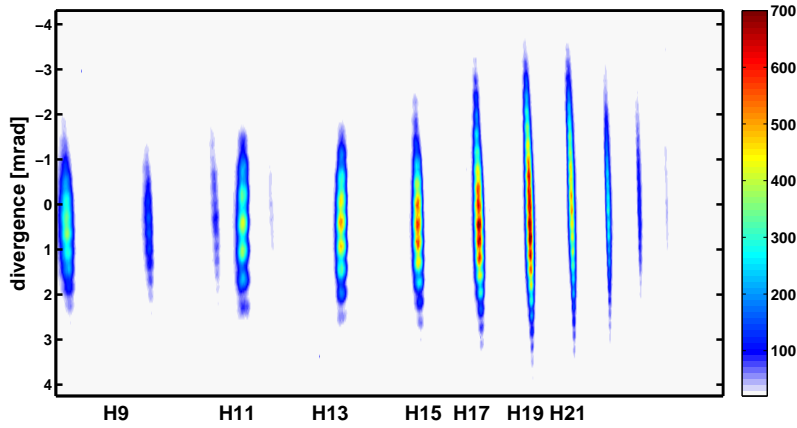


Figure 4.13: Detector image in the XUV interferometer. Higher frequencies get diffracted less and are on the right of the detector, while lower frequencies get diffracted more and are on the left of the detector. The ordinate is created with a geometrical divergence in units of mrad, where 0 mrad is equal to the optical axis of the laser beam. The divergence is not related to the phase of harmonics.

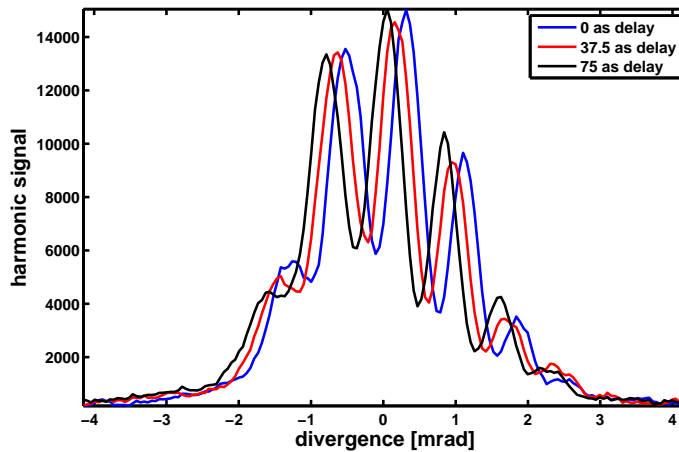


Figure 4.14: Fringe projection of harmonic 11 for experiments shown in Chapter 5

To form an ordinate dependent fringe projection in Figure 4.14, we integrate over the energy bandwidth of individual harmonics, given in our detector plane. Performing a fast Fourier transform, described in Equation 3.121 in section 3.4.2, on this lineout, we get an amplitude and phase for the spatial frequencies involved in the fringe pattern. For the different fringe projections in Figure 4.14, we would get Fourier transformations that are very similar in amplitude, but different in phase. The frequency representing the interference effect will have a different phase for the three different lineouts. We define a phase of 0 at the center of the abscissa at 0 mrad and associate a phase of 0π to the black line. The red line is shifted to the right and has a phase greater than 0π , while the blue line will yield a phase close to 1π . These phase values are always

relative to a chosen reference. In the later experiments they are as examples the phase at time zero, the phase of the harmonic, when the molecule is not aligned.

When generating different Young's double slits with separations of $120\ \mu\text{m}$ and $180\ \mu\text{m}$ in the experiment, we get fringes from the interfering harmonics and the fringe spacing will differ for different separations. In Figure 4.15 we plot the amplitude of the spatial frequencies. We can see distinct peaks in the amplitude spectrum that can be associated with the fringe spacing visible on the detector. Harmonic 9 generated from two slits separated by $120\ \mu\text{m}$ has a fringe separation of 12 pixels on the detector, while with a separation of $180\ \mu\text{m}$, the spacing reduces by a factor of 1.5 to 8 pixels. The same is valid for H15 in Figure 4.15. The relative spacing between H9 and H15 is given by $15/9$ and is present in the figure. With a separation of $100\ \mu\text{m}$ in Figure 4.16, we can see the frequency of the fringes increase with harmonic frequency. While we can observe 33 oscillations of harmonic 9 on the given detector height L , we will observe 90 oscillations for harmonic 23. The given figures show how well the proposed technique works as a Young's double slit, in which the distance between slits can be adjusted by adjusting the phase pattern on the SLM.

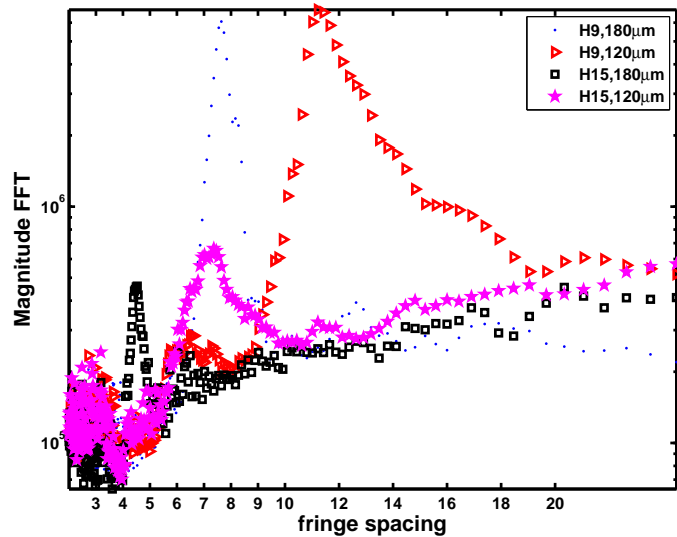


Figure 4.15: Amplitude of the fourier transform as a function of fringe spacing in pixels for different slit spacings and harmonic orders.

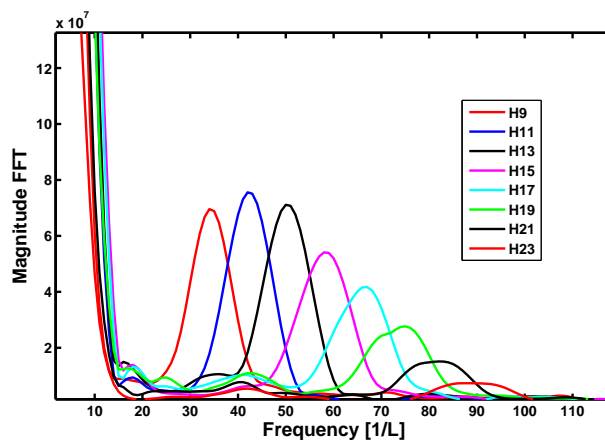


Figure 4.16: Amplitude of the fourier transformation for different harmonic orders. The length L is given by the detector height.

4.3.1 Resolution of a Young's double slit

A further discussion has to be made about the resolution of our phase measurements. We perform a measurement in the spatial domain and relate this measurement by a Fourier transform into the frequency space. A straight forward calculation is the frequency resolution given by the size of the detector. By applying zero padding the resolution in frequency can increase theoretically below the resolution of the detector itself. However, a discussion on the resolution in the phase value of the performed Fourier transform can be more complex. The resolution in the spatial domain is given by the detector size of the phosphor and by the pixel size of the camera. As previously stated, we can observe 90 oscillations for harmonic 23 on our given detector. After accounting for zero-padding in the Fourier transform, we have a reduced number of 30 oscillation on the physical detector. Each oscillations has its maximum at a value of close to 6 pixels, which would correspond to a resolution of $2\pi/6$ rad or roughly 1 rad. However, since the real oscillation of the fringe pattern is not an integer number, the measurement of the phase can be expressed as an equivalent to a common technique used in sampling oscilloscopes: Equivalent time sampling. Our trigger is given in increments of integer pixels, but our oscillation has a period that is not an integer number. By having multiple triggers or in this case multiple fringe oscillations, we can sample the phase with various delays given by the difference between the integer trigger and the actual spacing of the frequency of interest. This results in a increased sampling rate of the phase. Each oscillation corresponds to a measurable phase value of 2π , these 30 oscillations are spaced by 5.5 pixels, resulting in a maximum resolution of $2\pi/165$ or 40 mrad for this harmonic. In reference [87] the phase resolution of a Fourier transformation is given by

$$E(\delta\Phi_{rms}) = (n/2N)^{1/2}\sigma_n/(\pi m) \quad (4.9)$$

where n is the sampling of the frequency, e.g. 5.5 pixels, and N the total sampling length, given by 165 in the previous example. Assuming a modulation depth of $m = 0.3$, as given in Figure 4.14 and a noise estimate of $\sigma_n = 60$ mrad RMS, given by errors reported in a later chapter, we get a total resolution of 7.7 mrad for the phase of this particular harmonic. In the experiment, the modulation depth, frequency and RMS value are changing, so that for individual experiments, the absolute precision may vary, but the given estimate for the given case, shows the high phase resolution in a Fourier transformation, even when the detector resolution is low.

Chapter 5

Optical phase of high order harmonics

When high harmonic generation was first observed and studied experimentally, theoretical models were missing that were able to quantitatively describe HHG. When high harmonic generation was described in a perturbative picture by Brunel in 1990 [88], the harmonic efficiency would decrease with harmonic order exponentially, as expected from perturbative non-linear optics and the characteristic plateau of high harmonic generation could not be explained. We also know that in non-linear optics the harmonic dipole phase does not depend on the laser intensity in perturbative low order harmonic generation and we would not expect a perturbative process to have an intensity independent phase.

In our current picture of non-perturbative, non-linear high harmonic generation, we have seen the opposite: a pronounced plateau in the intensity of high harmonics and an intensity dependent dipole phase of high harmonics, which was discovered by the SFA theory. In the previous theoretical chapters, high harmonic generation was described as a product of amplitudes: an amplitude of ionization, an amplitude of a returning electron trajectory and an amplitude of re-scattering. In this picture, each step imprints a specific phase on the emitted harmonic. In this chapter I will introduce a first proof of principle experiment to show the power and precision of the used interferometer to measure phases and amplitudes in HHG. The proof of principle experiment is introducing a very precise delay between the sources. Our approach is to produce two identical harmonic sources, which will have identical phase and amplitude, so that any dependence from the target or intensity are canceled and only the effect from a change in delay is visible in our measurement.

By applying a delay/phase between the two fundamental laser beams, we record a change in phase between the two harmonic sources. The proposed method is an attosecond analog to a Young's double slit experiment. The creation of independent slits gives the ability to control properties of the individual sources. Because of the common path design (as shown in a pump-probe experiment in [89]) and homogeneous spatial sampling of the laser, the interferometer has good stability.

5.1 Experimental methods

In the experiment, shown in Figure 4.1, a 785 nm laser pulse is reflected off a spatial light modulator and focused with a $f=75$ cm lens into a gas source. The emitted radiation is detected with a XUV spectrometer. The focus of the laser is shaped into two spatially offset foci and result in a Young's double slit as shown theoretically in Chapter 3 Section 3.2.3 and in our experimental introduction in Chapter 4 Section 4.3. We give each source a opposite vertical offset and generate two identical sources of HHG light. The two sources are generated with the identical driving laser field and the emitted harmonic radiation travels along the optical axis of the driving laser field and is resolved on the detector. As the light spatially overlaps in the far field, the sources produce

an interferogram. A unknown phase difference may be present. This phase difference is given by a path difference from the interaction region to the far field, which cannot be eliminated from the experiment. At this particular configuration we can define the extracted phase to be zero. By definition, the spacing between two adjacent maxima in the fringe pattern is defined as a phase difference of 2π .

In our study, we then manipulate one of the HHG sources by delaying the fundamental laser itself. If we observe a fringe evolve/move as a function of delay, we can associate the movement to a change in phase between the two slits. Since the reference arm is not altered, we can map this change in phase directly to our signal arm only. In Figure 4.14, we observe a change in fringe position in three given interferograms, due to an external manipulation of one of the two sources. Each interferogram is given by a projection of an individual harmonic on its spatial profile, that is given as its divergence in Figure 4.13 in the vertical dimension. The observed change in fringe position in Figure 4.14 between the blue outline and the black outline approaches a phase difference of π , when the maxima move into the position of the previous minima. These changes are rather big and easy to discern by eye. In the experiment, we employ fast Fourier transformations to extract the relative phase of the fringe frequency, which is equal to a defined position of the minima and maxima in the interferogram. We show a more detailed procedure of the fast Fourier transformations in Chapter 4 Section 4.3. We apply a phase through the method introduced in Section 4.2.2 and collect the phase relation between our reference arm and signal arm as a function of the phase difference between the two identical driving laser fields. The two electric fields are

$$E_1(t, \tau, \vec{r}) = \epsilon(t - \tau) \cos(\omega(t - \tau) - \Phi_{CE}) A_1(\vec{r}) \quad (5.1)$$

$$E_2(t, \vec{r}) = \epsilon(t) \cos(\omega t - \Phi_{CE}) A_2(\vec{r}) \quad (5.2)$$

in two separate sources, where one of the two sources is manipulated by the delay τ . Both sources have the same CE-phase Φ_{CE} and the same spatial distribution $A_1 = A_2$. A

5.2 A self-referencing interferometer with 12.5 as resolution

In the experiment, we use a thin gas capillary with a inner diameter of $200\mu m$, which produces a diffusive gas jet at the tip of the capillary that expands rapidly in space further away from the exit. We generate a double focus of the laser by applying a phase mask, introduced in Section 4.2.1, with a tilt of $100\ \mu rad$ and a checkerboard pattern with a line width of 10 pixels. This will result in a focus separation of $100\ \mu m$ with a lens of focal length $f=50\ cm$ and the foci act as a Young's double slit. A delay, following Equations 5.2, is introduced to one of the two foci, resulting in a delay between the laser pulses in each focus. The intensity of an individual source is measured to be $2 \cdot 10^{14} W/cm^2$, with a measured pulse duration of 30 fs, a spot size of $38\ \mu m$, and a pulse energy of $146\ \mu J$. When the delay between the laser foci is changed, the fringes will move up or down, equivalent to the change in phase between the two harmonic sources. As we can see in Figure 5.1a, the fringes in harmonic 13 generated from the double slit are moving as a function of delay between the two slits. The minimum step size is given by the minimum increment of voltage: the minimum step size for light at 780 nm is given by 12.5 as, following the calibration curve of the SLM. With the 8-bit resolution of the SLM, a value of 205 out of 255 is needed to introduce a phase delay of 2π , which is equivalent to 2.62 fs based on the period of light with a wavelength of 780 nm. From a delay of 0 as to a delay of 2620 as with a step size of 12.5 as in Figure 5.1a, we can count 13 maxima as a function of time, while in Figure 5.1b, we can count 19 maxima over a delay of 2π between the two fundamental laser foci. Figure 5.1b shows the delay dependent fringe of harmonic 19. The S-shape present in the shown figures is due to additional diffraction in the SLM and discussed in the appendix A. For each delay, we perform a fast Fourier transform and select the frequency of the fringe beating. Each fringe frequency for individual harmonics has an associated phase and we show the phase as a function of delay in Figure 5.2 for harmonic orders 9 to 19. The extracted phase is normalized to the phase value at the initial delay of 0 as and we can see the phase of harmonic 19 gradually change from 0 rad to

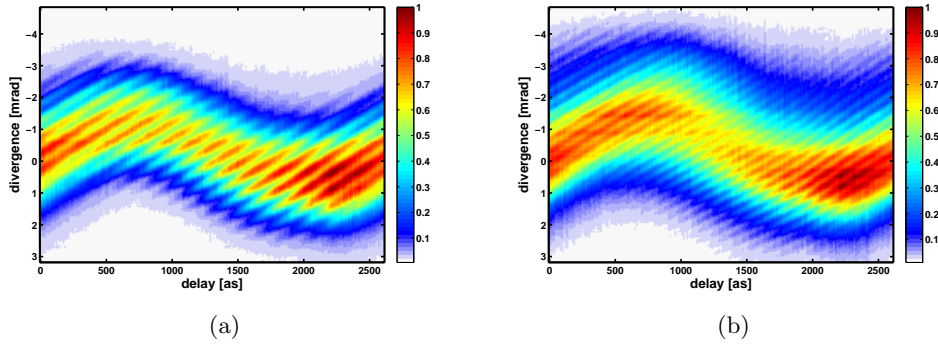


Figure 5.1: Fringe projection of harmonic 13 in panel (a) and harmonic 19 in panel (b) as a function of delay between the two slits.

120 rad as the delay is increased in increments of 12.5 as from 0 to 2620 as. For harmonic 13, we observe a change in phase of 80 radians over the measured delay range. Harmonic 9 gains a phase of 57 radian with an introduced delay of 2.62 fs or introduced phase of 2π . The standard error of our measurement is given with an average value of 20 to 30 mrad for harmonic orders 11 to 19. Harmonic 9 is suffering from a low signal strength and a resulting poor signal to noise ratio in the detector, which results in a standard error of 60 mrad in our measurement. The standard error is calculated by repeating the experiment multiple times to find the statistical mean and standard deviation for each individual harmonic phase. When we plot the measured phase of the

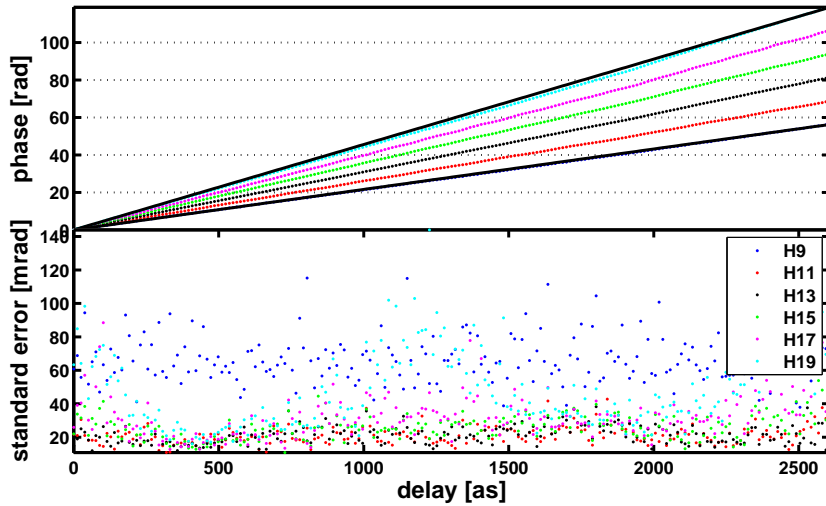


Figure 5.2: Top panel: Harmonic phase as a function of delay between two sources separated by $100 \mu m$. The black lines show the predicted behavior. Small differences are visible at delay between 1000 as and 1500 as. Bottom panel: The standard error of the extracted phase in mrad as a function of delay between the two sources.

harmonics in units of 2π in Figure 5.3 and as a function of delay between the two sources, we can see a difference in phase between 0 as and 2620 as to be an odd integer of 2π , where the integer number is the respective harmonic order. Harmonic 9 gains a phase of 9 times 2π , harmonic 13 gains a phase 13 times 2π . This can be expressed by an equation

$$\Delta\Phi_q = q \cdot \Delta\Phi \quad (5.3)$$

where the phase offset of the q -th harmonic is q -times the phase offset of the fundamental laser field, given by the electric fields in Equation 5.2. The electric field $\epsilon_q(t)$ of the q -th harmonic can be written as

$$\epsilon_q(t) = E_q e^{-a_q t^2} e^{i(q\omega t + \Phi_{field}(t) + \Phi_q)} \quad (5.4)$$

where E_q is the peak of the electric field, a_q is defined as $a_q = 2\ln(2)\frac{1}{\tau_q^2}$, where τ_q is the full width at half maximum of the harmonic pulse, $\Phi_{field}(t)$ is the total temporal phase, which can be written as

$$\Phi_{field,q}(t) = \Phi_{action,q}(E_1(t)) + \phi_{Laser,q}(t) \quad (5.5)$$

where $\Phi_{action,q}(E_0(t))$ will be investigated in the next chapter and $\phi_{Laser,q}(t)$ is given by $\phi_{Laser,q}(t) = qb_0 t^2$, where b_0 is the chirp of the fundamental laser pulse.

The standard error of the experimental measurement can also be expressed in units of time, where the calculated standard error in mrad is divided out by the period of the corresponding harmonic. The resulting error estimate in attoseconds is given in the bottom panel of Figure 5.3 and shows precision of < 1 as for all harmonics except harmonic 9, which shows a bigger error estimate due to poor signal strength. Our experiment is able to measure the scaling of

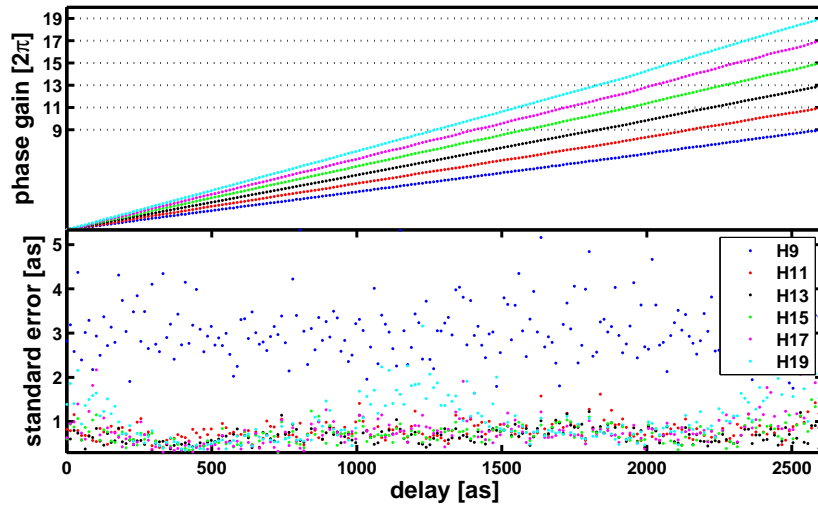


Figure 5.3: Top panel: Harmonic phase in units of 2π as a function of delay between two sources separated by $100 \mu m$. Bottom panel: Standard error of the extracted phase in attoseconds as a function of delay between the two sources. The standard error is below 1 as for harmonics 11 to 19.

harmonic phase with the phase/delay of the fundamental laser. We are measuring the scaling by delaying the fundamental in steps of 12.5 as with a measured precision of 1 as in time. We can also describe our observation in a time picture, following

$$\Delta_q k = q \cdot \omega \Delta \tau \quad (5.6)$$

where q is the order of the q -th harmonic with the fundamental frequency ω and $\Delta \tau$ describes the delay difference between the fundamental of each arm. When the fundamental electric field is delayed by $\Delta \tau$, the event of HHG is changed by the corresponding time. The emitted harmonic holds an imprint of the applied time delay given to the fundamental laser beam. A q -th harmonic will have q -times the oscillations in this introduced delay, giving rise to $\Delta_q k = q \cdot \omega \Delta \tau$.

Influences of the chromatic dispersion

In this section, we will discuss another observation in the presented experiment: We see an effect from the chromatic dispersion in the data, that is imprinted as a deviation from the calculated slope ϕ_{cal} . When we produce a slope ϕ_{cal} given by Equation 5.6, resulting in the solid black lines in Figure 5.2 for harmonic 9 and 19, a deviation from the expected behavior at delays between 1000 to 2000 as is visible, where the experimentally retrieved phase is smaller than the calculated phase $\phi_{cal}(1900 \text{ as})$. The deviation, described as $\Phi_{cal} - \Phi_{exp}$, is shown for all delays in the top panel of Figure 5.4. Comparing Figure 5.4 with the calculated chromatic dispersion in Figure 4.11, we can see identical behavior. A mask of $100 \mu\text{rad}$ and a checker board pattern of 10 pixel width was used to generate the two sources. With a voltage corresponding to a delay of 1900 as, an additional CE phase of 3 mrad is imprinted on the delayed pulse, which corresponds to 1.25 as in time. Both figures show an oscillatory behavior with small magnitude. When we divide out the specific harmonic order from the top panel of Figure 5.4 and plot the curves in the bottom panel, we get a spread for the difference between an expected CE-phase and the measured CE-phase that is below 3 as.

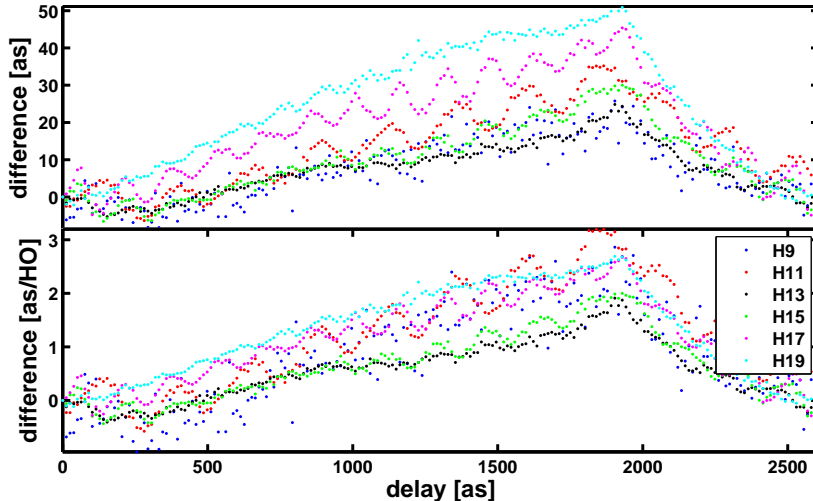


Figure 5.4: Top panel: Difference between the measured phase and the expected phase from the given delay in attoseconds. The error of the measured values is on the order of 1 as for harmonics 11 to 19. Bottom panel: When the harmonic order (HO) is divided out, all graphs lie on top of each other, which suggest a change of the fundamental laser.

5.3 Phase matching scaling

In Section 4.1.2, we introduced two different gas sources, which were used in this experimental study: a pulsed gas valve with a gas profile of roughly 5 mm full width (measured by an ion signal from a Channeltron) and a continuous flow glass capillary with an inner diameter of $200 \mu\text{m}$.

When we studied the phase dependence of high harmonics generated by the pulsed gas valve, we observed an abnormality in the delay dependence: When the relative position between laser focus and gas source is changed, the delay dependence changes. The results are shown in Figure 5.5, where we plot the phase of individual harmonics as a function of applied delay. For individual focus positions, we change the delay between the two laser foci and collect a delay dependent phase, as shown in the previous chapter. We move the focus from a position between the gas jet and the spectrometer (indicated with positive positions in Figure 5.5) to a position, where the gas jet would be between the focus and spectrometer (indicated with negative positions in

Figure 5.5) and collect, in increments of 1 mm, focus dependent phase measurements. For positions further away from the spectrometer the phase increases less with each step in added delay. This behavior was observed consistently for different SLM masks. On the bottom of Figure 5.5, the delay was introduced with a mask distributing the light with a checker board pattern and the slope for the 9th harmonic (left) and the 11th harmonic (right) change for different focus positions. This behavior is also observable for a SLM mask with alternating lines. The slope in the top panel of Figure 5.5 shows the same behavior as the bottom panel.

However, replacing the diffusive gas jet with a $200\ \mu\text{m}$ capillary, we did not observe this abnormality anymore. The gas profile is completely different and at the tip of the capillary, we get a very sharp density profile, that can still support two bright HHG sources separated by $200\ \mu\text{m}$ separation. When comparing the findings of a diffusive gas jet with the findings using a gas capillary in Figure 5.6, we get a completely focus independent change of phase, when using the $200\ \mu\text{m}$ capillary. In panels (a) and (b), we show the harmonic phase of harmonic 11 and 15 as a function of delay between the two driving laser fields. The harmonics are generated from a checker board pattern SLM mask and no change in phase between different focus positions is visible. The same is true for H17 and H23 in panels (c) and (d). However it should be noted that, when the focus was placed 1.5 mm after the jet, H23 did not yield a satisfactory signal to noise ratio in the fringe pattern and the phase was not plotted in the figure. Both experiments, given in Figure 5.5 and Figure 5.6 were taken back to back. The optical alignment did not change and only the gas source was replaced and optimized with a 3D-manipulator. For all experiments in section 5.3, we used the supersonic gas jet and changes from the predicted slopes are visible, when the laser is not placed in the center of the gas jet. We will discuss this change further in the following section.

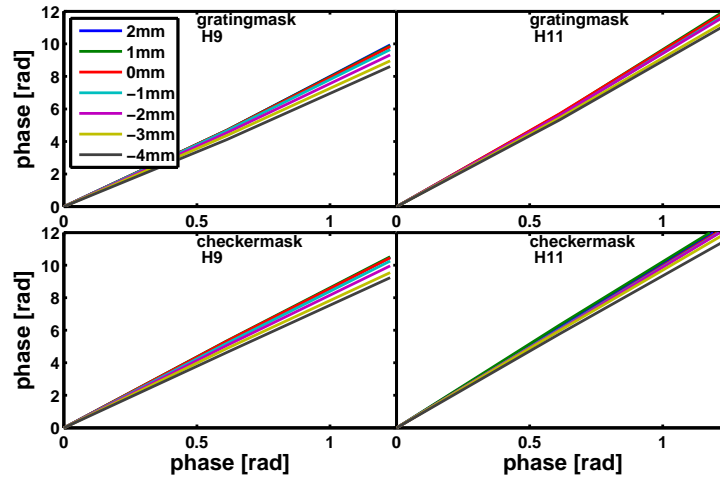


Figure 5.5: Phase of harmonic 9 and 11 as a function of phase between the two driving laser fields, Harmonics are generated from argon in a bell shaped pulsed valve. Top: SLM mask based on grating. Bottom: SLM mask based on checkers. As we change the focus from one side to the other side of the jet, the extracted phase changes its slope. A positive value in the legend is equal to a focus placed after the gas jet and a negative value for a focus placed before the gas jet.

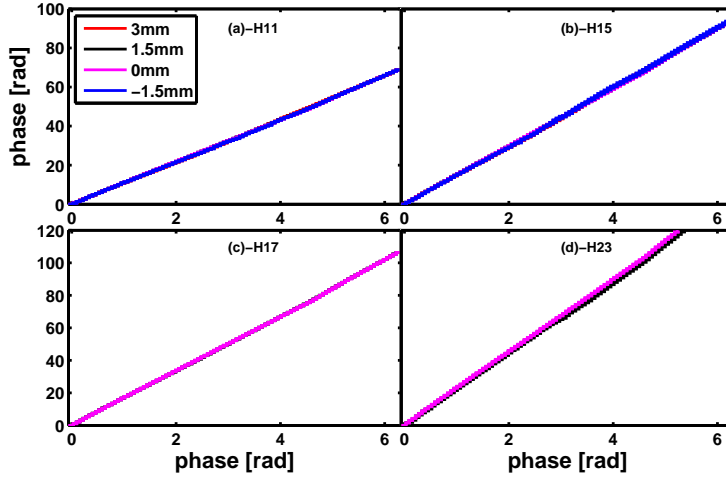


Figure 5.6: Phase of harmonics as a function of phase between the two driving laser fields. Harmonics are generated in argon from a $200 \mu\text{m}$ gas capillary. As we change the focus of the laser in respect to the gas, the slope of the harmonic phase does not change. Changes are within the given error bars. A positive value in the legend is equal to a focus placed after the gas jet and a negative value for a focus placed before the gas jet.

Study of phase matching behavior

In Figure 5.7a, we show the vertical profile of harmonic 11 produced from ethylene as a function of applied phase difference Δk between signal and reference. As we change the phase, the fringe observed on the detector is also changing the position of its minima and maxima. The focus of the lens is placed 7.5 mm before the gas jet and harmonics are generated at the center of the gas jet. Harmonics are then traveling towards the detector and interfere in the far field. We calculate a peak intensity of 125 TWcm^{-2} , with a pulse energy of $110 \mu\text{J}$, a pulse duration of 30 fs FWHM and a spot size of $60 \mu\text{m}$, $1/e^2$ Gaussian waist, with a lens of focal length $f=75 \text{ cm}$. We generate harmonics up to order 25 with an energy of up to 38.7 eV. In Figure 5.7b, we show the vertical profile of harmonic 15 as a function of delay, produced from ethylene gas at a peak intensity of 165 TWcm^{-2} , with a pulse energy of $150 \mu\text{J}$, a pulse duration of 30 fs FWHM and a spot size of $60 \mu\text{m}$, $1/e^2$ Gaussian waist. As we change the phase between signal and reference arm, the maxima are moving. We can see strong movement in the fringe pattern. Looking into the generated fringe pattern from harmonic 19 driven in argon gas in Figure 5.7c, we can see a bright on axis distribution with a divergence smaller than 2 mrad and a dim emission off axis with a divergence of 8 mrad. Both contributions show the same fringe spacing and slope as a function of delay.

When we now change the distance between the reference and signal arm from $120 \mu\text{m}$ to $180 \mu\text{m}$, the angle between maxima reduces linearly by a factor of 1.5, resulting in tighter fringe spacing as observed in Figure 5.7d, where nothing changed compared to Fig. 5.7c, but the fringe spacing, as previously shown in Section 4.3.

In Figure 5.8, we show the extracted phase between reference and signal arm for individual harmonics as a function of phase difference between reference and signal. The slopes follow Equation 5.6 for all harmonics. In Figure 5.9, the focus is moved to 7.5 mm away from the focus and the separation is set to $180 \mu\text{m}$. Harmonics from order 9 to 19 are not following the relation described in Eq. 5.6. We observe a smaller q -value in the experiment, when we look at the phase value at a delay of 2π .

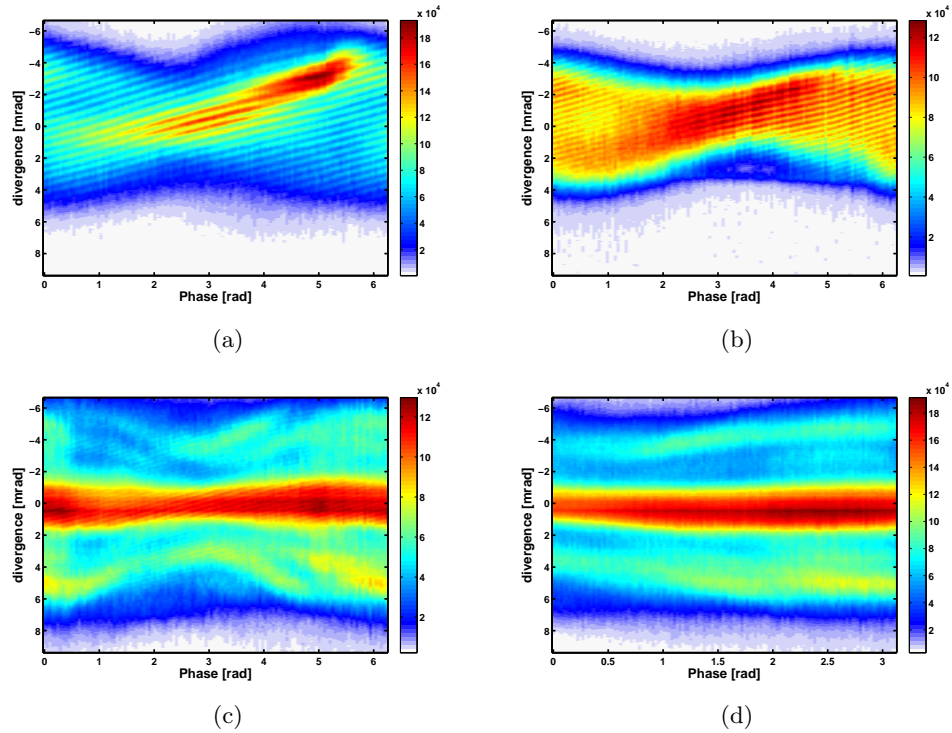


Figure 5.7: (a) Fringe projection of harmonic 11 in ethylene interfering with a reference source, separated by $120\mu m$. Over 2π we observe 11 maxima (b) fringe projection of harmonic 15 in ethylene interfering with a reference source, separated by $120\mu m$. We observe 15 oscillations over 2π (c) Fringe projection of harmonic 19 in argon interfering with a reference source, separated by $120\mu m$. The fringe projection shows 19 maxima over 2π and matches the spatial behavior of (for a phase of π to 2π): (d) fringe projection of harmonic 19 in argon interfering with a reference source, separated by $180\mu m$. The fringe projection has a reduced spacing, which is hard to discern by eye, the phase is measured from 0 to 2π

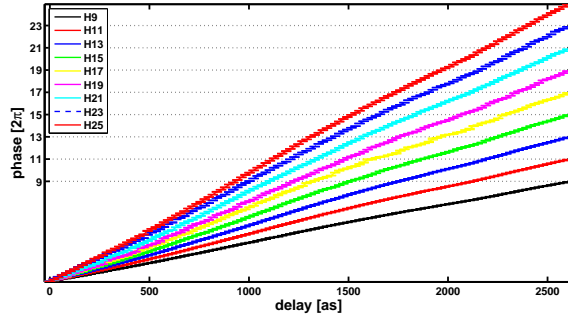


Figure 5.8: Phase of harmonic 9 to 25 in argon interfering with a reference source, separated by $120\mu\text{m}$ focused at 0 mm. The extracted phase follows $q \cdot \Delta\phi$.

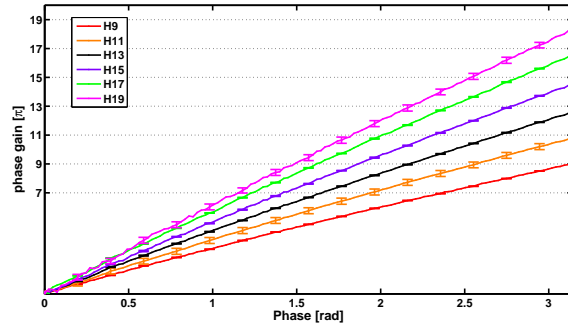
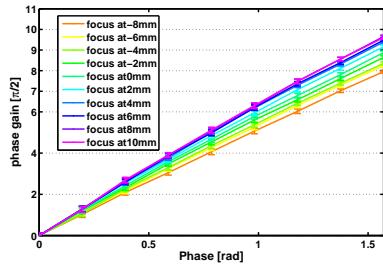


Figure 5.9: Phase of harmonic 9 to 21 in ethylene interfering with a reference source, separated by $180\mu\text{m}$ focused 7.5 mm before the gas jet

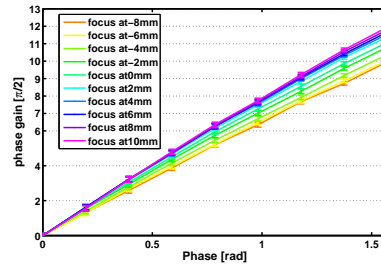
Investigating the focus-dependent behavior, we take a look at harmonic 9 to 13 from krypton, where the focus and phase relation were changed at the same time. The step in phase was set to $\pi/16$, so that for harmonics 15 and above the added phase value is expected to be $\gtrsim \pi$ and applied unwrapping processes are not able to construct the appropriate change of phase, but calculate a phase change smaller than π . For studies of harmonic order q , a step size of $< \pi/q$ is required to resolve the relation. In Figure 5.10a, we plot the phase of harmonic 9 as a function of delay for different focus positions relative to the gas jet. We observe a linear increase as a function of phase, but can see a change in slope for each focus dependent measurement. For a focus after the jet, the slope is smaller than when the focus is placed at the center of the jet. The slope of harmonic 9 is steeper with a focus placed before the gas jet. This behavior is also visible in Figure 5.10b, where we plot the phase of harmonic 11 as a function of delay for different focus positions and in Figure 5.10c, where we plot the same figure for harmonic 13 at the same focus positions.

This behavior is hard to disentangle. High harmonic generation is a phase-matched process. Only if the phases between fundamental and harmonics match, harmonics can be generated coherently. Otherwise the coherence length is too short compared to the absorption length. The coherence length is defined as $L_{coh} = \frac{1}{\Delta k}$, where Δk is the phase mismatch, and the absorption length is defined as $L_{abs} = \frac{1}{\sigma\rho}$, with σ the cross section for absorption and ρ the gas density [90]. Any phase mismatch due to the properties of the laser or the medium have to be accounted for. One of them being the focus dependent Gouy phase of a Gaussian laser beam, which might be the a cause for the observed deviation. We define a derivative q_{fit} out of Equation 5.6. For harmonic 9, we expect a derivative of $q_h = 9$, while for harmonic 13 we expect a derivative of $q_h = 13$. We define the difference $\Delta q = q_{fit} - q_h$ and produce a graph of the focus dependent behavior of Δq in Figure 5.11. The difference for all investigated harmonics has similar value. The change in

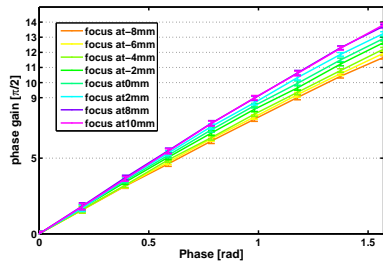
slope is not given by the harmonic emission, but has to be given by the fundamental laser field. If we plot the focus dependent Gouy phase for an expected rayleigh range of $z_R = 15\text{mm}$, given by our laser parameters, we see agreement with Δq , if we assume a difference of two times the gouy phase given by our laser parameters. If we assume a smaller Rayleigh range of $z_R = 7\text{mm}$ and shift its crossing through 0 by 2 mm, we get better agreement between the focus dependent Gouy phase and the experiment. Due to the increased interaction region with the pulsed valve, we are sensitive to the focus dependent phase mismatch. In the bell-shaped gas jet, the rayleigh range and gas density have a similar dimension and phase matching plays a more important role as when the bell-shaped gas jet is replaced by a few hundred μm thick gas jet produced by a capillary. Each harmonic has a different crossing through 0: harmonic 9 crosses 0 at a position of -3 mm, harmonic 11 crosses at a position of -4 mm, while harmonic 13 crosses at a position of -1 mm. This might be a hint to the optimal position of phase matching for the individual harmonics. However, since both sources have the exact same focusing geometry, both beams will have the same phase mismatch term stemming from the Gouy phase. The explanation of the Gouy phase may not be appropriate.



(a) 9th harmonic



(b) 11th harmonic



(c) 13th harmonic

Figure 5.10: Harmonic 9 to 13 in krypton interfering with a reference source, separated by $180\mu\text{m}$. The extracted phase follows $q \cdot \Delta\phi$, however, shows focus-dependent offsets in slope.

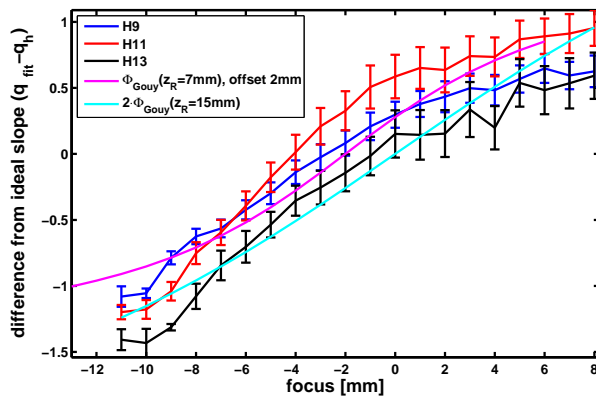


Figure 5.11: Slope of individual harmonics as a function of focus. The dependence is similar to a Gouy phase.

Chapter 6

Phase of the continuum electron wave packet

In this chapter, we investigate the intensity dependence on the harmonic phase of emitted harmonics. Citing [91], using a picture from Feynman's path integrals [92], the harmonic dipole of the q -th harmonic is given by

$$D_q = \sum_j A_j^q \exp[i\Phi_j^q(r_j(t', t, \vec{p}))] \quad (6.1)$$

with the path r_j defined by the quantum orbit j of an electron set free at time t' and recombining at time t . The phase given to the harmonic is then defined as

$$\Phi_j^q(r_j(t', t, \vec{p})) = q\omega t - \int_{t'}^t \left(\frac{(p - A(t''))^2}{2} + I_p \right) dt'' \quad (6.2)$$

where the integral is the classical action $S(t, t')$ of the electron in the electric field. The solution to the integral is explained through the Lewenstein model. Here we reduce our treatment from all possible orbits again to long and short trajectories that contribute to HHG the strongest.

6.1 Classical action in the saddle point approximation

In the Lewenstein model, the induced dipole moment is given by Equation 3.27, which contains an integral over momentum space. Over one optical cycle the strongest oscillation is given by the classical action of the electron. Therefore, the major contribution to the integral is given by stationary points of the classical action [21]. We can write this argument as

$$\nabla_p S(p, t, t') = 0 \quad (6.3)$$

which has the physical meaning of $\nabla_p S(p, t, t') = x(t) - x(t')$, where the electron born at time t' has to return to the same position x at time t . This statement is in harmony with our simple man's picture of the electron returning to the parent ion. Following through with the momentum integration in the saddle point approximation, where only certain trajectories return to the parent ion, the resulting dipole moment is

$$x(t) = i \int_0^\infty d\tau E \cos(t-\tau) d_x(p_{st}(t, \tau) - A_x(t)) d_x(p_{st}(t, \tau) - A_x(t-\tau)) \exp[-iS_{st}(p, \tau)] + c.c. \quad (6.4)$$

where τ is the return time $\tau = t - t'$. With this saddle point approximation, we get a stationary momentum

$$p_{st}(t, \tau) = E(\cos(t) - \cos(t - \tau)/\tau) \quad (6.5)$$

which allows the electron trajectory to return to the same position and the classical action becomes

$$S(t, \tau) = \int_{t-\tau}^t dt'' \left(\frac{[p_{st} - A(t'')]^2}{2} + I_p \right) = (I_p + U_p)\tau - 2U_p(1 - \cos(\tau))/\tau - U_p C(\tau) \cos(2t - \tau) \quad (6.6)$$

This way we acquire an analytical form of the classical action of the electron. When put into Equation 6.1, we get the phase of the harmonic dipole as

$$\Phi_j^q(t, \tau) = q\omega t - S(t, \tau) \quad (6.7)$$

$$= q\omega t - (I_p + U_p)\tau - 2U_p(1 - \cos(\tau))/\tau - U_p C(\tau) \cos(2t - \tau) \quad (6.8)$$

As we change the intensity of the fundamental field, the ponderomotive energy increases and besides an increase in the harmonic cutoff, we can observe a change in the phase of the harmonic dipole, following Equation 6.8. In Figure 6.1, we plot the classical action given by Equation 6.6 as a function of harmonic order and intensity, where the harmonic orders were calculated out of the solutions for ionization and recombination time by Equation 3.19 and 3.20. When we change the intensity of the laser field, the phase of the emitted harmonics will experience a phase change following $S' - S$, which can be expressed in a first order approximation as

$$\Delta\Phi(U_p, \tau) \approx \Delta U_p \tau + I_p \tau \quad (6.9)$$

where we omit the change in recombination time t , since the change due to classical action will be bigger than the change of recombination time. The second term of $I_p \tau$ is included in this approximation as we not only change the ponderomotive energy but potentially effect the excursion time τ as well. In Figure 6.2, we can see that for a higher ponderomotive energy, the excursion time of an electron associated with a fixed harmonic order is reduced. However, when we calculate the acquired phase due to the classical action, the effect due to an increase in ponderomotive energy has a bigger effect on the classical action than the effect of a shortened excursion time. We pick the intensity dependent classical action $-S_{19}(I)$ imprinted on harmonic

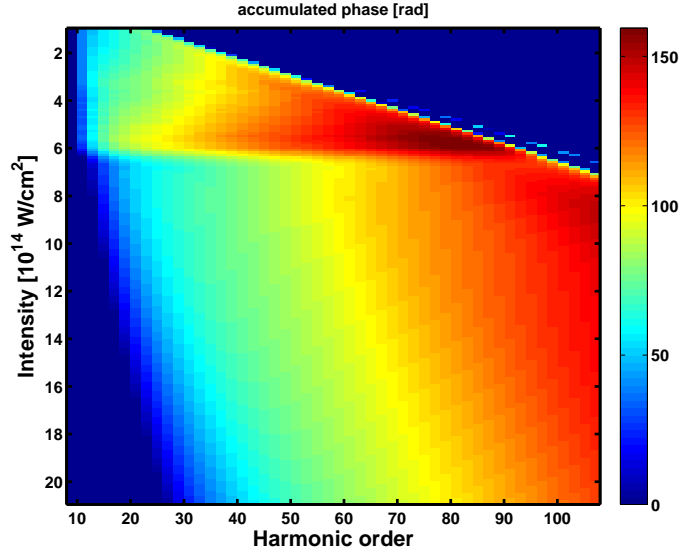


Figure 6.1: Phase due to the classical action in the electric field as a function of intensity and harmonic order, calculated with Equation 6.6

19 out of Figure 6.1 and show the intensity dependence in Figure 6.3. We see a linear increase in phase as the intensity increases. Until an intensity of $6 \times 10^{14} \text{W/cm}^2$, the acquired phase calculated by the Lewenstein model in Equation 6.6 increases linearly, especially when considering

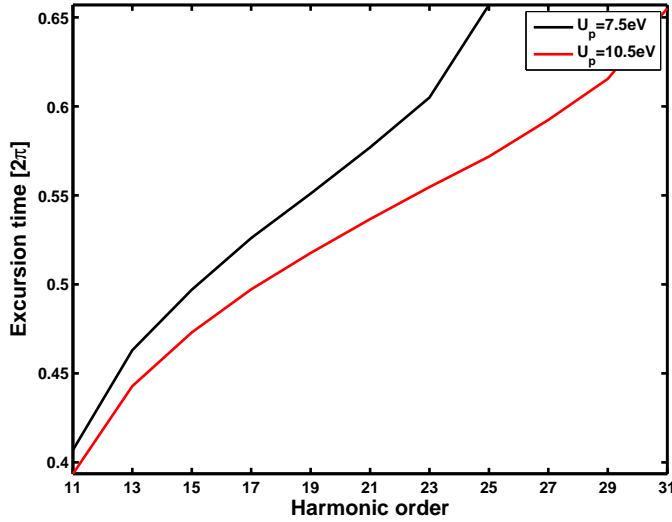


Figure 6.2: Excursion times of an electron in a laser field with different ponderomotive energies as a function of harmonic order. The ionization potential was set to the potential of argon (15.76 eV).

the leading terms as given through Equation 6.9, which gives rise to a change in phase of the q -th harmonic $\Delta\Phi_q$ in Equation 6.10

$$\Delta\Phi_q(\Delta I) = -\alpha_q \Delta I \quad (6.10)$$

with α_q depending on the involved trajectories. This nomenclature is used throughout the literature [93] and will be used to model the observed phase differences in the experiments and compare it to reported values. In a follow-up publication by Lewenstein in 1995 [94], focusing on the intensity dependent phase of high harmonics, Equation 6.10 can be readily seen, and we use a formula out of the Lewenstein model for a Gaussian model potential to plot the same result for different harmonics in Figure 6.4, where we extract the phase of given harmonics as a function of intensity. In this figure, we can see a linear slope for all harmonics with a α -coefficient of $\alpha = 11$. Compared to Figure 6.3, we can see a linear slope for low intensities that does not change its slope as a function of intensity. We can clearly see the effect of the total intensity on the harmonic phase. Harmonic 39 gains an additional phase linearly with the driving laser field's intensity up to $7 \times 10^{14} \text{W/cm}^2$, while for harmonic 19 the linear dependence ends at an intensity of $3 \times 10^{14} \text{W/cm}^2$. The discrepancies between the two figures 6.3 and 6.4 result from an incomplete treatment in each approach. While for Figure 6.3 we use classically calculated times of ionization and recombination for short trajectories, which will yield inaccuracies, we only use a single saddle point solution for Figure 6.4, which does not differentiate between long and short trajectories.

6.2 Phase of the wave packet in a single color field

In our experiment, the collinear interferometer allows us to change the relative intensity of the laser in the individual focus spots, as shown by spot size measurements in Section 4.2.1. Initially, both beams have the same intensity, according to an even distribution of pixels on the SLM. By changing this distribution through associating more SLM pixels to one of the two beams, we are able to tune the intensity of the individual sources. The total laser light incident on the SLM does not change and we do not have a reference source with constant intensity but still have a linear dependence on the difference in laser intensities between both foci. In Figure 6.5, we show calculations and measured intensities of the two beams at the laser focus. We define

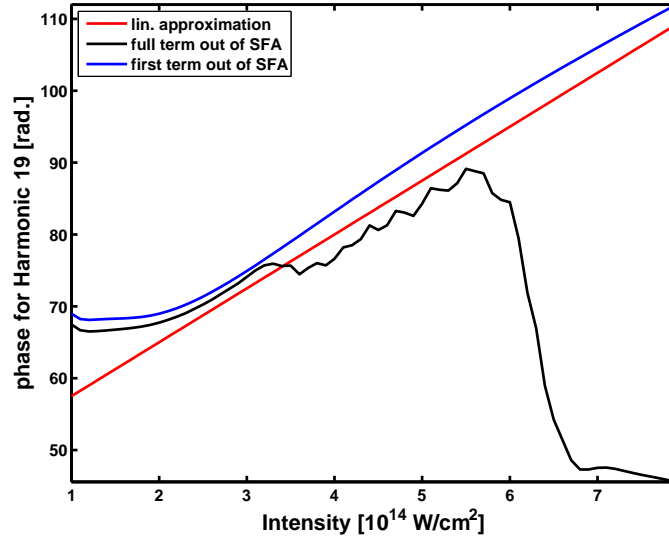


Figure 6.3: Phase due to the classical action in the electric field as a function of intensity for harmonic 19. Equation 6.6 is plotted in black and the leading term of the expression as given in Equation 6.9 is plotted in blue. We approximate the behavior with a linear equation depending on the intensity, given by Equation 6.10 and plot the function in red with a freely chosen offset.

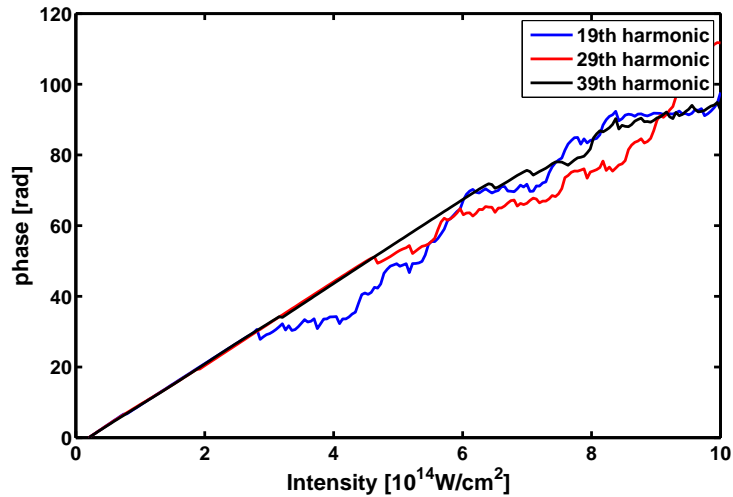


Figure 6.4: Phase of harmonic 19, 29 and 39 as a function of intensity of the driving laser field, calculated using the SFA model [21], with no distinction between long and short trajectory, resulting in $\Delta\Phi_q(\Delta I) = -10\Delta I$ for all harmonics

a distribution as an intensity manipulation of 0%, where both sources have the same amount of pixels. When we associate an extra 10% of the total amount of pixels with one of the two beams, the second beam will lose 10% of its associated pixel and we define this as an intensity manipulation of $\pm 10\%$. The calculated intensities for each source will follow accordingly. The error bar on the experimental value is an error estimate of 5% of the readout value of the CCD camera. In the experiment we get a difference in intensity $S_1 - S_2$, as given in Figure 6.5, that we use to study the intensity dependence of the electron wave packet in the continuum and extract the parameter α_q given in Equation 6.10. We collect the harmonic spectrum and phase

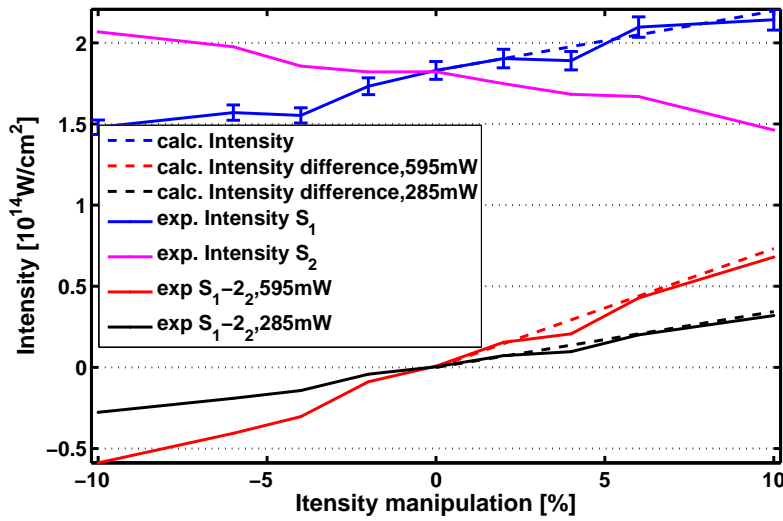


Figure 6.5: Intensity for S_1 and S_2 as a function of intensity manipulation on the SLM. The figure contains calculated variations and experimentally determined variations, which both result in an intensity difference between the sources.

at different peak intensities of the driving laser field as a function of intensity difference between the two foci. The total intensity is tuned by a half wave plate in front of a cube polarizer. The harmonic spectrum for different driving field intensities is shown in Figure 6.6. As we increase the intensity of the driving laser field, the cutoff increases, as expected by the cutoff law given in Equation 3.21. To measure the intensity dependent behavior of the harmonic dipole phase, we change the ratio of pixels associated with the two laser sources. In Figure 6.7a we show the collected interference pattern of harmonic 11 emitted from both sources in argon gas when we change the relative intensity between the two sources. As we change the relative brightness of the two sources, only minimal changes are observable by eye. This is explained by considering the fact that harmonic 11 is close to the threshold of argon (one photon above), and the electrons on these trajectories do not gain a significant amount of energy in the electric field, i.e. they do not gain a lot of phase. In Figure 6.7b we plot the intensity dependent interference pattern of harmonic 17, which shows a stronger behavior; the position of maxima in the fringe pattern shifts from left to right. Ultimately, as we change the relative brightness of the laser foci, we reduce the emission of harmonics from one of the two sources. This yields a reduced contrast in the fringes. For intensity differences of $6 \times 10^{14} \text{ W/cm}^2$, the fringe contrast is visibly reduced in Figure 6.7b.

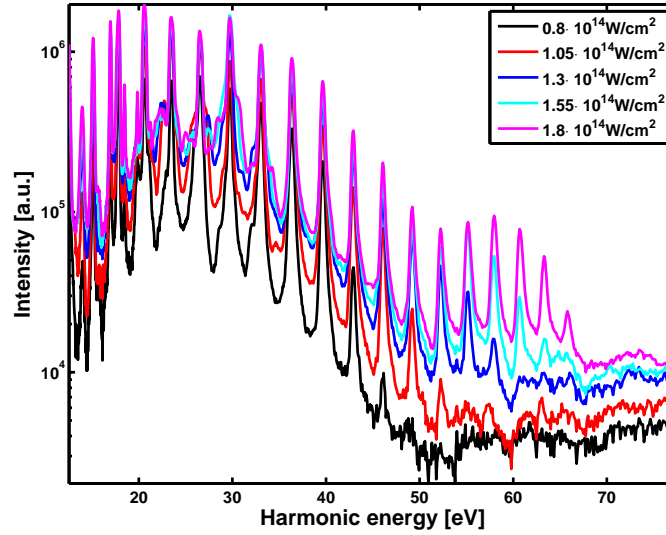


Figure 6.6: Harmonic spectra for different driving laser intensities. The cutoff in the spectra increases, as the intensity increases.

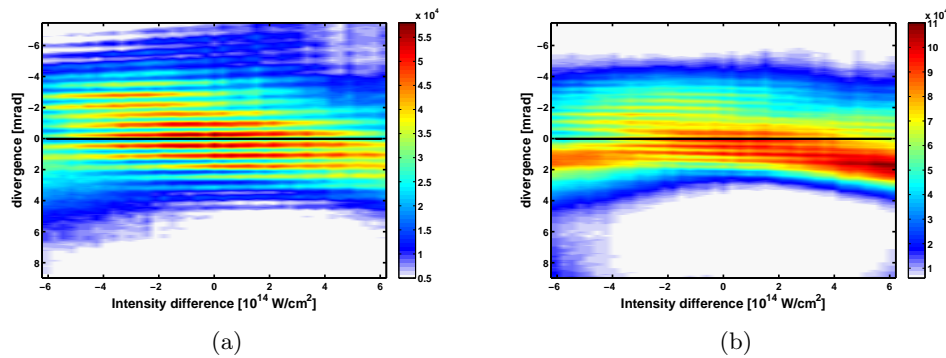


Figure 6.7: Fringe projection of harmonic 11 (a) and 17 (b) as a function of intensity difference between the two laser foci. Negative intensity differences indicates that source 2 is brighter than source 1, while positive differences indicate that source 1 is brighter. The black line is plotted to help the eye. No relative change to this line indicates no intensity dependent behavior.

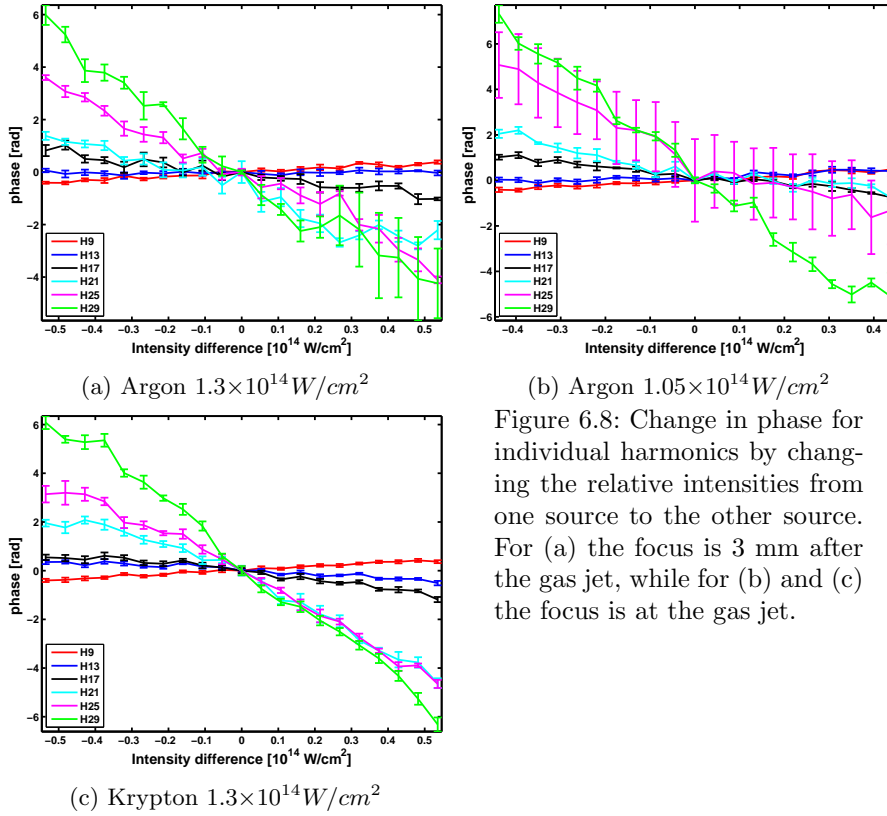


Figure 6.8: Change in phase for individual harmonics by changing the relative intensities from one source to the other. For (a) the focus is 3 mm after the gas jet, while for (b) and (c) the focus is at the gas jet.

In Figure 6.8a, we show a change in phase for selected harmonics as a function of intensity difference between the driving laser fields. The phase is relative to the phase extracted out of the fringe pattern at zero intensity difference. When both sources have the same amount of pixels, the intensity of each source was chosen to be $1.3 \times 10^{14} W/cm^2$ and the laser was placed 3 mm after the center of the gas jet. For harmonic 13, we do not observe a change in phase as a function of intensity difference, while for harmonic 21 the phase changes by 4 rad and the phase of harmonic 29 changes by 10 rad. Increased error bars for Harmonic 29 in Figure 6.8a show the issue of reduced fringe contrast. The experimental findings indicate a harmonic order dependent behavior: As we increase in harmonic order from H13 to H29 the absolute phase gain becomes steeper with increases in intensity.

Following the argument of excursion time, we expect the same behavior. When the electron is in the electric field for longer times and gains more kinetic energy, it will also acquire more phase. With our spectrometer, we are also able to collect below-threshold harmonics. Harmonic 9 shows opposite behavior compared to all other harmonics. Here the harmonic would reduce its acquired phase as we increase the electric field strength. In the three step model, we cannot explain this behavior. For a weaker field in Figure 6.8b, where the maximum difference in intensities is only $40 TW/cm^2$, compared to $60 TW/cm^2$, and the gas jet is placed directly in the focus we see similar behavior. Harmonic 9 shows opposite behavior to the plateau harmonics and as we increase the harmonic order, the gain in phase becomes bigger: for harmonic 21 we see a change in phase of 2 rad, applying an intensity difference of $-40 TW/cm^2$, and for harmonic 29 we see a phase difference of 6.5 rad in Figure 6.8b. With krypton gas in Figure 6.8c, where we also plot the change in phase of individual harmonics as a function of intensity difference, we can see similar magnitudes for harmonic 21 and 29, compared to argon gas. However, the phase of harmonic 13 is not flat as a function of intensity difference any more. It has the same negative slope as higher order harmonics. For all harmonics, we can generate a two dimensional picture in Figure 6.9, where the gradual change is more visible.

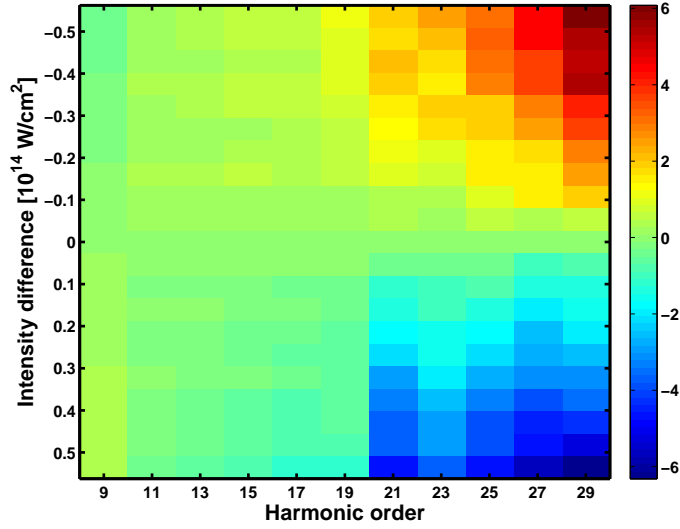


Figure 6.9: Change in phase for individual harmonics generated in krypton gas, by changing the relative intensities between the two sources. The figure shows the same data as 6.8c. The laser is placed at the center of the gas jet and the intensity is adjusted to be $1.3 \times 10^{14} \text{ W/cm}^2$. The phase is given in the color scale.

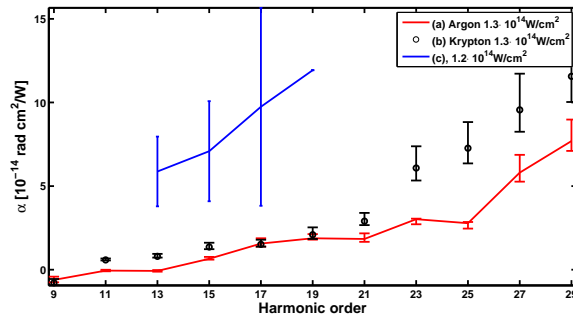


Figure 6.10: α -coefficients as a function of harmonic order for a laser field with peak intensities of $1.2\text{-}1.3 \times 10^{14} \text{ W/cm}^2$. Laser is placed at the center of the gas jet.

For every harmonic order, we collected the intensity dependent phase and performed a fit to Equation 6.10 using linear regression. The coefficients α_q are extracted and the error is estimated out of the residual of the linear regression and the uncertainty of the laser intensity, where we add a relative error of $-16\%/+20\%$. We plot the coefficients as a function of harmonic order for krypton and argon in Figure 6.10. The laser is placed at the center of the gas jet and the laser intensity was set to $1.3 \times 10^{14} \text{ W/cm}^2$. As a reference, we show the coefficients out of reference [95] for short trajectories of harmonic 13 to 19 in argon. No error bar for harmonic 19 was given. The α -coefficients for the short trajectories measured for argon and krypton in our experiment are close to 1 for harmonics 13 through 19. As the harmonic order increases, the α -coefficient increases as well. There is a discrepancy between Kr and Ar in the cutoff of the spectrum. However, when moving the focus of the laser by 3 mm, we extract similar α -coefficients for Kr and Ar in the cutoff. In Figure 6.11, we plot the α -coefficients for harmonics of argon and krypton. Increasing the intensity from panel (a) through (c), we can see an overall decrease of the α -coefficients of all harmonic orders. A small deviation for the α -coefficients of harmonics 15 and 17 is visible in Figures 6.11a and 6.11b.

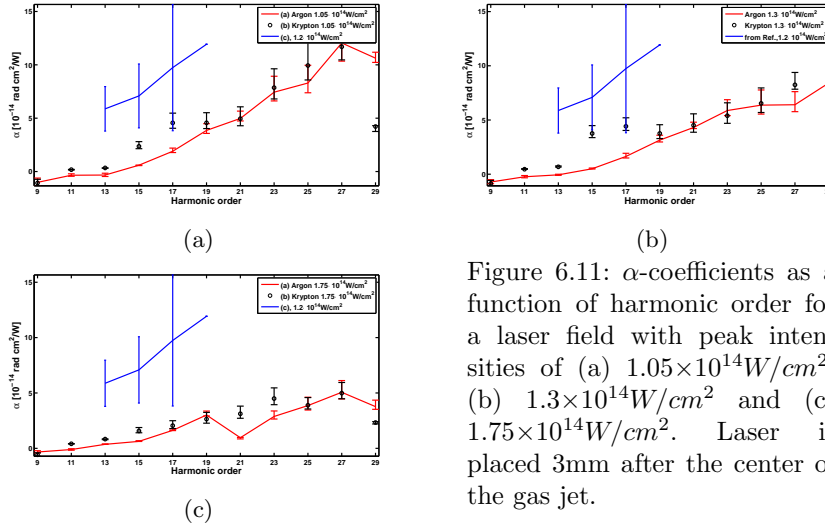


Figure 6.11: α -coefficients as a function of harmonic order for a laser field with peak intensities of (a) $1.05 \times 10^{14} \text{W/cm}^2$, (b) $1.3 \times 10^{14} \text{W/cm}^2$ and (c) $1.75 \times 10^{14} \text{W/cm}^2$. Laser is placed 3mm after the center of the gas jet.

As a function of harmonic order and intensity, we can see a change in the magnitude of the α -coefficient. As we increase the driving laser's intensity from 0.8 in panel (a) up to $1.75 \times 10^{14} \text{TW/cm}^2$ in panel (c), the cutoff region moves to higher harmonic orders, as seen in Figure 6.6. The trajectories to generate harmonics below the cutoff change and, with this, the excursion times for given harmonics. This will result in a difference in phase. This behavior is apparent for panels (a) through (c) in Figure 6.11. As the intensity increases, the extracted α -coefficients reduce. For selected harmonics, we plot the extracted α -coefficients as a function of intensity in Figure 6.12. For low intensities, the coefficient for H21 is on the order of 5, while with increased intensity the generation of this harmonic is done in the plateau and the coefficient reduces to 2. Harmonic 17 and 19 have the same trend, where the gain in phase changes its proportionality to the intensity of the driving laser field. At low intensities, the coefficients are equal to 3-4, while at the highest recorded intensity, the coefficients reach the same value as observed for harmonic 19. For Harmonic 15, we do not observe a change in proportionality over the measured intensity range, since the harmonic is in the plateau region at all intensities and has a coefficient equal to $\alpha = 1$. Harmonic order 11, however, shows an opposite sign in its coefficient that reaches a value of 0 when we increase the driving laser intensity.

The observations can be expanded to all harmonic orders: For argon in Figure 6.13a, we plot the intensity dependent α -coefficient for the given harmonics. We can observe an overall shift of harmonics with a high α -coefficient as a function of intensity. As we increase the intensity of the driving laser field, the α -coefficients decrease. This can be explained with the associated electron trajectories. With a high peak intensity, cutoff trajectories produce higher order harmonics and harmonics previously generated by cutoff trajectories are now generated by electron trajectories that spent less time in the electric field. In krypton in Figure 6.13b, we can observe the same trends: the cutoff moves from H21 at the lowest intensity to H29 at the highest intensity, and the α -coefficient reduces as we increase the laser intensity.

While investigating the behavior in the cutoff, another interesting region is the threshold area. For argon, we expect harmonic 9 and 11 to be below the threshold with an ionization potential of 15.76 eV, while krypton has an ionization potential of 14.0 eV, resulting in harmonic 11 being an above-threshold harmonic. This fact is mirrored in the extracted α -coefficients. While the behavior changes for argon with harmonic 13, in krypton we can see the change happening in harmonic 11, where we do not observe an opposite slope compared to plateau harmonics anymore.

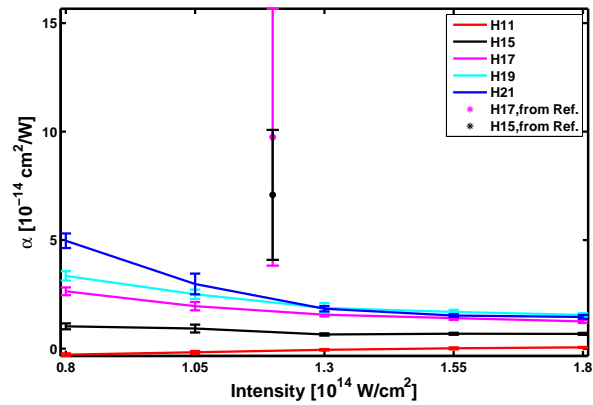


Figure 6.12: α -coefficients as a function of intensity in argon for harmonics 11,15,17,19 and 21.

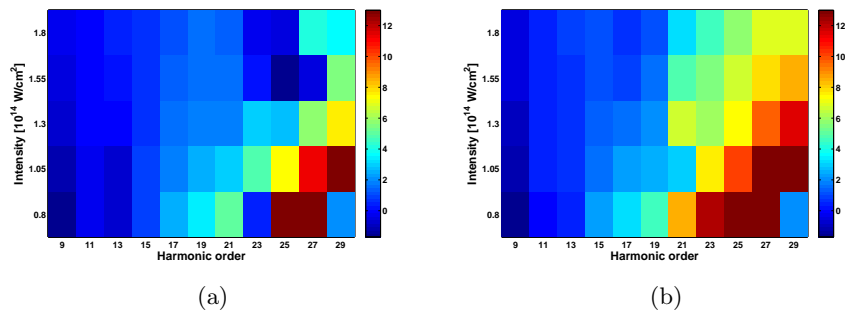


Figure 6.13: α -coefficients for measured intensities and harmonic orders for argon (a) and krypton(b). The α -coefficients are given on the color axis.

6.2.1 Comparison to literature

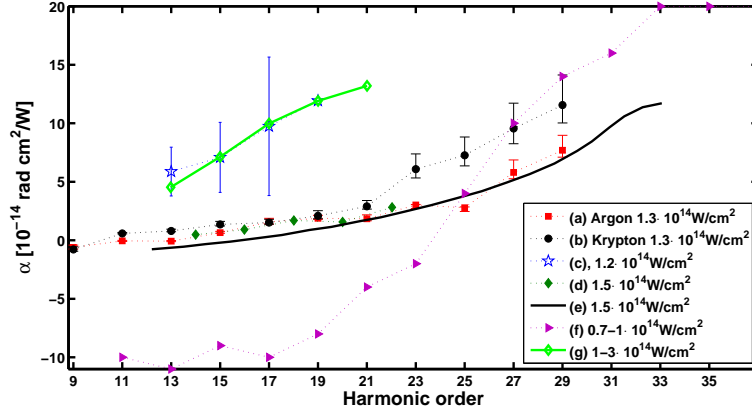


Figure 6.14: Extracted α coefficient as a function of harmonic order. (a)-(b) are from measurements in this thesis. (c) is done by [95] based on a Michelson interferometer, (d) is based on an XFROG measurement done by [91] and [96]. (e) is a SFA calculation from [91], (f) is based on an interference pattern in HHG from chirped driving fields by [97] and (g) is an extraction of the intensity dependent yield of high harmonics by [98]. All referenced measurements were performed in argon gas.

In Figure 6.14, we show our experimental results in argon and krypton with driving laser intensities of $1.3 \times 10^{14} \text{TW}/\text{cm}^2$, given by (a) and (b) in the legend of the figure. Our measured α -coefficients have an error estimate based on the residual out of the linear regression and the uncertainty of the intensity calculation. We associate an error of 20% with our given intensity estimate, which will result in a relative error on the α -coefficient of $-16\%/+20\%$ through the intensity and an additional error estimated by the linear regression. Our experimental results agree well with given SFA calculations from [91] given by (e) and experimentally retrieved values from this reference, given by outline (d) in Figure 6.14. The other referenced results [95, 97, 98] show deviations from our shown results. In an interferometric study [95], using the same approach as our experiment, with results plotted by (c) in Figure 6.14, the intensity of two independent Michelson interferometer arms was changed so that the harmonic sources generated by each arm had differing intensity from each other. As the intensity of one arm was increased, the phase of the generated harmonic was changed and the interference fringes moved accordingly. Using the relative position of fringes from short and long trajectories on the detector plane, an intensity dependent phase difference between trajectories was measured for krypton and argon. However, a measurement of the separate phase change of short or long trajectories was unfeasible, due to interferometer instabilities. Our experiment is more stable and can measure the components directly, resulting in smaller error bars.

Other experiments have shown the intensity dependent behavior for long trajectories [95, 99, 100] and have shown the difference between long and short [101]. Theoretical calculations on this topic were performed by [93], [94] and [79]. For the given intensity range shown in Figure 6.14, the expected intensity dependent wave packet in the continuum is well described with SFA theory given by Lewenstein. Experimentally we observe a strong trajectory dependent phase in the harmonic emission, where low order harmonics are influenced less by the external laser field and cutoff harmonics are strongly influenced by the driving laser field. The second observation in this chapter is the dependence of the harmonic phase as a function of the overall intensity magnitude of the driving laser field. In Figures 6.3 and 6.4, based on theoretical calculations, the change in phase as a function of driving laser field has a constant derivative for intensities of 2 to $7 \times 10^{14} \text{W}/\text{cm}^2$. The calculations, done for Figure 6.3, are based on the classical motion of the electron and deviate from the calculations based on the SFA in the low intensity regime. Our model does not account

for multiple saddle point solutions of the SFA and estimates an α -coefficient of $\alpha \approx 10$ across all intensities. However, our experimental findings do not agree with this statement. As the driving laser intensity increases, the phase is less influenced by smaller changes in the intensity and the reconstructed α -values decrease as a function of intensity. According to Figures 6.13a and 6.13b for low order harmonics, we can observe a very flat behavior as a function of intensity, as the harmonics cannot be explained by the three-step model. These harmonics are not generated by a freed electron gaining kinetic energy in the continuum. This feature was also previously measured in Reference [102], where the α -coefficient for the 5th harmonic was measured to be $0.5\text{-}0.6 \times 10^{-14} \text{cm}^2 \text{rad}/W$ for an intensity of $6 \times 10^{13} W/cm^2$. A second influence on the phase of the harmonics imprinted by the classical action of the electron is the ionization potential of the target. We see small differences between krypton and argon, most pronounced in the threshold region where the ionization potential difference between argon and krypton shifts the threshold from the 11th harmonic to the 13th harmonic. In previous publications, a destructive interference due to phases in mixed gases of helium and neon was observed in [103], where the phase difference then is proportional to $\Delta\Phi \approx \tau\Delta I_p$ and shows the difference in α -coefficients, due to the difference in ionization potential that is present in the classical term of Equation 6.6.

6.3 Phase of the wave packet in a saturated medium

In previous experiments, the study of the intensity dependence on phases of harmonics was done in intensity regimes with low intensities. Only a few of the previously listed references analyzed the intensity dependence on the harmonic phase with intensities above $2 \times 10^{14} W/cm^2$. In this section, I will discuss the phase dependence of high harmonics, when driven with laser fields with intensities reaching $7 \times 10^{14} W/cm^2$. The study was performed on argon. As the intensity reaches values greater than $2.5 \times 10^{14} W/cm^2$ [104], ionization rates are strong and the target is getting depleted, meaning our first approximation of an un-depleted ground state $|0\rangle$ is no longer valid. We can ultimately create a dense plasma that affects the absorption and phase matching of HHG through the medium. We do not investigate the intensity-dependent yield of high harmonics, but only focus on the intensity-dependent phase. We observe a decreased overall yield in the experiment at high intensities, but no drop to zero, as harmonics can be generated in a bigger volume at the wings of the focal volume. Calculating the classical action of the electron in Figure 6.3 for harmonic 19, we expect a linear slope in the phase of the harmonic at these high intensities. Experimentally, we start with two equally intense laser foci with a peak intensity of $3.8 \times 10^{14} W/cm^2$ and gradually change one source to an intensity of $0.8 \times 10^{14} W/cm^2$ and the other source to $6.8 \times 10^{14} W/cm^2$. This results in an intensity difference of $6 \times 10^{14} W/cm^2$.

We record the interference pattern of the two sources on the detector. In Figure 6.15, where we plot the interference pattern of harmonic 9 as a function of intensity difference between the two foci, we can observe a changing fringe pattern, moving its maxima to more negative divergence values, when we increase the intensity difference from zero to $6 \times 10^{14} W/cm^2$. At intensity differences of $> |4 \times 10^{14} W/cm^2|$, the yield on axis with a divergence angle of -1 mrad is reduced. The intensities are so high that absorption and phase matching are affecting the harmonic yield. Expanding the analysis onto all harmonic orders, we extract the phase of all harmonics out of intensity dependent interference pattern. We plot the phase of individual harmonics as a function of intensity difference in Figure 6.16 for a driving laser intensity of $3 \times 10^{14} W/cm^2$ and the phase of individual harmonics for an intensity $3.8 \times 10^{14} W/cm^2$ in Figure 6.17. We see phase changes of 2 rad over the given intensity difference of $6 \times 10^{14} W/cm^2$ for harmonic orders 9 to 17, while for higher order harmonics the measured phases now change as a function of intensity difference from a minimum of -12 rad to a maximum of +9 rad, resulting in an overall phase change for harmonic 27 of 20 rad, while in the case of a low intensity driving laser field with a peak intensity of $1.3 \times 10^{14} W/cm^2$ in Figure 6.13a, we saw a phase change of 12 rad.

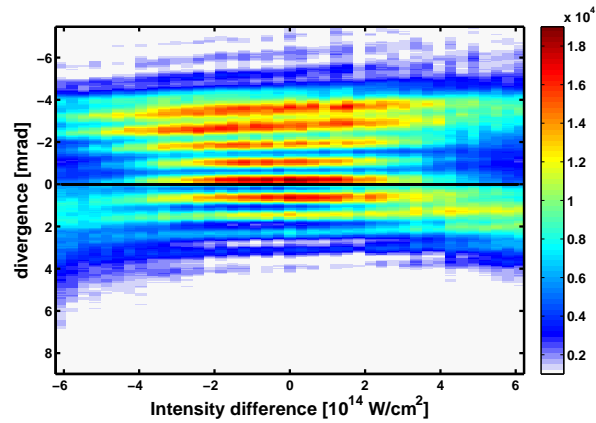


Figure 6.15: Fringe position depicted by divergence on the detector of harmonic 9 from Ar as a function of intensity difference between the two sources. The total intensity is $7.6 \times 10^{14} W/cm^2$

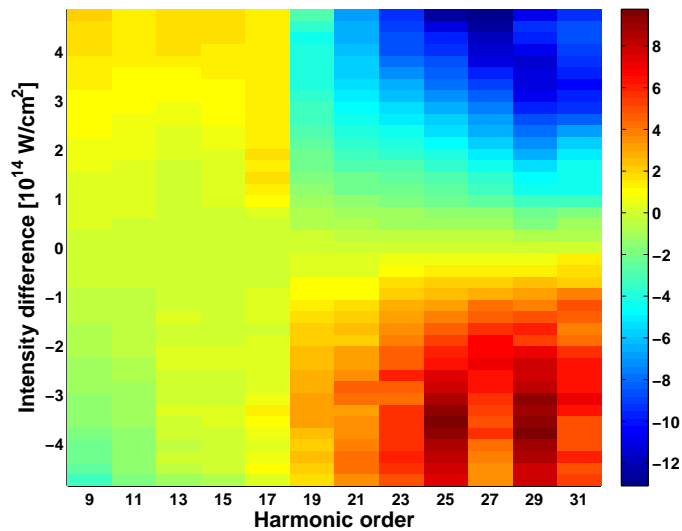


Figure 6.16: Phase difference between the two sources as a function of harmonic order and intensity difference, with a driving laser intensity of $3.0 \times 10^{14} W/cm^2$. Compared to lower intensity ranges, the harmonics from 9 to 17 show a flat or negative behavior as a function of intensity.

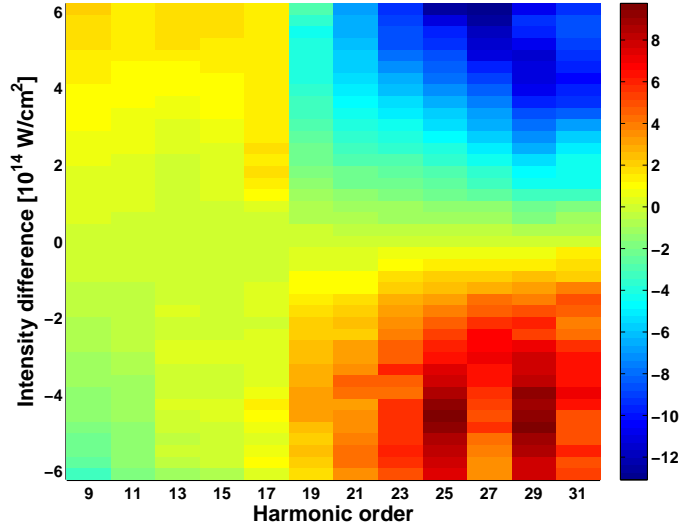


Figure 6.17: Phase difference between the two sources as a function of harmonic order and intensity difference, driven in a saturated medium for an intensity of $3.8 \times 10^{14} \text{ W/cm}^2$. Compared to lower intensity ranges, the harmonics from 9 to 17 show a flat or negative behavior as a function of intensity. Increasing the intensity by 30% overall yields a more extreme behavior for the low order harmonics, compared to Figure 6.16.

As the intensity reaches high values, the excursion time of electrons, producing harmonics 9 to 29, is reduced. The electrons recombining to these energies spend minimal time in the electric field, especially when considering low order harmonics. At such intensities the ionization potentials are field-dressed and can be shifted by the ponderomotive energy [105]. Ponderomotive shifts are observed in above threshold ionization [27]. Harmonics above the ionization potential are now below threshold harmonics and cannot be described with our typical three step model. This is explicitly seen in Figure 6.18, where harmonics 9 to 15 have opposite behavior to harmonic 19 and all previously reported harmonics generated from a weaker field in Section 6.2. These harmonics acquire an opposite phase as the laser field strength increases.

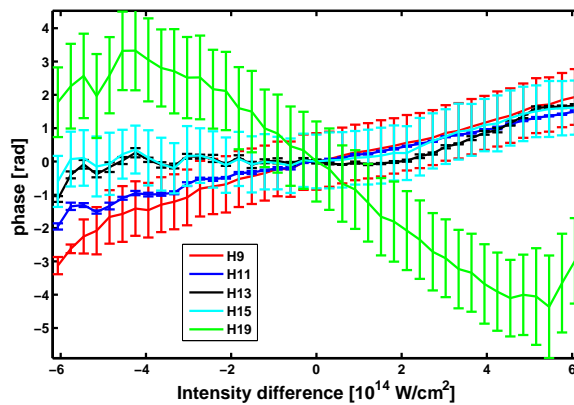


Figure 6.18: Phase difference for individual harmonics as a function of intensity difference. Harmonics 9 to 15 show an opposite behavior as a function of intensity, compared to the behavior of harmonic 19. At large intensity difference values, the measurements are compromised by vanishing fringe contrast on the detector.

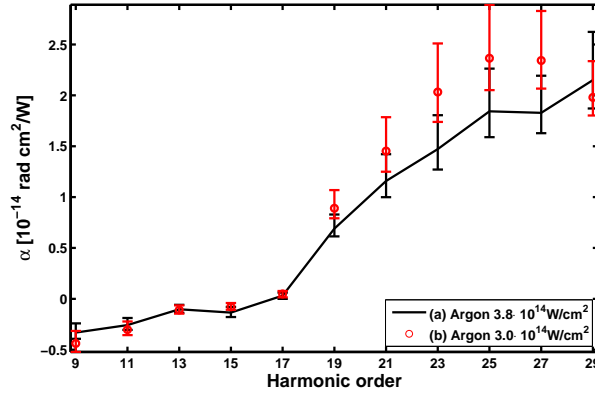


Figure 6.19: α -coefficients for harmonics driven by intense laser sources. Panel (a) and (b) are very close in the overall behavior. Harmonic orders 9 to 17 have a negative α -coefficient, while harmonics 19 to 29 have a small coefficient, compared to previous results in weak driving laser fields.

We calculate the α -parameter for the measured harmonic orders by using Equation 6.10 and use a linear regression. In Figure 6.19, we show the results of the linear regression for individual harmonics. In the figure we can see coefficients $\alpha < 5$ for all harmonic orders and negative coefficients for harmonics below order 17, where the new threshold is shifted to (H17=26.85 eV). This is a shift by 11 eV. The ponderomotive energy of the field is 23 eV at an intensity of $4 \times 10^{14} W/cm^2$. Comparing the two measurements with two different input pulse energies, we can compare a fixed source of intensity $1.5 \times 10^{14} W/cm^2$ with a source at $4.5 \times 10^{14} W/cm^2$ and a second source at $6.0 \times 10^{14} W/cm^2$, where we measure a phase difference for H25 of 8.5 rad and 9.7 rad respectively. This will result in α -coefficients of 2.8 and 2.15. As seen in the previous section, the coefficients decrease as a function of intensity in low intensity regions as well, when driven with intensities at 4.5 and $6 \times 10^{14} W/cm^2$.

6.4 Phase of the wave packet in a two color field

In this section we report the intensity dependence of the harmonic phase in a two color field with the experimental setup given in Figure 6.20. The 2nd harmonic is generated collinearly and the delay between 785 and 392 nm light is compensated by Calcite. An additional wave plate rotates the 785 nm light to make the fundamental and the second harmonic s-polarized. The resulting spectrum is given in Figure 6.21. All reported harmonics are reported as harmonics of the 785 nm light. Even and odd harmonics are generated, as discussed in Section 4.2.2. The magnitude of even harmonics is approximately half of the magnitude of neighboring odd harmonics. As we increase the driving laser field, the cutoff increases. We compensate for chirp in the fundamental and have a transform limited 785 nm pulse in the interaction region. We estimate the 392 nm pulse to be 50 fs in time, while the 785 nm is measured to be 30 fs FWHM.

Due to the fact that the 785 nm is chirped at the generation of the 2nd harmonic, our efficiency is reduced to 10-15% and the resulting field strength of 392 nm is at a total of 3.7% of the total field, estimated by the spot sizes given in Figure 6.22c, where the second harmonic component is focused in three peaks. Two of the foci overlap with the fundamental and the third peak is a summation peak of components tilted in opposite directions. The middle peak is the strongest, but does not influence the more intense 785 nm laser foci. Taking the ratio of these peaks we estimate that 3.7% of the total light is deposited in the second harmonic, overlapping with the fundamental. In a two-dimensional picture, where we project the focus in one dimension as a function of lens position, relative to a CCD-camera, we can observe the overall behavior of the fundamental in Figure 6.22a and the overall behavior of the second harmonic in Figure 6.22b,

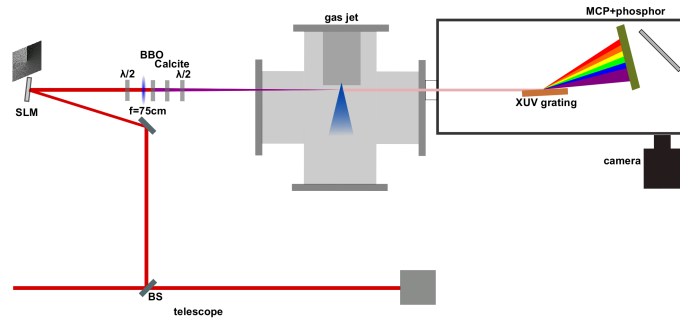


Figure 6.20: Experimental setup with a nonlinear crystal generating the second harmonic of 785 nm. A SLM shapes the red spectral components and the second harmonic is generated from the spatially shaped fundamental. Calcite matches the difference in time.

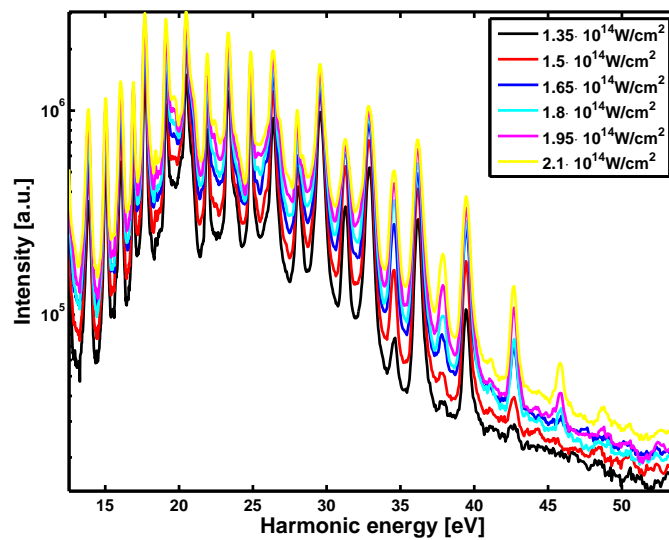


Figure 6.21: Harmonic spectrum generated from a two-color field for different driving laser intensities, where the intensities are calculated with a weak second harmonic component of 3.7 %. Generated in argon.

where most of the second harmonic does not spatially overlap with the fundamental. The total peak intensity is calculated with $I_{total} = I_{785} + I_{392} + 2\sqrt{I_{785}I_{392}}$.

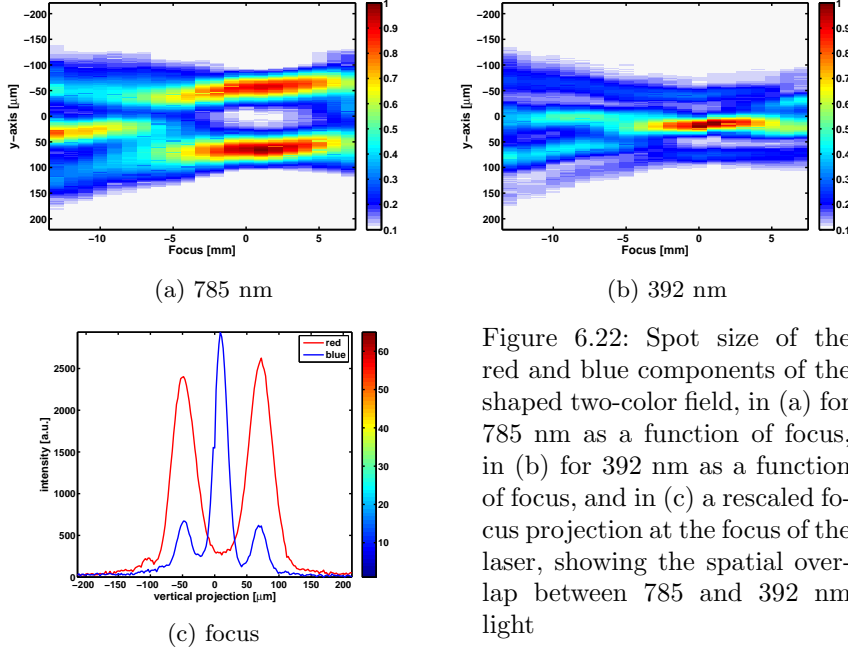


Figure 6.22: Spot size of the red and blue components of the shaped two-color field, in (a) for 785 nm as a function of focus, in (b) for 392 nm as a function of focus, and in (c) a rescaled focus projection at the focus of the laser, showing the spatial overlap between 785 and 392 nm light

6.4.1 Classical action in the saddle point approximation and two color field

When considering a perturbation to the fundamental laser field by introducing a weak second harmonic field [84], the classical action changes depending on the vector potential of the second field.

$$S_2(t_r, \phi) = S_1(t_r) - \sigma(t_r, \phi) = S_1(t_r) - \int_{t'}^{t_r} d\tau \vec{v}_{SFA}(\tau, t') \vec{A}_2(\tau, \phi) \quad (6.11)$$

In the given equation S_1 is the unperturbed action, S_2 the perturbed action, t' the time of ionization and t_r the time of recombination. σ is the additional phase induced by the second field, where $\vec{v}_{SFA}(\tau, t_r)$ is the velocity of the unperturbed trajectory and $\vec{A}_2(\tau, \phi)$ the vector potential of the second field. In the experiments in Section 6.4, the second harmonic stays in the perturbation regime, and when we alter the intensity of one beam, we will also see an altered intensity of the second harmonic in the focus of the beam. We assume a linear change in intensity of the second harmonic, when we change the intensity of the fundamental linearly. Furthermore, we assume a vanishing difference in the integral $\int_{t'}^{t_r} d\tau \vec{v}_{SFA}(\tau, t') \vec{A}_2(\tau, \phi)$ when the intensity is altered. The dominating part of the harmonic phase is given by the much stronger electric field of the fundamental. As we only change the intensity and do not alter the delay between the fundamental and the second harmonic, we extract a α -coefficient based on Equation 6.10 in the given two-color field with an intensity of $I_{total} = I_{785} + I_{392} + 2\sqrt{I_{785}I_{392}}$.

6.4.2 Experimental measurements

When we generate harmonics by our synthesized two-color field, we record a detector image as shown in Figure 6.23. We see fringes in both even and odd harmonics. The spectrum is dominated by short trajectories on axis with a divergence of -2 to 0 mrad. We can see very faint distributions from long trajectories at bigger divergence angles from -6 to 4 mrad. Out of the given detector image, we select single harmonics and perform a fast Fourier transformation on the fringe pattern. As discussed in the previous section and the first introduction in Section 4.3, we can extract the phase of the fringe frequency and associate the phase with the phase value

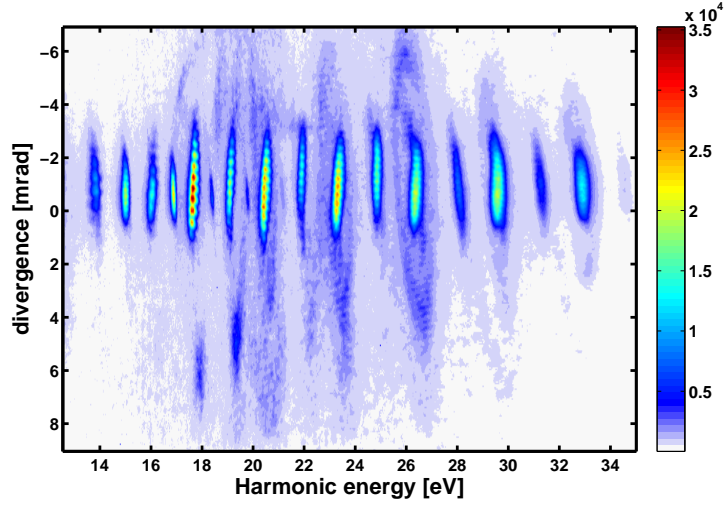


Figure 6.23: Two dimensional harmonic spectrum for a two color driving field, interfering with an identical copy.

of the respective harmonic. As we change the relative intensities in the two foci, we extract the intensity dependent phase between the two harmonic sources. We have discussed the intensity manipulation in Section 4.2.1. In Figure 6.24 we show the intensity dependent phase, relative to a phase between the two sources with no intensity difference, for long trajectories on the left and the corresponding short trajectories on the right. The short trajectories show a similar behavior to the single color case and we observe for harmonics 13 to 19 a uniform change of phase as a function of intensity on the order of 3 rad across the given intensity difference in Figure 6.24. We are able to extract long trajectory behavior for harmonic orders 13 to 19 as well. All other harmonic orders did not produce significant yield stemming from long trajectories. In the left panel of Figure 6.24, harmonics produced by long trajectories have an intensity dependent overall phase change of 13 rad. We are able to fit the information of all harmonics from the short trajectories to the linear model, but only harmonic 13 to 19 produced from long trajectories to the linear model. The overall behavior of long trajectories is expected to be stronger, due to the longer excursion time in the electric field. In Figure 6.25 we show the harmonic dependent

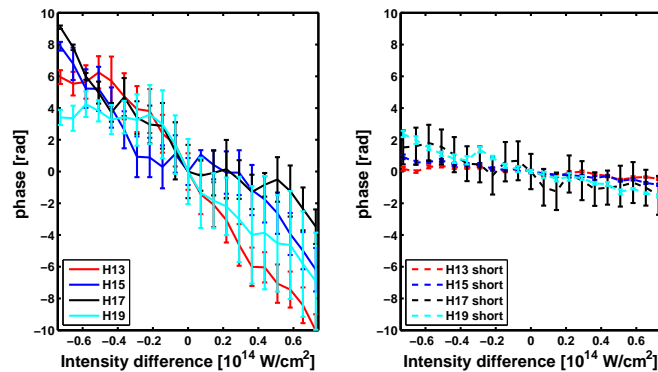


Figure 6.24: Change in phase for individual harmonics by changing the relative intensities between the two sources. Left: Long trajectories. Right: Short trajectories.

and intensity dependent phase of harmonics generated from short trajectories. While for low harmonics the slope is small, we see a bigger increase in phase for harmonics close to the cutoff. For harmonic orders 8 to 15, we observe a phase change on the order of 1 rad over the total range

of intensity differences, while for harmonic 19, we observe a phase difference of 3 rad between -0.8 and $+0.8 \times 10^{14} W/cm^2$ in intensity difference. The difference in phase rapidly increases as a function of harmonic order for orders higher than 19. For harmonic 22, we observe a phase difference of 9 rad and for harmonic 25 a phase difference of 14 rad.

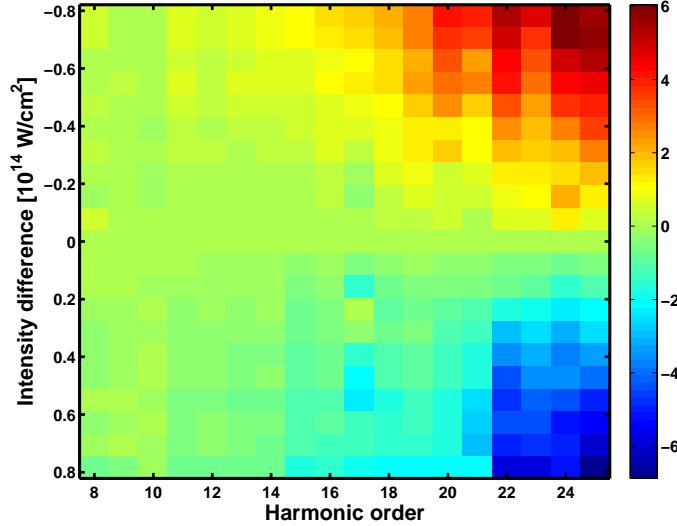


Figure 6.25: Change in phase for individual harmonics by changing the relative intensities between the two sources. We applied a gate on the spatial profile of short trajectories. The intensity of the driving laser is given as $1.5 \times 10^{14} W/cm^2$.

Extracting the α -coefficient for a given intensity of $1.5 \times 10^{14} W/cm^2$ in the two color field yields different magnitudes in the coefficient for short and long trajectories. We show the extracted values in Figure 6.26. The coefficients for short trajectories show the same trend as in the single color field. We observe an α -coefficient of 1 to 2 for harmonics of order 8 to 17, which constantly increases with harmonic order, while for harmonics of order 19 to 21, we observe an α -coefficient of 3-4. For the cutoff harmonics of order 22 to 25, we observe an α -coefficient of 8. Harmonics from long electron trajectories have a reduced strength and depend more strongly on the intensity of the driving laser field. In Figure 6.26, the α -coefficients of the detectable harmonics from long trajectories are given by empty circles. For harmonic 13, 15 and 17 we extract an α -coefficient of 12, while the extracted intensity dependent phase of harmonic 19 is smaller in amplitude, as shown in Figure 6.24, and the resulting α -coefficient has a value of 7. As we study the α -coefficient for higher order harmonics, we can observe an asymptotic limit in our experiment. Reaching harmonic 19 to 21, the parameters reach an asymptotic value associated with the cutoff trajectories, as seen in Figure 6.26. This would suggest that harmonics 19 and higher are produced by cutoff trajectories. In the detector image given in Figure 6.23, the divergence between long and short trajectories becomes comparable with increasing harmonic order, suggesting that the harmonics with harmonic energy > 32 eV (H21) are generated by the same trajectory. In the experiment, due to low SNR for long trajectories, we have bigger systematic errors on the α -coefficients for long trajectories, so that the shown α -coefficient for H19 may be an underestimate of the real value of H19, with the cutoff starting at H21.

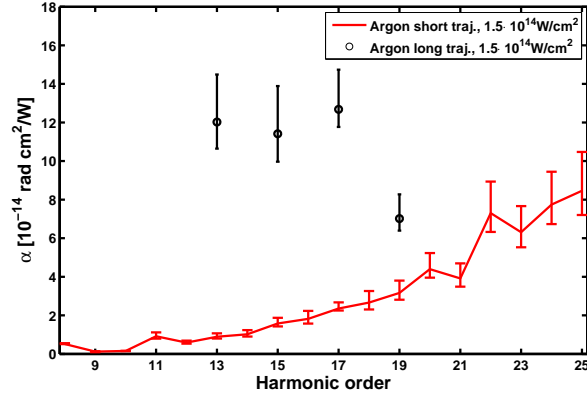


Figure 6.26: Extracted α -coefficients for even and odd harmonics driven by a laser intensity of $1.5 \times 10^{14} \text{W/cm}^2$ for a two color laser field with 3.7% light of wavelength $\lambda = 392 \text{ nm}$.

Compared to the results of harmonics driven with a single color field in argon in Figure 6.10, we can generate a figure comparing the single color case to the two color case in Figure 6.27, where we plot the α -coefficients for short trajectories driven by electric fields with similar intensities. Here we see smaller coefficients for the two color field, compared to the single color field in argon. However, the coefficients for krypton in a single color field agree well with the two-color data for argon at similar intensities. On top of this, we see discrepancies in the harmonic spectra. While for the single color case with an intensity of $1.75 \times 10^{14} \text{W/cm}^2$, we see a harmonic cutoff at harmonic energies of 60 eV in Figure 6.6, we only see a harmonic cutoff of harmonic energies of 42 eV in the two color field of strength $1.65 \times 10^{14} \text{W/cm}^2$ in Figure 6.21. The argumentation of Section 6.4.1 holds true: The phase of the electron wave packet is dependent on the intensity of the driving laser field, even when the driving laser field is a synthesized field of a intense laser field with a weak perturbative field.

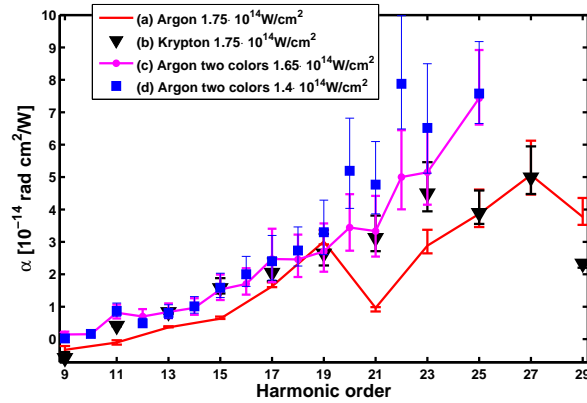


Figure 6.27: Extracted α -coefficients for a driving laser intensity of $1.65 \times 10^{14} \text{W/cm}^2$ and $1.4 \times 10^{14} \text{W/cm}^2$ for a two color laser field with 3.7% light of wavelength $\lambda = 392 \text{ nm}$, compared to the α -coefficients in argon and krypton from a single color field with similar peak intensity.

6.5 Concluding remarks

In this chapter I have shown the versatility of the common path interferometer. It allowed us to do a proof of principle experiment in the previous chapter to show a very impressive stability

and also allowed us insight to the microscopic dependency of the electron wave packet in the continuum on high harmonic generation. Vice versa, high harmonics then allow us to study the phase of the electron wave packet under the influence of an external field. Here we have seen that electrons born through tunnel ionization develop into a wave packet with very different phases as a function of the driving laser field's intensity. While the SFA theory [21] can describe the electron wave packet in the continuum and can show the general dependence on the driving laser field, we observe a phase of the electron wave packet that differs from SFA predictions, as the magnitude of the driving laser field is changed.

With an additional perturbation, the phase of the electron wave packet is further studied in this chapter. In the perturbative regime, we measure the intensity dependence of the electron wave packet and see agreement between the intensity dependence of harmonics driven with a single color field and the intensity dependence of harmonics driven by a two-color field with a second weak component. The electron wave packet phase is strongly influenced by the overall intensity of the driving laser field and not by the perturbation itself. When we drive the high harmonic generation with an intense laser field with intensity of 3 to $6.8 \times 10^{14} W/cm^2$, we can observe a very small intensity dependence given by small α -coefficients that does not agree with the described SFA model, and harmonics below the strongly shifted threshold of 26 eV (H17) have an opposite intensity dependence than previously reported plateau harmonics. In this chapter we did not discuss the influence onto the yield of the collected high harmonics. A high intensity can cause a drop in the high harmonic yield, which will however not affect the phase of the high harmonics.

Chapter 7

High harmonics driven with elliptical fields

After the description of high harmonic generation with elliptically driven fields in Section 3.2.2, with theory developed by Mikhail Frolov [52], we experimentally harness the knowledge and extract spectroscopic details from argon gas. We will show that the limitation in HHG spectroscopy to only retrieve a single photoionization parameter can be overcome by the simple addition of ellipticity to the driving laser field. By collecting the ellipticity dependent yield of HHG, we can collect the angle and energy dependent target photoionization cross section (PICS) [17], where the angle dependence has not been extracted prior to our publication [51]. In photoionization experiments, we can define the photoionization cross section to be

$$\sigma(E, \theta) = \frac{\sigma_0(E)}{4\pi} \left[1 + \frac{\beta(E)}{2} (3 \cos^2 \theta - 1) \right], \quad (7.1)$$

where $\sigma(E)$ is the energy dependent photoionization cross section and $\beta(E)$ the energy dependent dipole parameter. The angle θ describes the angle of electron emission in respect to the polarization direction of the ionizing, linearly polarized light. Through the concept of time reversal and detailed balance, we postulated in section 3.2 that the photoionization process is the time reversal of photorecombination, which is the third step of high harmonic generation. Previously, the energy dependent $\sigma(E)$ feature of the PICS was shown in high harmonic generation spectra [15, 38, 39]. However, we expand this investigation to the β -parameter, to show the equivalence between photoionization measurements by synchrotron facilities and photoionization measurements by HHG. Our experimental setup is a simple investigation of the harmonic yield in an elliptically polarized laser field. We only have to measure the total harmonic yield and do not rely on a measurement for the HHG polarization either. The measurements are done in the presence of a strong field. However, at the point of recombination, the electric field is changing sign and weak in field strength, so that the features of a field-free recombination are present in the HHG yield. Other procedures, using HHG spectroscopy, for retrieving σ_0 and β have been derived theoretically [24, 106], but their requirements for either harmonic polarization measurements [24] or stabilization of the relative phase of a two-color field [106] are experimentally more challenging than our suggested experimental technique.

7.1 Theoretical tools for the photoionization measurements

As in Equation 3.41 in Section 3.2.2, we write the rate of high harmonic emission for a fixed laser intensity as the factorization

$$Y \propto W(E)\sigma(E), \quad E = E_\Omega - I_p, \quad (7.2)$$

where the high harmonic yield Y is proportional to the product of the propagation factor $W(E)$ in the continuum (measured in $cm^{-2}s^{-1}$) and the energy dependent photorecombination cross section $\sigma(E)$, with the energy of the electron E . When describing the ellipticity dependent yield of high harmonic generation (as previously described in Section 3.2.2 of Chapter 3), we get a function $Y(E, \eta)$ that depends on the ellipticity η of the electric field

$$F(t) = \epsilon(\hat{x} \cos \omega t + \hat{y} \eta \sin \omega t). \quad (7.3)$$

In the experiment, we normalize the ellipticity dependent yield with the harmonic yield collected at an ellipticity of $\eta = 0$

$$\hat{Y}(E, \eta) = \frac{Y(E, \eta)}{Y(E, \eta = 0)} \quad (7.4)$$

Previously [107, 108], the harmonic yield revealed a dependence on the ellipticity given by a Gaussian distribution for harmonics generated out of a s-orbital with

$$\hat{Y}(E, \eta) \propto e^{-\alpha \eta^2} \quad (7.5)$$

However, for orbitals with angular momentum $l > 0$, the harmonic yield cannot be expressed by the simple factorization given in Equation 7.2. The harmonic yield is now a sum of dipole moments in perpendicular directions, as shown in Section 3.2.2. Through the use of the introduced theory we can re-write the ellipticity dependent yield for a p-orbital as the sum of a harmonic yield parallel to the major axis of the laser polarization with $\theta = 0^\circ$ and a harmonic yield perpendicular to the major axis of the laser polarization with $\theta = 90^\circ$

$$Y(E, \eta) = W(E)[a_- \sigma(E, 0^\circ) + a_+ \sigma(E, 90^\circ)] \quad (7.6a)$$

$$\propto e^{-\alpha \eta^2} \sigma(E, 0^\circ) \left[1 + f(\eta^2) \frac{1 - \beta(E)/2}{1 + \beta(E)} \right], \quad (7.6b)$$

where the yield now depends again on degenerate states in the expansion, yielding dipole moments parallel ("+") and perpendicular ("-") to the laser's major axis, as shown in section 3.2.2 of chapter 3. For an s-orbital, the formula reduces to Equation 7.5 and for a p-orbital, this yields the ability to get access to the angle dependent β -parameter, as the harmonic yield becomes a function of the cross section at 0° and 90° . $f(\eta^2)$ is defined as $f(\eta^2) = a_+/a_-$, where a_\pm takes into account the difference for ionization between the "+" and "-" states. The yield for a p-orbital is now energy-dependent and will allow us to extract both parameters σ_0 and $\beta(E)$ for the description of photorecombination.

Equation 7.6b is the major finding of our published paper [51]: We are able to express the harmonic yield as a function of $\beta(E)$. After the normalization of the harmonic yield with the aid of a reference harmonic, that shows the fastest exponential decay of the collected harmonics, we can define a harmonic yield $\hat{Y}^{(G)}$, following Equation 7.5, and we can define \hat{R} , which gives us the deviation from the expected gaussian decay:

$$\hat{R}(E, \eta) = \frac{\hat{Y}(E, \eta)}{\hat{Y}^{(G)}(\eta)} - 1 = B(E)\eta^2 \quad (7.7)$$

The measured value for \hat{R} is used in a fit to determine the parameter $B(E)$ in Equation 7.7 and we write

$$B(E) = b \frac{1 - \beta(E)/2}{1 + \beta(E)}, \quad \beta(E) = \frac{1 - B(E)/b}{1/2 + B(E)/b}. \quad (7.8)$$

which yields the β -parameter as a function of energy, where $f(\eta^2)$ is approximated to be $f(\eta^2) \approx b\eta^2$ and b is extracted from the reference harmonic.

7.2 The photoionization cross section of argon

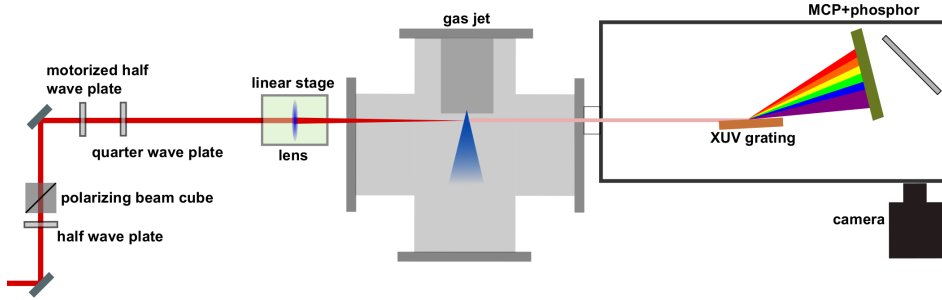


Figure 7.1: Experimental setup to measure the ellipticity dependent harmonic yield.

In this section we combine experimental measurements with the previously described theory to extract the β -parameter in argon for energies accessible in our experiment. We measure the harmonic yield as a function of ellipticity of 785 nm. The experimental setup is given in Figure 7.1, where we control the ellipticity with a half wave plate and quarter wave plate in front of the focusing lens. To change the ellipticity, we rotate the half wave plate on an automated stage, which alters the ratio of minor and major axis incident on the quarter wave plate. This way, we realize a major axis that is always pointing towards the original s-polarization and we do not have to account for a rotation of the major axis, until the light is completely circular polarized with an ellipticity of $\eta = 1$. The electric field is given by Equation 7.3. The intensity is adjusted with a half wave plate in front of a polarizing beam cube and is set to $3.8 \cdot 10^{14} \text{W/cm}^2$, resulting in a Keldysh parameter of $\gamma = 0.6$. We optimize the harmonic yield by changing the distance between gas source and lens. In the experiment, we collect the yield as a function of harmonic order and ellipticity. In Figure 7.2, panel (a), we plot the yield, normalized to an ellipticity of $\eta = 0$, for all harmonic orders. We observe a harmonic decay to zero at values of $\eta = 0.3$. Here we can see a homogenous behavior of the harmonic yield as a function of ellipticity, except for harmonic orders around order 33. At harmonic order 33, the re-colliding electron had a kinetic energy of roughly 37 eV, which has a reduced photorecombination cross section due to the Cooper minimum in the argon 3p-orbital. In panel (b) of Figure 7.2, we plot the normalized harmonic yield of harmonic 23 as a function of ellipticity and fit an expected harmonic decay to it. We use the extracted α -parameter to describe $\hat{Y}^{(G)}$ in Equation 7.7. For a similar decay in yield we would expect a \hat{R} -value of 0 as a function of ellipticity. However in Figure 7.3 panel (a), we plot the value of \hat{R} as a function of ellipticity and harmonic order and we can see an increasing deviation from 0, as the ellipticity increases. This increase in \hat{R} can be connected with the theoretically calculated ratio of $\sigma(E, 90^\circ)/\sigma(E, 0^\circ)$ in Figure 7.3, panel (b), where we plot the ratio as a function of electron energy. Both figures show the strongest deviation at harmonic order 33 and the electron energy associated with harmonic 33. After the calculation of \hat{R} , we can use the fit, given in Equation 7.7 to extract the values of $B(E)$ for all harmonic orders. In panels (a) and (b) of Figure 7.4, we show the ellipticity dependent behavior of \hat{R} for harmonic orders 29 and 33, the deviation becomes bigger with increased ellipticity, and we extract the values for $B(E)$ with Equation 7.7.

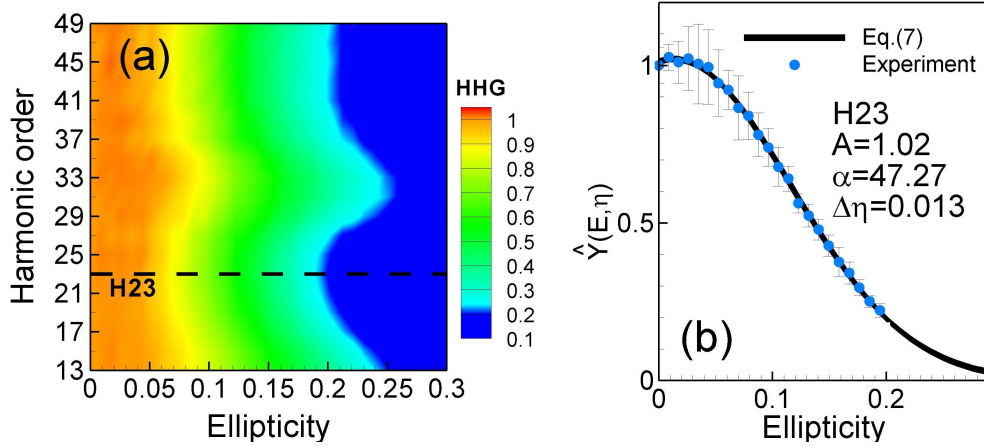


Figure 7.2: In panel (a) we show the experimentally collected harmonic yield as a function of ellipticity and harmonic order from argon. The data is normalized to its values at an ellipticity of $\eta = 0$ and in panel (b) we show an exponential fit to the ellipticity dependence upon harmonic 23. Picture taken from [51]

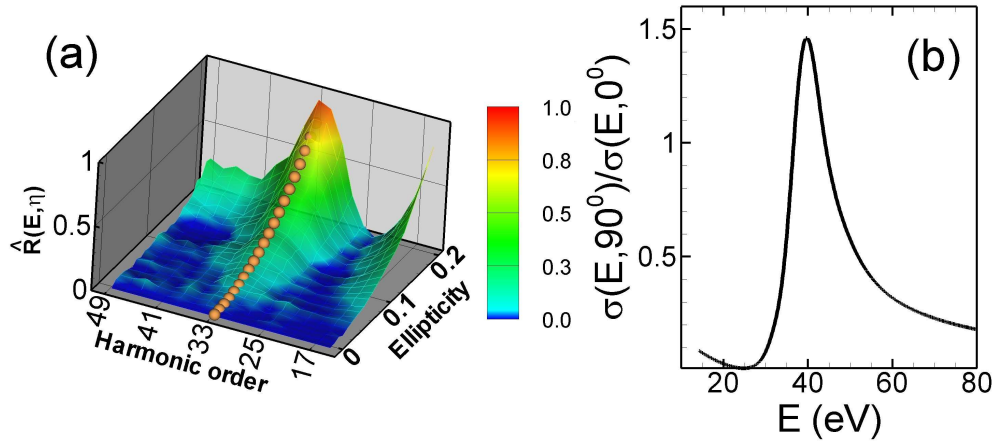


Figure 7.3: (a) For harmonic 33 from argon a strong deviation given by \hat{R} is given as a function of ellipticity. This deviation is strongly visible in the ratio of horizontal and vertical photoionization cross section plotted in panel (b) for an energy of 40 eV. Picture taken from [51]

After the extraction of $B(E)$ for all harmonic orders, we can extract the energy dependent β -parameter by solving Equation 7.8 and show the result in Figure 7.5. The experimentally retrieved values in blue dots agree well with experimental photoionization experiments [12] in red squares and theoretical photoionization calculations [13], plotted with a solid black line. A deviation at low energies is visible and can be associated with inaccuracies in the calculation of the electron wave packet at such low energies. The energy-dependent β -parameter shows different angle dependencies in the recombination of an electron to the 3p-orbital. Electrons with an energy of 37 eV have an uniform recombination cross section for all recombination angles, while electrons with an energy of 20 eV have an increased cross section at angles of 90° and a node at 0° , where no recombination is expected. The overall recombination cross section has a local minimum at 37 eV, which can be seen in the spectra recorded in a later Figure 7.7. We test the stability of the result by checking the harmonic yield at different focus positions.

In Figure 7.6 we show the ellipticity dependent yield of all harmonic orders for three different phase matching conditions. The deviation at H33 survives. The feature can be extracted and is not

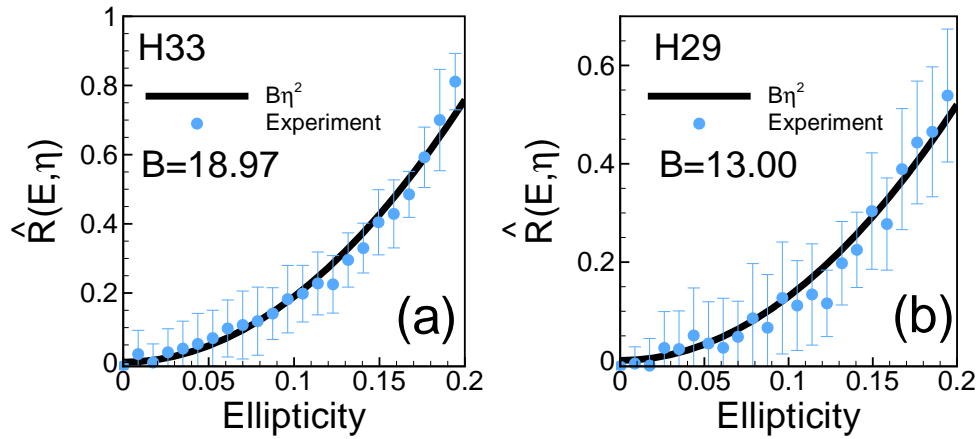


Figure 7.4: Extracted value for \hat{R} as a function of ellipticity of the driving laser field for harmonic 33 in panel (a) and harmonic 29 in panel (b). The coefficient B changes drastically. Picture taken from [51]

influenced by the relative position between laser focus and gas jet. The harmonic cutoff in panel 3 is reduced, due to reduced phase matching and lower peak intensity. The presented β -parameters are extracted from the harmonic data from the middle panel with a focus position 2.79 mm in front of the gas source, while the left panel shows harmonic yield generated from a focus position further away from the gas source and the third panel show the ellipticity dependence of harmonics generated from a focus placed after the gas jet, closer to the spectrometer.

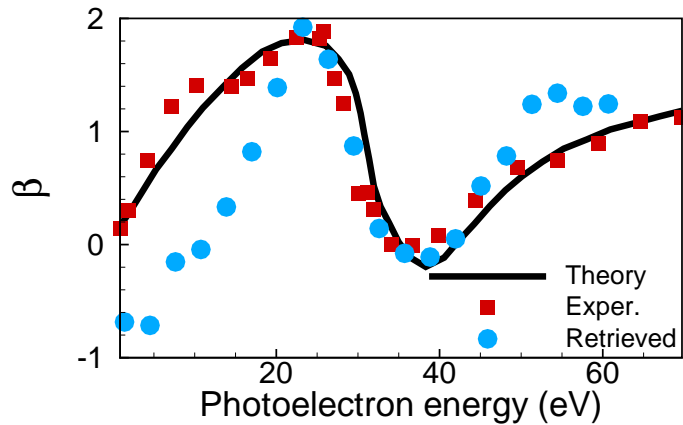


Figure 7.5: β -parameter as given out of Equation 7.1 for returning electron energies between 0 and 60 eV. Theory is calculated using photoionization cross section models. The red squares are given by a classical photoionization experiment at a synchrotron facility and the circular blue marks are extracted out of our theory model and experimental data. Picture taken from [51]

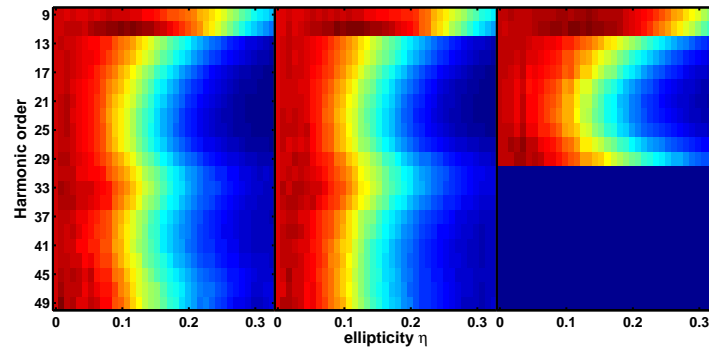


Figure 7.6: Ellipticity dependent harmonic yield for harmonics 9 to 49. On the left the focus position is placed before the gas jet. The middle panel is from a laser position between the left panel and the gas jet, but still before the gas jet. The right panel is produced by a laser focus placed behind the gas jet. The harmonic cutoff is reduced. However, all panels show a deviation from the expected harmonic decay at harmonic orders 29 to 33. The deviation is given independent of focus position.

7.3 Extension to long wavelength

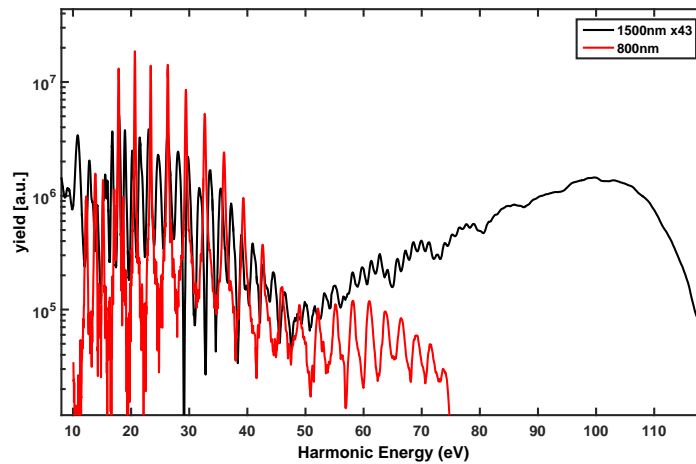


Figure 7.7: Harmonic yield in argon driven by 800 nm and 1500 nm light. The yields are normalized to laser-gas interaction. Comparable gas densities and MCP gains were used. We compensate for efficiency differences between the driving laser fields by multiplying the spectrum from 1500 nm by a factor of 43.

We extend this experiment to longer driving wavelengths, in an effort to collect harmonics with a wider energy range. Due to the scaling of the ponderomotive energy with λ^2 and the cutoff law of harmonic generation being proportional to the ponderomotive energy, we will see a higher cutoff in HHG and can study a broader energy range with the same peak intensity. As we increase the wavelength of the driving laser from 785 nm to 1500 nm, we collect a harmonic spectrum with a longer cutoff. In Figure 7.7, we show a HHG spectrum as a function of photon energy in argon driven by 785 nm in red and a spectrum driven by 1500 nm in black. We see dramatic differences in the generated harmonic spectra. The spacing between harmonics, given by $2h\nu$ is reduced for harmonics driven by 1500 nm light. The minimum in the Cooper minimum at 50 eV is more pronounced and reduces the harmonic yield. The cutoff is extended to 120 eV, compared to 75 eV,

when driven by 785 nm light. However at the same time, the conversion efficiency is reduced. We multiplied the spectrum for 1500 nm by a factor of 43 (given an estimated conversion efficiency $\propto \lambda^{-6} = (1500/800)^{-6}$ [109, 110]). The two experiments were performed with different focusing optics and pulse energies. The scaling worked really well in the given logarithmic scale. After re-scaling, the intensity in the Cooper minimum is on the same scale. This shows the problem present in HHG experiments driven with long wavelength lasers. In the Cooper minimum, the spectral region of most interest, the signal is reduced to a minimum level due to conversion efficiencies. Our signal to noise ratio is becoming poor. However, overall, the effect of the Cooper minimum is more pronounced and the yield slowly recovers at energies above 80 eV to reach values in yield comparable to the yield at energies below 35 eV. The presented spectrum, driven with 1500 nm, was taken with a focus placed 5 mm in front of the gas jet. If we further test the focus dependent behavior of generated harmonics, we can see a Gaussian behavior in the total harmonic yield and ionization as a function of focus position in Figure 7.8. However, switching to the opposite site with a focus position 5 mm after the gas jet, we can generate a harmonic spectrum in Figure 7.9 and compare it to the previously given spectrum. In the red spectrum, the yield in the Cooper minimum is reduced and is on the noise level. After threshold subtraction, no yield is visible at 50 eV. A analysis on the ellipticity dependent yield is not possible.

We move our lens back again and place the focus before the gas jet, with a resulting spectrum

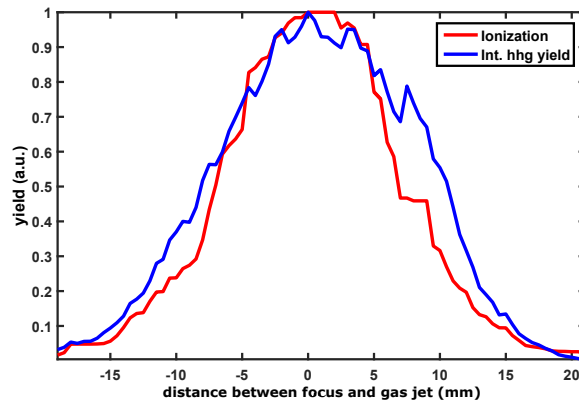


Figure 7.8: Focus dependent ionization and total harmonic yield for a driving laser field at 1500 nm.

as shown in the black line of Figure 7.9. We again rotate the half wave plate on an automated rotational stage and collect the harmonic yield as a function of ellipticity. In Figure 7.10, we show the ellipticity and photon energy dependent yield. We can see a bright harmonic emission at energies below 40 eV and a bright continuous emission at energies above 70 eV. In the Cooper minimum around 50 eV, we can see no harmonic yield on the given linear color scale, but normalized to each individual maximum, we can show the ellipticity dependence in Figure 7.11, where we plot the normalized yield of harmonics as a function of ellipticity. Additional noise is visible at the region of interest at 50 eV. No deviation from the expected exponential decay is visible for harmonics above 30 eV. The previously measured deviation is gone or hidden in noise. The laser intensity is estimated to be $1.7 \cdot 10^{14} \text{ W/cm}^2$ with a Keldysh parameter of $\gamma = 0.5$.

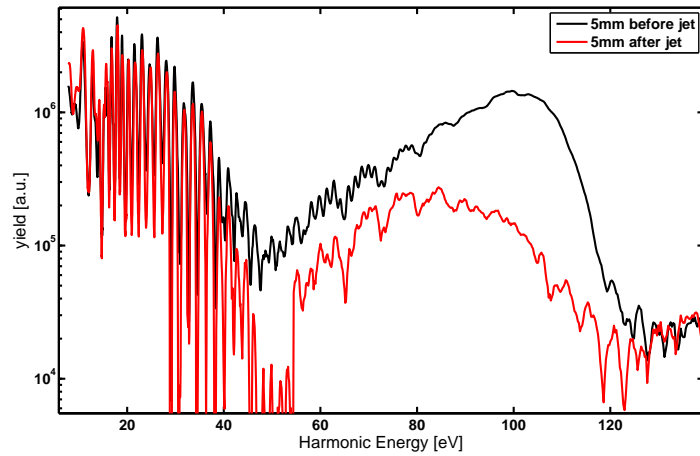


Figure 7.9: Harmonic yield in argon, driven by 1500 nm captured at two relative focus positions.

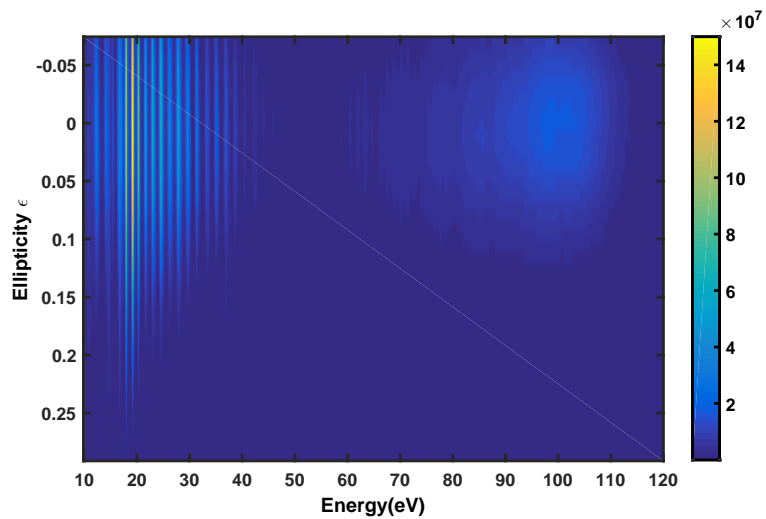


Figure 7.10: Raw harmonic yield as function of ellipticity and harmonic energy for driven at 1500 nm. The focus is placed 5 mm before the jet.

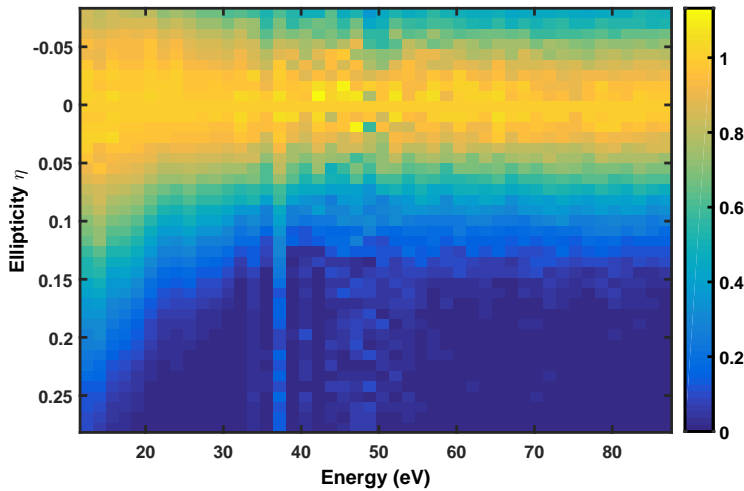


Figure 7.11: Harmonic yield normalized to the yield of individual harmonics at an ellipticity of $\eta = 0$. Only discrete harmonic orders from 10 to 80 eV are plotted in this figure.

When we switch targets to krypton and ethylene, we can generate harmonic spectra for argon, krypton and ethylene in Figure 7.12. The laser center wavelength was tuned to 1400 nm. Each spectrum has a different shape as a function of harmonic energy. Argon has a Cooper minimum at 50 eV, where the yield is reduced. Krypton has a very slow decay in harmonic yield as a function of increasing photon energy, which can be explained by the presence of a Cooper minimum of the 4p-orbital in krypton at 80 eV [16, 111]. The photoionization cross section has an increased cross section at 110 to 120 eV after the Cooper minimum. Since we did not observe photon energies above 95 eV, we do not pass the Cooper minimum and we can only see a reduced cutoff and no effect of the Cooper minimum. With ethylene, we reach a harmonic cutoff of 60 eV and no structural feature is visible in the spectrum.

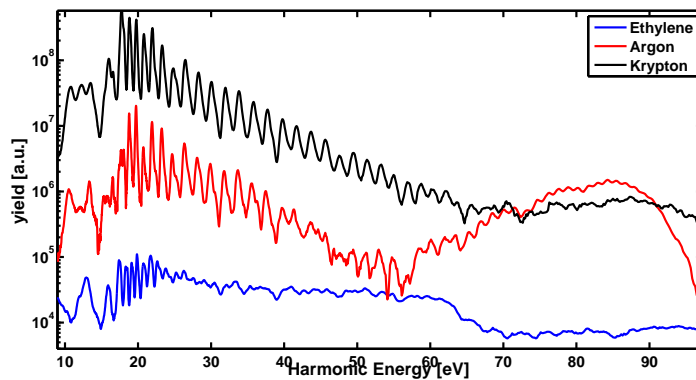


Figure 7.12: Harmonic yield from ethylene, argon and krypton at 1400 nm.

Chapter 8

The complex photoionization dipole of nitrogen

This chapter serves as an introduction to the concept of measuring complex signals $S(\omega, t) = |S(\omega, t)|e^{i\phi(\omega, t)}$ from high harmonic generation to study structural details of molecules. As introduced in Section 3.2, high harmonic generation holds complex-valued information about the recombination dipole matrix element $d(\omega, \theta) = |d(\omega, \theta)|e^{i\phi(\omega, \theta)}$. The recombination process is the time reversal of photoionization. Single-photon ionization has been used by chemists as a tool to investigate atomic and molecular structures. However, in the weak field regime of photoionization, phase information about the transitions cannot be easily retrieved.

In contrast to this, HHG offers direct access to amplitude and phase of the photoionization cross section. Calculations of the complex photoionization dipole matrix element yields the cross section $\sigma(\omega, \theta) = |d(\omega, \theta)|^2$ and a phase in the matrix element $\phi(\omega, \theta)$. The values have been presented in nitrogen [112] and show energy and angle dependent fluctuations. A shape resonance at 30 eV shows dramatic enhancement of the cross section and a variation of the phase as a function of energy.

In our experimental setup, we do not have access to the relative phase between harmonics, but can study the angle dependence of individual harmonics with molecular alignment. In nitrogen, similar measurements have already been performed and showed similar observations: In a 2015 publication Camper et al, [113] used a binary phase mask to study the change in phase of harmonics, as the molecules rotate in time and shows for harmonics 9 to 17 an oscillatory behavior of the phase, while a measurement by Lock et al [114] showed no change in phase for harmonic 19. We show our results and try to extend the measurements to the molecular frame. In our setup, we use a slightly different approach that gives us better control over the experimental difficulties in such experiments.

In the previous chapter, where we established a quantitative relation between HHG and the double differential cross section for the 3p orbital of argon, we did not have to consider other orbitals in the interaction of light and matter. In contrast to atoms, molecules have an electronic configuration approximated by single particle orbitals [115–117]. We describe the electronic configuration with molecular orbitals, where the electron in the highest occupied molecular orbital (HOMO) has the smallest binding potential with the molecule and the next lower lying orbital is defined as the HOMO-1. In nitrogen, these two orbitals have ionization potentials of 15.6 eV for the HOMO and 16.9 eV for the HOMO-1. These binding potentials are very close to each other and ionization rates can become similar, so that electrons from either orbital can produce harmonic emission. The HOMO is a molecular orbital described as a $3\sigma_g$ orbital and the HOMO-1 is described as a $1\pi_u$ orbital. We show the orbital symmetries in Figure 8.1 in respect to the molecular axis z given in the stick model on the right of the figure.

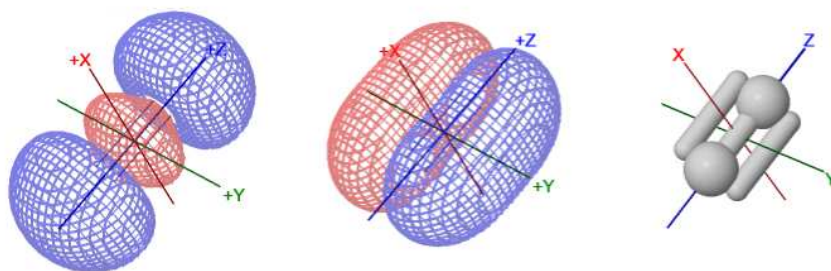


Figure 8.1: HOMO of diatomic nitrogen on the left, HOMO-1 of diatomic nitrogen in the middle in respect to the stick model of nitrogen on the right, where the molecular axis points in the z-axis. Images were created with Jmol.

8.1 Fundamentals of describing the molecular frame signal

As seen in the QRS model in Section 3.2.2, the harmonic yield of molecules in the molecular frame depends on the angle between the molecular axis and the laser polarization axis. In Section 3, Figure 3.3 and in Figure 8.1, we show the description of the coordinate systems for the laboratory and molecular frame: the molecule's axis is given by the z -axis and the pump and probe laser polarization is defined by the Z -axis. In nitrogen, when we assume that we only have ionization from HOMO, we expect a signal influenced by the symmetry of the HOMO. The orbital has the symmetry of a σ_g orbital, which has an angular density distribution that aligns with the molecular axis and has two nodes perpendicular to the molecular axis. If we were to fix a nitrogen molecule in space and were to rotate the probe polarization, we would see a harmonic signal that would follow this molecular symmetry, but is influenced by the angle dependent ionization rate and the angle dependent recombination cross section, as described by the QRS model in Section 3.2.2 Equation 3.44.

We use an ansatz suggested in [22] to describe the angle dependent signal of nitrogen as a sum of $\cos^{2n} \theta$ -terms and $\sin^2 \theta \cos^{2n} \theta$ -terms. In our expansion terms of order $\sin^2 \theta \cos^{2n} \theta$ can be expressed as the difference between higher order $\cos^{2n} \theta$ -terms, which reduces the expansion to $\cos^{2n} \theta$ -terms. By adding an appropriate amount of terms of order n to the expansion, we will be able to describe the correct angle dependence. We formulate the angle dependent yield $S(\theta, \omega)$ in the molecular frame of a harmonic with energy ω as

$$S(\theta, \omega) = \sum_n C_n(\omega) \cos^{2n} \theta. \quad (8.1)$$

In the experiment we do not have access to a perfectly aligned molecule and the molecular frame signal is convoluted in the laboratory frame signal. The molecular axis has a distribution function that depends on the non-adiabatic alignment of the molecule. We can write the molecular axis distribution ρ as

$$\rho(\theta, t) = g_i \frac{e^{E_i/kT}}{Z} |\Psi_i(\theta, t)|^2 \quad (8.2)$$

where $i = \{J_0, M_0\}$ are the quantum numbers of the involved states, g the nuclear spin state weights, k the Boltzmann constant, T the rotational temperature and Z the partition function. The molecular axis distribution ρ can be interpreted as a probability function of finding the molecule at time t aligned at the angle θ .

In the laboratory frame, we can define the time dependent signal as an integral over all angles θ

$$S(t) = \int \rho(\theta, t) S(\theta) \sin \theta d\theta = \sum_n C_n \int \rho(\theta, t) \cos^{2n} \theta \sin \theta d\theta \quad (8.3)$$

where we can solve the integral for a particular order n to be

$$\int \rho(\theta, t) \cos^{2n} \theta \sin \theta d\theta = \langle \Psi_i | \cos^{2n} \theta | \Psi_i \rangle (t) \quad (8.4)$$

as previously shown in Chapter 3, Equation 3.106. Each term of the expansion is averaged over the molecular axis distribution. In the experiment, we measure the power spectrum of the emitted light $P(\omega)$ and the phase of the light $\Phi(\omega)$. We have a power spectrum

$$P(\omega) = |\mathfrak{F}(\ddot{d}(t))|^2 \quad (8.5)$$

where $d(t) = |d(t)|e^{i\phi(t)}$ is the induced dipole that holds information of ionization, propagation and recombination, as previously discussed in Chapter 3. We also measure the phase of the emitted light

$$\Phi(\omega) = \arg(|\mathfrak{F}(\ddot{d}(t))|) - \Phi(\omega)_{ref} \quad (8.6)$$

where the phase is defined as the argument of the complex dipole and measured with respect to our reference source in the Young's double slit experiment. In the Young's double slit, the sources are identical, but are influenced by the change of the molecular axis distribution as we change the time between rotational excitement and probing the molecules. As we measure the spectrum and argument as a function of time between pump and probe, we can write the harmonic field as a complex function of time between pump and probe pulses

$$S(\omega, t) = \sqrt{P(\omega, t)} e^{i\phi(\omega, t)} \quad (8.7)$$

where we can use our time dependent expansion given through Equation 8.3 to write the measured signal $S(\omega, t)$ as

$$S(\omega, t) = \sum_n C_n \langle \Psi_i | \cos^{2n} \theta | \Psi_i \rangle (t) \quad (8.8)$$

where the coefficients C_n are now complex and follow $C = A + iB$. We perform multiple linear regression fits, in which we change the parameters, which define the molecular axis distribution. We do so to minimize the residual and have more confidence on the molecular axis distribution. For the smallest residue, we acquire values for the coefficients C_n that can be inserted in the angle-dependent expansion in Equation 8.1 to define a molecular frame harmonic yield $S(\omega, \theta)$. In the case of nitrogen, we express the degree of alignment in the metric $\langle \cos^2 \theta \rangle$ that describes the projection of the molecular axis z onto the laser polarization axis Z : For a value of 1, we have perfectly aligned molecules in respect to the Z -axis, while for a value of 0.33, we have no preferential alignment of the molecules with respect to the laser polarization axis. In Figure 8.2, we show an example for the calculated expectation values for a molecular ensemble with a rotational temperature of 25 K, excited by two 100 fs long 785 nm-pulse with an intensity of 14 TW/cm^2 and 18 TW/cm^2 . As the expansion order increases, the expansion term has smaller overlap with the rotational wave function and the expectation value in time has smaller values. Higher order revivals can be fitted with higher order terms, while there is a diminishing difference in the high order fractional revivals given by $\cos^4 \theta$ and $\cos^6 \theta$. We need good confidence in the data and a good degree of alignment to fit with a large basis set.

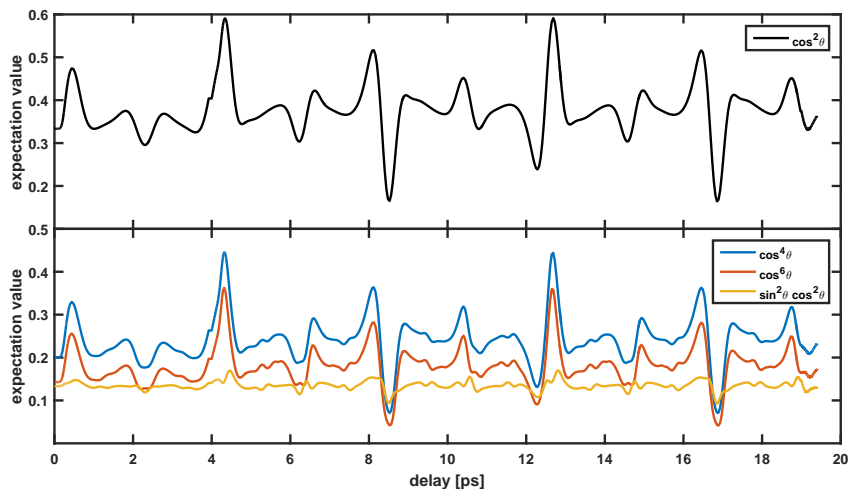


Figure 8.2: Expansion terms as a function of time after the interaction with the first pump beam at time 0 ps and a second pump delayed with 3.97 ps in respect to the first pump

8.2 Measurement of the complex dipole of Nitrogen

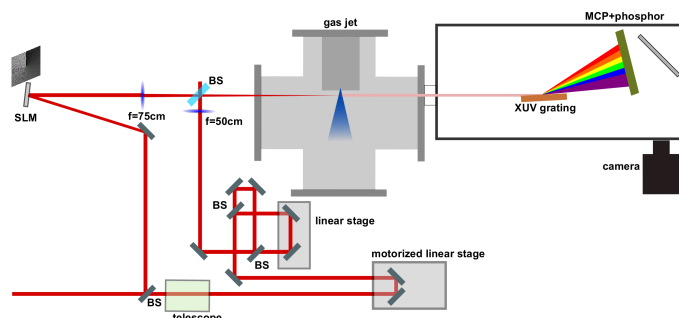


Figure 8.3: Experimental pump probe setup

We use a pump-probe scheme, where the pump pulse is inducing molecular alignment and the probe is driving high harmonic generation, which is used as our spectroscopic tool. We can control the relative delay between pump and probe pulses by changing the optical beam path of the pump pulses by moving a mirror on a motorized linear stage. The experimental setup is shown in Figure 8.3. In this setup, the probe arm is reflected off a beam splitter and is shaped by a SLM to form a two source focus spot. The probe is focused by a $f=75$ cm lens into the gas jet and harmonics are generated by both focus spots. As the harmonics travel into the far field, harmonics from the two sources interfere and form a fringe pattern on the detector, which allows us to detect the relative phase between the harmonic sources.

The pump arm is transmitted through the first beam splitter and contains initially 80% of the total pulse energy. After shrinking the beam by a factor of two with a telescope, the beam is split again by a set of two beam splitters in another interferometer inside the pump arm. By controlling the relative delay between the two pump pulses, we can tune the interaction of the pumps upon the molecular target and enhance the molecular alignment [118]. The pump beams are focused with a separate lens of $f=50$ cm into the center of the gas jet as seen in Figure 8.3. The pump and probe beams are recombined with a beam splitter. The pump focus is placed at the center of the jet and is overlapped with one of the two probe beams.

The spot size of the pumps are measured to be $68 \mu m$ by $83 \mu m$ and hold a pulse energy of $200 \mu J$ with a pulse duration of 100 fs, measured by a cross correlation between the measured probe of 30 fs and the pump beams, which results in an experimentally determined pump intensity of $21 TW/cm^2$ and a probe intensity of $110 TW/cm^2$. Temporal and spatial overlap is initially achieved by overlapping the pump beam with the probe on a camera and checking for a spatial interference pattern on the near field beam, when both beams are present. When overlapped in space and time, we can see a circular interference pattern in the near field, where light is interfering constructively and destructively with each other. The overlap between pump and probe is then optimized on the live harmonic signal and we check that only one of the two sources is interacting with the pump beams. In the data acquisition, amplitude and phase of the harmonics are collected as a function of delay between pump and probe in step sizes of 40.04 fs. This step size is a sufficient sampling in time to capture smallest features in the revival structure from nitrogen, with a rotational period of 8.3 ps. In the later experimental data, we can see smaller features with periods of 240-400 fs, that can be resolved with the given step size.

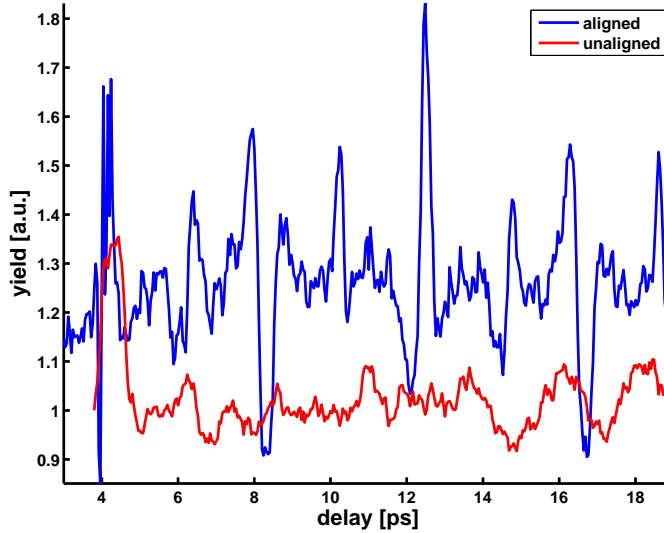


Figure 8.4: Harmonic yield as a function of time between pump and probe for the bottom and top source reproduced by a shaped focus to match the focus of the two slit experiment.

As explained in the previous section 3.5.2 and 4.2.1, when the SLM shapes the fundamental beam spatially, the two sources are generated through the interference of two counter-rotating Laguerre Gaussian beams with OAM $l = +1$ and $l = -1$. As described in Section 3.5.1, a destructive interference at angles $\phi = \pi/2$ and $\phi = -\pi/2$ occurs, where ϕ is the angle in the plane perpendicular to the laser propagation. It is causing the formation of two foci spots and the generation of a tightly spaced Young's double slit. Our experimental solution enables us to generate a single source, able to represent a single source of our double slit experiment, as shown in Section 3.5.1. We align the probe beams through the spectrometer and align our pump beams spatially to one of the two sources. We check for overlap in both sources by generating an individual source with OAM $l = 0$ and $l = +1$, and a fixed offset of $\phi = \pi$ or $\phi = -\pi$, to cause a destructive interference at the angle of one of the two sources in the double focus. An additional tilt is applied to give the appropriate vertical offset, as proposed in Section 3.5.2. The individual sources produce an intensity profile very similar to the individual sources, as seen in theoretical calculations in Chapter 3 Section 3.5.2 and also given in the spot size measurements in Section 4.2.1. However, the phase profile in the calculations show a horizontal gradient (see Figure 3.25 in Chapter 3) and so our individual sources are not identical to the double slit sources. We can use them, nevertheless, to check for spatial overlap between the sources and the pump beams in our harmonic signal.

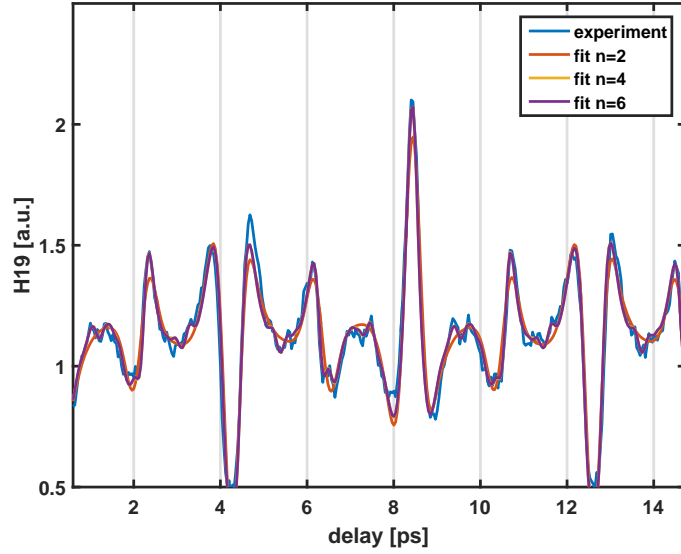


Figure 8.5: Amplitude of harmonic 19 in the experiment. Experimental data versus fits with different orders of fitting.

The first step is to properly align the pump beams in respect to a single source and to check the overlap in the experiment beyond the spatial overlap on a CCD camera. When we plot the delay dependent yield of the top and bottom sources in Figure 8.4, we see for the aligned source a harmonic yield that strongly depends on the time between pump and probe: At 8.3 ps, the yield is reduced to a value of 0.9 and at 12.1 ps, the yield increases to a value of 2. The yields are normalized to their isotropic value, when no pump beam is present. We can see quarter revivals at 6.1 ps, 10.2 ps and 14.2 ps. 1/8th revivals are visible at 5 ps, 7 ps, 9 ps and 11 ps. The unaligned source, where no spatial overlap is visible with the pump pulse in the imaging setup, is plotted in red and shows no periodicity in time. We do, however, observe a crosscorrelation feature at 4 ps, when pump and probe are incident at the same time. To extract the molecular frame signal, the linear regression is based on the experimental data after the interaction with the pump pulse and the autocorrelation peak does not influence the real physical observations between the unaligned reference source and the aligned second source. After we have checked the individual sources and made sure that no rotational alignment is visible in our unaligned source, we switch to the two-source interference mask and collect the harmonic yield and phase as a function of time between pump and probe. The yield from the aligned source is normalized to the total yield of both sources. In Section 4.3, Equation 4.8, we gave an equation for the total harmonic yield, where the fringe-angle-integrated yield is equal to $I_{total} = I_1 + I_2$. I_1 and I_2 are identical sources, when no aligning pump beam is present. We then can define the isotropic yield of our individual harmonic source to be $I_{1,2,iso} = I_{total}/2$. We normalize our delay dependent yield measurement to this isotropic value and get the intensity of a single source as a function of time. To calculate the amplitude of this source, we take the square root of the intensity.

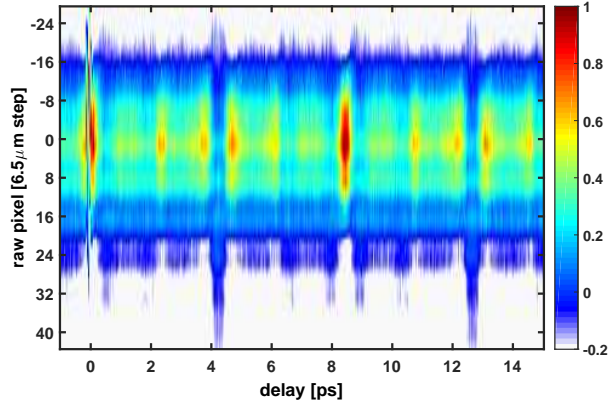


Figure 8.6: Interference pattern of harmonic 19 on the detector as a function of time between pump and probe. The fringe spacing is 8 pixel, which equals 2π in phase. A shift of 1 pixel equals a phase change of 0.78 rad. At 4.25 ps and 12.5 ps, we can observe a change of this magnitude.

In Figure 8.5, we show the time dependent amplitude of harmonic 19, normalized to the isotropic value. The experimentally collected data shows an amplitude of harmonic 19 between 0.5 and 2, when normalized to the isotropic value. At a time of 4.1 ps and 12.3 ps, we see a strong anti-alignment dip in the harmonic amplitude, while we observe a maximum at 8.2 ps. Besides quarter revivals at 2.1 ps and 6.1 ps, we can observe smaller revivals in between the mentioned revivals, where the oscillation is on the order of 0.1 compared to the isotropic value. A fit with the expansion in Equation 8.8 is performed and higher order terms are added. Only through the addition of higher order terms with $n = 2, 3$, smaller features in the delay dependence can be fitted. 1/8th revivals at 3 and 5 ps occur and are fitted with higher order terms. The phase of harmonic 19 as a function of delay is extracted using fast Fourier transformations of the collected Young's double slit fringe pattern. In Figure 8.6, we show the fringe pattern of harmonic 19 as a function of delay between pump and probe. We can observe a subtle fringe movement at a time of 4.1 ps and 12.2 ps in the given fringe pattern. With a fringe spacing of 8 pixels, we get a change in phase of $\pi/4 = 0.79$ rad for each pixel the fringe pattern moves. In the experiment, the observed phase change is on the order of 0.5 rad in the fast Fourier transformation and the equivalent pixel shift is on the order of 2/3 pixel for the shown harmonic, which we can resolve as discussed in Section 4.3.1. We perform a series of Fourier transformations for all delays and harmonic orders and extract the phase of individual harmonics as a function of time.

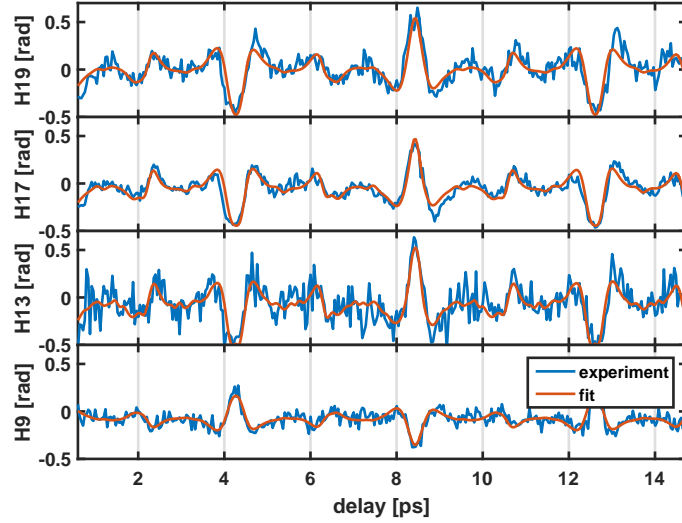


Figure 8.7: Phase of harmonic 9, 15 and 19 as a function of time between pump and probe. A fit, based on estimates for the alignment distribution, is shown.

From the measured interference, we obtain a complex valued quantity with $S(\omega, t) = \sqrt{P(\omega, t)}e^{i\phi(\omega, t)}$, in which the imaginary and complex part depend on the phase and amplitude measured in the experiment. To perform a linear regression, as shown in the Appendix A, we split the complex number into real and imaginary part and perform two linear regressions, as the equation splits into two linear equations. After we have performed the linear regressions, we convert the complex numbers back into amplitude and phase. In Figure 8.7, we show the measured phases of harmonic 9, 13, 17 and 19. At times of alignment and anti-alignment, we observe the biggest phase offset compared to the reference source. The measured phase of harmonic 9 shows a maximum in phase at a delay of 4.1 ps, while higher order harmonics show a minimum in phase at this delay. Harmonic 19 shows a variation of up to 1 rad as a function of time to the isotropic value. The shown fits, based on least square fits, show agreement with the overall trends, however does not match the width of the peaks at times of anti-alignment at 4.1 ps and 12.4 ps. The experimental curves show a broader feature in time than the fits can re-produce. No higher order features, e.g. 1/8th revivals, are measured in the harmonic phase.

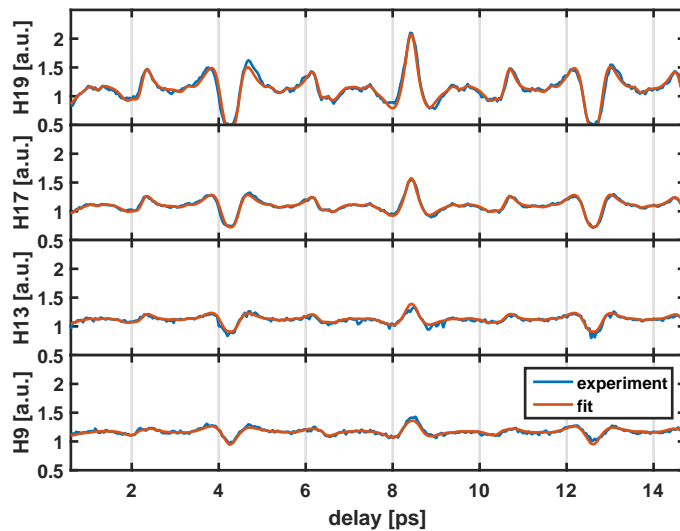


Figure 8.8: Amplitude of harmonic 9, 15 and 19 as a function of time between pump and probe. A fit, based on estimates for the alignment distribution, is shown.

In Figure 8.8, the delay dependent amplitudes of the same harmonics are given. Here, the harmonic amplitude has the same trends for all harmonic orders, where the harmonic yield is reduced at times of anti-alignment and increases at times of alignment. Harmonic 9 and 13 have fluctuations as a function of time between 0.9 and 1.3, while harmonic 17 and 19 show stronger fluctuations as a function of time. For harmonic 17 and 19, we can clearly see higher order revivals at times of 3.1 ps and 5.1 ps. The previous inversion, visible in the phase of harmonic 9, is not present in the amplitude of harmonic 9.

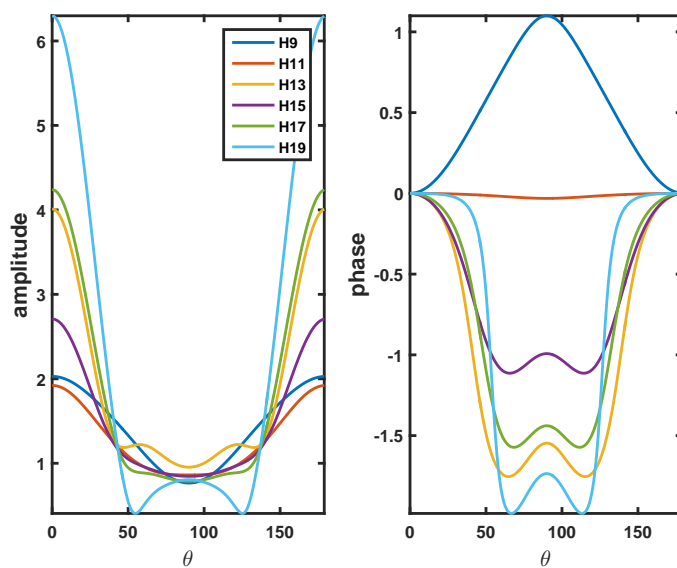


Figure 8.9: Phase and amplitude of the harmonic emission in the molecular frame as a function of angle between probe polarization and molecular axis for measured harmonics.

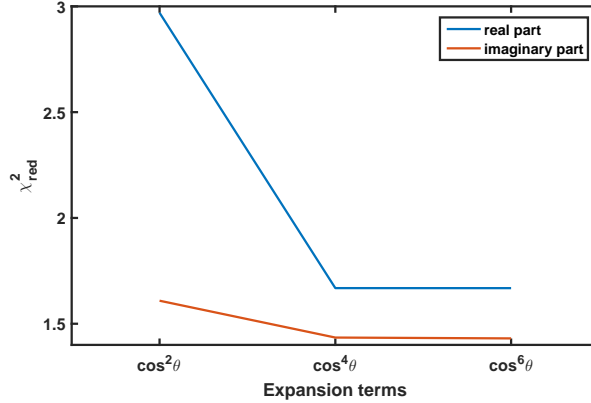


Figure 8.10: Residual as a function of expansion terms for the fit of imaginary and real part of experimentally collected harmonic 17 of aligned nitrogen.

In Figures 8.9 we used the extracted coefficients C_n to show the angle dependent amplitude in the left panel and phase of the harmonic emission in the molecular frame in the right panel, as defined in Equation 8.1. The shape resonance in HOMO from nitrogen at harmonic order 19 is showing a strong angle dependence in amplitude with a angle-resolved amplitude of six times the isotropic value at an angle of $\theta = 0^\circ$. We observe a phase difference of 1.6 rad between harmonic emission at $\theta = 0^\circ$ and $\theta = 90^\circ$. A consistent feature, visible in the angle dependent phase measurement is a feature at 90° that shows that the harmonic emission has a different phase than harmonics emitted from 60° . This feature can be explained with an occurrence of harmonics from HOMO-1. The residuals for the imaginary and real part of the time dependent signal of the 17th harmonic is given in Figure 8.10, where the addition of terms of order $2n = 6$ do not improve the fit to the experimental data. As previously seen in Figure 8.2, orders $2n = 4$ and $2n = 6$ can predict smaller fractional revivals and do not differ drastically for the given temperature and pulse intensities, so that a fit to $2n = 6$ does not improve the delay dependent fit to the experimental data. In Figure 8.11a, we plot the extracted phase and amplitude of harmonic 15 as a function of angle between molecular axis and driving laser polarization. We compare the angle-dependence to the angle dependence calculated by the factorization in QRS:

$$D_{total}(\omega, \theta) = N_{HOMO}(\theta)^{1/2} d_{HOMO}(\omega, \theta) + (N_{HOMO-1}(\theta))^{1/2} d_{HOMO-1}(\omega, \theta) e^{i\Delta\eta} \quad (8.9)$$

where $D_{total}(\omega, \theta)$ is the coherent sum of harmonic dipoles from HOMO and HOMO-1 with the ionization potential difference of HOMO and HOMO-1 of 1.3 eV. The ionization rates $N(\theta)$ are given by a theoretical ionization calculation of HOMO and HOMO-1 by MO-ADK theory extracted from [119] and $d(\omega, \theta)$ is supplied from [112] with $d = \sqrt{\sigma} e^{i\phi}$. For the ionization rates of HOMO and HOMO-1, we use a ratio of 5:1 for the preferential ionization of HOMO over HOMO-1 at 90° . The angle dependent ionization rate for HOMO has a ratio of 9:1 for ionizing parallel to the molecular axis compared to ionizing perpendicular to the molecular axis. The angle dependent ionization rate is given in Figure 8.12. A phase difference given by the classical action of the electron in the continuum is given by the ionization potential difference between the two molecular orbitals and is accounted for by $e^{i\Delta\eta}$. The theoretical PICS calculation, given in Figure 8.13, then allow us to calculate the harmonic dipole as a product of the given complex-valued amplitudes of ionization rate, photoionization cross section and electron wave packet. The harmonic dipoles are plotted for harmonic order 15 to 19. Only by using non-vanishing probabilities of HOMO-1 to the total harmonic dipole, we can match the retrieved angle dependent phase of harmonic 15 and 17. Harmonic 19 can be explained by HOMO only, but shows better agreement with the experiment, when a portion of HOMO-1 is added to the calculated total dipole. Here we assumed a ionization rate similar to the MO-ADK model rate given by publication [?], where the ratio of parallel to perpendicular ionization rate of HOMO is given with 10:1. However, rates of 3.3:1 [?, ?] and 4.5:1 [?] have been measured. Since we

did not measure the angle-dependent single-ionization yield in our experiment, we used the MO-ADK rate. In this experiment, we report HHG from HOMO and HOMO-1 for low order harmonics, which match the characteristic features of the photoionization cross section in phase and amplitude. In previous work [?], features from HOMO-1 in nitrogen were restricted to cut-off harmonics and harmonic orders of order 35 and higher. Here we report low order harmonics in nitrogen that are generated from HOMO-1.

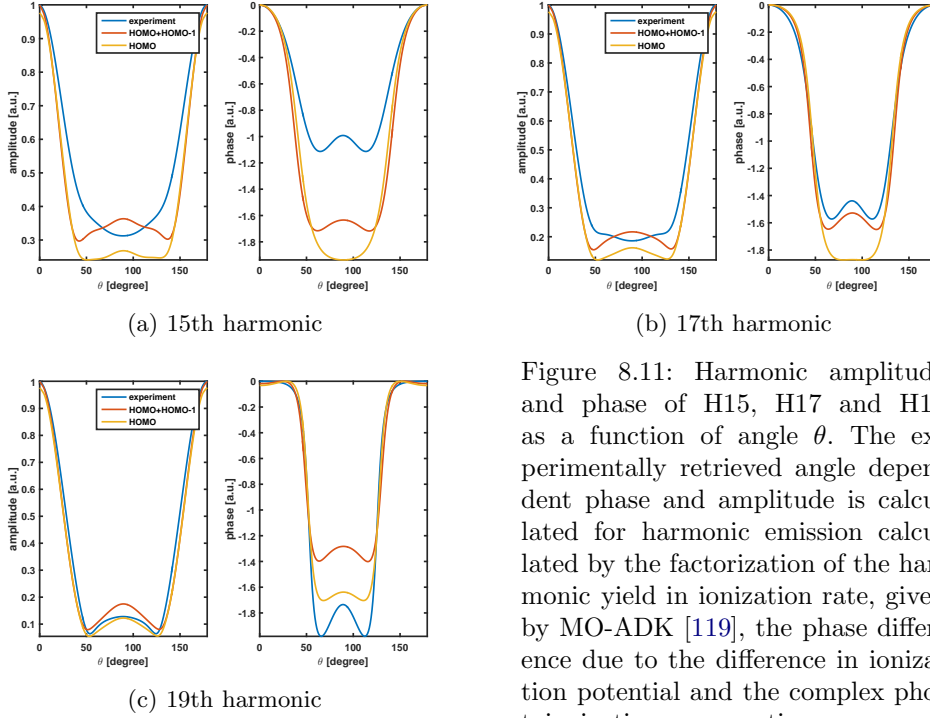


Figure 8.11: Harmonic amplitude and phase of H15, H17 and H19 as a function of angle θ . The experimentally retrieved angle dependent phase and amplitude is calculated for harmonic emission calculated by the factorization of the harmonic yield in ionization rate, given by MO-ADK [119], the phase difference due to the difference in ionization potential and the complex photoionization cross section

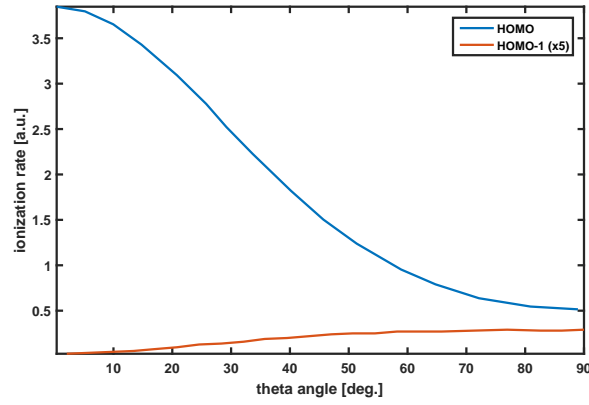


Figure 8.12: Ionization rates for HOMO and HOMO-1 as a function of molecular axis orientation. The data is taken from [119] and calculated for a driving laser intensity of $1 \cdot 10^{14} \text{W/cm}^2$. The HOMO-1 rate is multiplied by a factor of 5. Both orbitals have significant ionization rates at an angle of 90 deg.

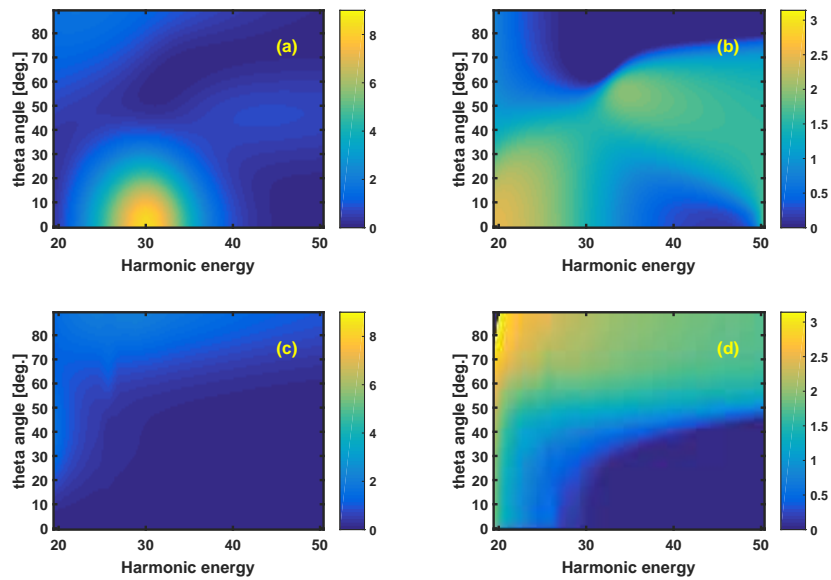


Figure 8.13: Photoionization cross section (a) for HOMO and phase in (b) as function of harmonic energy and molecular axis orientation. In panel (c) the amplitude for the photoionization cross section of HOMO-1 is given and its phase in panel (d). A shape resonance at 30 eV is visible followed by a Cooper minimum at 50 eV. At angles bigger than 45° features are visible at lower photon energies.

Chapter 9

The complex induced dipole of ethylene

Experiments in HHG have been limited to the study of one dimensionally aligned molecules [46,57,123] and, more recently, to the study of oriented molecules [124]. We extend the study to the asymmetric rotor of ethylene, which allows us to study the dependence of HHG on two Euler angles, which define the orientation of the molecule with respect to the polarization axis of the pump and probe pulses. In Section 3.3.4, we showed that with a linearly polarized pump pulse and an asymmetric rotor, we can extract the harmonic dipole as a function of the Euler angles θ and χ . This extends the pioneering work of Varun Makhija [64] on strong field ionization of two dimensionally aligned ethylene to the process of HHG. As we pump the molecular ensemble with a non-adiabatic pump pulse, we form a rotational wave packet that depends on the two Euler angles θ and χ , where we defined the angles in Figure 3.3 in Section 3.3 and Figure 9.1. Since the laser polarization axis is directed along Z, the angular distribution will not depend on the precession ϕ around the z-axis, as the pump pulse does not align this axis over the multiple cycles of the laser. If we are able to describe the evolution of the molecular ensemble well, we can extract the double-angle dependent yield and phase of the produced harmonics. We start with the same ansatz as proposed in the previous chapter: We fix the molecule in space and rotate the molecule to a particular set of χ, θ and probe the molecule with high harmonic generation. The generated harmonic yield will depend on the molecular symmetry and will change as we change the two angles. For nitrogen we used orders of $\cos^{2n} \theta$ with $n = 0, 1, 2, 3$ to describe any angle dependence in θ , but for the dependence in χ and θ we have to use a basis set that can describe any dependence in both angles. We chose Wigner functions $D_{m,k}^j(\theta, \phi, \chi)$ and can expand our unknown signal S with

$$S(\theta, \chi) = \sum_{j,k} C_k^j D_{m,k}^j(\theta, \phi, \chi) \quad (9.1)$$

where $m = 0$ and the dependence on ϕ is lost, due to the cylindrical symmetry around the Z axis with a linearly polarized pump beam. In the experiment we do not have access to a perfectly aligned molecule and the molecular frame signal is hidden in the convoluted laboratory frame signal that is washed out due to the imperfect alignment. The molecular axis has a distribution function that depends on the non-adiabatic alignment of the molecule. We can write the molecular axis distribution ρ as a function of the angles θ, χ

$$\rho(\theta, \chi, t) = g_i \frac{e^{E_i/kT}}{Z} |\Psi_i(\theta, \chi, t)|^2 \quad (9.2)$$

where $i = \{J_0, M_0\}$ are the quantum numbers of the involved states, g the nuclear spin state weights, k the Boltzmann constant, T the rotational temperature and Z the partition function. The molecular axis distribution ρ depends on both angles and can be interpreted as a probability function of finding the molecule at time t aligned at the angles θ, χ . We can write the time

dependent signal as the integral over all angles of the product of the molecular frame signal of HHG and the molecular axis distribution

$$S(t) = \int \rho(\theta, \chi, t) S(\theta, \chi) \sin \theta d\theta d\chi = \sum_{j,k} C_{j,k} \int \rho(\theta, \chi, t) D_{0,k}^j(\theta, \chi) \sin \theta d\theta d\chi \quad (9.3)$$

where we can solve the integral following Equation 3.106 for every summand with index j, k of the expansion given in Equation 9.1

$$\int \rho(\theta, \chi, t) D_{0,k}^j(\theta, \chi) \sin \theta d\theta d\chi = \langle \Psi_i | D_{0,k}^j | \Psi_i \rangle (t) \quad (9.4)$$

In our experiment, we measure the power spectrum and phase of the emitted light, given by the power spectrum

$$P(\omega) = |\mathfrak{F}(\ddot{d}(t))|^2 \quad (9.5)$$

with $d(t)$, the dipole moment of the electron. The dipole moment $d(t) = |d(t)|e^{i\phi(t)}$ is a complex number that holds phase and amplitude information of ionization, propagation and recombination. We measure in our Young's double slit the phase $\Phi(\omega)$

$$\Phi(\omega) = \arg(|\mathfrak{F}(\ddot{d}(t))|) - \Phi_{ref}(\omega) \quad (9.6)$$

which is the argument of the dipole moment in respect to the reference source. The harmonic field is a function of the pump-probe delay and can be written as the time dependent complex-valued signal

$$S(\omega, t) = \sqrt{P(\omega, t)} e^{i\phi(\omega, t)} \quad (9.7)$$

or as a complex-numbered expansion

$$S(\omega, t) = \sum_{j,k} C_k^j(t) \langle \Psi_i | D_{0,k}^j | \Psi_i \rangle (t) \quad (9.8)$$

where $C = A + iB$ is a complex number and the expansion term $\langle \Psi_i | D_{0,k}^j | \Psi_i \rangle (t)$ a real number. At no time during a revival is a molecular axis distribution given, where the molecular axis aligns preferentially to a set of angles χ, θ in respect to the laser polarization of the pump pulse. Only, while solving the time dependent molecular axis distribution and having a good confidence level, we can extract structural features out of the complex-valued high harmonic yield of aligned ethylene gas. Ethylene has a electronic structure given by the HOMO with an ionization potential of 10.51 eV, while the next lower lying orbital has an ionization potential of 12.82 eV. This target could potentially produce harmonics from the HOMO-2 orbital as well, as the ionization potential is given at 14.69 eV. In Figure 9.1, we show the symmetry of the HOMO and HOMO-1 orbital in respect to the stick model of C_2H_4 on the right.

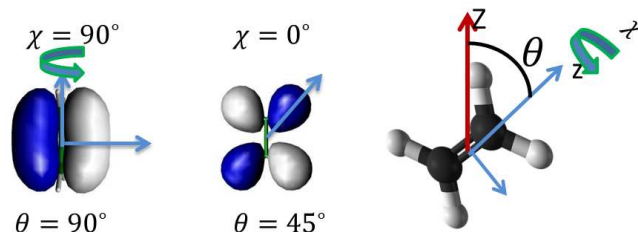


Figure 9.1: The molecular axis z of C_2H_4 is given by the C-C bond and the angle θ is defined as the angle between the laser polarization along Z and the molecular axis z , where the molecule's intrinsic rotation around z is given by χ . On the left, we show the symmetry of the HOMO and in the middle the symmetry of HOMO-1 with the arrows and values giving the maximum in the electron density of the individual orbital.

9.1 Measurement of the absolute harmonic dipole

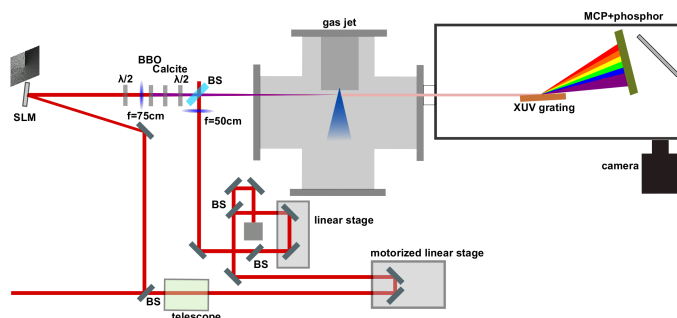


Figure 9.2: Experimental pump probe setup

As introduced in Section 8.2, we use the two source interferometry setup to measure the relative phase between two harmonic sources generated from ethylene gas. In Figure 9.2, we use the same optical setup as in the experiment with nitrogen, but block one of the two pumps. The probe arm is shaped by the SLM into two sources through interference of two beams with opposite angular momentum, explained in Sections 3.5.1 and 4.2.1. After the light passes a $f=75$ cm lens, which will focus it at the position of the gas jet, we place a beta barium borate (BBO) crystal in the laser beam. It creates the second harmonic of the fundamental laser and we control the overlap between the fundamental and second harmonic with calcite plates and the polarization of light with a half-wave plate. Both pulses are s-polarized after passing through the optics. The relative flux of the second harmonic is 25% of the the total flux. Spot size measurements were shown in Figure 4.7 of Chapter 4 for the 785 nm component and spot size measurements of the second harmonic showed matching focusing behavior. The chirp of the 785 nm pulse is adjusted with a grating based compressor inside the chirped pulse amplifier. The pulse has a measured duration of 30 fs. The harmonic cutoff is a good indicator to find the shortest pulse, resulting in the highest peak intensity and cutoff. The pulse duration of the second harmonic is estimated between 50 and 60 fs and the intensity of the second harmonic is given with $0.1I_{785}$. As introduced in Section 4.2.2, the synthesized electric field produces a harmonic spectrum of even and odd harmonics in the experiment, while we now have two harmonic sources, driven by a two-color field, that produce a interference for individual orders in the far field on our detector. We are using two colors to increase the number of harmonics from 4 to 7 harmonics and we can study a more detailed energy dependence in the experiment. In the experiment, we check the spatial and temporal overlap between the pump and the two probes, as described in Chapter 8, where the target was nitrogen. We switch between phase masks on the SLM and overlap the pump

beam with a single beam, after which we switch back to the two-source phase mask and proceed with the measurement of amplitude and phase. As a function of delay between pump and the harmonic generating probe, we measure the amplitude of the light as well as the relative phase between the reference and the signal. In the experiment, ethylene gas is expanding into a vacuum chamber. The molecules can cool rotationally through supersonic expansion to a temperature of 40 K. With this temperature, the molecule's initial rotational wave function is described by 700 rotational states. The aligning beam has a pulse duration of 150 fs FWHM, a spot size of $75 \mu\text{m}$, $1/e^2$ Gaussian beam waist and a resulting intensity of 16 TW cm^{-2} .

The intensity of the probe is measured and estimated with the two color field synthesization to be $1.2 \cdot 10^{14} \text{ W/cm}^2$. The molecule is rotationally excited and we can describe the evolution of the wave packet using TDSE calculations [64], where we described the fundamentals of non-adiabatic alignment of an asymmetric rotor in Section 3.3.4. As the molecule rotates, we expect to observe changes in phase and amplitude. Depending on the molecular structure of the molecule, we will be able to see stronger or weaker oscillations as we probe a different molecular axis distribution at each delay point. In Figure 9.3, we plot the amplitude of harmonic orders 8,11,13 and 15 as a function of time between pump and probe. At a time of 0 ps, a crosscorrelation peak is visible, which reduces the harmonic signal, as we ionize more electrons out of $|0\rangle$, the ground state as introduced in the SFA in Chapter 3, and reduce the amplitude of the ground state, which then reduces the strength of the matrix element $\langle k | \vec{r} | 0 \rangle$ and the harmonic yield. For delays greater than 0 ps, we can observe a baseline shift from 1 a.u. to 0.97 a.u., where a.u. stands for arbitrary units in the chapter. The amplitudes are normalized to the recorded amplitudes, before the pump pulse has interacted with the gas at times less than 0 ps. As the molecule forms revival structures as a function of time after the initial kick, we see different amplitudes, when we probe the molecule with our intense driving field and collect the harmonic emission. At a time of 9.1 ps, we observe a J-type revival, where the amplitude for harmonic 15 initially increases and drops immediately to its lowest local value of 0.92 a.u.. It then increases again to its local maximum at 9.5 ps, before the next revival occurs at a time of 10 ps: a C-type revival. These two revivals are the most dominant revivals in the time-dependent behavior of non-adiabatically aligned ethylene for the experimentally achievable rotational temperatures. Faster revivals are small in amplitude and hard to discern from half-revivals of the C-type and J-type revival. J- and C-type revivals reoccur at 18 and 20 ps and, when probed with HHG, show a different time dependence in respect to the same revivals at 9.1 and 10 ps. At a time of 27 to 31 ps, there is no more clear revival structure and the periodicity is not discernable by eye. At no time during a revival is a molecular axis distribution, where the molecule aligns preferentially in θ and χ with respect to the laser polarization of the pump pulse. Previously, in the case of nitrogen, we had an alignment of the molecular axis with the laser polarization at every half and full B-type revival, where the revival structure does not change after multiple revivals. This is not the case in ethylene.

While the harmonic amplitude was defined as the square root of the total intensity of Young's double slit, the phase is extracted out of the time dependent fringe projection. We show the time-dependent fringe-projection of harmonic 11 in Figure 9.4. At each time, we perform a fast Fourier transformation and extract the phase of the fringe frequency, which is equivalent to the phase between the two harmonic sources.

Revival	position	time
A-type	$t = n/4A$	1.71 ps
C-Type	$t = n/4C$	10.07 ps
K-Type	$t = n/4A - 2B - 2C$	2.11 ps
J-Type	$t = n/2(B + C)$	9.12 ps

In Figure 9.5a, we plot the phase of harmonic orders 8,11 and 13 as a function of time between pump and probe. At a time of 0 ps, we see a similar crosscorrelation peak between pump and probe, as previously seen in the collected amplitudes. A completely washed out fringe pattern appears in the detector image at a delay of 0 ps. The measured phases are relative to the extracted phase of the harmonic emission at a delay of 0 ps, before the pump interacted with the gas. As a function of time, we see changes in the phase. For harmonic 8 in Figure 9.5a at a time of

9.1 ps, we observe a phase relative to the isotropic phase of 70 mrad, that reduces to 0 mrad at a time of 9.7 ps between pump and probe. This feature correlates with the J-type revival of the rotational wave packet. We see a broad feature in the phase of harmonic 8 at a time of 19 ps, associated again with the J-type revival. Fast revivals with smaller amplitude are detected. The phase of harmonic 11 in Figure 9.5b shows the strongest magnitude in oscillations as a function of delay between pump and probe. At a delay of 9.1 ps the phase is measured to be 220 mrad relative to the isotropic phase, before the pump interacts with the molecule. At a delay of 19 ps we see a broad feature in time, where the phase changes by an absolute value of 100 mrad from a value at 18 ps. The phase shows another sharp feature at 27 ps, where the rotational wave packet forms another J-type revival. The signal at 30 ps is a systematic error signal in our study and does not influence the result of this study. It is a sharp feature in our measurement with a much bigger error bar, compared to the measurements at other delay values. In Figure 9.5c, the phase of harmonic 13 as a function of time has a reduced magnitude in oscillations. We observe similar features as in the delay dependence of harmonics 8 and 11. A peak at 9.1 ps gives a phase difference of 30 mrad compared to the isotropic value. A broader feature at 19 ps is visible in the phase measurement, but only shows a oscillation of 40 mrad. The error bars for harmonic 13 are comparable to the observed modulation in phase.

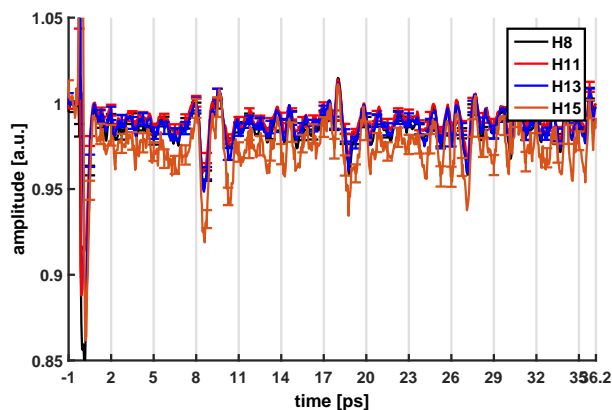


Figure 9.3: Measured amplitude of harmonics generated in Ethylene. Harmonics 8,11 and 13 show similar behavior. Harmonic 15 shows a stronger delay dependence.

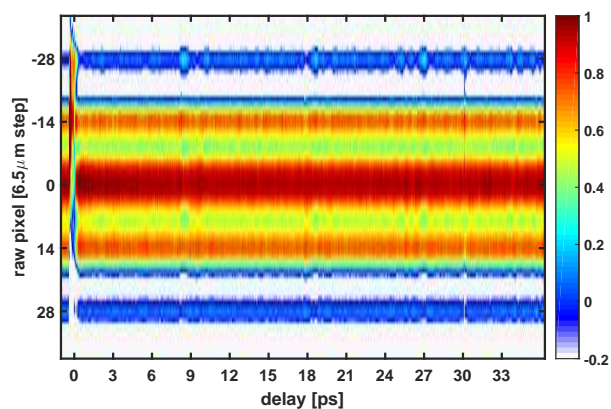


Figure 9.4: Measured interference pattern of harmonic 11 generated in Ethylene as a function of pump-probe delay. A raw pixel count of 14 pixel is equal to a phase difference of 2π

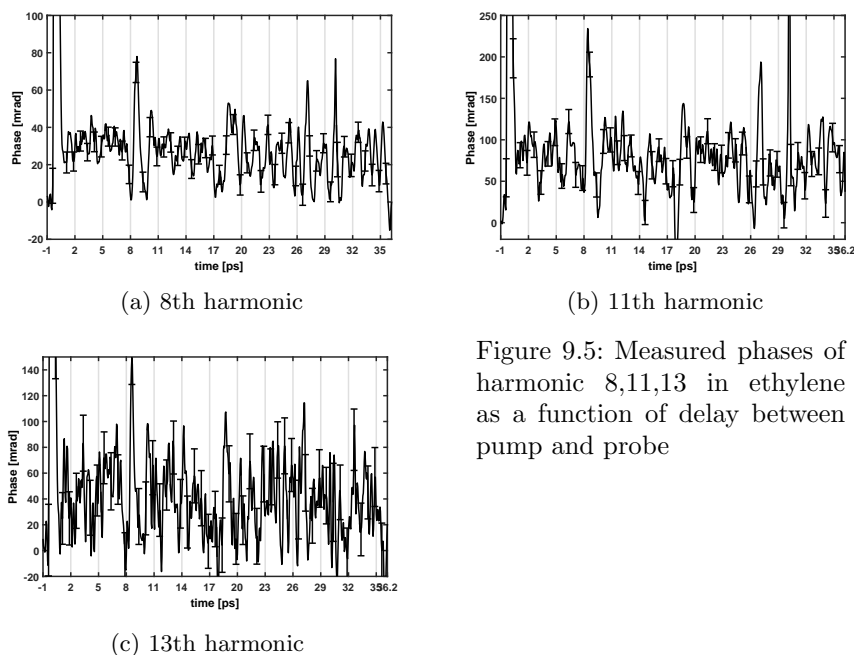


Figure 9.5: Measured phases of harmonic 8,11,13 in ethylene as a function of delay between pump and probe

9.2 Extraction of the angle dependence out of the time-dependent observations

We express the molecular frame signal with Equation 9.1, where we use orders up to $j = 0, 2, 4$ and $k = 0, 2, 4$. The time dependent laboratory frame signal can be written with Equation 9.8. Our experimentally collected data in phase and amplitude is converted to a complex number, while we cut the experimental and theoretical data to a window in time starting after the end of the crosscorrelation peak. We perform a linear regression to our experimental data in the window of 2 ps to 35 ps. The linear regression is explained in Appendix A. We perform multiple linear regressions to find the molecular axis distribution that describes the experimental results with the smallest residue. In each linear regression, we change the input properties to calculate the molecular axis distribution. We create an array of pulse durations, pulse intensities and temperature and for each linear regression, we get a value of χ^2 , which defines the quality of the fit. We choose the minimum value, as it describes the best overlap to the experimental data. After the extraction of the values of C in Equation 9.8, we convert the fit from the complex values to amplitude and phase and compare the fit to our experimental data. In Figure 9.6a we show the fit for the time-dependent amplitude of harmonic 8. The agreement between fit and experimental data is good. Small features as a function of time can be expressed by our fit. In Figure 9.6b experiment and fit agree as well. The experimental fit shows a deviation from the experiment in the time window below 5 ps. We show the amplitude of harmonic 15 in Figure 9.6c. Within our experimental error, the data and fit agree. Figure 9.6d shows the one-dimensional expectation value of $\langle \Psi_i | \cos^2 \theta | \Psi_i \rangle (t)$ of the projection of the molecular axis onto the lab frame given Z axis, the metric used in nitrogen to describe the degree of alignment. We can observe the characteristic revival times present in our time-dependent amplitude signal, where smaller features cannot be expressed by this metric and warrant an expansion in the two angles θ and χ .

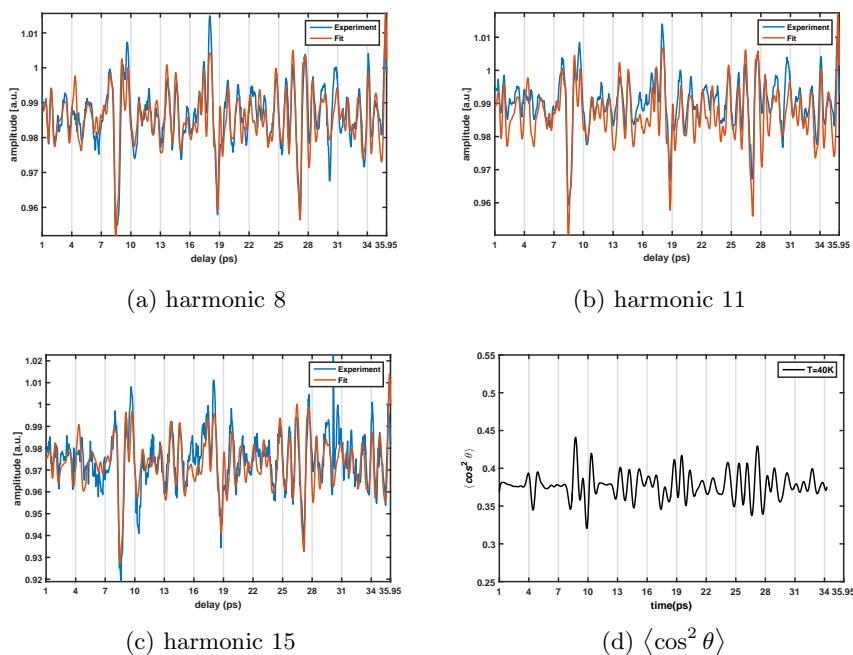


Figure 9.6: Fitted amplitudes of harmonic 8,11,15 in ethylene as a function of delay between pump and probe

In the comparison of the experimentally collected phase and fit for the phase of harmonic 8 in Figure 9.7a, we see good agreement between fit and data at the J-type revival at 9.1 ps. Features at the J-type revivals at 19 ps and 27 ps can be fitted with our expansion as well. However, the residual of the fit has a value of $\chi^2 < 1$, even, when fitted with an expansion that only uses the leading terms $D_0^0 = 1$ and $D_0^2(\theta, \chi)$. The fit is overfitting the experimental data. The experimental determined error bars are smaller than the deviation of the fit from the experimental data. The error bars are on the order of 9 mrad for the phase of harmonic 8 and 30 mrad for harmonic 11. In Figure 9.7c, we can compare the fit with the smallest residue to the experimentally collected phase of harmonic 15. We can see features in fit and data that coincide with the revival times of the J-type revival at 9.1 ps and 18 ps. However, the residue of the fit is still with a value of $\chi^2 < 1$ too small and we are overfitting the experimentally determined phase of harmonic 15. For the phase of harmonic 11 in Figure 9.7b, we can report a fit with a χ^2 -value above 1. The fit with the smallest residue is given in the figure. We can observe matching features between fit and experiment. The retrieved modulations of up to 220 mrad can be matched by the fit. In Figure 9.8, we plot the residue χ^2 as a function of terms in our expansion. When we use an expansion of $C_0^0 D_0^0 + C_0^2 D_0^2$, we get a residual for the imaginary part of the fit of $\chi^2 = 1.25$. By adding D_2^2 to the expansion, so that the fit is now the sum $C_0^0 D_0^0 + C_0^2 D_0^2 + C_2^2 D_2^2$, we get a reduced residual of $\chi^2 = 1.07$, which reduces further, when adding higher order terms as shown in the Figure. In Figure 9.9, the molecular frame amplitude and phase of high harmonic emission of the 11th harmonic is given as a function of the angles θ and χ . In panel (a), the amplitude shows a local maxima at an angle of $\theta = 90^\circ, \chi = 90^\circ$, with a maximum of 1.5 times the isotropic value. In panel(b), the angle dependent phase shows a positive phase for harmonics emitted from an angle $\theta = 90^\circ, \chi = 90^\circ$ and a negative phase for harmonics emitted at angles $\theta = 0^\circ, \chi = 45^\circ$. Investigating the reconstructed angle dependent phase of harmonic 11 as a function of expansion terms in Figure 9.10, where we plot the phase in the molecular frame as a function of the angles θ and χ , we can see that the biggest change in the molecular frame phase is produced when changing from the top left panel (a) to the top right panel (b), where the additional term $C_2^2 D_2^2$ is added. Expansions with higher order terms in the bottom of the figure in panel (c) and (d), do not change the overall trend in the dependency of the phase in the molecular frame: We measure a phase difference of 1 rad between harmonics emitted at an angle of $\theta = 90^\circ, \chi = 90^\circ$ and

harmonics emitted at an angle of $\theta = 45^\circ$, $\chi = 0^\circ$ in the retrieved molecular frame signal.

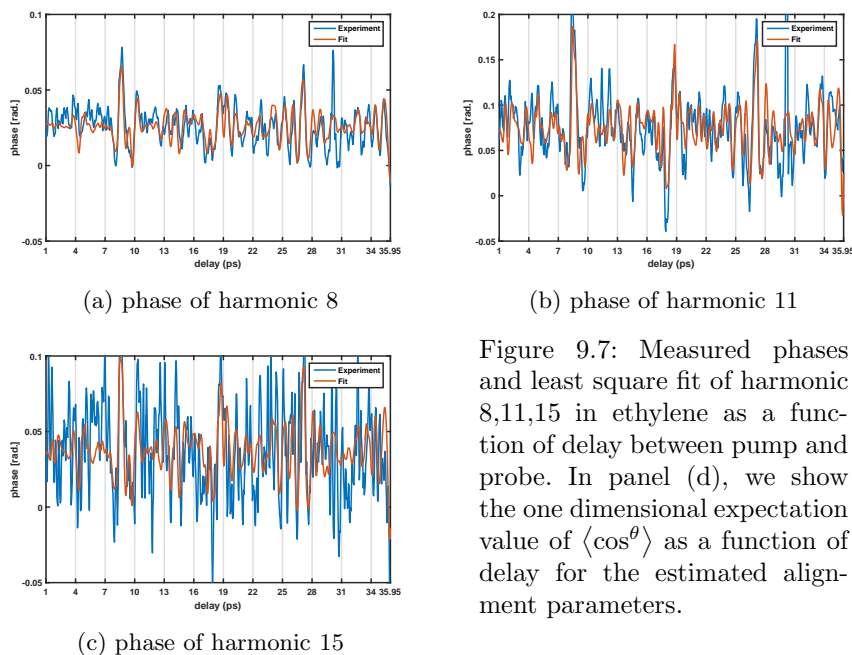


Figure 9.7: Measured phases and least square fit of harmonic 8,11,15 in ethylene as a function of delay between pump and probe. In panel (d), we show the one dimensional expectation value of $\langle \cos^\theta \rangle$ as a function of delay for the estimated alignment parameters.

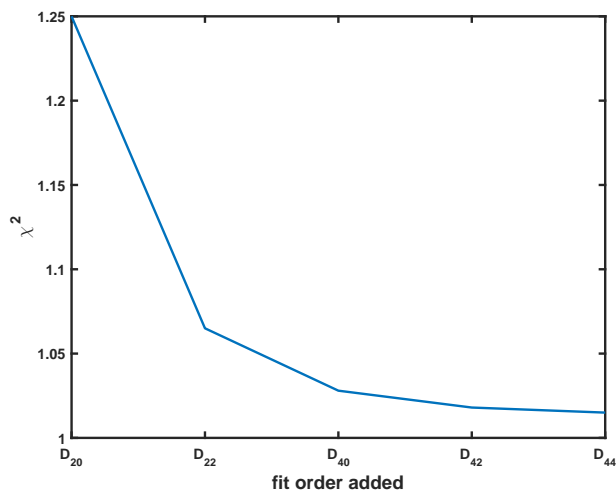


Figure 9.8: Fit residue as a function of additional terms added to the expansion. The residue is shown for the fit to the imaginary component of the complex signal.

Comparing the results for harmonic 11 with QRS calculations of the harmonic dipole of the 11th harmonic (supplied by Ahn Thu Le), we can plot the absolute value of the dipole moment and the phase in Figure 9.11. We give the absolute value of the dipole generated with the HOMO orbital in the top left panel (a) of the figure and its phase in the top right panel (b). In panel (a) the maximum in the molecular frame resolved absolute value of the dipole is given at the angles $\theta = 90^\circ$, $\chi = 90^\circ$, which follows the molecular symmetry of the HOMO given in Figure 9.1, where the electron density of the orbital also has the maximum at these values. The molecular frame resolved phase of harmonic 11 shows the opposite behavior in the χ angle, with a increasing phase from $\phi(\chi = 90^\circ) = 4rad$ to $\phi(\chi = 0^\circ) = 4.5rad$. In the bottom panels (c,d), we plot the absolute value of the dipole generated out of the HOMO-1 orbital on the left (c) and its phase on the right (d). The absolute value of the harmonic dipole out of HOMO-1 shows a maximum in its strength

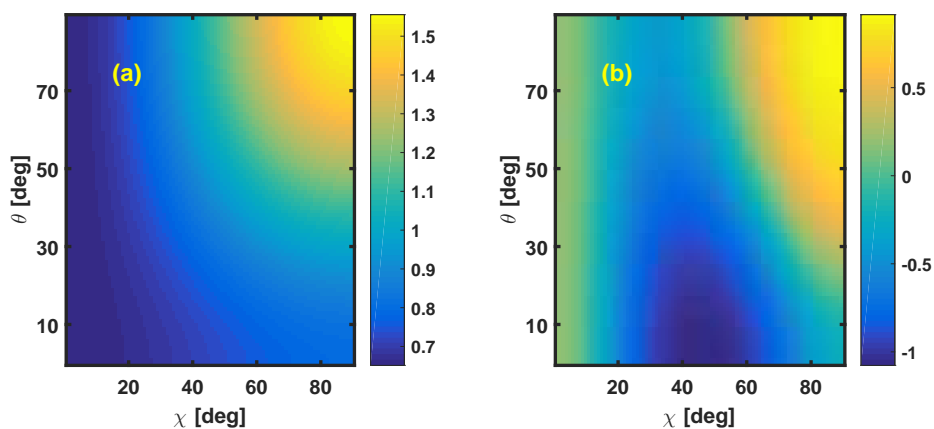


Figure 9.9: Amplitude (a) and phase (b) in the molecular frame retrieved from an expansion with $j = 4, k = 0$ and lower order terms and fit to the time dependent amplitude and phase of harmonic 11.

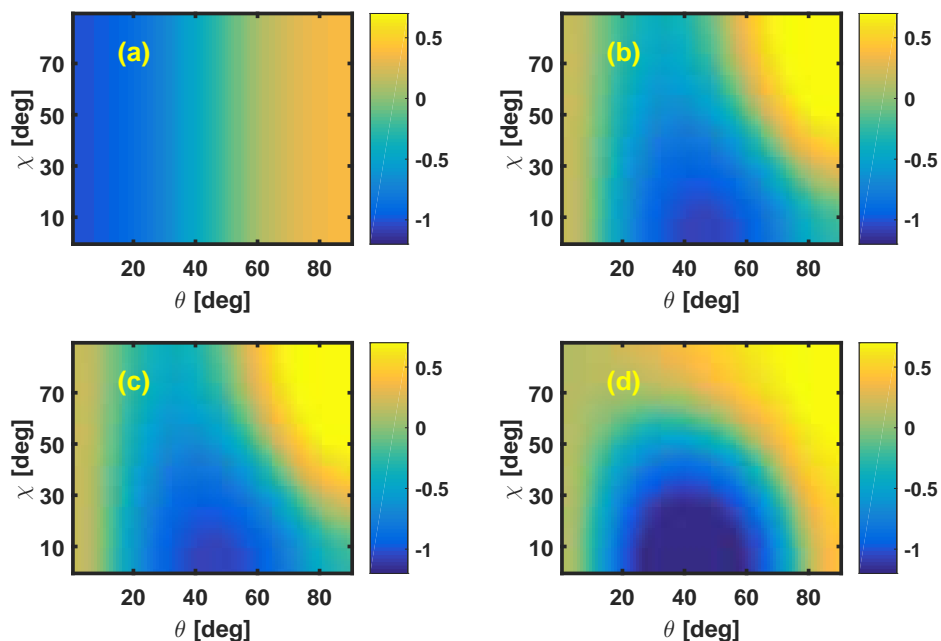


Figure 9.10: Harmonic phase as a function of θ, χ extracted out of the fit. In panel (a), the expansion is for terms of order D_0^0 and D_0^2 . In panel (b) we add the term D_2^2 and in panel (c) we have the terms D_0^0, D_0^2, D_2^2 and D_0^4 , while in panel (d), we further add the term D_2^4 . Adding additional terms, the result shows a phase difference between $\theta = 90^\circ, \chi = 90^\circ$ and $\theta = 45^\circ, \chi = 0^\circ$

at the angles $\theta = 45^\circ, \chi = 0^\circ$, but an overall strength weaker by a factor of 3, compared to the strength of the harmonic dipole out of HOMO shown in panel (a). The harmonic dipole of H11 from HOMO-1 resembles the molecular symmetry of HOMO-1 given in Figure 9.1. However, the phase of the harmonic dipole shows an opposite behavior in χ again; with an increasing phase from $\phi(\chi = 0^\circ) = 3rad$ to $\phi(\chi = 90^\circ) = 4.5rad$. In the absolute values of the dipole, we can see the symmetry of the molecular orbitals, while the phase does not resemble the molecular orbital symmetry, but shows a maximum for HOMO at an angle of $\theta = 90^\circ, \chi = 0^\circ$ and the HOMO-1 shows a local maximum at $\theta = 90^\circ, \chi = 90^\circ$. The molecular frame phase extracted in our experiment in Figure 9.9, panel (b) does not match the phase of the HOMO dipole moment, given in Figure 9.11 panel (b), while the extracted absolute value does match the harmonic dipole calculated with QRS.

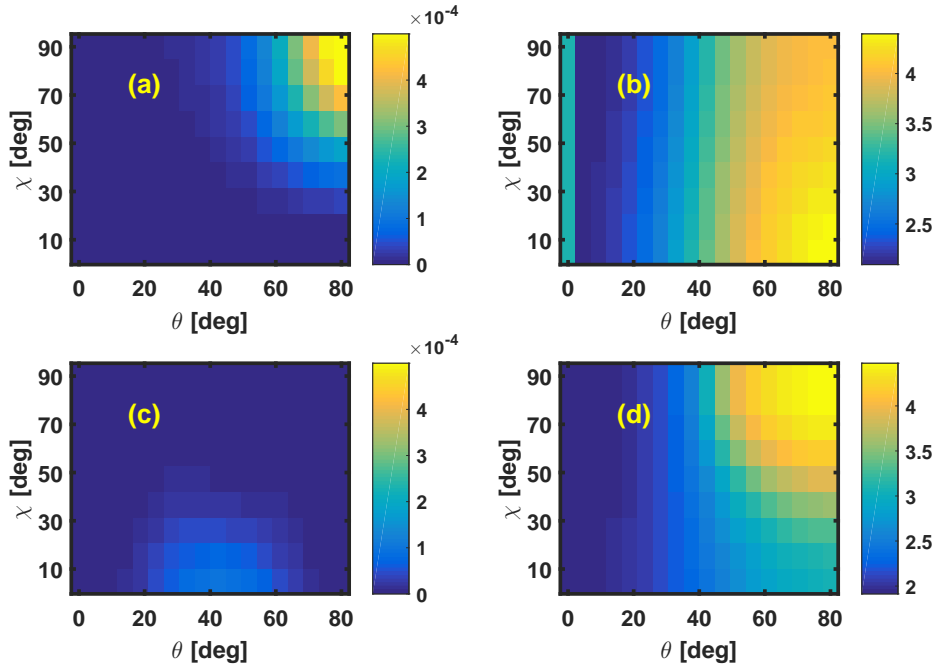


Figure 9.11: QRS calculations for the amplitude in panel (a) of harmonics emitted from HOMO and phase in panel (b). In panel (c) we show QRS calculations for the amplitude of the induced dipole for harmonics out of the HOMO-1. In panel (d) we show the associated phase.

However, considering ionization from HOMO and HOMO-1 with the given ionization potentials of 10.52 and 12.82 eV, we define the total harmonic dipole, emitted from ethylene, as the coherent sum of harmonic dipoles of the individual orbitals

$$d_{total} = d_{HOMO}e^{i\phi_{HOMO}} + R \cdot d_{HOMO-1}e^{i\phi_{HOMO-1}} \quad (9.9)$$

where the phase and amplitude are determined by the argument and absolute value of d_{total} . We give the absolute value in Figure 9.12 and the phase in Figure 9.13, where we assume a value for R , which weighs the contribution of HOMO-1 to the total harmonic dipole, based on a relative ionization rates, that we do not know experimentally. As soon as we add a value for $R \neq 0$ to the equation and plot the angle dependent phase and amplitude, we can see an improved agreement between the experimentally retrieved data and the harmonic emission. In Figure 9.12 panel (a) we show the experimentally retrieved angle dependent amplitude of harmonic 11 with a maximum in amplitude at $\theta = 90^\circ, \chi = 90^\circ$ of 1.5 a.u. and decrease in amplitude as a function of θ and χ , while the amplitude at $\theta = 0^\circ$ has a global minimum at every angle in χ , due to

nodes of the HOMO and HOMO-1 at $\theta = 0^\circ$. In panels (b) through (d), we show a molecular frame amplitude of harmonic 11 calculated through the coherent sum of harmonic dipoles of the HOMO and HOMO-1. In panel (b), no HOMO-1 is added and we see a harmonic amplitude that has a maximum at $\theta = 90^\circ, \chi = 90^\circ$, and when we add a component from the HOMO-1 harmonic dipole in panel (c), the amplitude does not change at the angles $\theta = 90^\circ, \chi = 90^\circ$, but we get a molecular frame dependent harmonic amplitude that now has a small component at the angles $\theta = 45^\circ, \chi = 0^\circ$ that stems from HOMO-1. Comparing the calculations in panel (c) with the experimentally retrieved data in panel (a), we can see still good agreement, where the feature at $\theta = 45^\circ, \chi = 0^\circ$ is a very faint feature in both panels. As soon as we add more weight to the dipole from HOMO-1 to the coherent sum, we can see increased contributions to the total harmonic amplitude at $\theta = 45^\circ, \chi = 0^\circ$, which is still weaker by a factor of 3 compared to the harmonic amplitude at $\theta = 90^\circ, \chi = 90^\circ$. When discussing the phase of harmonic 11 in Figure 9.13, we can see the necessity of including a harmonic dipole from HOMO-1 to the total harmonic dipole. In the experimentally retrieved harmonic phase in the molecular frame we can observe a phase difference of harmonics emitted from $\theta = 45^\circ, \chi = 0^\circ$ and harmonics emitted from $\theta = 90^\circ, \chi = 90^\circ$ of $\Delta\phi = 1$ rad. When considering the harmonic phase of the HOMO, calculated by QRS, the phase does show a phase difference of 0.5 rad, but opposite to what we have experimentally retrieved. As soon as we add a component from HOMO-1 to the total harmonic dipole, we can observe matching differences in the experiment and theory. The molecular frame phase is a very strong indicator that the harmonic generation in ethylene is driven by ionization from multiple orbitals.

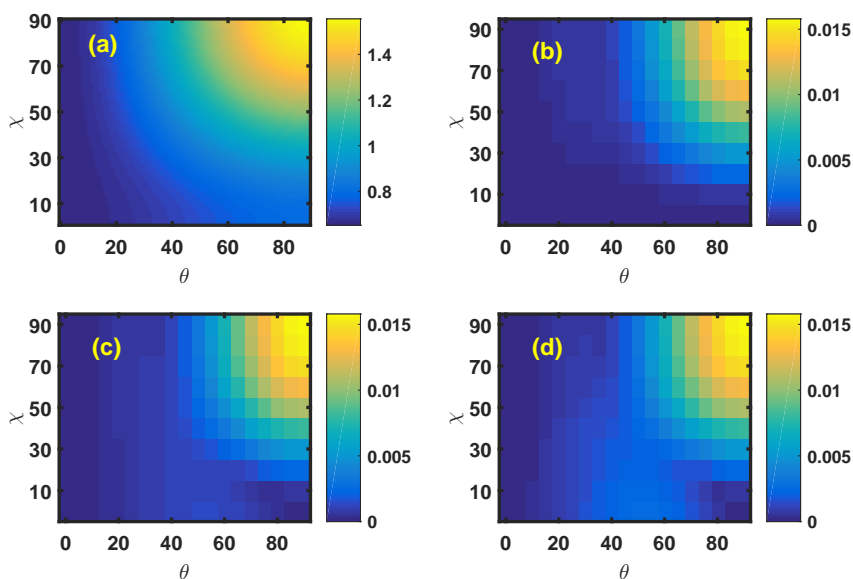


Figure 9.12: Molecular frame amplitude of H11 in the experiment (a), amplitude of the dipole of HOMO only (b), amplitude of the dipole emitted from HOMO and HOMO-1 with a value of $R = 0.1$ (c), and amplitude of the dipole emitted from HOMO and HOMO-1 with a value of $R = 0.2$ (d)

Retrieving the molecular frame amplitude and phase for all measured harmonics, we can plot the angle dependence in Figure 9.14. In the retrieved molecular frame amplitude, we see a local maximum at an angle of $\theta = 90^\circ, \chi = 40 - 80^\circ$. In the molecular frame phase of the detected harmonics we can observe a local maximum in phase at $\theta = 90^\circ, \chi = 40 - 80^\circ$ and a local minimum at angles $\theta = 45^\circ, \chi = 0^\circ$. These features match the molecular structure of the HOMO and HOMO-1 orbital in ethylene, where the HOMO is a π_u orbital and the HOMO-1 a π_g orbital. All fits, except for harmonic 11, are overfitting the experimentally collected imaginary

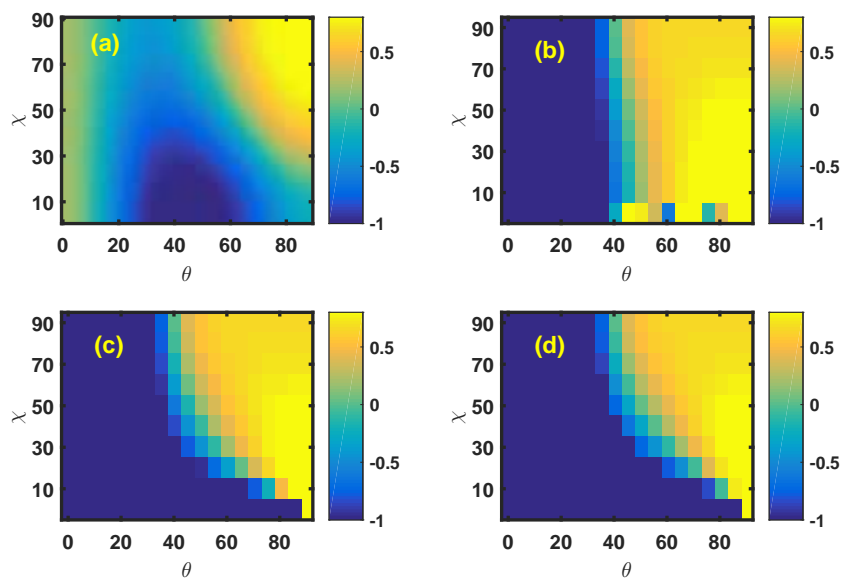


Figure 9.13: Molecular frame phase of H11 in the experiment (a), phase of the dipole of HOMO only (b), phase of the dipole emitted from HOMO and HOMO-1 with a value of $R = 0.1$ (c), and phase of the dipole emitted from HOMO and HOMO-1 with a value of $R = 0.2$ (d)

part of the complex signal.

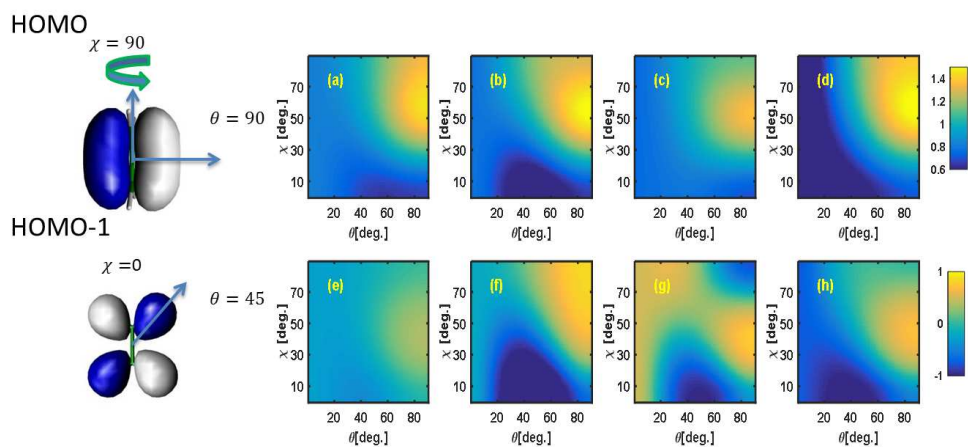


Figure 9.14: Measured molecular frame signal in amplitude (top) and phase (bottom) for various harmonics 8 (a,e), 11 (b,f), 12 (c,g) and 15 (d,h), with the molecular orbital structure given on the left.

Chapter 10

Conclusion and outlook

As discussed in the motivation of this thesis, high harmonic generation is a non linear process of photon up-conversion to the VUV/X-ray region and as such, it depends on the microscopic and macroscopic properties of the medium and laser. Microscopically HHG can be expressed through a three step model, which we have used to investigate the electron wave packet in the continuum and perform coherent, dynamical measurements on the structure of the molecules. On the macroscopic level, we investigated the phase of emitted high harmonics as a function of a delayed driving laser field.

We get access to the phase of the harmonics by an interferometric technique. We systematically improved the technique. Two neighboring foci are produced in a very controlled way from the same driving laser pulse. The harmonics emitted from these two coherent sources interfere in the far field and the phase difference between these two harmonics beams can be extracted from the interference. If one now changes the condition in one of the foci, e.g. by aligning the molecules in the gas of delaying the laser pulse, the phase shifts of the harmonics resulting from the change, can be measured precisely. By delaying one source in respect to the reference source, as previously discussed in Chapter 5, the phase of higher orders scales linearly with the fundamental phase $\Delta\phi_q = q \cdot \Delta\phi$, which we can expect out of the time-dependent picture stated in the experimental chapter. In the experiment, we show a temporal resolution of 12.5 as with error estimates of 1 as and produce two identical sources of HHG.

An important assumption here is that the rayleigh range of the laser is much bigger than the size of the gaseous target and no macroscopic phase mismatches effects the result. When this assumption could not be held in a thicker gas medium, we observed a macroscopic effect on the retrieved phase of high harmonics.

Microscopically, the phase of emitted harmonics is influenced by the electron wave packet in the continuum and the phase of the photoionization cross section. In Chapter 6, we performed intensity dependent measurements of the harmonic phase, which relates directly to the phase of the electron wave packet in the continuum. We have shown a good agreement between SFA theory [21] and our measured intensity dependent phase, which is expressed in SFA with $\Delta\phi = -\alpha I$. However this is only matching calculations in the given intensity regime of $1.3 \cdot 10^{14} \text{W/cm}^2$. For higher intensities, SFA overestimates the intensity dependence of the phase. For very strong laser fields, we see very strong phase modulations, however, the phase differences result in α -coefficients much smaller than the previously calculated coefficients of 10 or the measured coefficients of 5 at low intensities would suggest.

When considering a driving laser field with a small perturbation, given by a second harmonic, we can observe phase manipulations to the the emitted harmonics as expected by SFA by a electric field of the given intensities. The second harmonic purely acts as an perturbation to the recombination step and does not affect the electron wave packet in the continuum to alter the phase of the harmonics.

In the experiments of Chapter 7, we have shown from simple ellipticity dependent measurements of HHG that we can reconstruct the double differential photoionization cross section of argon's valence shell. As we self-probe the atom with different electron energies, we can see the strong

influence from its Cooper minimum at 40 eV. At this energy, the differential cross section not only has a local minimum as observed in the collected harmonic spectra in Figure 7.7, but also has a completely different angular distribution with $\beta = 0$, compared with an electron with 20 eV energy upon recombination. At this energy the photorecombination cross section has an angular distribution following $\approx 3 \cos^2 \theta$. The recombination cross section for an electron with 40 eV is angle-independent, so that the relative yield of harmonics emitted from electrons with this particular energy have a smaller ellipticity dependence in the experiment.

After reconstructing the double differential photoionization cross section of an atom with a very strongly defined Cooper minimum, we investigate features of the photoionization cross section in molecular nitrogen. The photoionization dipole is a complex entity, where the operation $\langle \Psi_k | d | 0 \rangle$ does not have a real eigenvalue. High harmonics enable us to measure the phase and amplitude of the photoionization cross section. We can study it as a function of non-adiabatic alignment in nitrogen. In the atomic target of argon, ionization is occurring from the 3p orbital with an ionization potential of 15.76 eV, while it is safe to assume that we do not ionize from the lower lying orbital of 3s with an ionization potential of 27.63 eV. However in molecular targets, this gap is much smaller. In the experiment in Chapter 8, we studied the high harmonic generation of nitrogen and resolved the molecular-frame dependent phase and amplitude by means of non-adiabatic alignment. We are able to relate the high harmonic yield measured in the laboratory frame as a function of time to the molecular frame dependent yield and phase of the observed harmonic radiation. In the angle dependent phase and amplitude, we can observe features that cannot be explained by the emission of harmonics produced by electrons out of the HOMO only, but have to be explained by a coherent sum of harmonic emission from the HOMO and the next lower lying orbital HOMO-1 with a gap of 1.3 eV to the potential of the HOMO. Using the factorization of HHG, we can construct the molecular frame induced harmonic dipole with given ionization rates and photoionization cross section, while accounting for the phase difference of the electron wave packet in the continuum, due to the difference in ionization potential. The measured and theoretical constructed dependencies match.

A very interesting molecule to study is an asymmetric top such as ethylene. In ethylene, the alignment pulse excites rotations in the nutation angle θ and in the angle of intrinsic rotation χ and we get access to these angles in the experiment. Ionization experiments [64] show features from HOMO and HOMO-1 in the angle dependent ionization yield measurements. We extend this study to the plane of single-photon ionization using HHG, where we can measure the complex-valued cross sections. In the experiment, phase oscillations are small and, although collected over a very long period of time, we are at the limit in the signal to noise ratio. With standard errors in the 10 mrad range, statistical error bars are excellent, but systematic errors and the absolute resolution of the device start to play a bigger role. Some of the delay dependent phase measurements are still noisy and only one harmonic out of 7 shows a reasonable agreement with the expansion in Wigner functions. For this harmonic we get an angle dependent complex dipole moment that can be explained with supplied QRS calculations. When both HOMO and HOMO-1 induced dipoles coherently add to a total dipole, we can successfully show the angle resolved complex harmonic dipole for an asymmetric rotor.

In the future one can further improve the experimental setup. By using a longer wavelength, we can get better energy resolution and commercial SLM's are available for 1500 nm. To get the best energy-resolution, one can use optical gating techniques to create a quasi-continuum in the spectrometer that might enable the energy-dependent phase measurement in an in-situ optical experiment, that is so far only possible with RABBIT-type measurements [54]. Unfortunately both techniques will result in a reduced yield and statistics that will make the experiment harder. A different weak spot of the measurements is the ability to resolve the interference pattern. Higher resolution detectors like XUV-cameras are limited in the active area and are very expensive. To solve this, one can still rely on MCP-detectors, but increase the distance between interaction and MCP detector and/or decrease the distance between the two slits. Combining these techniques might give further insights to different processes in HHG.

Chapter 11

Acknowledgement

After finishing up this dissertation, I would like to thank my advisors Reinhard Dörner and Carlos Trallero-Herrero for their trust and the opportunity to work on my dissertation with them. It has been 8 years, since I took my first class with Reinhard in Frankfurt and 6 years, since he offered me a project for my Bachelor's thesis.

It continued with my Master's and the joint work with Carlos in Manhattan, KS. 5 years later, I enjoyed working on my dissertation project, while it was sometimes troubled with broken laser systems. However, the problems were always solved by skilled and devoted co-workers, which I am grateful for: Ren Xiaoming, Adam Summers, Derrek Wilson and Stefan Zigo. Especially Ren Xiaoming, Varun Makhija and their advisor Vinod Kumarappan introduced me to molecular alignment and complex experimental setups. Their expertise helped me form the direction of my dissertation in the experiments of molecular targets.

I enjoyed the collaboration with Mickael Frolov, Benjamin Wilson, Kristen Gould and Erwin Poliakoff on the atomic photoionization experiment. In the last chapter of my work at the JRM laboratory, I enjoyed working with Georgios Kollopiolos on the experiments involving the ultra-stable interferometer and the intensity-dependent phase of HHG. He and I are currently working with Travis Severt on multiple projects of two-color driven HHG sources.

Writing all these words and spending all the hours in the lab, I am thankful for my friends and family. Especially for one person outside this space: Christina Klein. It was hard spending these years in different states of the USA, but I am looking forward to spending the rest of my life with her.

Chapter 12

Lebenslauf



Jan Troß

Akademischer Lebenslauf

PERSÖNLICHE ANGABEN

<i>Geburt</i>	2. März, 1988
<i>Geburtsort</i>	Lich, Deutschland
<i>Tel. USA</i>	785 770 5356
<i>Tel. D</i>	06043 3619
<i>Email USA</i>	tross@phys.ksu.edu
<i>Email D</i>	tross@atom.uni-frankfurt.de
<i>privat</i>	jan.tross@gmx.de

AUSBILDUNG

Bsc. of Science, physics

2007-2011

Johann Wolfgang Goethe Univeristät

Abschluss mit Note 2.0, Bachelorthesis: Untersuchung der Rechts-Links-Asymmetrie und des nondipole-Parameters bei Photoionisation

Ms. of Science, physics

2011-2013

Johann Wolfgang Goethe Univeristät

Abschluss mit Note 1.0, Masterthesis: Study of phasematching dependent HOMO-1 contribution in HHG from N₂

FORSCHUNGAUFENTHALTE

Bachelorarbeiten	2010
<i>Johann Wolfgang Goethe Univeristät</i>	
Basisverständnisse in COLTRIMS	
Bachelorarbeiten	2010
<i>Lawrence Berkeley National Laboratory</i>	
Vorbereitung einer COLTRIMS-Apparatur, Analyse vorhandener Daten für die Bachelorthesis	
Masterarbeiten	2011-2017
<i>James R. MacDonald Laboratory</i>	
Arbeit an der Masterarbeit und Doktorarbeit	

VERÖFFENTLICHUNGEN

2013	Measuring the angle-dependent photoionization cross section of nitrogen using high-harmonic generation [46]
2016	Atomic photoionization experiment by harmonic-generation spectroscopy [51]
2016	Imaging the Temporal Evolution of Molecular Orbitals during Ultrafast Dissociation [125]
2016	High order harmonic generation from SF6: Deconvolution of macroscopic effects [126]
2016	Direct measurement of multi-orbital angular contributions in N2 using high harmonic generation, submitted
2017	HHG interferometry with Laguerre Gaussian beams, in preparation
2017	A self-referencing attosecond interferometer, in preparation

Appendix A

Appendix

A.1 Linear regression of a complex entity

Describing a unknown Y as a function of x with coefficients β and an error ϵ

$$Y = x\beta + \epsilon \quad (\text{A.1})$$

we can define the solution β of the equation as

$$\beta = \frac{\sum x_i y_i}{\sum x_i^2} = \frac{XY}{X^2} \quad (\text{A.2})$$

which we can write as the quotient of covariance and variance of the system

$$\beta = \frac{Cov(x, y)}{Var(x)} \quad (\text{A.3})$$

Using weights Ω , we can write the solution β

$$\beta = (X'\Omega X)^{-1} X'\Omega Y \quad (\text{A.4})$$

where Ω is a diagonal matrix with off diagonal terms = 0. The generalized least squares reduces, with $S = \sum w_{ii} r_i^2, w_{ii} = \frac{1}{\sigma_i^2}$ to

$$(X'^T w X')\beta = X'^T w Y \quad (\text{A.5})$$

and the solution

$$\beta = (X'^T X')^{-1} X'^T Y' \quad (\text{A.6})$$

with $X' = wX, Y' = wY$ where the goodness of the fit is given by χ_{red}^2

$$\chi_{red}^2 = \frac{1}{\nu} \sum \frac{(O - E)^2}{\sigma^2} \quad (\text{A.7})$$

where ν is the number of degrees of freedom $\nu = N - P$, with N number of observations and P number of fitted parameters. We can define 3 areas for χ_{red}^2 with $\chi_{red}^2 \gg 1$, where the fit does not reflect the data, $\chi_{red}^2 = 1$ where the fit represents the data with the given error bars and $\chi_{red}^2 \ll 1$, where the data is potentially over-fitted or the error bars overestimated. In our experiments in Chapter 9 and Chapter 8, we collect a complex value Y and we have to solve a complex linear regression, which we can as

$$Re(Y) + iIm(Y) = X \cdot (Re(\beta) + iIm(\beta)) \quad (\text{A.8})$$

where $Re(Y)$ is the real part of the complex number Y and $Im(Y)$ is the imaginary part of the

complex number Y . X is a set of independent linear vectors. We can now write a set of two equations that only share the same X

$$\text{Re}(Y) + X \cdot \text{Re}(\beta) \quad (\text{A.9})$$

$$\text{Im}(Y) = X \cdot \text{Im}(\beta) \quad (\text{A.10})$$

Our weights can be calculated on the basis of complex numbers $z = a + ib$, where through conversion we can write $a = A \cos \theta$ and $b = A \sin \theta$. We get

$$\Delta a = (\cos^2 \theta \Delta A^2 + A^2 \sin^2 \theta \Delta \theta^2)^{0.5} \quad (\text{A.11})$$

$$\Delta b = (\sin^2 \theta \Delta A^2 + A^2 \cos^2 \theta \Delta \theta^2)^{0.5} \quad (\text{A.12})$$

and with $\theta \approx 0$, which is the case for ethylene, we can write

$$\Delta a = \Delta A \quad (\text{A.13})$$

$$\Delta b = A \Delta \theta \quad (\text{A.14})$$

A.2 Spot size measurements

As seen in Chapter 4, we are able to shape the laser focus with a spatial light modulator. We showed symmetric spot sizes as a function of focus for various approaches. When interfering Laguerre Gaussian beams with OAM, we were able to generate a double focus in space that allows us to generate interference pattern in HHG to collect phases between the two harmonic sources. However, due to the interference requirement, these spatially shaped foci have to be aligned carefully. In Figure A.1, we did not properly align the incoming laser beam in respect to the surface of the SLM and the resulting focus as a function of relative position is no symmetric. One source is weaker than the other and the overall focus is not symmetric in respect to 0 mm. However, if we switch to a phase mask on the spatial light modulator that does not shape the focus through interference effects, but uses the approach of tilted beams as introduced in Section 4.2.1, we can measure a completely symmetric and balanced two source focus in Figure A.2. These two focus projections were taken back to back and nothing was changed, except the exposure and the phase mask on the SLM. Asymmetric Laguerre Gaussian beams [127] have been studied in other fields of research. In the reported experiments, we carefully align the optical beam path and carefully check that the two sources are equal, as seen in Figure 4.7 in Chapter 4.

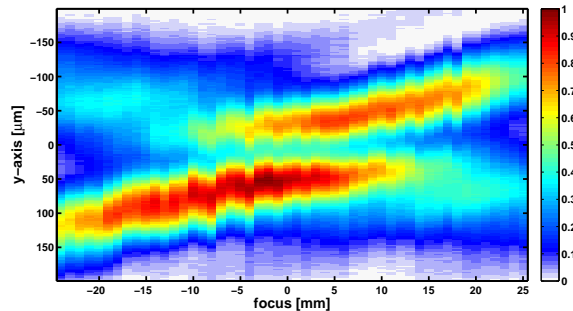


Figure A.1: Beam waist projection of a LG two source interference focus as a function of CCD camera position in respect to the laser focus.

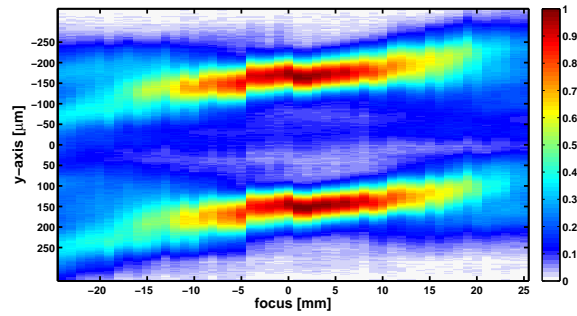


Figure A.2: Beam waist projection of a tilted beam two source focus as a function of CCD camera position in respect to the laser focus

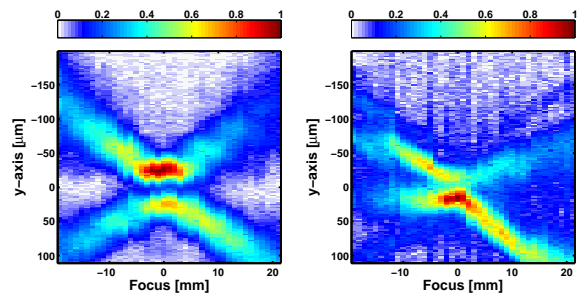


Figure A.3: Beam waist projection of a LG two source interference focus as a function of CCD camera position in respect to the laser focus. A second harmonic is present. On the left, a filter to block 392 nm light was installed and on the right, a filter to block 785 nm light was installed.

A.3 Bending effects

As the delay between the two foci is changed, we observed a change in phase between the emitted harmonics. On top of this change in phase, we observed a small change in pointing of the harmonic beam. This change can be explained with Figure A.4, as it shows a gradient in the phase of the focus light that depends on the delay between the two foci. This shows that even with the rather big separation of $100\ \mu\text{m}$ of our two foci of Gaussian beam waist $40\ \mu\text{m}$, our double slit is still influenced by interference effects. However, they are small and the harmonic sources are affected the same way at each delay.

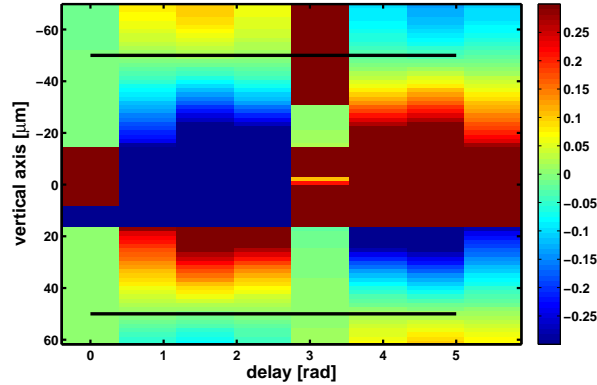


Figure A.4: Phase distribution in the focus as a function of delay between the two foci. The two foci have a center of mass on the black line and as we change the delay, the flat phase profile tilts down with a gradient pointing down. At a phase of π , the profile is flat again and then points in the opposite direction as the delay is increased.

A.4 SLM efficiencies

When a grating like mask is applied, we create a diffraction effect in the reflected light that results in a less efficient reflectivity. In the masks, used in Section 5, we create a mask of two opposite tilted beams and add a phase value of $0 - 2\pi$ on top of one beam, while the second beam has a phase of 0 rad. At a delay of π between, we create a grating like structure with steps of π between adjacent arrays. When the grating is created, the intensity drops and the ion signal as a function of time in Figure A.6a reduces at a value of 1900 as to its minimum.

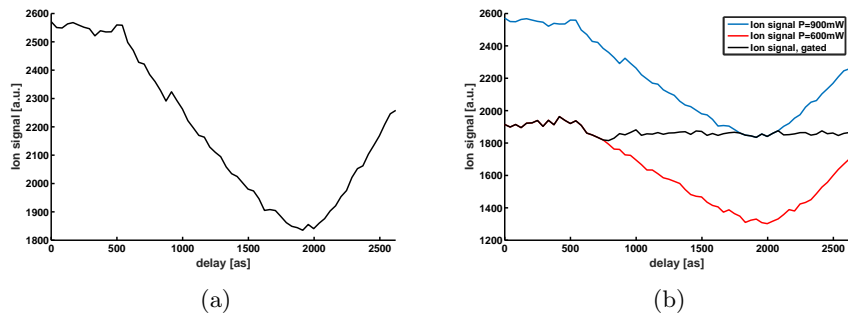


Figure A.5: (a) Collected ionization signal as a function of delay between the two harmonic sources. As we increase the delay on the mask, we generate a diffraction grating with groove jumps of π at a delay of 1800 as. The efficiency of the SLM is decreased. (b) compensating with the intensity by increasing the value by up to 50%, results in a almost flat intensity signal as a function of delay.

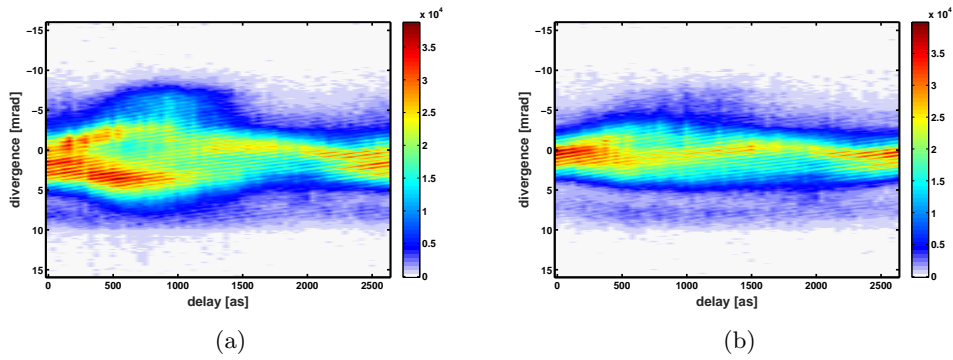


Figure A.6: (a) Collected fringe signal as a function of delay between the two harmonic sources. As we increase the delay on the mask, we generate a diffraction grating with groove jumps of π at a delay of 1800 as. The efficiency of the SLM is decreased and the brightness of harmonics reduced (b) compensating with the intensity by increasing the value by up to 50%, results in a almost flat intensity signal as a function of delay.

A.5 Rotational Constants

Molecule	A	B	C	$\alpha_{\perp}/\alpha_{XX}$	$\alpha_{\parallel}/\alpha_{ZZ}$	α_{YY}	Spin ratio
N_2 [45]	0	1.99824	0	1.45	2.38	0	2:1
C_2H_4 [128]	4.864	1.001	0.828	3.63	5.022	3.25	7:3:3

Table A.1: Rotational constants

Bibliography

- [1] PB Corkum and Ferenc Krausz. Attosecond science. *Nature Physics*, 3(6):381–387, 2007.
- [2] Ferenc Krausz and Misha Ivanov. Attosecond physics. *Reviews of Modern Physics*, 81(1):163, 2009.
- [3] Arthur L Schawlow and Charles H Townes. Infrared and optical masers. *Physical Review*, 112(6):1940, 1958.
- [4] Donna Strickland and Gerard Mourou. Compression of amplified chirped optical pulses. *Optics communications*, 56(3):219–221, 1985.
- [5] Ahmed H Zewail. Femtochemistry: Atomic-scale dynamics of the chemical bond. *The Journal of Physical Chemistry A*, 104(24):5660–5694, 2000.
- [6] Jeffrey L Krause, Kenneth J Schafer, and Kenneth C Kulander. High-order harmonic generation from atoms and ions in the high intensity regime. *Physical Review Letters*, 68(24):3535, 1992.
- [7] Paul B Corkum. Plasma perspective on strong field multiphoton ionization. *Physical Review Letters*, 71(13):1994, 1993.
- [8] KC Kulander, KJ Schafer, and JL Krause. Dynamics of short-pulse excitation, ionization and harmonic conversion. In *Super-intense laser-atom physics*, pages 95–110. Springer, 1993.
- [9] Tenio Popmintchev, Ming-Chang Chen, Dimitar Popmintchev, Paul Arpin, Susannah Brown, Skirmantas Ališauskas, Giedrius Andriukaitis, Tadas Balčiunas, Oliver D Mücke, Audrius Pugzlys, et al. Bright coherent ultrahigh harmonics in the kev x-ray regime from mid-infrared femtosecond lasers. *science*, 336(6086):1287–1291, 2012.
- [10] Michael Chini, Kun Zhao, and Zenghu Chang. The generation, characterization and applications of broadband isolated attosecond pulses. *Nature Photonics*, 8(3):178–186, 2014.
- [11] Richard N Zare. Photoejection dynamics [1]. *Mol. Photochem*, 4:1, 1972.
- [12] RG Houlgate, JB West, K Codling, and GV Marr. The angular distribution of the 3p electrons and the partial cross section of the 3s electrons of argon from threshold to 70 ev. *Journal of Electron Spectroscopy and Related Phenomena*, 9(2):205–209, 1976.
- [13] M Ya Amusia, NA Cherepkov, and LV Chernysheva. Angular distribution of photoelectrons with many-electron correlations. *Physics Letters A*, 40(1):15–16, 1972.
- [14] Stefan Haessler, B Fabre, J Higuët, J Caillat, T Ruchon, P Breger, B Carré, E Constant, A Maquet, E Mével, et al. Phase-resolved attosecond near-threshold photoionization of molecular nitrogen. *Physical Review A*, 80(1):011404, 2009.
- [15] Hans Jakob Wörner, Hiromichi Niikura, Julien B Bertrand, PB Corkum, and DM Villeneuve. Observation of electronic structure minima in high-harmonic generation. *Physical review letters*, 102(10):103901–1, 2009.

- [16] AD Shiner, BE Schmidt, C Trallero-Herrero, PB Corkum, JC Kieffer, F Légaré, and DM Villeneuve. Observation of cooper minimum in krypton using high harmonic spectroscopy. *Journal of Physics B: Atomic, Molecular and Optical Physics*, 45(7):074010, 2012.
- [17] MV Frolov, NL Manakov, TS Sarantseva, and Anthony F Starace. Analytic formulae for high harmonic generation. *Journal of Physics B: Atomic, Molecular and Optical Physics*, 42(3):035601, 2009.
- [18] Eadweard Muybridge and Ventura Mozley. *Muybridges complete human and animal locomotion: all 781 plates from the 1887 'Animal locomotion' by Eadweard Muybridge, introduction to the Dover Edition by Ventura Mozley, Vol. 1, containing original volumes 1 & 2: Males (nude), 3 & 4: Females (nude)*. Dover Publications, Incorporated, 1979.
- [19] LV Keldysh. Ionization in the field of a strong electromagnetic wave. *Zh. Eksperim. i Teor. Fiz.*, 47, 1964.
- [20] MV Ammosov, NB Delone, and VP Krainov. Tunnelling ionization of complex atoms and of atomic ions in an alternating electromagnetic field. *Sov. Phys. JETP*, 64(6):1191–1194, 1986.
- [21] M Lewenstein, Ph Balcou, M Yu Ivanov, Anne Lhuillier, and Paul B Corkum. Theory of high-harmonic generation by low-frequency laser fields. *Physical Review A*, 49(3):2117, 1994.
- [22] S Ramakrishna and Tamar Seideman. Information content of high harmonics generated from aligned molecules. *Physical review letters*, 99(11):113901, 2007.
- [23] M Bellini, C Lyngå, A Tozzi, MB Gaarde, TW Hänsch, Anne L’Huillier, and C-G Wahlström. Temporal coherence of ultrashort high-order harmonic pulses. *Physical Review Letters*, 81(2):297, 1998.
- [24] MV Frolov, NL Manakov, TS Sarantseva, and Anthony F Starace. High-order-harmonic-generation spectroscopy with an elliptically polarized laser field. *Physical Review A*, 86(6):063406, 2012.
- [25] M Ferray, A l’Huillier, XF Li, LA Lompre, G Mainfray, and C Manus. Multiple-harmonic conversion of 1064 nm radiation in rare gases. *Journal of Physics B: Atomic, Molecular and Optical Physics*, 21(3):L31, 1988.
- [26] J - J Macklin, JD Kmetec, and CL Gordon III. High-order harmonic generation using intense femtosecond pulses. *Physical review letters*, 70(6):766, 1993.
- [27] RR Freeman, PH Bucksbaum, H Milchberg, S Darack, D Schumacher, and ME Geusic. Above-threshold ionization with subpicosecond laser pulses. *Physical review letters*, 59(10):1092, 1987.
- [28] KJ Schafer, Baorui Yang, LF DiMauro, and KC Kulander. Above threshold ionization beyond the high harmonic cutoff. *Physical review letters*, 70(11):1599, 1993.
- [29] Arnold Sommerfeld. Über die verteilung der intensität bei der emission von röntgenstrahlen. *Physikalische Zeitschrift*, 10:969–976, 1909.
- [30] Bruce R. Wheaton. *Bremsstrahlung*, pages 78–81. Springer Berlin Heidelberg, Berlin, Heidelberg, 2009.
- [31] Joseph Larmor. Lxiii. on the theory of the magnetic influence on spectra; and on the radiation from moving ions. *The London, Edinburgh, and Dublin Philosophical Magazine and Journal of Science*, 44(271):503–512, 1897.

- [32] Ariel Gordon and Franz X Kärtner. The ehrenfest theorem and quantitative predictions of hhg based on the three-step model. In *Ultrafast Optics V*, pages 183–186. Springer, 2007.
- [33] AM Perelomov, VS Popov, and MV Terentev. Ionization of atoms in an alternating electric field. *Zhurnal Eksperimental'noi i Teoreticheskoi Fiziki (USSR) For English translation see Sov. Phys.-JETP (Engl. Transl.)*, 50, 1966.
- [34] Misha Yu Ivanov, Michael Spanner, and Olga Smirnova. Anatomy of strong field ionization. *Journal of Modern Optics*, 52(2-3):165–184, 2005.
- [35] Zenghu Chang. *Fundamentals of attosecond optics*. CRC Press, 2011.
- [36] Jiro Itatani, Jérôme Levesque, Dirk Zeidler, Hiromichi Niikura, Henri Pépin, Jean-Claude Kieffer, Paul B Corkum, and David M Villeneuve. Tomographic imaging of molecular orbitals. *Nature*, 432(7019):867–871, 2004.
- [37] C Vozzi, M Negro, F Calegari, G Sansone, M Nisoli, S De Silvestri, and S Stagira. Generalized molecular orbital tomography. *Nature Physics*, 7(10):822–826, 2011.
- [38] Shinichiro Minemoto, Toshihito Umegaki, Yuichiro Oguchi, Toru Morishita, Anh-Thu Le, Shinichi Watanabe, and Hirofumi Sakai. Retrieving photorecombination cross sections of atoms from high-order harmonic spectra. *Physical Review A*, 78(6):061402, 2008.
- [39] AD Shiner, BE Schmidt, C Trallero-Herrero, HJ Wörner, S Patchkovskii, PB Corkum, JC Kieffer, F Légaré, and DM Villeneuve. Probing collective multi-electron dynamics in xenon with high-harmonic spectroscopy. *Nature Physics*, 7(6):464–467, 2011.
- [40] Hans Bethe and Walter Heitler. On the stopping of fast particles and on the creation of positive electrons. In *Proceedings of the Royal Society of London A: Mathematical, Physical and Engineering Sciences*, volume 146, pages 83–112. The Royal Society, 1934.
- [41] Lev Davidovitch Landau and Evgueni Mikhailovitch Lifshitz. *Course of Theoretical Physics. Volume 3: Quantum Mechanics*. Pergamon, 1965.
- [42] J Clerk Maxwell. On the dynamical theory of gases. *Philosophical transactions of the Royal Society of London*, 157:49–88, 1867.
- [43] Ludwig Boltzmann. Weitere studien über das wärme-gleichgewicht unter gasmolekülen. In *Kinetische Theorie II*, pages 115–225. Springer, 1970.
- [44] Lars Onsager. Reciprocal relations in irreversible processes. i. *Physical review*, 37(4):405, 1931.
- [45] Anh-Thu Le, RR Lucchese, S Tonzani, T Morishita, and CD Lin. Quantitative rescattering theory for high-order harmonic generation from molecules. *Physical Review A*, 80(1):013401, 2009.
- [46] Xiaoming Ren, Varun Makhija, Anh-Thu Le, Jan Troß, Sudipta Mondal, Cheng Jin, Vinod Kumarappan, and Carlos Trallero-Herrero. Measuring the angle-dependent photoionization cross section of nitrogen using high-harmonic generation. *Physical Review A*, 88(4):043421, 2013.
- [47] Anh-Thu Le, Hui Wei, Cheng Jin, and CD Lin. Strong-field approximation and its extension for high-order harmonic generation with mid-infrared lasers. *Journal of Physics B: Atomic, Molecular and Optical Physics*, 49(5):053001, 2016.
- [48] FA Gianturco, RR Lucchese, and N Sanna. Calculation of low-energy elastic cross sections for electron-cf4 scattering. *The Journal of chemical physics*, 100(9):6464–6471, 1994.
- [49] WR Johnson and CD Lin. Multichannel relativistic random-phase approximation for the photoionization of atoms. *Physical Review A*, 20(3):964, 1979.

- [50] Anh-Thu Le, RR Lucchese, and Chii Dong Lin. High-order-harmonic generation from molecular isomers with midinfrared intense laser pulses. *Physical Review A*, 88(2):021402, 2013.
- [51] MV Frolov, TS Sarantseva, NL Manakov, KD Fulfer, BP Wilson, J Troß, X Ren, Erwin D Poliakoff, AA Silaev, NV Vvedenskii, et al. Atomic photoionization experiment by harmonic-generation spectroscopy. *Physical Review A*, 93(3):031403, 2016.
- [52] MV Frolov, NL Manakov, TS Sarantseva, and Anthony F Starace. Analytic confirmation that the factorized formula for harmonic generation involves the exact photorecombination cross section. *Physical Review A*, 83(4):043416, 2011.
- [53] Dylan C Yost, Thomas R Schibli, Jun Ye, Jennifer L Tate, James Hostetter, Mette B Gaarde, and Kenneth J Schafer. Vacuum-ultraviolet frequency combs from below-threshold harmonics. *Nature Physics*, 5(11):815–820, 2009.
- [54] Y Mairesse, A De Bohan, LJ Frasinski, H Merdji, LC Dinu, P Monchicourt, P Breger, M Kovačev, R Taïeb, B Carré, et al. Attosecond synchronization of high-harmonic soft x-rays. *Science*, 302(5650):1540–1543, 2003.
- [55] P - M Paul, ES Toma, P Breger, Genevive Mullet, F Augé, Ph Balcou, HG Muller, and P Agostini. Observation of a train of attosecond pulses from high harmonic generation. *Science*, 292(5522):1689–1692, 2001.
- [56] Giuseppe Sansone, E Benedetti, Francesca Calegari, Caterina Vozzi, Lorenzo Avaldi, Roberto Flammini, Luca Poletto, P Villoresi, C Altucci, R Velotta, et al. Isolated single-cycle attosecond pulses. *Science*, 314(5798):443–446, 2006.
- [57] Xibin Zhou, Robynne Lock, Wen Li, Nick Wagner, Margaret M Murnane, and Henry C Kapteyn. Molecular recollision interferometry in high harmonic generation. *Physical review letters*, 100(7):073902, 2008.
- [58] Paul AM Dirac. The quantum theory of the emission and absorption of radiation. In *Proceedings of the Royal Society of London A: Mathematical, Physical and Engineering Sciences*, volume 114, pages 243–265. The Royal Society, 1927.
- [59] Enrico Fermi. Nuclear physics. In *A course given by Enrico Fermi at the University of Chicago, 1949*, Chicago: University of Chicago Press, 1950, Rev. ed., volume 1, 1950.
- [60] Philip R Bunker and Per Jensen. *Molecular symmetry and spectroscopy*, volume 2. NRC Research Press, 1998.
- [61] Thomas Grohmann and Monika Leibscher. Nuclear spin selective alignment of ethylene and analogues. *The Journal of chemical physics*, 134(20):204316, 2011.
- [62] Richard N Zare. *Angular momentum: understanding spatial aspects in chemistry and physics*. Wiley-Interscience, 2013.
- [63] SC Wang. On the asymmetrical top in quantum mechanics. *Physical Review*, 34(2):243, 1929.
- [64] Varun Makhija. Laser induced rotational dynamics as a rout to molecular frame measurements. *dissertation*, 2014.
- [65] Henrik Stapelfeldt and Tamar Seideman. Colloquium: Aligning molecules with strong laser pulses. *Reviews of Modern Physics*, 75(2):543, 2003.
- [66] David George Voelz. *Computational fourier optics: a MATLAB tutorial*. Spie Press Bellingham, Wash, USA, 2011.

- [67] Herbert G Winful et al. Physical origin of the gouy phase shift. *Optics letters*, 26(8):485–487, 2001.
- [68] Bob Mellish. taken from <http://www.optique-ingenieur.org/>.
- [69] Les Allen, Marco W Beijersbergen, RJC Spreeuw, and JP Woerdman. Orbital angular momentum of light and the transformation of laguerre-gaussian laser modes. *Physical Review A*, 45(11):8185, 1992.
- [70] R Bourouis, K Ait Ameer, and H Ladjouze. Optimization of the gaussian beam flattening using a phase-plate. *journal of modern optics*, 44(7):1417–1427, 1997.
- [71] Nicolas Passilly, François Treussart, Rolland Hierle, Renaud de Saint Denis, Kamel Aït-Ameer, and Jean-François Roch. Simple interferometric technique for generation of a radially polarized light beam. *JOSA A*, 22(5):984–991, 2005.
- [72] NL Smith, WH Heathcote, G Hechenblaikner, E Nugent, and CJ Foot. Quasi-2d confinement of a bec in a combined optical and magnetic potential. *Journal of Physics B: Atomic, Molecular and Optical Physics*, 38(3):223, 2005.
- [73] TP Meyrath, F Schreck, JL Hanssen, C-S Chuu, and MG Raizen. A high frequency optical trap for atoms using hermite-gaussian beams. *Optics express*, 13(8):2843–2851, 2005.
- [74] JB Bertrand, HJ Wörner, P Salières, DM Villeneuve, and PB Corkum. Linked attosecond phase interferometry for molecular frame measurements. *Nature Physics*, 9(3):174–178, 2013.
- [75] JH Poynting. The wave motion of a revolving shaft, and a suggestion as to the angular momentum in a beam of circularly polarised light. *Proceedings of the Royal Society of London. Series A, Containing Papers of a Mathematical and Physical Character*, 82(557):560–567, 1909.
- [76] Richard A Beth. Mechanical detection and measurement of the angular momentum of light. *Physical Review*, 50(2):115, 1936.
- [77] Benjamin Langdon, Jonathan Garlick, Xiaoming Ren, Derrek J Wilson, Adam M Summers, Stefan Zigo, Matthias F Kling, Shuting Lei, Christopher G Elles, Eric Wells, et al. Carrier-envelope-phase stabilized terawatt class laser at 1 khz with a wavelength tunable option. *Optics express*, 23(4):4563–4572, 2015.
- [78] Toshiaki Kita, Tatsuo Harada, N Nakano, and Hiroto Kuroda. Mechanically ruled aberration-corrected concave gratings for a flat-field grazing-incidence spectrograph. *Applied Optics*, 22(4):512–513, 1983.
- [79] Mette B Gaarde, Jennifer L Tate, and Kenneth J Schafer. Macroscopic aspects of attosecond pulse generation. *Journal of Physics B: Atomic, Molecular and Optical Physics*, 41(13):132001, 2008.
- [80] Daniel Irimia, Dimitar Dobrikov, Rob Kortekaas, Han Voet, Daan A van den Ende, Wilhelm A Groen, and Maurice HM Janssen. A short pulse (7 μ s fwhm) and high repetition rate (dc-5khz) cantilever piezovalve for pulsed atomic and molecular beams. *Review of Scientific Instruments*, 80(11):113303, 2009.
- [81] Shin-Tson Wu. Birefringence dispersions of liquid crystals. *Physical Review A*, 33(2):1270, 1986.
- [82] RA Soref and MJ Rafuse. Electrically controlled birefringence of thin nematic films. *Journal of Applied Physics*, 43(5):2029–2037, 1972.
- [83] G Labrunie and J Robert. Transient behavior of the electrically controlled birefringence in a nematic liquid crystal. *Journal of Applied Physics*, 44(11):4869–4874, 1973.

- [84] N Dudovich, Olga Smirnova, J Levesque, Yu Mairesse, M Yu Ivanov, DM Villeneuve, and Paul B Corkum. Measuring and controlling the birth of attosecond xuv pulses. *Nature physics*, 2(11):781–786, 2006.
- [85] Dror Shafir, Hadas Soifer, Barry D Bruner, Michal Dagan, Yann Mairesse, Serguei Patchkovskii, Misha Yu Ivanov, Olga Smirnova, and Nirit Dudovich. Resolving the time when an electron exits a tunnelling barrier. *Nature*, 485(7398):343–346, 2012.
- [86] Lin Xu, TW Hänsch, Ch Spielmann, A Poppe, T Brabec, and F Krausz. Route to phase control of ultrashort light pulses. *Optics letters*, 21(24):2008–2010, 1996.
- [87] Donald J Bone, H-A Bachor, and R John Sandeman. Fringe-pattern analysis using a 2-d fourier transform. *Applied Optics*, 25(10):1653–1660, 1986.
- [88] F Brunel. Harmonic generation due to plasma effects in a gas undergoing multiphoton ionization in the high-intensity limit. *JOSA B*, 7(4):521–526, 1990.
- [89] Jens Köhler, Matthias Wollenhaupt, Tim Bayer, Cristian Sarpe, and Thomas Baumert. Zeptosecond precision pulse shaping. *Optics express*, 19(12):11638–11653, 2011.
- [90] E Constant, D Garzella, P Breger, E Mével, Ch Dorrer, C Le Blanc, F Salin, and P Agostini. Optimizing high harmonic generation in absorbing gases: Model and experiment. *Physical Review Letters*, 82(8):1668, 1999.
- [91] Katalin Varjú, Y Mairesse, B Carré, MB Gaarde, Per Johnsson, S Kazamias, R López-Martens, Johan Mauritsson, KJ Schafer, Ph Balcou, et al. Frequency chirp of harmonic and attosecond pulses. *Journal of Modern Optics*, 52(2-3):379–394, 2005.
- [92] Pascal Salières, B Carré, L Le Déroff, F Grasbon, GG Paulus, H Walther, R Kopold, W Becker, DB Milošević, A Sanpera, et al. Feynman’s path-integral approach for intense-laser-atom interactions. *Science*, 292(5518):902–905, 2001.
- [93] Mette Borg Gaarde, F Salin, E Constant, Ph Balcou, KJ Schafer, KC Kulander, and Anne LHuillier. Spatiotemporal separation of high harmonic radiation into two quantum path components. *Physical Review A*, 59(2):1367, 1999.
- [94] Maciej Lewenstein, Pascal Salieres, and Anne Lhuillier. Phase of the atomic polarization in high-order harmonic generation. *Physical Review A*, 52(6):4747, 1995.
- [95] Chiara Corsi, Angela Pirri, Emiliano Sali, Alessandra Tortora, and Marco Bellini. Direct interferometric measurement of the atomic dipole phase in high-order harmonic generation. *Physical review letters*, 97(2):023901, 2006.
- [96] Johan Mauritsson, Per Johnsson, R López-Martens, Katalin Varju, W Kornelis, J Biegert, U Keller, MB Gaarde, KJ Schafer, and Anne LHuillier. Measurement and control of the frequency chirp rate of high-order harmonic pulses. *Physical Review A*, 70(2):021801, 2004.
- [97] Jana Preclíková, Stefanos Carlström, Eleonora Lorek, Esben Witting Larsen, Christoph M Heyl, David Paleček, Donatas Zigmantas, Kenneth J Schafer, Mette B Gaarde, and Johan Mauritsson. Spatially and spectrally resolved quantum path interference with chirped driving pulses. *arXiv preprint arXiv:1606.08697*, 2016.
- [98] Lixin He, Pengfei Lan, Qingbin Zhang, Chunyang Zhai, Feng Wang, Wenjing Shi, and Peixiang Lu. Spectrally resolved spatiotemporal features of quantum paths in high-order-harmonic generation. *Physical Review A*, 92(4):043403, 2015.
- [99] C M_ Heyl, J Gütde, U Höfer, and Anne LHuillier. Spectrally resolved maker fringes in high-order harmonic generation. *Physical review letters*, 107(3):033903, 2011.

-
- [100] Enrico Benedetti, Jean-Pascal Caumes, Giuseppe Sansone, Salvatore Stagira, Caterina Vozzi, and Mauro Nisoli. Frequency chirp of long electron quantum paths in high-order harmonic generation. *Optics express*, 14(6):2242–2249, 2006.
- [101] G Kolliopoulos, Boris Bergues, Hartmut Schröder, PA Carpeggiani, László Veisz, George D Tsakiris, D Charalambidis, and P Tzallas. Revealing quantum path details in high-field physics. *Physical Review A*, 90(1):013822, 2014.
- [102] Taro Sekikawa, Tomotaka Katsura, Satoshi Miura, and Shuntaro Watanabe. Measurement of the intensity-dependent atomic dipole phase of a high harmonic by frequency-resolved optical gating. *Physical review letters*, 88(19):193902, 2002.
- [103] Tsuneto Kanai, Eiji J Takahashi, Yasuo Nabekawa, and Katsumi Midorikawa. Destructive interference during high harmonic generation in mixed gases. *Physical review letters*, 98(15):153904, 2007.
- [104] Jan Chaloupka, Robert Lafon, Louis DiMauro, Pierre Agostini, and Kenneth Charles Kulander. Strong-field double ionization of rare gases. *Optics express*, 8(7):352–357, 2001.
- [105] P Mulser, S Uryupin, R Sauerbrey, and B Wellegehausen. Ponderomotive potential and dynamical stark shift in multiphoton ionization. *Physical Review A*, 48(6):4547, 1993.
- [106] TS Sarantseva, MV Frolov, NL Manakov, M Yu Ivanov, and Anthony F Starace. Harmonic generation spectroscopy with a two-colour laser field having orthogonal linear polarizations. *Journal of Physics B: Atomic, Molecular and Optical Physics*, 46(23):231001, 2013.
- [107] Peter Dietrich, Neil H Burnett, M Ivanov, and Paul B Corkum. High-harmonic generation and correlated two-electron multiphoton ionization with elliptically polarized light. *Physical Review A*, 50(5):R3585, 1994.
- [108] Max Möller, Yan Cheng, Sabih D Khan, Baozhen Zhao, Kun Zhao, Michael Chini, Gerhard G Paulus, and Zenghu Chang. Dependence of high-order-harmonic-generation yield on driving-laser ellipticity. *Physical Review A*, 86(1):011401, 2012.
- [109] AD Shiner, C Trallero-Herrero, N Kajumba, H-C Bandulet, D Comtois, F Légaré, M Giguère, JC Kieffer, PB Corkum, and DM Villeneuve. Wavelength scaling of high harmonic generation efficiency. *Physical review letters*, 103(7):073902, 2009.
- [110] EL Falcão-Filho, VM Gkortsas, Ariel Gordon, and Franz X Kärtner. Analytic scaling analysis of high harmonic generation conversion efficiency. *Optics express*, 17(13):11217–11229, 2009.
- [111] GV Marr and JB West. Absolute photoionization cross-section tables for helium, neon, argon, and krypton in the vuv spectral regions. *Atomic Data and Nuclear Data Tables*, 18(5):497–508, 1976.
- [112] Cheng Jin, Julien B Bertrand, RR Lucchese, HJ Wörner, Paul B Corkum, DM Villeneuve, Anh-Thu Le, and Chii Dong Lin. Intensity dependence of multiple orbital contributions and shape resonance in high-order harmonic generation of aligned n 2 molecules. *Physical Review A*, 85(1):013405, 2012.
- [113] Antoine Camper, Amélie Ferré, Nan Lin, Emmanouil Skantzakis, David Staedter, Elizabeth English, Bastian Manschwetus, Frédéric Burgy, Stéphane Petit, Dominique Descamps, et al. Transverse electromagnetic mode conversion for high-harmonic self-probing spectroscopy. In *Photonics*, volume 2, pages 184–199. Multidisciplinary Digital Publishing Institute, 2015.
- [114] Robynne M Lock, Xibin Zhou, Wen Li, Margaret M Murnane, and Henry C Kapteyn. Measuring the intensity and phase of high-order harmonic emission from aligned molecules. *Chemical Physics*, 366(1):22–32, 2009.

- [115] Kenichi Fukui, Teijiro Yonezawa, and Haruo Shingu. A molecular orbital theory of reactivity in aromatic hydrocarbons. *The Journal of Chemical Physics*, 20(4):722–725, 1952.
- [116] John C Slater. A simplification of the hartree-fock method. *Physical Review*, 81(3):385, 1951.
- [117] Charlotte Froese Fischer. Hartree–fock method for atoms. a numerical approach. 1977.
- [118] James P Cryan, Philip H Bucksbaum, and Ryan N Coffee. Field-free alignment in repetitively kicked nitrogen gas. *Physical Review A*, 80(6):063412, 2009.
- [119] Anh-Thu Le, RR Lucchese, and CD Lin. Uncovering multiple orbitals influence in high harmonic generation from aligned n2. *Journal of Physics B: Atomic, Molecular and Optical Physics*, 42(21):211001, 2009.
- [120] Domagoj Pavičić, Kevin F Lee, David M Rayner, Paul B Corkum, and David M Villeneuve. Direct measurement of the angular dependence of ionization for n 2, o 2, and co 2 in intense laser fields. *Physical review letters*, 98(24):243001, 2007.
- [121] Igor V Litvinyuk, Kevin F Lee, Patrick W Dooley, David M Rayner, David M Villeneuve, and Paul B Corkum. Alignment-dependent strong field ionization of molecules. *Physical review letters*, 90(23):233003, 2003.
- [122] Brian K McFarland, JP Farrell, PH Bucksbaum, and M Gühr. High-order harmonic phase in molecular nitrogen. *Physical Review A*, 80(3):033412, 2009.
- [123] Olga Smirnova, Yann Mairesse, Serguei Patchkovskii, Nirit Dudovich, David Villeneuve, Paul Corkum, and Misha Yu Ivanov. High harmonic interferometry of multi-electron dynamics in molecules. *Nature*, 460(7258):972–977, 2009.
- [124] PM Kraus, D Baykusheva, and HJ Wörner. Two-pulse field-free orientation reveals anisotropy of molecular shape resonance. *Physical review letters*, 113(2):023001, 2014.
- [125] H Sann, T Havermeier, C Müller, H-K Kim, F Trinter, M Waitz, J Voigtsberger, F Sturm, T Bauer, R Wallauer, et al. Imaging the temporal evolution of molecular orbitals during ultrafast dissociation. *Physical Review Letters*, 117(24):243002, 2016.
- [126] BP Wilson, KD Fulfer, S Mondal, X Ren, J Tross, ED Poliakoff, J Jose, Anh-Thu Le, RR Lucchese, and C Trallero-Herrero. High order harmonic generation from sf6: Deconvolution of macroscopic effects. *The Journal of Chemical Physics*, 145(22):224305, 2016.
- [127] AA Kovalev, VV Kotlyar, and AP Porfirev. Asymmetric laguerre-gaussian beams. *Physical Review A*, 93(6):063858, 2016.
- [128] A Rouzée, S Guérin, O Faucher, and B Lavorel. Field-free molecular alignment of asymmetric top molecules using elliptically polarized laser pulses. *Physical Review A*, 77(4):043412, 2008.